Large Eddy Simulation of Mixing and Combustion in Combustion Systems under Non-adiabatic Conditions

Vom Fachbereich Maschinenbau
an der Technischen Universität Darmstadt
zur
Erlangung des Grades eines Doktor-Ingenieurs (Dr.-Ing.)
genehmigte

Dissertation

vorgelegt von

M.Sc. Pradeep Kumar Goud Pantangi

aus Nalgonda, Indien

Berichterstatter:	Prof. Dr. habil. Amsini Sadiki
Mitberichterstatter:	Prof. Dr. Friedrich Dinkelacker
Mitberichterstatter:	Prof. Dr.-Ing. Johannes Janicka
Tag der Einreichung:	20. Oktober 2015
Tag der mündlichen Prüfung:	20. Januar 2016

Darmstadt 2016

D17

Hiermit erkläre ich an Eides Statt, dass ich die vorliegende Dissertation selbstständig verfasst und keine anderen als die von mir angegebenen Hilfsmittel verwendet habe. Ich erkläre außerdem, dass ich bisher noch keinen Promotionsversuch unternommen habe.

Pradeep Pantangi

Darmstadt, den 20. Oct 2015

”Knowledge is a burden if it robs you of innocence.
Knowledge is a burden if it is not integrated into life.
Knowledge is a burden if it doesn’t bring joy.
Knowledge is a burden if it gives you an idea that you are wise.
Knowledge is a burden if it doesn’t set you free.
Knowledge is a burden if it makes you feel you are special.”
–Sri Sri Ravi Shankar, An Intimate Note to the Sincere Seeker, Volume 5

for my wife Aruna, sons Srijan & Vihaan and parents

Acknowledgements

This Ph.D. thesis work was carried out during my employment at Institute of Energy and Power Plant Technology (EKT), Darmstadt University while carrying out four different projects TIMECOP-AE, DFG-SPP1141, DFG-SA 836/5-1 and DFG-EXC 259. Pursuing the Ph.D. studies was a great experience and enjoyable. It taught me many aspects of professional, social life alongside getting deep into combustion technology and research domain as a whole. This was possible because of great support from many personal both in professional and personal life.

Prof. Dr.-Ing. Johannes Janicka had provided me this wonderful opportunity to work at one of the world's best combustion institutes where I could have access to state of the art facilities CFD software programs, computational resources, and wealth of expertise on the subject. His vision, hard work, vast experience and his supervision helped me to carry out my work very efficiently and effectively. Foremost, I take this opportunity to thank Prof. Dr.-Ing. Johannes Janicka.

I thank Prof. Dr. Amsini Sadiki for his support and enthusiasm in my research work. He was the one who invited me to pursue my Ph.D. at EKT. He was always available to help me in the combustion research and his advice is always very valuable for my personal and professional life. His great interest, knowledge, diversity of the subjects with strong fundamentals in both physics and mathematics were necessary to carry out the innovative research work to meet the objectives of the next generation combustion systems. I am glad to have an opportunity to work under his constant guidance.

Special thanks to Prof. Dr. Friedrich Dinkelacker for accepting to be co-referent for my thesis work. The master thesis work on combustion at his group laid down my future career path and his support was invaluable. I take this opportunity to thank Prof. Jeroen A. van Oijen for his continuous support and discussions on both adiabatic and non-adiabatic FGM tables.

The office room environment is crucial to accomplishing research work successfully. I thank my office roommates Dmitry Goryntsev, Mouldi Chrigui, Roozbeh Haghighi and Fernando Sacomano for their support. I also thank my colleagues at EKT Wahidullah Ahmadi, Jeremy Weckering, Lukas Schneider, Mejía Juan and Kaushal Nishad for providing friendly environment and scientific discussions.

I thank Arash Hosseinzadeh, Markus Schwind, Zahra Niroobakhsh and Soravit Tangkana who contributed to this work through their Master thesis/ Bachelor thesis/ HiWi job/ summer internship.

I am very grateful to my mother, father and brother for their love, support and motivation during my PhD thesis. I thank Rajesh Chitta for his time and support.

I am lucky to have wonderful, loving and supportive wife Aruna Pantangi. This work might have not possible without her dedication, motivation, understanding and hard work. I couldn′t spend quality time with my son Srijan during my Ph.D., however his presence was a key instrument to get away from the daily stress and get fresh each day. I sincerely thank my wife and son.

Darmstadt, Oct 2015
Pradeep Pantangi

Abstract

The application of combustion modeling in achieving the objective of predicting the combustion systems very precisely is increasing rapidly and it is a necessary tool. Combustion systems involve complex unsteady process such as flow, turbulence, mixing, chemistry, heat transfer and interaction of this phenomenon with each other. The present thesis work is focused on advanced modeling of combustion, mixing and flame wall interaction.

First part of the work aims at an evaluation of the ability of combustion-LES by FASTEST3D CFD code to correctly describe turbulent premixed combustion, especially a rod stabilized unconfined flame. For this purpose the flamelet generated manifold (FGM)-tabulated chemistry approach, in which a variable local equivalence ratio due to a possible entrainment of the environment air is included through a mixture fraction variable, and it is integrated into an appropriate complete model. Since the state of the local distribution of scalars is strongly dependent on the scalar flux known to generate or produce the scalar variance which is a measure of the mixedness, a newly developed Subgrid-scale (SGS) model for scalar flux is investigated. In general, SGS model assessment was mainly achieved through comparisons with Direct Numerical Simulation (DNS) results limited to low Reynolds numbers. Based on a comprehensive, highly resolved experimental database of SGS and mean scalar field quantities, an assessment of this new anisotropic SGS scalar flux model is carried out for a rod stabilized premixed methane V-flame configuration characterized by high Reynolds numbers for which DNS-data are not available. For that purpose, Large Eddy Simulations are performed using the dynamic Smagorinsky SGS model for the flow field. The new anisotropic SGS scalar flux model used to describe the turbulent scalar flux combines the conventional linear eddy diffusivity model with an additional contribution that couples in a thermodynamically consistent way the deviatoric SGS stress tensor and the gradient of the filtered scalar field. The combustion is modeled by a detailed tabulated chemistry based method following the FGM approach. To assess the prediction capability of the anisotropic SGS scalar flux model, LES achievements are compared against the highly resolved experimental data available and other simulation results performed under use of existing SGS scalar flux models. The behavior of SGS scalar fluxes is especially analyzed. It turns out that the new anisotropic model retrieves the overall expected features of the SGS scalar fluxes at both resolved and SGS levels and in both non-reacting and reacting premixed environments. It also allows achieving LES results for the flow and scalar field that are in better agreement with experimental data. A satisfactory agreement for the flow field quantities and species concentrations is achieved along with an assessment of the SGS scalar flux model used.

In the second part, the FGM model based combustion modeling is extended to a complex fuel system for a reliable description of combustion in a gas turbine combustion

chamber. In order to evaluate the capability of the model for predicting combustion processes induced by complex real fuels a high pressure single sector combustor (SSC) is investigated. This combustion chamber is fuelled with pre-vaporized kerosene fuel and features very complex unsteady swirling flow and partially premixed combustion properties. The validation of the designed tool along with the prediction analysis is carried out in terms of comparison between experimental data (achieved with a nozzle fired at 0.4 and 0.6 MPa) and numerical results. This reveals that the proposed LES model is able to capture satisfactorily the flow and combustion properties involving. In particular the flame is predicted to be not always attached to the nozzle. It fluctuates between a lifted and an attached regime. This agrees with experimental findings.

In the last part focus is given on development of the combustion modeling under non-adiabatic conditions. Initially the FGM table generation for non-adiabatic combustion is considered and evaluated with existing methods and thereby it was extended to generate non-adiabatic FGM table from non-unity Lewis number flamelets. A special focus is given to find the optimized reaction progress variable to construct the non-adiabatic FGM table. Firstly the suitable RPV was found, then validated for non-adiabatic combustion taking advantage of 1D flame by an independent (Cantera) CFD solver. The validated non-adiabatic FGM table is used for simulating a 3D laboratory scale non-adiabatic configuration.

The developed FGM table methodology was used to investigate non-adiabatic flame wall interaction (FWI) resulting from a premixed methane fuel jet impinging on a spherical disk. This is achieved by FASTEST3D explicit time stepping LES CFD solver. Here, nitrogen is used as co-flow in order to avoid the interaction with the surrounding air and combustion. The flow field is described by means of the Smagorinsky model with Germano procedure for SGS stresses. The SGS scalar flux in scalar transport equations is modeled by the linear eddy diffusivity model. Artificially thickened flame (ATF) combustion model is used to describe the combustion phenomenon more precisely by LES solver. Catalytic effects on the wall are not considered. Two aspects are especially addressed in this work. First focus is on the grid resolution required near the wall without including a special wall-adapted SGS modeling in reacting configurations. The second aspect is devoted to the integration of the near wall kinetic effects into the FGM framework. For this purpose the enthalpy has been considered as an additional variable in generating the FGM table. Such a tabulated non-adiabatic FGM combustion modeling is applied to FWI for a first time in the present work. The results for the flow field, mixing and combustion properties are presented and analyzed in terms of grid resolution, Reynolds number (in reacting and non-reacting case) and adiabaticity. The results obtained from applied artificially thickened flame combustion models based LES simulations were compared for flow, concentration, temperature and heat flux values from the experimental investigation. Comparisons with available experimental data show satisfactory agreement. An outline of the thermal and flow boundary layer analysis is subsequently provided and special focus is given on heat flux prediction dependency on the type FGM tables considered.

This work is completed by conclusions and outlook which summarize the main findings.

Zusammenfassung

Die Verbrennungsmodellierung wird immer ein wichtiger Bestandteil der Auslegungs- und Optimierungsaufgaben von Verbrennungssystemen bleiben. Solche Systeme beinhalten komplexe instationäre Prozesse, wie Strömung, Turbulenz, Mischung, Chemie, Massen- und Wärmetransport in wechselseitiger Interaktion. Die vorliegende Arbeit beschäftigt sich mit der Entwicklung und Validierung von fortgeschrittenen Modellen zur Beschreibung der Verbrennungs- und Mischungsprozesse sowie der Flammen-Wand Interaktion mit Hilfe der Technik der Grobstruktursimulation (im Englischen Large Eddy Simulation, LES).

Der erste Teil der Arbeit evaluiert die Fähigkeit der Verbrennungs-LES für Vormischverbrennung mit dem "FASTEST3D CFD"Code. Das Modell basiert auf einer tabellierten Chemie, welche im Rahmen des sogenannten Flamelet Generated Manifold (FGM) tabellierten Chemie-Ansatzes generiert wird. In diesem Verfahren wird ein lokales aber variables Äquivalenzverhältnis integriert, um den Effekt der Umgebungsluft in den Mischungsgrad zu berücksichtigen.

Da die Skalarflusskomponenten zur Produktion der skalaren Varianz eine entscheidende Rolle spielen, welche den Stand der lokalen Verteilung von Skalaren und somit die Güte der skalaren Vermischung in turbulenten Mischungsprozessen bestimmt, wird ein neues anisotropes Feinstrukturmodell (im Englischen Sub-Grid-Scalar (SGS) Model) für den Skalarflussvektor entwickelt. In dieser Arbeit wird eine umfassende, experimentelle Datenbank der SGS und gemittelten Skalarfelder aus einer turbulenten vorgemischten V-Flamme zur Verfügung gestellt, um das neu SGS Skalarflussmodell zu validieren. Die erzielten Resultate werden mit der Vorhersage von existierenden Modellen verglichen bzw. kritisch evaluiert. Das neue anisotrope SGS Skalarflussmodell kombiniert die Eigenschaft eines herkömmlichen linearen Wirbeldiffusivitätsmodells mit einem zusätzlichen Beitrag, welcher die Anisotropie in einer thermodynamisch konsistenten Weise durch die Kopplung des deviatorischen SGS Spannungstensors und des Gradienten des gefilterten Skalarfelds miteinbezieht. Es stellt sich heraus, dass das neue anisotrope Modell die erwarteten Merkmale der SGS skalaren Flüsse sowohl für den aufgelösten Anteil als auch für die SGS Größen unter nicht-reagierenden und reagierenden Bedingungen zufriedenstellend liefert. Im zweiten Teil wrd das auf dem FGM-Ansatz basierende Verbrennungsmodell erweitert, um die Verbrennung komplexer Kraftstoffe in Gasturbinen zuverlässig beschreiben zu können. Um die Leistungsfähigkeit des Modells zur Vorhersage von Verbrennungsprozessen mit komplexen realen Brennstoffen zu validieren, wird eine Hochdruck-Einzelsektor Brennkammer (SSC) untersucht. Diese Brennkammer ist mit vor-verdampftem Kerosin angetrieben und weist sehr komplexe instationäre Drallströmung und teil-vorgemischte Verbrennungseigenschaften auf. Die Validierung des Modells und die Analyse der Vorhersage werden durch Vergleiche zwischen experimentellen Daten und numerischen Ergebnissen erreicht. Diese zeigen, dass das vorgeschlagene LES-Modell in der Lage ist,

die Strömungs- und Verbrennungseigenschaften zufriedenstellend zu erfassen. Insbesondere wird die Position der Flamme korrekt erfasst, die zwischen einen angehobenen Flammetyp und einem angehängten Flammeregime in Übereinstimmung mit experimentellen Ergebnissen schwankt.

Im letzten Teil der Arbeit wird die Entwicklung eines Verbrennungsmodells für nicht-adiabatische Verbrennung beschrieben. Zunächst wird die FGM Tabellierung für nicht-adiabatische Verbrennungsbedingungen erweitert, wobei das bestehende Verfahren für die Generierung der FGM-Tabelle für Lewis-Zahl ungleich Eins zunächst verwendet wird. Dann wird eine Strategie entwickelt, um die optimalen Reaktionsfortschrittsvariablen für die Erzeugung der nicht-adiabatischen FGM Tabelle zu bestimmen. Diese Vorgänge werden mit der 1D Flamme aus einem klassischen CFD Löser (Cantera) validiert.

Anschließend wird die entwickelte Methode für die Beschreibung der Flamme-Wand-Interaktionsprozesse (FWI) in einem vorgemischten Methankraftstoffstrahl eingesetzt. Hier wird Stickstoff als Co-flow verwendet, um die Wechselwirkung zwischen der Umgebungsluft und der Flamme zu vermeiden. Wie in anderen Teilen der Arbeit wird das Strömungsfeld mit dem Smagorinsky Modell und Germano-Verfahren für die Schließung des SGS-Spannungstensors verwendet. Insbesondere wird der SGS Skalarfluss in den skalaren Transportgleichungen durch das lineare Wirbeldiffusionsmodell hier modelliert, um die spezifischen Effekte des Verbrennungsmodells zu untersuchen. Das künstlich verdickte Flammen- (im Englischen Artificially Thickened Flame (ATF) Model) Verbrennungsmodell wird verwendet, um die Dicke der Flamme genauer mit LES auflösen zu können. Katalytische Effekte auf der Wand sind nicht berücksichtigt. Zwei Aspekte stehen vor allem im Zentrum der Untersuchung. Zunächst wird der Schwerpunkt auf die Gitterauflösung in Wandnähe einer reagierenden Konfiguration ohne spezielle Wandfunktion gelegt. Der zweite Aspekt beschäftigt sich mit der Integration der in der Nähe der Wand existierenden kinetischen Effekte in die FGM Tabellen. Zu diesem Zweck wird die Enthalpie als zusätzliche Variable bei der Generierung der FGM-Tabelle betrachtet. Eine so resultierende FGM-Tabellierungsstrategie wird für die Untersuchung der FWI im Rahmen dieser Arbeit erstmalig eingesetzt. Die Ergebnisse des Strömungsfelds, der Misch- und Verbrennungseigenschaften werden dargestellt und analysiert als Funktion der Gitterauflösung, Reynolds-Zahlen (im reagierenden und nicht-reagierenden Fall) sowie der Adiabatizität. Die erzielten Resultate für die FWI werden für die Strömung, Konzentration, Temperatur und den Wärmefluss mit den experimentellen Daten verglichen und beurteilt. Diese Vergleiche zeigen zufriedenstellende Übereinstimmungen. Eine Analyse der thermischen und Strömungs-Grenzschichten wird anschließend durchgeführt, wobei die Abhängigkeit der Wärmeflussvorhersage von der FGM Tabellen auch betrachtet wird.

Zum Schluss werden die wichtigsten Resultate dieser Arbeit zusammengefasst und einen Ausblick gegeben.

Contents

1 Introduction **1**
- 1.1 State of the art . . . 3
  - 1.1.1 Turbulent mixing of scalars . . . 4
  - 1.1.2 Flame wall interaction . . . 5
- 1.2 Structure of the thesis . . . 7

2 Theory and Modeling **9**
- 2.1 Fundamentals of flow and mixing . . . 9
  - 2.1.1 Conservation of mass . . . 11
  - 2.1.2 Conservation of momentum . . . 12
  - 2.1.3 Conservation of scalars . . . 12
- 2.2 Fundamentals of turbulent flow . . . 15
  - 2.2.1 The scales of turbulent flow . . . 16
  - 2.2.2 The scales of turbulent mixing . . . 19
- 2.3 Modelling of turbulent flows . . . 21
  - 2.3.1 Direct numerical simulation (DNS) . . . 21
  - 2.3.2 Reynolds averaged numerical simulation (RANS) . . . 22
  - 2.3.3 Large eddy simulation (LES) . . . 23
  - 2.3.4 Near wall flow modelling . . . 25
- 2.4 Fundamentals of combustion . . . 25
  - 2.4.1 Chemical kinetics and reaction mechanism . . . 26
  - 2.4.2 Modes of combustion . . . 28
  - 2.4.3 Combustion regimes . . . 32
  - 2.4.4 Reduction methods for combustion chemistry . . . 35
  - 2.4.5 Turbulent chemistry interactions . . . 36
- 2.5 Non-adiabatic combustion . . . 38
  - 2.5.1 Fundamentals of Flame wall interaction . . . 39

3 LES of flow, mixing, combustion with and without heat loss **40**
- 3.1 Filtering of variables for LES . . . 40
- 3.2 Modeling technique . . . 42
- 3.3 Modeling sub-grid scales of the flow . . . 43
  - 3.3.1 Eddy viscosity model . . . 44
- 3.4 Modeling of scalar sub-grid scales . . . 47
  - 3.4.1 Classical eddy difusivity SGS scalar flux model . . . 47
  - 3.4.2 Eddy diffusivity SGS scalar flux model with dynamic procedure . . . 48
  - 3.4.3 Scale similarity SGS scalar flux model . . . 49
  - 3.4.4 SGS scalar flux mixed model . . . 49
  - 3.4.5 Non-linear anisotropy SGS scalar flux model . . . 50

3.4.6 Explicit algebraic anisotropy SGS scalar flux model 51
3.5 Modeling of LES combustion 53
3.5.1 Artificially thickened flame model 54
3.6 Modeling of LES with heat loss 59
3.7 Modeling of LES with heat loss for non-unity Lewis effects 59

4 Numerical method **62**
4.1 Finite volume method 64
4.2 Coordinate transformation 67
4.3 Discretization of the convective, diffusion and accumulation (time) terms . 68
4.3.1 Spacial discretizaion 69
4.3.2 Time dependent discretization 72
4.4 Pressure velocity coupling 75

5 Tabulated chemistry **80**
5.1 Three dimensional tabulated chemistry (FGM) 80
5.2 Non-adiabatic combustion 81
5.2.1 Construction of non-adiabatic FGM table 83
5.2.2 FGM and LES CFD solver coupling 85
5.3 Validation of enthalpy based FGM table 85

6 LES solution procedure **91**
6.1 Boundary conditions 91
6.1.1 Inlet boundary conditions 91
6.1.2 Outlet boundary conditions 93
6.1.3 Wall boundary conditions 93
6.1.4 Symmetry boundary conditions 94
6.1.5 Periodic boundary conditions 94
6.2 Solver 95
6.3 Time-Averaging Procedure 97
6.4 Parallelization 98
6.5 Study of boundary conditions in perforated nozzle 99

7 Combustion processes of complex fuels **103**
7.1 Premixed combustion of rod stabilized V-flame 103
7.1.1 Configuration and boundary conditions 104
7.1.2 Results and discussions 107
7.1.3 Combustion modeling with advanced SGS scalar flux models 110
7.1.4 Conclusion 116
7.2 Non-premixed prevaporized kerosene combustion in a swirl SSC 117
7.2.1 Configuration and boundary conditions 117
7.2.2 Results and discussions 120
7.2.3 Conclusions 128

8 Complex combustion process with heat loss **129**
8.1 Flame wall interactions - Non-adiabatic configuration 129
8.2 Experimental setup 129
8.3 Computational setup 130

8.4 Results and Discussions 135
8.4.1 Near wall resolution under isothermal conditions (Non-reacting results) 135
8.4.2 Reacting cases 139
8.4.3 Outline of thermal and flow boundary layer analysis 150
8.5 Dependency of wall heat flux on Lewis number in FGM table 151
8.6 Conclusions 155

9 Conclusions and Outlook **157**

References **159**

List of Figures

2.1 Reynolds experiment laminar (Top), Transition(middle) and Turbulent (bottom) in a pipe for a trace injected (dark blue line) 11
2.2 Development of boundary layer on a flat plate [88] 11
2.3 Two-point velocity correlation function versus the distance between two point Δx for homogeneous isotropic turbulence 17
2.4 Schematic representation of the turbulent kinetic energy spectrum as a function of the wavenumber k_ω for isotropic homogeneous turbulence. (L_I, L_T and L_K correspond to the integral length scale, the Taylor length scale and Kolmogorov length scale, respectively.) 18
2.5 Schematic representation of scalar energy spectrum normalized by the integral scales as a function of the wave number k_ω for isotropic homogeneous scalar field turbulence [85]. 20
2.6 Turbulent scales resolved/modeled by RANS, LES, and DNS (velocity ---, scalar —) [69]. 23
2.7 Schematic representation of n-Hepetane premixed combustion for both species mass fractions and temperature, simulated with Cantera [32] 29
2.8 A schematic drawing of an idealized steady premixed flame in a duct . . . 32
2.9 Premixed combustion regime diagram [151] 33
2.10 Premixed combustion regime in the LES context, while non-dimensional filter width is represented in terms of the Karlovitz number.[161, 58] 35
2.11 A schematic represenation flame wall interaction phenomenon [163] 39

4.1 A typical CV and the notation used for a Cartesian 3D grid [63, 181, 115] . 65
4.2 Topology and control volume notification[39, 1] 66
4.3 Variables arrangement on staggered and collocated grid [63, 181, 115] . . . 66
4.4 Coordinate system transormation [63, 181, 115] 67
4.5 Central Differencing Scheme (bottom), Upwind Differencing Scheme (top)[63, 115] 69
4.6 Labelling neighouring cells for TVD 72
4.7 Mach number values and the corresponding flow regimes 76

5.1 Maximum CO_2 and H_2O mass fractions achieved by simple balance, adibataic and non-adibatic combustion 81
5.2 Procedure for generating various flamelets required for non-adiabatic FGM table 84
5.3 Representation of 1D Flamelets transformed into independent combustion variables space 85
5.4 LES solver coupling with FGM table for non-adiabatic case 86

5.5 CO_2 mass fraction profiles in physical space of grid number obtained from RPV1 based FGM table for methane(ϕ=0.83,1.0,1.2) and n-heptane (ϕ=1.0) and compared wuth 1D DNS Cantera simulations 87
5.6 Temperature and mass fraction profiles of CO,OH,CH3,H20 in physical space of grid number obtained from 1D DNS Cantera simulations for methane(ϕ=0.83,1.0,1.2) and n-heptane (ϕ=1.0) 88
5.7 Validation of non-adiabatic FGM tabulation: Temperature, mass fraction profiles of CO,OH,CH3,H20 in physical space of grid number obtained from various definitions of RPVs in tabulating FGM look-up table for methane(ϕ=0.83,1.0,1.2) and n-heptane (ϕ=1.0) compared against 1D DNS Cantera simulations 89

6.1 Recommended parallelization of block structured mesh in the FASTEST3D [115] 99
6.2 Opposed jet configuration including the perforated plate(TGP): Red line indicated mesh used for reducing the boundary layer and for obtaining uniform flow in the upstream of the TGP 100
6.3 The representation of boundary layer development and effective diameter at the exit of TGP plate 101
6.4 The effective hole diameter calculated as function of Reynolds number for the single jet flow 101

7.1 Burner set up 105
7.2 Simulated domain with nozzle and flame stabilizing rod 106
7.3 Representation of mesh on a plane across the stabilization rod and passing through centre line of the nozzle with super imposed by instantaneous mixture fractip 106
7.4 Experimentally measured reaction progress variable (left), numerically obtained reaction progress variable (right) 107
7.5 Reaction progress variable source term (left) and Temperature gradient (right) 108
7.6 Comparison of measurements against numerically obtained corresponding data: Axial velocity(left), right: radial velocity (right) (Num-solid line, experimental-dashed line) 108
7.7 Comparison of numerical simulations (x-axis) against experiments (y-axis) in form of scatter plots : First from top: Axial velocity (left)Axial velocity locations(right), Second from top: Radial velocity (left) Radial velocity fluctuations (right), Third from top: RPV (left) RPV fluctuations (right), Bottom: Axial SGS fluxes(left) and Radial SGS fluxes(right) 109
7.8 Comparison of axial (top) and radial (bottom) SGS flux experimentally measures (dashed line) against the numerically obtained (solid line) at four different locations above the flame stabilization rod 109
7.9 Correlation plots between directly measured SGS flux (x-axis) and modelled SGS-flux (y-axis, with different analytical models). Diagonal line indicates perfect correlation. All fluxes are in m/s. Gray symbols: < 0.5 (< 0.13), black symbols: > 0.5 (> 0.13) [127, 154, 152] 111

7.10 Time averaged mean axial (left), radial (right) velocity. Experimental results(.....), EDM (.....), Dynamic EDM (.....), Anisotropic (.....) at y = 0.002 m 111
7.11 Time averaged mean axial velocity (left); fluctuations (right) EDM (.....), Dynamic EDM (.....), Anisotropic (.....) at y = 0.012 m (bottom), y = 0.05 m (middle), y = 0.1 m (top) 111
7.12 Time averaged mean radial velocity (left); fluctuations (right) EDM (.....), Dynamic EDM (.....), Anisotropic (.....) at y = 0.012 m (bottom), y = 0.05 m(middle), y = 0.1 m (top) 112
7.13 RPV from Experiment (left), Eddy diffusivity model (second from left), Dynamic eddy diffusivity model (third from left)anisotropic(right) 113
7.14 RPV from Experiment (left), Eddy diffusivity model (second from left), Dynamic eddy diffusivity model(third from left) Anisotropic model(right) . 114
7.15 RPV from Experiment (left), Eddy diffusivity model (second from left), Dynamic eddy diffusivity model (third from left) Anisotropic model(right) 114
7.16 RPV SGS scalar flux axial (left), adial (right) in normalized RPV space, Experimental (red, EDM (green, Anisotropic model (pink) 115
7.17 SGS scalar flux components (top: axial; bottom: radial) as function of reaction progress variable (distance from nozzle exit: 17.9 mm left, 19.4 mm right): Red: gradient ansatz, Green: anisotropic model and Blue: Experiment 116
7.18 Experimental setup (bottom) and swirled nozzle (top) 118
7.19 Computational domain with instantaneous isosurfaces of the reaction source term 119
7.20 Time averaged axial velocity magnitude (m/s) (top) and time averaged velocity streamlines computed from LES (bottom) 121
7.21 Radial profiles of time averaged axial (u), radial (w) and tangential (v) velocity components and turbulent kinetic energy (TKE) at 5 mm (top) and 10 mm from the exit of the nozzle (_simulated , • Exp) 122
7.22 : Radial profiles of time averaged axial (u), radial (w) and tangential (v) velocity components and turbulent kinetic energy (TKE) at 15 mm (top) and 20 mm from the exit of the nozzle (_simulated , • Exp) 123
7.23 Contour plots of instantaneous (top) and time averaged (bottom) a) RPV source (kg/m3-s) b) CO mass fraction c) temperature (K) d) source term (kg/m3-s) e) RPV resolved source variance f) temperature (K) on a plane passing through the center of nozzle 124
7.24 Qualitative representaion of OH concentration and kerosene. Top: Experiment (bold contour: 25% of maximum; middle contour: 50% of maximum; light contour: 75% of maximum). Bottom: simulation 125
7.25 Temperature (K) (top) RPV source term (kg/m^3-s) (bottom) on a plane passing through the center of nozzle - 4 bar case 126
7.26 Radial profiles of time averaged axial (u)(top) and turbulent kinetic energy (TKE)(bottom) at 5, 10, 15 and 20 mm (left to right) from the exit of the nozzle (_simulated , • Exp) - 4 bar case 127
7.27 Power spectral density Experimental (left) Numerical(right) dashed line(left), blue line(right) denotes a -5/3 slope - 4 bar case 128

8.1 Schematic representation of the experimental setup. 130
8.2 Computational domain including the nozzle and the impinging wall. 134
8.3 Schematic representation of the mesh on a plane passing through the nozzle. This mesh is constructed using block structured grid with 4.2 million CVs. 134
8.4 The original perforated plate used in simulation include the blockage on holes (which are beyond 30 mm diameter, left). Grey contours represent fuel nozzle geometry. Iso-surfaces of axial velocities Vy (second from left) and Cartesian velocities Ux (third from from left), Wz (right) at 3.0 m/s , ±0.15m/s and ±0.15m/s, respectively. 136
8.5 Profiles of normalized axial velocities and their fluctuations at upstream distances from the fuel nozzle exit d = 20, 30, 35, 40 and 47 mm. (CFA05 = —, Exp = ♦ [19]. 137
8.6 y^+ value in the first cell on the wall along the impinging wall stream-wise direction, green line = CFA05, green dashed line = CCA05, blue line = CFA25, pink line = CFA50, pink dashed line = CCA50. 137
8.7 $\triangle/\eta$ on a plane passing through the center of the nozzle in the main fuel jet core (zoomed in right figure). 138
8.8 Instantaneous axial velocity (left in m/s) and radial velocity (right m/s) contours on a plane passing through the center of the nozzle. 138
8.9 Axial profile at three radial positions (r = 0 mm (left), r = 1 mm (middle) and r = 5 mm (right)) of axial velocities (bottom) and their fluctuations (top) normalized by bulk velocity of non-reacting cases [green line = CFA05, green dashed line = CCA05, blue line = CFA25, pink line = CFA50, pink dashed line = CCA50, ♦ = Experiment (Non-reacting case)]. 138
8.10 Axial profile at three radial positions (r = 0 mm (left), r = 1 mm (middle) and r = 5 mm (right)) of radial velocities (bottom) and their fluctuations (top) normalized by bulk velocity of non-reacting cases [green line = CFA05, green dashed line = CCA05, blue line = CFA25, pink line = CFA50, pink dased line = CCA50, ♦ = Experiment (Non-reacting case)]. . 139
8.11 Comparison of temperature $[K]$ (top-left), RPV source $[1/s]$ (top-middle), density (kg/m^3)(top-right) and concentrations of CO (bottom-left), OH (bottom-middle) and CH_4(bottom-right) from 1D adiabatic premixed simulations at equivalence ratio 1.0. Red line are results obtained from adiabatic table and blue line results are obtained using non-adiabatic FGM table. 141
8.12 Reacting adiabatic cases: Axial profile at three radial positions (r = 0 mm (left), r = 1 mm (middle) and r = 5 mm (right)) of time-averaged axial velocities (bottom) and their fluctuations (top) normalized by bulk velocity of reacting cases, ♦ = Experimental reacting case. 142
8.13 Reacting adiabatic cases: Axial profile at three radial positions (r = 0 mm (left), r = 1 mm (middle) and r = 5 mm (right)) of radial velocities (bottom) and their fluctuations (top) normalized by bulk velocity. 143
8.14 Reacting adiabatic cases: Axial profile at two radial positions (r = 0 mm, r = 20 mm) of averaged CO species mass fraction (First two from left) and their fluctuations (last two from right). 143

8.15 Reacting adiabatic cases: Axial profile at two radial positions (r = 0 mm, r = 20 mm) of averaged temperature (First two from left) and their fluctuations (last two from right). 143
8.16 Instantaneous enthalpy contours superimposed by line contours of RPV source term (left), a magnified view of the selected area (right)for case RFN05. 144
8.17 Instantaneous iso-surface of OH mass fraction at 0.012 colored by temperature scale (in K) and clipped mixture fraction on a plane passing through center of plane (left) and magnified view of the selected area (right). 144
8.18 Time averaged reaction progress variable source term: Top Left-RFN05, Top Right-RCN05, Bottom Left-RFA05N, Bottom Right-RCA05. 145
8.19 Axial profile at three radial positions (r = 0 mm (left), r = 1 mm (middle) and r = 5 mm (right)) of time-averaged axial velocities (bottom) and their fluctuations (top) normalized by the bulk velocity of reacting cases, ♦ = Experimental reacting cas.e 146
8.20 Reacting cases: Axial profile at three radial positions (r = 0 mm (left), r = 1 mm (middle) and r = 5 mm (right)) of radial velocities (bottom) and their fluctuations (top) normalized by the bulk velocity. 147
8.21 Reacting cases: Axial profile at two radial positions (r = 0 mm, r = 20 mm) of averaged CO species mass fraction (First two from left) and their fluctuations (last two from right). 147
8.22 Reacting cases: Axial profile at two radial positions (r = 0 mm, r = 20 mm) of averaged temperature (First two from left) and their fluctuations (last two from right). 148
8.23 Radial heat flux on impinging wall, radial temperature profile imposed on the impinging wall in CFD simulations for RFN05 case. (measured heat flux = ♦ , simulated heat flux = — , Temperature profile imposed = —). 149
8.24 Schematic representation of a 1D premixed stagnation point flame on the water cooled non-adiabatic wall (thick orange line represents temperature profile). 149
8.25 Radial profiles heat flux on impinging wall, radial temperature profile imposed on impinging wall in CFD simulations for RFN05 case. Results are obtained using heat transfer coefficient (measured heat flux = ♦ , simulated heat flux = — , Heat transfer coefficient = —, (Calculated heat transfer coefficient from measured data = ♦). 149
8.26 Axial profiles of flow and thermal boundary layers comparison from case RFN05 on radial positions of r = 1 mm (red), r = 5 mm (green) , r = 10 mm (blue) , r = 15 mm (pink) and r = 20 mm (aqua). Note that local gas temperature (T) at T_N = 1 corresponds to premixed fuel jet temperature and at T_N=0 to adiabatic flame temperature. 150
8.27 Axial profile at three radial positions (r = 0 mm(left), r = 1 mm(middle) and r = 5 mm(right)) of time-averaged axial velocities(bottom) and their fluctuations(top) normalized by the bulk velocity of reacting cases,♦ = Experimental reacting case 152
8.28 Reacting cases: Axial profile at three radial positions (r = 0 mm(left), r = 1 mm(middle) and r = 5 mm(right)) of radial velocities(bottom) and their fluctuations(top) normalized by the bulk velocity 153

8.29 Bottom: Axial profile at two radial positions (r = 0 mm, r = 20 mm) of averaged CO species mass fraction (First two from left) and their fluctuations(last two from right), Top: Axial profile at two radial positions (r = 0 mm, r = 20 mm) of averaged temperature (First two from left) and their fluctuations(last two from right) 153
8.30 Radial heat flux on impinging wall, radial temperature profile imposed on the impinging wall in CFD simulations for F1, F2, F3, F4 and F5 cases . . 155

9.1 Flow diagram for chronological interactive flame wall interaction CFD model in FASTEST3D CFD solver 158

List of Tables

3.1 Classification of LES combustion modeling 54

4.1 Advantages of implicit and explicit time integration methods 73

5.1 1D DNS/ 0D cases (^{s} = Stagnation flame, ^{a} = Free propagating adiabatic flame) 82
5.2 RPV Definitions 87

7.1 Boundary conditions 105
7.2 Operating conditions for 4 bar and 6 bar cases 119

8.1 Boundary conditions for FGM and FASTEST under adiabatic conditions. . 133
8.2 Boundary Conditions for FGM and FASTEST under non-adiabatic conditions. 134
8.3 Operating conditions. 135
8.4 Investigated cases. 135
8.5 3D case details, All cases with premixed methane at $\phi = 1.0$ and N_2 as Co-flow. Note that the case F5 corresponds to Re = 5000, Le = 1, Efficiency = 1, Mix = Yes RPV = Yes and with constant thickening factor of 2. 151

Chapter 1

Introduction

Combustion is one of the oldest technologies known to mankind and its applications were evolved hand-in-hand with the evolution of human civilization. It is being assumed that fire was used and manipulated as early as Paleolithic era and for cooking around more than 1.8 million years ago. Invention of smelting, which is a combustion driven process, was the primary reason for the evolution of Stone Age into the Bronze Age. In the subsequent times, combustion was used for various purposes such as cooking, heating, hunting, protection. etc. The well-documented studies for systematic understanding of combustion process were rare until the 16^{th} century. Sir Francis Bacon, Robert Fludd, Otto von Guericke, Robert Hooke were considered as the pioneers who had worked towards understanding of combustion physics in 17^{th} century. In 1772, French chemist Antoine-Laurent Lavoisier had discovered for the first time that air combined with Sulfur resulting in the higher weight of the products. Sir Humphry Davy's works on combustion experiments to determine the flame temperatures, a catalytic combustion were important stepping stones towards the ongoing combustion research. The critical role of heat in combustion process was discovered by Sir Benjamin Thompson. Substantial progress had been made during the 19^{th} century in understanding and developing new theories such as kinetic theory of gases and its relationship with thermodynamics and themochemistry. During the same period concepts such as flame speeds, combustion mechanisms were developed. In 20^{th} century, combustion of fossil fuels has became the main source of energy in transportation (aero, surface, rail and water transportation), space exploration, energy for electricity, energy for heating and various metal processing techniques. Advances in experimental techniques and computational methods allowed to gain a deeper understating about combustion and there by developing more compatible systems in both 20^{th} and 21^{st} centuries. Combustion is one of the primary driving forces of development in each generation during last millennium and especially during the last 150 years. As per the recent estimations combustion of fossil fuels will remain as one of the primary source of energy at least for next few generations. More than 80% of the world's energy consumption involves some form of combustion of fossil fuels (coal, gas, oil, waste & etc.). And the demand is expected to rise in absolute numbers by about 7% from 2011 to 2030, i.e. 7500 TWH [145, 144]. Ensuring the energy security is imperative as fossil fuel resources are scarce and rapidly depleting.

The sustainable development of combustion technology is very crucial for the rapid development of the world economy [2, 82], especially in developing courtiers. The very competitive, fast- changing scenarios of the world socio-economic policies made it necessary to have:

- Energy efficient combustion systems

- Lower emission combustion systems
- Optimized operating parameters under various circumstances
- Minimized maintenance cost
- Longer life time
- Cheaper initial and operating costs

Above mentioned objectives can be achieved by various means independently, for example:

- Smaller size ICE (internal combustion engine) with turbo charger and efficient heat management with optimized designs
- In the context of gas turbines, the RQL (rich burn - quick quench - lean burn) or LPP (lean premixed pre-vaporized) concepts for lower NOx
- Re-defining a new paradigm of operational procedure based on study of detailed physics involved in complete process flow like in furnaces [246].

Achieving these mentioned objectives through experiments and prototyping is neither time-efficient nor economical. It is imperative to respect the deadlines of the Kyoto protocol [169] of the United Nations framework convention on climate change and to find the sustainable solutions beyond. The rapid developments in emerging technologies, very competitive market forces and fast approaching stringent emission norms made it necessary to have tools which can be used in achieving above mentioned objectives precisely and quickly. These technologies which need to be addressed for meeting these objectives, are involved with flow, turbulence, multiphase (spray), combustion, heat and mass transfer, boundary layer problems on flow/fluid side. The time and length scales involved in this phenomenon are of wide range. The majority of combustion systems operate under turbulent region, and simplest combustion is involved in many intermediate reaction steps (i.e. reaction mechanism). In recent times computational fluid dynamics (CFD) is found to be very useful tool in understanding the physics involved in combustion process. CFD was already proven a very useful, predictive and a design tool for many applications involving simple physics such as flow, since late 1950's. The potential of a use of CFD technology in many applications is realized recently and being applied to the wide spectrum of industrial applications such as filtration, ground water, petrochemicals, automobile, polymers, metallurgy, mineral, process industry, aerospace, building ventilation, semiconductors, thermal management, movies and many more. The complexity of combustion process has made it necessary to develop methods and tools for addressing wide range of physics involved in it. CFD is the branch of applied science which converts involved physics of flow, thermal, reaction process into non-linear, partial derivative equations (PDEs) called Navier-stokes equations. These equations are solved in a domain which is divided into many finite control volumes (CV) (finite difference and finite element methods also exist). In general, the physics of the flow don't change within a single CV. In contract, process- determined physics of turbulent flows modifies within a CV (sub- grid scale or SGS) and thereby beyond CVs. The evolution CFD methods during the last 60 years have contributed substantially with wide range of models in capturing accurately these SGS physics. The PDEs representing are discretized

on computation domain grid and solved iteratively in time-domain. The main CFD methods for turbulent combustion single phase flows are direct numerical simulations (DNS), large eddy simulations (LES), Reynolds stress models (RSM), unsteady Reynolds averaged simulations (URANS) and steady state Reynolds averaged simulations (RANS), a brief overview of these models will be presented in the next chapters 2 and 3. The most of the energy is carried by the large scales of the flow, solving large scales and modeling SGS scales of the flow is more accurate than RANS approach and less expensive than DNS simulations. So, LES approach is more practical and suitable for solving industrial applications as the rapid development in computation methods, cheaper and faster computing resources are available now. The application of LES for combustion systems with advanced SGS models was demonstrated as a very promising tool for more precise modeling of flow, turbulence, heat transfer, mixing and combustion. In the present work, two important aspects of combustion modeling are addressed. While the first one is on mixing of the scalars at sub- grid -scales (SGS) levels the other one is about the modeling of combustion and with special focus towards the flame wall interaction (FWI). Also a section on the state of the art on the SGS mixing and combustion modeling of FWI is presented.

1.1 State of the art

Turbulent premixed combustion plays an important role in many technical applications, e.g., in spark ignition engines and in gas turbines. While RANS computations of premixed flames are well reported in the literature, LES of premixed combustion remains difficult due to the thickness of the premixed flame is about 0.1-1 mm and generally smaller than the LES mesh size. Physical and chemical features of combustion LES have been discussed by Janicka and Sadiki [93], and Pitsch [160] with emphasis focused on important aspects of an overall model. Several approaches have been reviewed for modeling of premixed turbulent combustion; this comprehends turbulence controlled models (eddy break up, eddy dissipation models), statistical approach based models (PDF Transport equations, CMC, etc.), flamelet based models (surface Density models, G-equations, BML based models), artificially thickened flame (ATF) or (filtered) tabulated chemistry for LES (F-TACLES) approach. With regard to chemistry, the details of chemistry is unavoidable if one has to address auto-ignition, flame stabilization, recirculation products which may include intermediate species, and the prediction of some pollutants [214, 166, 204]. The reduction and tabulation of chemical species behavior prior to LES remains one of the available options that is being investigated to downsize combustion chemistry in order to make it compatible with flow solvers [203, 207, 53].

The turbulent mixing is very crucial in determining the homogeneous mixing which is crucial in combustion process, absorption, extraction, drying, etc. In combustion applications, chemical engineering processes which deal with scalars (mass fractions, heat and etc) and momentum transfer the need of efficient mixing systems and a reliable prediction of mixing is strongly increased, (e.g. [21]). Although studies have been extensively carried out to clarify the physics of turbulent mixing processes (e.g. [91]), the extreme complexity due to the intriguing complex topology of fluid motions and scalar fields does not

yet allow a satisfactory understanding (as discussed in [69]). For complex configurations of technical importance in which experimental investigations are difficult to be accomplished, a comprehensive knowledge of phenomena can well be achieved only by solving the equations governing the processes involved in the frame of CFD [224]. In the field of CFD, Large Eddy Simulation (LES) [31] stands in the middle of the range of turbulent flow prediction tools, between Direct Numerical Simulation (DNS) [138] and Reynolds Averaging Numerical Simulation (here RANS) [193]. Under certain conditions RANS can be precise, but it turns out that it experiences some limitations for transient flows, where the averaging process smears out most of the important characteristics of a time- dependent solution, which is important in a turbulent mixing process and combustion. DNS, on the other hand, attempts to resolve all temporal and spatial scales. As a result, the solution is very accurate. Regrettably, DNS is computationally not viable for turbulent flows of high Reynolds number or high Schmidt/Prandtl number. That is, to resolve all spatial and temporal scales, the grids and time step width would need to be extremely small, resulting in a problem which would take an extraordinarily long time to solve with today's technology. The relevance of SGS modeling of scalars particularly very important in combustion flows mainly for predicting accurately the anisotropic mixing within in the thin reaction zone. The state of the art is presented firstly on turbulent mixing of scalars and then followed by the flame wall interaction.

1.1.1 Turbulent mixing of scalars

The performance of a RNG k-Epsilon RANS model and LES applying a standard Smagorinsky for accurately describing the effects such as vortex shedding, lift and drag forces were studied extensively in the literature. Where, the SGS scalar flux has been described by a classical linear gradient approximation for capturing the mixing induced by the flow field turbulence. However, new experimental findings show that structured functions and derivative skewness of scalar field do not follow the assumption of isotropy at inertial and dissipation scales in presence of a mean scalar gradient [133, 98]. To account for this observed anisotropy behavior of the micro-mixing in the modeling, similarity models, serial decomposition closures and (non-linear) gradient models have been recently proposed along with a one-transport equation (see in [86, 85, 219, 170, 90, 91, 180, 168, 69]). Analysis of DNS data confirms elevated correlation between real scalar flux vector (measured from the data) and modeled SGS scalar flux vector obtained by using these models [96, 25, 213]. When implemented in the simulations, the mixed models and the serial decomposition closure lead to more satisfactory results than the (non-linear) gradient model at least in simple configurations, such as turbulent homogeneous isotropic flows, homogeneous shear layers and temporally developing shear layers as well as channel flows with differentially heated side [69].

Since the net chemical species formation rates due to chemical reactions strongly depend on the fluctuations at the smallest unresolved SGS quantities, it appears essential that turbulent SGS models for scalar in CFD should be able to address accurately major mixing transport effects at low computational cost [241, 218, 86, 116, 127, 154, 170, 91, 90, 180, 168, 25, 98, 28, 69, 149, 41, 85, 213, 78, 197]. Computational models for reactive flows are often parameterized by small-scale statistics of the scalar field, such as the scalar variance and flux [69, 197, 95], which are thought to directly influence

the availability of the scalar for reactions occurring at the molecular level, along with a possible selectivity. The accurate determination of such parameters, in turn, depends on understanding the processes by which the scalar, generally introduced at large scales in the flow, is made available by the turbulence for use in these small-scale processes [166, 177, 69, 236].

While the macromixing may be well described by the temporal and spatial transport of large scale structures that are resolved in LES, it is worth mentioning that the mesomixing occurs primarily due to turbulent fluctuations in the energy-containing range of the velocity spectrum, and the micromixing small-scale process is controlled by the viscous-convective deformation of fluid elements followed by molecular diffusion. In the non-resolved inertial convective range, this may be expressed by gradient correlations. On the small scale, a simple way of characterizing the mixture structure is to express the variance of the local concentration distribution of the scalar around its average value. Thereby the scalar variance is seen as a measure of the departure of the scalar field from small scale homogeneity. One can then easily understand the importance of capturing well this quantity in turbulent mixing applications [240, 25, 41, 95]. It must further be stressed that the state of the local distribution of scalars is, in turn, strongly depending on the scalar flux known to generate or produce the scalar variance. Therefore, transport and dynamics of scalar flux have to be carefully solved in conjunction with models for variances. This work focuses on the scalar flux transport.

Genuine validations of subgrid scale (SGS) scalar flux models are few, typically using DNS data [53, 198, 95, 33]. However, DNS still remains limited to low Reynolds number not interesting for practical applications. Given the importance of the mixing problem, it is relevant that SGS scalar flux models be subjected to rigorous assessment, including turbulent flows with high Reynolds numbers using experimental data. For this purpose, different SGS scalar flux models were evaluated along with a new developed dynamic anisotropy model in [86, 127, 153, 84]. Thereby the new SGS scalar flux model is the simplest explicit anisotropy-resolving algebraic form of a cubic formulation in terms of the scalar gradients derived in [240] and that is thermodynamically consistent as shown in [240, 175]. The simplest form combines the conventional linear eddy diffusivity model with an additional term coupling the (deviatoric) SGS stress tensor and the gradient of the filtered scalar field giving rise to a diffusivity tensor. The latter depends on the deviatoric part of the SGS stress tensor and includes transport properties of the fluid incorporated into the vortices through the SGS flow fluctuations, the turbulent Reynolds number and the molecular Schmidt number making the model sensitive to sub-Kolmogorov scales in case of high Schmidt numbers dominated flows [240]. It will be called as anisotropic SGS model throughout the thesis.

1.1.2 Flame wall interaction

The presence of walls in many combustion systems strongly influences combustion processes. This may lead to important modifications of the flame and the wall dynamics. Experimental observations show that the flame strength is reduced near cold wall surfaces, leading to possible (partial or total) quenching, while the gas-solid heat flux takes peak

values at flame contact [163, 77]. The evaluation of such wall heat fluxes is a key issue in design process of cooling devices and in determining the lifetime of combustion systems. Furthermore, excess emissions of unburned hydrocarbons in combustion engines have long been attributed to the presence of cool walls. Indeed, the presence of the wall may cause an increase in the pollutant emissions and a degradation of the energy performances [212, 139]. Together with the pollutant emissions, turbulent fuel-air temperature mixing, flame extinction and wall surface heat transfer are relevant processes to be understood. Therefore the flame-wall interaction (FWI) appears as one of the essential issues in modeling not only the turbulent combustion in engines but also wall heat transfer during combustion in combustion systems, especially since a downsizing trend is observed in modern combustion technologies.

Both modeling combustion and carrying out measurements near wall are challenging. The fluid, thermal and combustion boundary layer thicknesses at the wall could be in order of 1 mm [163]. Very few experimental studies are available for numerical validation while LES (Large Eddy Simulation) of premixed combustion remains difficult in this special situation due to the thickness of the premixed flame of about 0.1-1 mm and generally smaller than the LES mesh size. Recent reviews of combustion LES are provided by Janicka and Sadiki [93] and Pitsch [160]. The reduction and tabulation of chemical species behavior prior to LES remains one of the available options that are being investigated to downsize combustion chemistry in order to make it compatible with flow solvers [142, 204, 241, 66]. The extensions to non-adiabatic environments is still challenging [66, 243, 104, 54, 64]. Efforts to extend the application of LES technique to premixed turbulent flame description under consideration of non-adiabatic combustion are pursued here for the first time in the frame of FWI.

Non-reacting LES based studies to identify the influence of grid resolution and different advanced SGS (Sub Grid Scale) near-wall modelings on the accuracy of simulations have been investigated in [47, 31, 100, 210, 199, 146, 13]. Recently Muhamed [139], and Uddin [201] studied heat transfer of impinging non-reacting jet on wall using LES. Heat transfer characteristics of single and multiple isothermal turbulent air and flame jets impinging on surfaces were reviewed by Viskanta [209] while, Zhang et al.[232] provided characterization of the impinging jet flames. It appears that the FWI studies in the literature are mainly focused on laminar flow conditions [122, 35, 46, 5]. Focusing on combustion systems Boust et al. [22] investigated experimentally the behavior of wall heat losses with respect to pressure and gas dynamics of flame-wall interaction in a constant volume combustion chamber. They described and evaluated quenching distance from wall, heat flux and mixture properties for combustion of quiescent methane-air mixtures over the pressure range of 0.05-0.35 MPa. Bruneaux et al. [27] studied interaction between turbulent premixed flames and channel walls using DNS to evaluate various parameters like quenching distances, maximum wall heat fluxes, flame surface density and effect of wall strain on laminar flames in stagnant fluid and stagnation line flow. Besides some further 2D DNS and 3D DNS [77] for low Reynolds number (Re) configurations, LES of FWI are very rare. As reported in [232] basically five types of flames are possible from a premixed fuel jet impinging on water cooled wall, namely ring flame, conic flame, disc flame, envelop flame and cool central core flame. If the main flame jet velocity is sufficiently high, the flame detaches the nozzle and stabilizes near

the impinging wall forming a disk flame. Thereby the radial flow velocity plays a crucial role in determining the flame shape. Disk flames can be established for wide range of bulk stretch and equivalence ratio based on the flame initiation position.

In the present work focus is put on the development of the flamelet generated manifolds (FGM) [142, 204, 241, 66, 216] based LES model for predicting the overall flow field quantities and species concentrations near a water cooled wall. Catalytic effects on the wall are not considered.

To account for near wall kinetic effects and flame stabilization in this work, the FGM method considered is especially extended for non-adiabatic conditions and redesigned for a suitable coupling to LES. This is achieved by incorporating an additional filtered transport equations for the reaction progress variable and enthalpy besides the mixture fraction equation and the classical flow governing equations for LES into the CFD. The resulting complete model is applied to simulate a laboratory-scale turbulent impinging jet for which experimental investigations were carrying out in parallel. In particular, the configuration consists of a premixed methane fuel jet injected through a pipe and impinging on a spherical wall disk. In a laminar flow environment, the reaction layer propagates against the incoming fluid and a premixed flame is built. In the case of a turbulent flow, the flame is wrinkled by velocity fluctuations and possible vortices are formed at near wall due to impinging jet. The flame is stabilized by the burnt products passing through fresh gases due to the impinging situation causing stagnation zone and thereby converting axial component velocities into radial components.

Two aspects will be addressed throughout this thesis for flame wall interaction. The first focus is put on the grid resolution required near the wall without including specific near wall-adapted SGS models [100, 199, 146, 13] in reacting configurations. For this purpose, we rely on processes in IC-engines in which the combustion mainly occurs at moderate Reynolds numbers and in the vicinity of the combustion chamber wall [163, 77]. The FWI plays here a significant role. Sick [185] recently determined the Reynolds number in internal combustion engines (ICE) based on ICE cylinder diameter to be in the range of 1000 to 10000. The second aspect under consideration is dedicated to the integration of near wall kinetic effects into the FGM framework by considering non-adiabatic properties through an enthalpy variable.

1.2 Structure of the thesis

This work is organized into nine main chapters. In chapter 2, theory of the flow, turbulence, combustion and the non-adiabatic combustion is presented. The discussion is also focused on the different theories available for modeling of the related physics. The fundamentals of combustion are presented in detail. In chapter 3, modeling techniques used in this work for sub grid scale (SGS) modeling of LES, SGS scalar flux models, combustion modeling, enthalpy transportation models are presented. In chapter 4, a general overview of numerical techniques used for finite volume method based CFD codes is presented. In the later part of this chapter, the FASTEST3D code structure

and its numerical methods, procedures implemented in this work are discussed in detail. In chapter 5, the fundamentals of tabulated chemistry modeling is discussed, a special attention is provided on the enthalpy based FGM tabulation and its validation for both adiabatic and non-adiabatic cases. The importance of reaction progress variable definition in the non-adiabatic context is discussed. In chapter 6, the definitions of different boundary conditions and their implementation in this work together with the solution procedure of FASTEST3D solver used in this work is presented. The block structured multi processor CFD code parallelization for the FASTEST is also discussed. Finally a case study is presented on boundary conditions definitions for the perforated nozzle. In this work models discussed are categorized mainly into two types namely the adiabatic and the non-adiabatic based combustion configurations. In chapter 7, the adiabatic configurations with a focus on the SGS mixing models and combustion modelling of both premixed and non-premixed combustion are presented. The results are discussed to give the predictability of the advanced SGS scalar flux models implemented especially in reactive flows and combustion context respectively. The chapter also presents the modeling of pre-vaporized kerosene single sector combustion chamber using FGM tabulated chemistry for the complex fuels. In chapter 8, the non-adiabatic simulations of flame wall interaction are presented. The discussion of the near wall resolution required for resolving the flow, thermal and combustion boundary layer is presented. The analysis of the results also focused on the applicability of both Lewis unity and mixture averaged FGM based tabulation while using the ATF combustion model for flame wall interactions. A special attention is given to the capability evaluation of various methods used in this work in capturing the heat flux at the wall accurately. In chapter 9, the results obtained with the various models and their relevance in reactive flows especially for both adiabatic and non-adiabatic combustion used in this work are summarized to conclude.

Chapter 2

Theory and Modeling

The earth system and its atmosphere is hard to imagine without fluid mechanics. The atmosphere, clouds, air, rains, storms, ground water, rivers, petrochemical, various flow systems (blood circulations, fluid circulation and breathing) of living organisms, fish and other aqua organisms living in water, birds flying in the sky and so on are classical examples of fluid mechanics of the nature. The fluid mechanics happens in everyday life of humans from sports (football, cricket, golf, etc.), commuting (surface, air and water), cooking and agriculture. The combustion systems from any source of fuels are coupled with fluid mechanics very strongly. In fact the fluid mechanics determines combustion phenomenon to a great extent. The combustion in many industrial applications happens in turbulent regions, which is the focus of the thesis. The turbulent combustion process is controlled by the mixing of various species and flow streams. The combustion process is a thermochemical phenomenon affected by diffusion at micro level (assuming a batch reactor or within a single CV). The mixing determines various species reactions within a batch reactor which are controlled by diffusion of various species. Mixing takes place at both large and sub-grid scales. The mixing phenomenon at sub-grid scales called SGS scalars mixing and it is one of the main focus of this thesis. The mixing between the streams and scalars across the different CVs in the complete combustion system also interesting and it could be combustion rate determining step. In turn, mixing is determined by the fluid mechanics and its turbulent features of the flow. In this chapter, firstly various aspects of the fluid mechanics and its turbulent features, SGS scalar flux models, combustion modeling and flame-wall interaction will be provided. The second part of this chapter is dedicated to discussing the modeling techniques applied in this work.

The basic theory of flow turbulence, mixing and combustion is presented and discussed briefly.

2.1 Fundamentals of flow and mixing

The fluid flows in many combustion systems are turbulent, other type of flow is being laminar flow and these aspects are discussed in detail for instance by Durst [57], Bird Stewart and Lightfoot [18], and White [222]. A transition flow region also exists which is considered to be between these two regimes. The turbulent flows are very complex and solving them mathematically is very challenging. Reynolds, at the end of the nineteenth century, observed the instability of transition and turbulence in a pipe flow. He had noticed in his experiments that the flow behavior was dependent upon a non-dimensional parameter. This parameter, which also provides a criterion for dynamic similarity, is the

Reynolds number given by

$$Re = \frac{UL\rho}{\mu} = \frac{UL}{\nu} \tag{2.1}$$

where U is mean average velocity, and L is characteristic length scales of the mean flow, ρ is fluid density and μ, ν are the dynamic and kinematic fluid viscosity. The Reynolds number is defines as the ratio of inertial forces Uρ to viscous forces ν/L and is used for determining whether a flow is laminar or turbulent. Laminar flow occurs at low Reynolds numbers, where viscous forces are dominant, and is characterized by smooth, constant fluid motion, while turbulent flow, on the other hand, occurs at high Reynolds numbers and is dominated by inertial forces. The famous experiment of Reynolds in determining flow type is illustrated in Fig. 2.1, where the blue line represents a trace injected in a developed flow. The path of trace injected is a straight line in laminar case, a slightly disturbed line in case of transition flow and a very random and highly disturbed in turbulent case. The boundary layer development and the flow transition from laminar to turbulent is observed in a classical example of development of boundary layer on a flat plate as shown in Fig. 2.2. In this example a developed flow is ejected on to a flat plate, where boundary layer starts to develop and gets thicker along the plate length. In this process the friction of wall induces turbulence. In turbulent region the viscous sublayer, a buffer layer and a turbulent region exists as shown in Fig. 2.2. Viscous sub layers in turbulent cases are very thin and some times it is only fraction of a millimeter.

The physical nature of turbulence has been introduced in many works [166], which can be summarized as the fluid motion in which the flow properties, such as velocity, are varying randomly both in time and in space resulting in a wide range of flow scale structures. Thereby the turbulence energy is dissipated from larger scales to small scales. At the smallest scales, due to viscous effects the kinetic energy of the fluid is converted into heat. However the smallest scales are much larger than the molecular mean free path, so that turbulence is a continuum phenomenon. This phenomenon is intrinsically three-dimensional and diffusive which causes mixing and rates of mass, momentum, and heat transfer much more effectively than a comparable laminar flow. That turbulence can produce rapid mixing is one of important dynamics of turbulent flows. A mixing problem can be described as a configuration that is initially composed of two distinct and segregated scalar constituents which may be differentiated by different chemical compositions, different temperatures, different trace elements, or any other scalar marker. The mixing process, throughout its development, is to mix these different constituents at the molecular level to produce a homogeneous mixture. The ability of turbulent flows to effectively mix entrained fluids to a molecular scale has wide-ranging consequences in nature and engineering.

The physical process of turbulent mixing is categorized in general into two types, namely turbulent stirring (convection), and molecular diffusion. In addition for reactive flows the chemical reaction rate contribution should be considered. The chemical reaction process starts only when the mixing of the different reactants is achieved at molecular level. If a turbulent flow field containing two different constituents, initially unmixed comes into contact by the turbulent convection, then the action of this flow field on the scalar field is to disorder and increase the surface area of the interface between the two

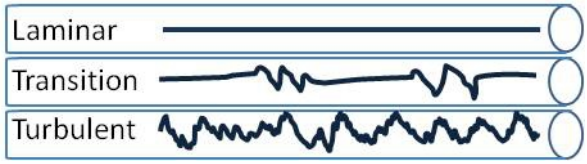

Figure 2.1: Reynolds experiment laminar (Top), Transition(middle) and Turbulent (bottom) in a pipe for a trace injected (dark blue line)

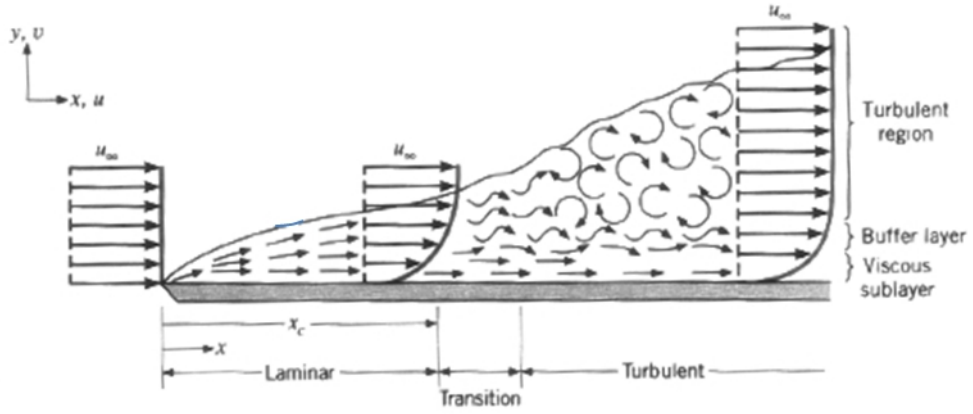

Figure 2.2: Development of boundary layer on a flat plate [88]

constituents. As a result, the gradients of the scalar constituents will be increased and the scalar length scale will be decreased due to this stirring process and it results in the evolution of a complex structure of the scalar field. Stirring has the effect of redistributing the scalar field throughout the flow field. Mixing at the molecular level is a diffusion process. The turbulent stirring process described above processes only to redistribute or to convect scalar field throughout the flow domain. The molecular diffusion determines and controls the intermixing of separate components. The macroscopic view of molecular diffusion is a result of random motion (Brownian motion) of fluid particles at the molecular level. This process is most effective in the regions of high gradients of scalars and acts most effectively at the smallest scales of the flow. A very few works in literature are dedicated to understand mixing process at molecular level in turbulent mixing. It is important to understand this phenomenon of turbulent mixing more precisely and it is challenging to model and study experimentally. It is necessary to describe scalar fields with an equation(s) in addition to mass conservation and momentum equations.

2.1.1 Conservation of mass

The present study focus is on mixing and combustion where the mass neither be created nor destroyed within the process. The mass of each atom in the combustion systems is conserved. The various atoms of the systems are available in different forms or in various molecules during the combustion process. The conservation of mass is given in general for single phase combustion by:

$$\frac{\partial \rho}{\partial t} + \frac{\partial \rho u_i}{\partial x_i} = 0 \quad (i \, \epsilon \, 1, 2, 3) \tag{2.2}$$

Equation Eq. 2.2 describes local change of density ρ in time t, which is equal to the convective transport of mass. The mass transported by the velocity u_i in x_i direction. The more details on derivation of Eq. 2.2 can be found in [18]. The Eq. 2.2 is valid for both compressible and incompressible fluids. In the present work is only focused on the *incompressible flows*. In both combustion and mixing process the density changes, which is considered in this study. In a constant density flows Eq. 2.2 can be reduced to a purely kinematic criterion.

2.1.2 Conservation of momentum

The conservation of momentum states that the fluid particle (or parcel) will not change its velocity unless an external forces acts on it. Therefore momentum of the fluid particle is conserved and is given by [18, 57]:

$$\frac{\partial \rho u_i}{\partial t} + \frac{\partial \rho u_i u_j}{\partial x_j} = -\frac{\partial p}{\partial x_i} + \frac{\partial \tau_{ij}}{\partial x_j} + \rho g_i \quad (i, j \, \epsilon \, 1, 2, 3) \tag{2.3}$$

The Eq. 2.3 states that rate of accumulation of ρu_i in time t is sum of convective transport, forces due to deformation, pressure and gravity. The convective term describes the momentum of ρu_i by velocity of u_j in x_j direction. The stress tensors τ_{ij} is local deformation by surface forces and it also depends on fluid property. The stress tensor gradients in x_j spatial directions contribute to the conservation of momentum by $\partial \tau_{ij}/\partial x_j$. The $\partial p/\partial x_i$ and ρg_i are forced due to spatial pressure gradient and earth's gravity. From Stokes [18, 57] hypothesis stress tensors τ_{ij} for Newtonian fluids can defines as:

$$\tau_{ij} = \rho\nu \left(\frac{\partial u_i}{\partial x_j} + \frac{\partial u_j}{\partial x_i} \right) - \frac{2}{3} \rho\nu \frac{\partial u_k}{\partial x_k} \delta_{ij} \tag{2.4}$$

where ν is the kinematic viscosity, δ_{ij} is the Kronecker delta. The Navier-Stokes equation is derived by substituting Eq. 2.4 in Eq. 2.3 for incompressible isothermal flow and it is given by:

$$\frac{\partial \rho u_i}{\partial t} + \frac{\partial \rho u_i u_j}{\partial x_j} = -\frac{\partial p}{\partial x_i} + \frac{\partial}{\partial x_j} \left[\rho\nu \left(\frac{\partial u_i}{\partial x_j} + \frac{\partial u_j}{\partial x_i} \right) - \frac{2}{3} \rho\nu \frac{\partial u_k}{\partial x_k} \delta_{ij} \right] + \rho g_i \quad (i, j, k \, \epsilon \, 1, 2, 3) \tag{2.5}$$

2.1.3 Conservation of scalars

In combustion process many scalars like mixture fractions, species, enthalpy, variances of various scalars, etc. are being transported. These scalars are transported by the main flow field in general. These scalars could have source and sink within the systems. These scalars could also modify the mean flow properties at molecular level like thermo-chemical and flow behavior. It is very important to track all these scalars and these scalars are

conserved to model mathematical various processes in systems. The generalized transport equation for any scalar in *incompressible flows*(low-mach assumptions) Φ is given by:

$$\frac{\partial \Phi}{\partial t} + \frac{\partial \Phi u_i}{\partial x_i} = -\frac{\partial J_i^{\Phi}}{\partial x_i} + \dot{\omega}_{\Phi} \tag{2.6}$$

In combustion process where the flow is modified by density change, so here in Eq. 2.6 Φ is replaced by $\rho\Phi$. The J_i^{Φ} from second term in RHS of equation 2.6 is diffusive flux for scalar Φ, $\dot{\omega}_{\Phi}$ is the source term. In a combustion process the scalar Φ could be a mixture fraction (ξ), a reaction progress variable (RPV) and the enthalpy(h). Please note that here the 3D CFD code FASTEST-3D only unity Lewis number(Le) is assumed and all the work is carried out for a single phase combustion. The single phase combustion don't have the complexity of heat sink, mixture fraction source due to vaporization. However, in this work for flame wall interaction configuration heat sink is present at the wall. A short definition of mixture fraction and total enthalpy are provided here below.

Mixture fraction: In the present work only *single phase combustion* is defined. This definition avoids the source term for mixture fraction transport Eq. 2.6. The mixture fraction played a very vital role in combustion research and it is very important variable in the combustion modeling. The mixture fraction defines the mixing process. In combustion systems especially in case of diffusion flames mixing is rate determining step; as it combustion chemistry is very fast at high temperatures compared to the mixing process. The mixture fraction can be used in many other applications. The mixture fraction here is defined in the context of combustion following the Shvab-Zeldovich formalism (see e.g. [151]. ξ can be defined via the mass fractions z of element α as

$$\xi = \frac{Z_{\alpha} - Z_{\alpha,O}}{Z_{\alpha,F} - Z_{\alpha,O}} \tag{2.7}$$

where O, F indicate the concentrations in the oxidizer and fuel streams, respectively. The conservation equation of mixture fraction is provided by Eq. 2.15.

Equivalence ratio: The parameter equivalence ratio (θ) is important in combustion process and it is defined as function of mixture fraction as here below:

$$\theta = \frac{\xi}{1-\xi}\frac{1-\xi_{st}}{\xi_{st}} \tag{2.8}$$

where ξ_{st} is stoichiometric mixture fraction, which is 0.055 in the case of methane and air combustion. The θ is equal to 1 when the mixture fraction equal to stoichiometric. The $\theta < 1$ indicates excessive air available for the combustion process and defined as lean combustion and $\theta > 1$ corresponds to the insufficient air available for combustion and it is termed as rich combustion.

Total enthalpy: In the present work enthalpy (h) is defined as the sum of heat of formation and sensible heat. This definition avoids the enthalpy change within the combustion systems, except at the walls where non-adiabatic walls are present. Thus the source term

in transport equation of enthalpy (h) is avoided for a single phase combustion. The total enthalpy is defined as:

For any species α

$$h_\alpha = \int_{T_0}^{T} C_{p,\alpha} dT + \Delta h_{f,\alpha}^{T_0} \tag{2.9}$$

The first term in RHS of Eq. 2.9 is the sensible heat and second term is heat of formation. The h_α and $C_{p,\alpha}$ denote the enthalpy and the specific heat capacity at constant pressure of each species α, respectively. $h_{f,\alpha}^{T_0}$ is the enthalpy of formation of species α at the reference temperature T_0.Thus enthalpy total species (N_s) is given by

$$h = \sum_{\alpha=1}^{N_s} h_\alpha Y_\alpha \tag{2.10}$$

where Y_α is the mass fraction of species α.

Molecular transport: The molecular transport of enthalpy J_i^h is given by

$$J_i^h = -\frac{\lambda}{C_{p,\alpha}} \frac{\partial h}{\partial x_i} + \sum_{\alpha=1}^{N_s} h_\alpha J_i^{Y_\alpha} \tag{2.11}$$

The first term is diffusion of enthalpy due to temperature gradients (Fourier law) and the second term describes enthalpy diffusion connected to mass transport known as Dufour effect. For the diffusive flux of the species mass fractions Y_α we assume

$$J_i^{Y_\alpha} = -\rho D_\alpha \frac{\partial Y_\alpha}{\partial x_i} \tag{2.12}$$

which is known as Fick's law of diffusion. Other transport processes can occur due to *body-forces, volume forces or temperature gradients* [18, 57], but are neglected here. The Eq. 2.12 is also valid for mixture faction variable. The species diffusivities D_α can be linked to the thermal conductivity λ via the Lewis-number.

$$Le_\alpha = \frac{\lambda}{\rho C_{p,\alpha} D_\alpha} \tag{2.13}$$

The second term in RHS of Eq. 2.11 can be neglected assuming unity Lewis number approximation resulting equation is of the form:

$$J_i^h = -\frac{\lambda}{C_{p,\alpha}} \frac{\partial h}{\partial x_i} = -\rho D_h \frac{\partial h}{\partial x_i} \tag{2.14}$$

Substituting Eq. 2.14, 2.12 for ξ, Y_α and h in Eq. 2.6 gives the following mixture fraction, species and enthalpy transport equations.

$$\frac{\partial \rho\xi}{\partial t} + \frac{\partial \rho\xi u_i}{\partial x_i} = -\frac{\partial}{\partial x_i}\left(\rho D_\alpha \frac{\partial \xi_\alpha}{\partial x_i}\right) \tag{2.15}$$

$$\frac{\partial \rho Y_\alpha}{\partial t} + \frac{\partial \rho Y_\alpha u_i}{\partial x_i} = -\frac{\partial}{\partial x_i}\left(\rho D_\alpha \frac{\partial Y_\alpha}{\partial x_i}\right) + \dot{\omega}_{Y_\alpha} \tag{2.16}$$

$$\frac{\partial \rho h}{\partial t} + \frac{\partial \rho h u_i}{\partial x_i} = -\frac{\partial}{\partial x_i}\left(\rho D_h \frac{\partial h}{\partial x_i}\right) \tag{2.17}$$

For laminar, simple flow Eq. 2.2, 2.3, 2.15, 2.16 and 2.17 can be integrated numerically to obtain solutions for any possible flow. The only parameter that needs to be determined is the diffusion coefficient for scalars D_ξ, D_{Y_α}, D_h. Diffusion coefficient is a parameter expressing the transfer rate of a substance by random molecular motion. It is expressed, as a ratio of kinematic viscosity ν and molecular Schmidt (Sc) number as:

$$D_\xi, D_{Y_\alpha}, D_h = \frac{\nu}{Sc/Pr} \tag{2.18}$$

$$\rho D_\xi, \rho D_{Y_\alpha}, \rho D_h = \frac{\mu}{Sc/Pr} \tag{2.19}$$

whereas Sc/Pr is a dimensionless parameter and is proportional to the ratio of kinetic viscosity to molecular diffusivity, which is used in mass transfer in general; in particular for diffusion calculations of flowing systems. Analogous to the Schmidt number (Sc), the Prandtl number (Pr) is proportional to the ratio of thermal diffusivity to molecular diffusivity and is used in heat transfer in general and free and forced convection calculation. In many practical applications, obtaining solution from these equations is prohibitive due to the phenomenon of turbulence and the difficulties imposed by chemical kinetics.

2.2 Fundamentals of turbulent flow

In section 2.1 it was shown that classification of fluid flow motions into laminar, transitional and turbulent flows is based on its properties. In laminar flows diffusion phenomena are characterized only by molecular diffusion. The fluctuations which are present in turbulent flows will also contribute to the diffusion in addition to molecular diffusion. Turbulent flows can be observed in very wide range of flows, especially in most of the combustion systems. At high Reynolds numbers, the flow is very strongly irregular, with an extremely high diffusivity which can exceed the molecular-dependent transport processes by several orders of magnitude. This results in an increased intermixing of the fluid and an increased transport rate of the momentum, and also increased heat and mass transport. A solution to the problem of turbulence remains elusive despite the intensive research effort of the past century (see e.g. [48, 166, 57, 159]). The basic transport equations presented in the section 2.1 cannot be solved directly in the high Reynolds number turbulent flows due to the presence of wide range of length and time scales.

The experimental studies (see e.g. [57, 6, 202]) are intensively carried out to gain insight in the understanding of the structure of turbulent flows. Flow visualization has been particularly useful in the identification of the coherent eddies that are responsible for most of the energy production, especially in regions of high shear. Measurement techniques have progressed significantly and it is now possible to obtain single-point measurements of velocity and velocity gradient components using Laser-Doppler Velocimetry

or multiple wire anemometers, or velocity distributions in a plane, through Particle-Image or Particle-Tracking Velocimetry [57]. Experiments have proved to be an efficient means of measuring global parameters, like drag, lift, pressure drop, or heat coefficient, etc. However, experiments are very difficult if not impossible in other cases. For example, the measuring equipment might disturb the flow or the flow may be inaccessible. Some quantities are simply not measurable with available techniques or can be measured only with an insufficient accuracy. In many cases where details are important, or when new high technology applications or design processes demand predication of flows for which the database is insufficient, comprehensive experiments may be too costly and/or time consuming.

The advanced modeling technology, faster computers have made numerical solutions as an alternative tool. The numerical technique gives more insight into the flow properties and a deeper understanding. In this chapter, a general overview of mathematical formulations and numerical techniques used for the solution of turbulent flows and mixing is presented. Among different strategies for analysis of turbulent phenomena, the statement below focuses on presenting the state of the development of RANS, DNS and LES, and on outlining some challenges that are ahead, in terms of applications, numerical and modeling issues. The major difference of these analysis methodologies is stemmed from the resolution degree of turbulent scales. The first two sections therefore begin with an introduction of the scales of turbulent motion and mixing. Section 2.3.1 will focus on DNS followed by RANS in Section 2.3.2. The last section in this chapter, Section 2.3.2, is devoted to LES which is the method applied in this work.

2.2.1 The scales of turbulent flow

Turbulent flows are characterized by different flow structure sizes. The large but not the largest eddies contain major part of the turbulent kinetic energy. Due to this fact the large eddies are often called as energy containing eddies. The length and time scales of these eddies are of interest. In particular the size of the energy containing eddies depends on the geometry of a spatial domain as well as the local intensity of turbulence. This size can be related to the integral turbulent length scale that can be determined from the two-point spatial correlation function or coefficient for statistically steady (time independent) turbulence

$$R_{ij}^{L}(x, x+\Delta x) = \frac{\overline{\acute{u_i}(x)\acute{u_j}(x+\Delta x)}}{\sqrt{\overline{\acute{u_i}^2(x)}}\sqrt{\overline{\acute{u_i}^2(x+\Delta x)}}} \tag{2.20}$$

$$L_{ij} = \frac{1}{2}\int_{-\infty}^{+\infty} R_{ij}^{L}(x, x+\Delta x)d(\Delta x) \tag{2.21}$$

Here L_{ij} is the length scale tensor. For homogeneous isotropic turbulence the integral length scale, which is independent of the direction, is given by

$$L_I = \frac{1}{3}L_{ii} \tag{2.22}$$

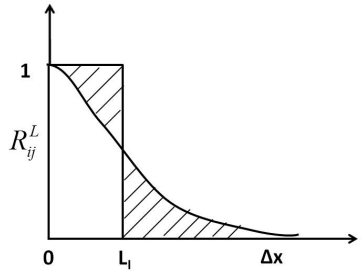

Figure 2.3: Two-point velocity correlation function versus the distance between two point Δx for homogeneous isotropic turbulence

The two-point velocity correlation function for homogeneous isotropic turbulence and the corresponding integral turbulent length scale are schematically shown in Fig. 2.3.

Here the integral length scale L_I can be interpreted as the length scale, from this point velocity fluctuations are predominantly uncorrelated. $R(x, y)$ is a measure for the corrolation of the velocity fluctaions u' measured at the point $x+\Delta x$, thereby indicating to what degree the turbulent properties of two points with distance Δx influence each other. L_I is located where the shaded areas above and below the two-point velocity correlations are of equal size. The corresponding time scale can be determined from the known time correlation function

$$R_{ij}^T(x, t + \Delta t) = \frac{\overline{\acute{u}_i(t)\acute{u}_j(t + \Delta t)}}{\sqrt{\overline{\acute{u}_i{}^2(t)}}\sqrt{\overline{\acute{u}_i{}^2(t + \Delta t)}}} \tag{2.23}$$

$$T_{ij} = \frac{1}{2}\int_{-\infty}^{+\infty} R_{ij}^T(x, t, t + \Delta t)d(\Delta t) \tag{2.24}$$

The assuming isotropy and homogeneity leads to

$$T_I = \frac{1}{3}T_{ii} \tag{2.25}$$

The turbulence integral length and time scales can be defined in terms of k (turbulent kinetic energy) and ϵ (energy dissipation rate) as

$$L_I = k^{3/2}/\epsilon \tag{2.26}$$

$$\tau_I = k/\epsilon \tag{2.27}$$

The integral turbulent time scale can be interpreted qualitatively as an averaged inverse rotational frequency of the typical big eddy appearing in the spatial location x.

Though the character of turbulence in practical flows is neither isotropic nor homogeneous, the idealized integral length scale provides at least coarse quantitative information about spatial correlation and sizes of typical energy containing eddies in turbulent flows. The integral turbulent length scale can be qualitatively interpreted as an averaged radius

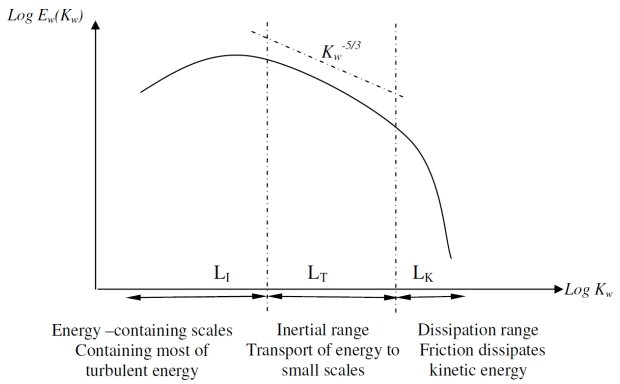

Figure 2.4: Schematic representation of the turbulent kinetic energy spectrum as a function of the wavenumber k_ω for isotropic homogeneous turbulence. (L_I, L_T and L_K correspond to the integral length scale, the Taylor length scale and Kolmogorov length scale, respectively.)

of the typical big eddy appearing in the spatial location x.

Note that the rate at which the turbulent kinetic energy is transferred from bigger eddies to smaller eddies is called the dissipation rate ϵ. The smaller an eddy, the greater the velocity gradient inside the eddy and the greater the viscous stress that counteracts the eddying motion. The cascade of energy can not be extended infinitely because of the viscous forces. Consequently, there is a statistical lower limit of the smallest eddy size that corresponds to a minimum scale of turbulence and a maximum frequency in the turbulent motion. In this stage the kinetic energy of the fluctuating motion will dissipate completely into the internal energy of the flow. The length scale for the smallest eddies is called as Kolmogorov scale and is related to the dissipation rate by:

$$_k = \nu^{3/4}/\epsilon^{1/4} \tag{2.28}$$

Through the fluid viscosity ν a corresponding Kolmogorov time scale is given as

$$\tau_k = \nu^{1/2}/\epsilon^{1/2} \tag{2.29}$$

The turbulent kinetic energy spectrum which is obtained from the Fourier transformation of the spatial isotropic two-point correlation function R_{ij}^T is schematically plotted in Fig. 2.4. $E_\omega(k_\omega)$ is the kinetic energy density per wave number k_ω or the inverse turbulent length scale. The maximal values of $E_\omega(k_\omega)$ correspond to the energy containing scales that are related to the turbulent length scale L_I. Taylor micro scales which are discussed later part of this section are located between L_I and L_K, and these two scales are related by $L_T = \sqrt{Re}L_K$. Eddies of size smaller than the energy containing eddies build the inertial subrange. Kolmogorov showed that the transfer of energy from large to small scales within the inertial subrange is independent on the geometry and eddy size and follow the profile $k_\omega^{-5/3}$. At the right side of the inertial subrange the wave number corresponding to the Kolmogorov scale L_k is located.

Other widely used length scales are Taylor microscales L_T, which can be determined by autocorrelation functions near the origin. In terms of the longitudinal autocorrelation function $R_f(r,t)$ and the transversal autocorrelation function $R_g(r,t)$ [48, 57, 166], two corresponding quantities can be defined at the Taylor microscale level as:

$$L_T^{11}(t) = \left(-\frac{1}{2} \frac{\partial^2 R_f}{\partial^2 r^2}(0,t) \right)^{-(1/2)} \tag{2.30}$$

and

$$L_T^{22}(t) = \left(-\frac{1}{2} \frac{\partial^2 R_g}{\partial^2 r^2}(0,t) \right)^{-(1/2)} = \frac{1}{\sqrt{2}} L_T^{11}(t) \tag{2.31}$$

2.2.2 The scales of turbulent mixing

The mixing is very common phenomenon in many industrial flow processes with or without reactions. The advection of any given scalar (Φ = temperature, mixture fraction, species, traces, etc.) in the flow systems is influenced by turbulent flow fields. Similar to the velocity field, there is a statistical lower limit of smallest scale of turbulent mixing and maximum frequency in mixing processes. This smallest scale is called Batchelor scale L_B [12] and defined in terms of the Kolmogorov scale and Schmidt number(Sc, [194]), by

$$L_B = \left(\frac{L_K}{Sc^{1/2}} \right) \tag{2.32}$$

Like the Kolmogorov scale in a turbulent fluid flow, the Batchelor scale characterizes the smallest length scales of scalar eddies that can exist before being dominated by molecular diffusion. It is important to note that for $Sc > 1$, which is common in many liquid flows (some liquids exhibits Sc as high as 1000), the Batchelor scale is small when compared to the Kolmogorov micro scales. This means that scalar transport occurs at scales smaller than the smallest eddy size. On contrary, for most of the gases $Sc \simeq 1$, so the smallest scalar lengths are approximately equal to Kolmogorov scale. This means for high Sc flows the scalar field contains much more fine-structures than the velocity field. The scales at which diffusion is occurring are much smaller. Then computational requirements to numerically solve these scales and thus accurately describe the mixing process are correspondingly increased. For scalar eddies much larger than the Batchelor scales, molecular diffusion is negligible. Thus, initially non-premixed scale fields will remain segregated at scales larger than the Batchelor scale. This has important consequences for turbulent reaction flows because it implies that the chemical source term will be strongly coupled to turbulent mixing for many chemical reactions of practical importance. At high Reynolds numbers, the small scales of scalar field are usually assumed to be nearly isotropic (H.S. Kang & C. Meneveau [98] showed that scalar fields at small scale level are not so isotropic as assumed.) and will evolve on a time scale that is much smaller than that of the large scales. Moreover, for a passive scalar, the characteristic time scales for mixing at length scales above the Batchelor scale will be determined solely by turbulent flow.

In the scalar field largest energy carrying scales are scalar integral length scales. These scales are primarily determined by two processes:

- initial condition : the scalar field can be initialized with a characteristic length scale of system $L_{\Phi I}$ that is completely independent of turbulence field

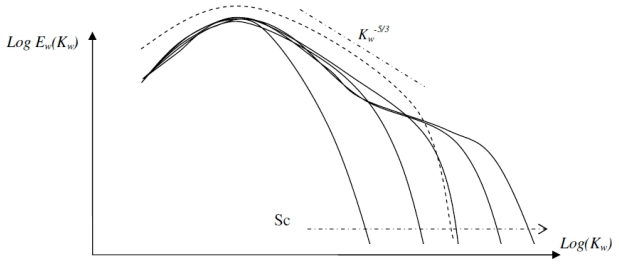

Figure 2.5: Schematic representation of scalar energy spectrum normalized by the integral scales as a function of the wave number k_ω for isotropic homogeneous scalar field turbulence [85].

- turbulent mixing : the energy containing range of a turbulent flow will create scalar eddies with characteristic length scalar $L_{\Phi I}$ that is approximately equal to L_I

The scalar spatial correlation function provides the length scale information about the underlying scalar field similar to the velocity correlation discuss earlier part of this chapter. For a homogeneous isotropic and statistical steady (time independent) scalar field, the spatial correlation function can be written in terms of the fluctuating scalar field Φ' [69] as:

$$R_\Phi^L(\Delta x, t) = \frac{\langle \Phi'(x)\, \Phi'(x+\Delta x)\rangle}{\langle \Phi'(x)\, \Phi'(x)\rangle} \tag{2.33}$$

And from Eq. 2.33 the scalar integral scale is defined by

$$L_{\Phi I}(t) = \int_0^\infty R_\Phi(\Delta x, t)\, d(\Delta x) \tag{2.34}$$

and scalar Taylor microscale is defined by

$$L_{\Phi T}(t) = \left(-\frac{1}{2}\frac{\partial^2 R_\Phi^L}{\partial^2 r^2}(0,t)\right)^{-(1/2)} \tag{2.35}$$

The scalar energy spectrum of homogeneous scalar field is correlated using Eq. 2.33. The scalar energy spectrum illustration is presented in Fig. 2.5 for a flow with $Re = 500$ for various Schmidt number (see e.g. [69]). The schematic velocity spectrum is included in the Fig. 2.5 for a comparison of Schmidth number influence on energy cascade. Analogous to the velocity field, the scalar mixing in inertial convective subrange can be interpreted as a cascade process. The inertial sub-range exhibits the same profile ($\sim 5/3$) similar to velocity field for moderate Schmidt numbers. For low Schmidt number, the scale spectrum falls off much faster than the velocity spectrum. For high Schmidt number, viscous convective/diffusive subrange (Batchelor spectrum) with (~ 1) scaling is evident.

The turbulent integral time scales for mixing (T_Φ) and for flow (T_T) are crucial in determining mixing process and they are defined as [69]:

$$T_T = \sqrt{Re}\, T_K \tag{2.36}$$

$$T_\Phi = 2\frac{\langle \Phi'^2\rangle}{\varepsilon_\Phi} \tag{2.37}$$

In the turbulent mixing literature, the scalar mixing time is usually reported in a non-dimensional form as ratio of the mechanical to scalar time scales ratio R_Φ^T and it is defined by

$$R_\Phi^T = \frac{k\varepsilon_\Phi}{\varepsilon\langle\Phi'^2\rangle} \tag{2.38}$$

where ε_Φ is the scalar dissipation rate and Φ'^2 is the scalar variance, k is kinetic energy. The turbulent mixing is experiences wide range of flows. The section 3.4 will give more details in modeling turbulent mixing to capture all required scales more accurately.

2.3 Modelling of turbulent flows

In last decades many turbulent modeling techniques were developed, verified and applied to industrial problems successfully. The models are generally finite volume models (FVM). The basic idea of all models is to capture the energy carrying by all length scales of turbulence as discussed earlier. The proposed robust models are some times limited by requirement of computational resources. In this section a brief overview of the turbulent combustion models is presented.

2.3.1 Direct numerical simulation (DNS)

The flow can be converted into physics, physics can be defined by equations (e.g. Eq. 2.2, 2.3), equation can be solved using analytical methods and computational methods. The flow is volumetric phenomena, the flow domain is divided into many number of small volumes for solving those equations. Here in this work Navier-Stokes equations that describe the motion of any Newtonian fluid can be numerically solved by means of CFD [147, 63]. The ideal method is to divide domain into a very tiny sub domains such that thee is no further change happens within the tiny sub domain. This means all energy carrying scales are solved accurately. This approach is known as the direct numerical simulation (DNS) approach, which don't need to model any turbulent scales. Thereby the whole ranges of spatial and temporal scales of the turbulence are resolved. The small scales exist down to $\sim Re^{-3/4}$, as per Kolmogorov's theory [111]. Thus, in order to capture all of the scales on a grid, a grid size of should be less than $\sim Re^{-3/4}$, translating to a grid of approximately to $\sim Re^{-3/4}$ grid points. In some applications Reynolds number can go as high as $2X10^7$. However, a typical Reynolds number is $\sim$ 80000 [148] in many industrial gas turbine, for simulating such configuration it requires more than 100 billion grid points.

Present computational resources make such calculations are not practical especially with combustion and heat transfer. Moreover, in an expensive DNS a huge amount of information would be generated which is mostly not required by the practical user. A design engineer is interested more in the average flow and some lower moments to a precision of a few percent. Hence, for many applications a DNS which is of great value for theoretical investigations and model testing is not only unaffordable but would also result in high computational cost. The DNS is very valid tool in some cases for validating other

turbulence models. For example Kim et al. [105] present a DNS of channel flow, and Le et al. [118] present a DNS of flow over a backward-facing step. Both of these studies were conducted to gain new insight into the physical mechanisms involved in turbulent flow. DNS approach solely based on the Navier-Stokes equations required huge amount of grid point. Hence it is not suitable for most turbulent flows, therefore researchers had to find different approaches to apply CFD for industrial applications.

2.3.2 Reynolds averaged numerical simulation (RANS)

The limited and expensive computational resources available to solve the industrial application forced to find other alternatives to DNS. One of very widely and successfully used CFD methods is Reynolds averaging based Numerical Simulation (here RANS). RANS method is based on the statistically averaged governing equations with appropriate turbulence models. By using the Reynolds' averaging, any instant value of flow parameter Φ is represented by the mean value $\langle\Phi\rangle$, and a fluctuating part, Φ' as:

$$\Phi\left(x_i,t\right)=\left\langle\Phi\left(x_i,t\right)\right\rangle+\Phi'\left(x_i,t\right) \tag{2.39}$$

The time averaged mean quantity of Φ is defined by

$$\left\langle\Phi\left(x_i,t\right)\right\rangle=\overline{\Phi\left(x_i\right)}=\left\langle\Phi\left(x_i\right)\right\rangle=\lim_{T\to\infty}\frac{1}{t}\int_0^T\Phi\left(x_i,t\right)dt \tag{2.40}$$

where T is a time interval which is sufficient large enough for obtaining mean averages accurately for all the time scales of the turbulent flow. Note that the mean value can also be obtained by an ensemble averaging more appropriate for unsteady flow processes as:

$$\left\langle\Phi\left(x_i,t\right)\right\rangle=\frac{1}{N}\sum_{n=1}^{N}\Phi_n\left(x_i,t\right) \tag{2.41}$$

where N is number samples collected with constant time interval and by keeping both inlet and outlet conditions constant throughout the process. Introducing equation 2.39 into conservation equations for mass, momentum, mixture fraction; the time averaged transport equation are obtained as:

$$\frac{\partial\langle\rho\rangle}{\partial t}+\frac{\partial\langle\rho\rangle\langle u_i\rangle}{\partial x_i}=0 \tag{2.42}$$

$$\frac{\partial\langle\rho\rangle\langle u_i\rangle}{\partial t}+\frac{\partial\langle\rho\rangle\langle u_i\rangle\langle u_j\rangle}{\partial x_j}=\frac{\partial\langle p\rangle}{\partial x_i}+\frac{\partial\langle\tau_{ij}\rangle}{\partial x_j}-\frac{\partial\langle\rho\rangle\langle u_i'u_j'\rangle}{\partial x_j}+\langle\rho\rangle g_i \tag{2.43}$$

$$\frac{\partial\langle\rho\rangle\langle\xi\rangle}{\partial t}+\frac{\partial\langle\rho\rangle\langle\xi\rangle\langle u_j\rangle}{\partial x_j}=\frac{\partial}{\partial x_j}\left(\langle\rho\rangle D_f\frac{\partial\langle\rho\rangle}{\partial x_j}\right)-\frac{\partial\langle\rho\rangle\langle\xi'u_j'\rangle}{\partial x_j} \tag{2.44}$$

The time averaging process discussed here leads to a loss of instantaneous flow details. The new terms appeared in Eq. 2.43 and 2.44 and these are unknowns from the flow details. New averaged transport Eq. 2.42 2.43 and 2.44 can be solved by approximating of the unknown terms (i.e. the turbulent stresses tensor (or Reynolds tensor) $u_i'u_j'$ and turbulent flux $\xi'u_j'$) as a function of the averaged variables (closure problem). The

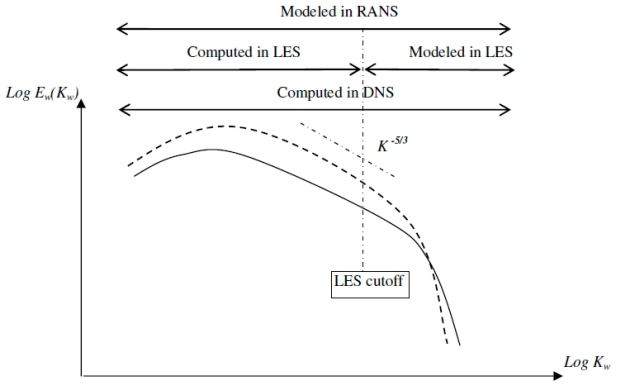

Figure 2.6: Turbulent scales resolved/modeled by RANS, LES, and DNS (velocity ---, scalar —) [69].

approximations or models used in the closure problem need to be as general and accurate as possible to model different turbulent phenomena. Different procedures used to handle the closure problem lead to different RANS turbulent models, such as differential Reynolds Stress models, algebraic Reynolds Stress models, eddy viscosity models and etc (see e.g. [48, 166, 57, 1, 126]).

The RANS modeling provides only limited information about the flow and all the information of turbulence is modeled (see Fig. 2.6), which brings a high challenge on modeling. Even for time-accurate simulations of unsteady flows, the RANS simulations are designed to include only the largest flow structures (those that scale with the dominant flow-length/time scale) in the flow and the smaller scales are not included. The extent to which the absence of the smaller flow structures affects the prediction of the larger vortex structures is quite open question in this framework. This problem is however configuration dependent and usually cannot be judged a priori.

2.3.3 Large eddy simulation (LES)

The Large eddy simulation (LES) is the trade of method between LES and DNS. In the DNS simulation most of the computational recourses (some times as high as ~ 99) are being used for resolving dissipative range scales (see Fig. 2.4, 2.6), which are not important in determining of flow of related behavior[69, 48, 57, 166]. However, the energy-containing scales determine most of the flow-dependent transport properties. The RANS simulations which are carried out by averaging complete energy spectrum loose vital information of the flow. It was demonstrated in the literature that the most of energy is carried by large scales in the flow. The flow could be solved more accurately than RANS and much cheaper cost than that of DNS by resolving large scales and modeling small scales. This approach is known as large eddy simulation (LES).

The LES consists a direct computation of large eddies and modeling of small (quasi-universal) eddies so-called subgrid scales (SGS). In this method, not the whole turbulent spectrum has to be resolved. It uses a filtering operation that allows for removing in a proper way the small scales. This operation introduces new unknown terms representing the small-scale information lost by the filtering (for more details see chapter 3). Thus,

some models for the small scales called as SGS-models are needed in order to close the system of filtered equations. From the modeling point of view this approach simply displaces the problem into the less important part of the energy spectrum. As a subgrid parameterization is still necessary, its influence is expected to be rather small, at least when the most important scales are all resolved on the computational grid.

Because in LES small eddies are modeled, computational grid will be therefore much larger than the Kolmogorov length scale, and time steps can be chosen much larger than in DNS. So the computing resources for LES are much lower than DNS. The area of applications of LES has considerably increased with rapid development of computer facilities. On other hand, solving wall bounded flows by LES is very challenging. It is apparent that near the wall all vortices are small so that both space and time steps needed for LES scale down to values which are in order of characteristic for DNS. SGS CFD models available for flows such as anisotropic models and dynamic procedures provided very encouraging results in many flow systems, though some difficulties exist, especially for near walls. One of the solution for the wall problem for LES appears to be a combination of LES and the Reynolds averaging numerical simulation (here RANS) in the line of the so-called hybrid RANS/LES models.

The many approached for LES modeling for proposed in literature, for example Smagorinsky model (Smagorinsky, [187]), Algebraic Dynamic model (Germano, et al. [74]), Dynamic Global-Coefficient model (You & Moin, [229]), Localized Dynamic model (Kim & Menon, [106]), WALE (Wall-Adapting Local Eddy-viscosity) model (Nicoud & Ducros, [140]) and etc. These advanced models together with rapid and cheaper computational resources allowed more accurate computations to be performed with less empiricism than before, LES is now being used in industrial application. Though RANS still dominates as CFD tool for industrial applications, LES is gaining its share very quickly. The resolution degree of the turbulent scales with respect to the energy spectrum of the velocity and scalar (when $Sc \sim 1$) for the three methods (DNS, RANS and LES) is depicted in Fig. 2.6.

Computational effort required by LES can be estimated considering that the smallest resolved scale has to be situated in the inertial sub range of turbulent kinetic energy spectrum, where the effect of SGS is expected to be problem-independent. A measure of these scales is the Taylor microscale.

The number of grid points required for resolving the three dimensional flow by LES can be expressed as [177]:

$$N_{LES} \sim \left(\frac{L_c}{L_T}\right) \sim Re_t^{(3/2)} \tag{2.45}$$

where Re_t is turulent Reynolds number, L_c is characteristic length scale of the flow. The required number of CVs (N_{LES}) for LES the way below the CVs required by the case of DNS. In order to maximize the benefits from LES, it should be applied to those problems for which the cost is comparable to that of the solution obtained from RANS approach, or for problems in which lower-level turbulence models may fail. Such problems include unsteady or three-dimensional boundary layers, separated flows and flows involving unsteady mixing processes. For mixing processes in which

passive scalar fields have to be computed, the requirement of grid points is similar to the one in velocity field when the gas phase flows ($Sc \sim 1$) are considered. A detailed presentation of different issues of LES [16] is beyond the scope of this thesis. However, the underlying idea of LES formulation will be outlined in the next chapter which deals in detail with the modeling of the SGS stress tensor and scalar flux vector.

2.3.4 Near wall flow modelling

The advantage of LES is true in free shear layer flows, but it altered completely when LES is applied to turbulent boundary layers. In fact boundary layers are multi-scale phenomena where the energetic and dynamically important motions in the inner layer become progressively smaller as the Reynolds number (Re) is increased [99]. This leads to requirement of very fine mesh which is in order of DNS mesh size.

Therefore, to overcome this difficulty most of the approaches in literature [158, 191] proposes to model the inner boundary layer rather than resolving by fine DNS mesh. These approaches generally fall into one of two categories: (1) methods that model the wall shear stress τ_w directly and (2) methods that switch to a Reynolds-averaged Navier-Stokes (RANS) description in the inner layer. The second category includes hybrid LES/RANS and detached eddy simulation (DES). Many works in literature are dedicated to address the wall boundary layer modeling in LES context [99, 157, 226]. However, in this work fine resolved mesh is considered near the impinging wall and thereby requirement of special wall model(s) is avoided as discussed in subsection 8.4.1.

2.4 Fundamentals of combustion

In simple terms combustion is defined as the sequence of exothermic chemical reactions between a fuel and an oxidant accompanied by the production of heat and conversion of chemical species. The combustion process produces flame with high temperatures, also could radiate the heat. In modern day application combustion takes place as single phases, multiphase and catalytic combustion. Combustion process influences other processes such as flow, radiation, compressibility, material modifications (expansion, erosion and etc.) and etc. The macroscopic theory of combustion deals with investigation of the role of convection, diffusion and heat exchange and their interaction in chemical reaction processes. The elements of chemical kinetics necessary for further considerations are briefly described in latter part of this section. In technical combustion systems combustion can be subdivided into two major parts. These include non-premixed or diffusion and premixed combustion that are described in the next sections. The less idealized and more commonly occurring in practice partially premixed combustion is also discussed briefly. In latter part of this section an overview of chemical kinetics followed by a short discussion of reduction strategies and turbulent chemistry is introduced.

2.4.1 Chemical kinetics and reaction mechanism

The chemical kinetics is combination of physics involved of thermo-chemical properties associated with reaction processes. A chemical reaction involves of a reactant converting into a product. The conversion is associated with many phenomenon like amounts reacted, formed, and the speed of their formation, i.e., the rate at which the concentration of reactants and products change. Consider the following example:

$$\nu'_A A + \nu'_B B \rightarrow \nu'_C C + \nu'_D D \tag{2.46}$$

Coefficients ν'_A, ν'_B, ν'_C and ν'_D denote the molar stoichiometric coefficients of species A, B,C and D. The Eq. 2.46 states that the chemical reaction involves direct conversion from reactant in to product. In reality the chemical reaction can have not only one step, but also few steps, that complicate the chemical kinetics and allow many possible reaction mechanisms. A complete mechanism must also account for all reactants used, and all products formed. For illustrating reaction mechanism an example of methane CH_4 reacting with oxygenO_2 to convert into carbon-dioxide CO_2 and water (H_2O reaction considered here. A global reaction of it looks like as:

$$\mathrm{CH_4 + 2\,O_2 \rightarrow CO_2 + 2\,H_2O}$$

These types of reaction doesn't happen in a single step as represented above. They are broken up into smaller molecules or single atoms, which then recombine to form a new species. The detailed elementary reactions need to be considered for investigating complete chemical kinetics in detail. An chemical reaction mechanism with more intermediate steps is shown here [151, 217].

$$\begin{gathered}\mathrm{CH_4 + H \rightarrow CH_3 + H_2}\\ \mathrm{CO + OH \rightleftharpoons CO_2 + H}\\ \mathrm{H + O_2 + M \rightarrow HO_2 + M}\\ \mathrm{H + O_2 \rightleftharpoons OH + O}\end{gathered}$$

The single step global reaction is written with other intermediate reactions. Some of them are irreversible, which are indicated by unidirectional arrow. The one of the widely used chemical reaction mechanism for methane, GRI 3.0 consists more than 300 reaction steps. The Eq. 2.46 is then not enough to describe a chemical reaction and a system of equations arise:

$$\sum_{k=1}^{N_k} \nu'_{k,j} M_k \rightleftharpoons \sum_{k=1}^{N_R} \nu''_{k,j} M_k \text{ for } j \epsilon (1, ..., N_R) \tag{2.47}$$

where M_k represents the symbol of species k, $\nu'_{k,j}$ and $\nu''_{k,j}$ are molar stoichiometric coefficients of species k in reaction j, N_k and N_R are number of species and number of reactions respectively. The Eq. 2.47 obey mass conservation given by:

$$\sum_{k=1}^{N_k} \nu'_{k,j} W_k \rightleftharpoons \sum_{k=1}^{N_R} \nu''_{k,j} W_k \tag{2.48}$$

here W_k denotes the molecular weight of species k. However the balanced Eq. 2.48 does not give information if the reactants become products. The rate of the overall process

will be determined by the slowest (highest energy) step in the reaction mechanism. The mass reaction rate $\dot{w}_{k,j}$ of species k in the reaction j is given by [214]:

$$\dot{w}_{k,j} = r_j W_k \nu_{k,j} \text{ where } \nu_{k,j} = \nu''_{k,j} - \nu'_{k,j} \tag{2.49}$$

where r_j represents the rate of progress of reaction j. By considering all reactions N_R, which take place within a reaction mechanism, the mass reaction rate $\dot{w}_k$ is the sum of all produced rates $\dot{w}_{k,j}$ of species M_k in all reactions N_R

$$\dot{w}_k = \sum_{j=1}^{N_R} \dot{w}_{k,j} = W_k \sum_{j=1}^{N_R} r_j \nu_{k,j} \tag{2.50}$$

The sum of all mass reaction rates $\dot{w}_k$ in complete system for all species N_k is given by Eq. 2.51 following mass conservation law.

$$\sum_{k=1}^{N_k} \dot{w}_k = \sum_{k=1}^{N_k} \left(W_k \sum_{j=1}^{N_R} r_j \nu_{k,j} \right) = 0 \tag{2.51}$$

The reaction progress rate r_j of reaction j, which denotes the change of products formation in time, can be affected by concentration of species, phase of reactant, temperature, the presence of catalyst and more important the degree of mixing of the system.

Instantaneous reaction rate at any point of time can be determined by the slope of a tangent of the concentration plot in time space [163, 214]. The reaction for any reaction j can be written as :

$$r_j = K_{f,j} \Pi_{k=1}^{N_k} \left(\frac{\rho y_k}{W_k} \right)^{\nu'_{k,j}} - K_{r,j} \Pi_{k=1}^{N_k} \left(\frac{\rho y_k}{W_k} \right)^{\nu''_{k,j}} \tag{2.52}$$

where $K_{f,j}$ and $K_{r,j}$ are the forward and reverse constants of the reaction rates, $\rho y_k / W_k$ is the molar concentration of species k. The rate constants are difficult to determine and are related to the temperature of the system by what is known as the Arrhenius equation:

$$K_{f,j} = A_{f,t} T^{\beta_j} e^{\left(-\frac{E_j}{RT}\right)} = A_{f,t} T^{\beta_j} e^{\left(-\frac{T_{a,j}}{T}\right)} \tag{2.53}$$

where R is the ideal gas constant (8.314 J/mol-K), T is the temperature in Kelvin with the temperature exponent β_j, E_j is the activation energy in joules/mole, $T_{a,j}$ is the activation temperature in K, and $A_{f,t}$ is a constant called the frequency factor; which is related to the fraction of collisions between reactants having the proper orientation. The backwards constant rates $K_{r,j}$ are calculated using the equilibrium and the forward rates constants:

$$K_{r,j} = \frac{K_{f,j}}{\left(\frac{p_a}{RT}\right)^{\sum_{k=1}^{N_k} \nu_{k,j}} e^{\left(\frac{\Delta S_j^0}{R} - \frac{\Delta H_j^0}{RT}\right)}} \tag{2.54}$$

where p_a=1 bar, Δ refer difference attained during conversion from reactant to products in the j_{th} reaction, ΔH_j^0 and ΔS_j^0 are respectively enthalpy and entropy changes for the

reaction j. These quantities are obtained from predefined database, for example chemical reaction mechanism [163, 214]. The computing of r_j for every reaction necessitate the calculation of forward and backward constants, i.e., the knowledge of all variables: frequency factors $A_{f,t}$, temperature exponents β_j and the activation energy E_j. The huge number of variables and parameters required for the computation of r_j makes the tasks very complex. Using a detailed mechanism in the frame of numerical combustion leads to the resolution of a balance equation for each species included. Consequently it aggravates the tasks for the CFD.

In order to use numerical simulation of practical combustion processes, simplified models for the chemical kinetics i.e. the one step reaction mechanism, equilibrium model [200], Flamelet model [150] or ILDM [128] are proposed and discussed briefly at the end of this chapter.

2.4.2 Modes of combustion

The combustion research classifies combustion mainly into diffusion flames, premixed flames and partially premixed flames. The brief description of each flames is provided in the following subsections.

2.4.2.1 Non-premixed combustion

Diffusion flames also known as non-premixed combustion represent a specific class of combustion problems where fuel and oxidizer are not mixed before they enter the combustion domain. The mixing phenomenon brings both fuel and oxidant reactants into the reaction zone where thin layers of burnable mixtures at different equivalence ratios are formed and combustion takes place. Thus, mixing plays a vital role in defining combustion process. Combustion occurs in the mixing layer which is very small compared to that of a combustion system. This brings difficulties in controlling combustion and beyond this core mixing region mixture is either too rich (fuel side) or too lean (oxidizer side) for chemical reactions to proceed. In contrast to premixed flames, diffusion flames are not able to propagate against the flow. A definite thickness can not be assigned to these flames either. From the design and safety point of view, diffusion flames are simpler because no premixing with a given equivalence ratio is required and the flame may not start even fuel and oxidant exposes to high temperatures. However, their burning efficiency is restricted compared with premixed flames because the mixing or rather the rate of mixing limits the speed at which chemical reactions may proceed. In modern stationary gas turbines these flames are only employed for the piloting (or stabilization) of the main flame mostly in start-up regimes. The main disadvantage of pure diffusion flames is that they are less effective in terms of combustion temperature. The other major issue with diffusion flames is the formation of thermal NOx. The fuel can be diluted with nitrogen or exhaust gases (flamless combustion), but the maximal combustion temperature is always achieved in the region of stoichiometric mixture where the greatest NOx formation rates take place. Nevertheless, the fundamental understandings as well as modeling details of diffusion combustion phenomena are very important in context of partially premixed flames that actually appear in stationary gas turbine combustors.

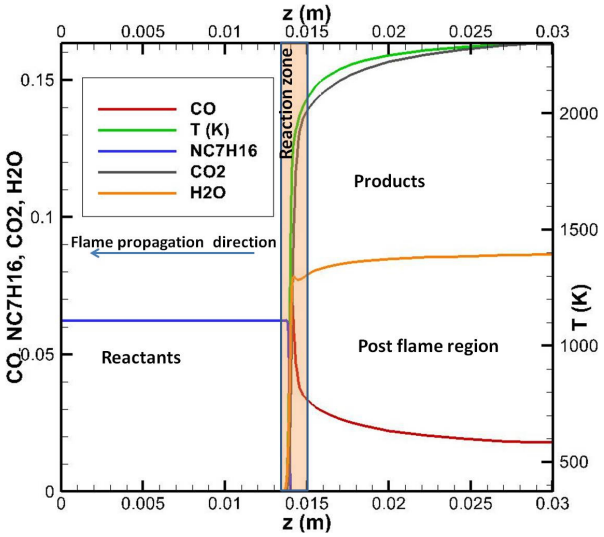

Figure 2.7: Schematic representation of n-Hepetane premixed combustion for both species mass fractions and temperature, simulated with Cantera [32]

Besides the more complex methods like the flamelet [128], the simplest approach for the modeling of diffusion flames is the well-known mixture fraction [163, 214, 217] description. The transport equation of mixture fraction equation does not have reaction source term. All scalars such as temperature, species concentrations, and density are related to this variable by pre-defined relations. Bilger [17] and Klimenko [109] proposed a conditional moment closure (CMC) concept for non-premixed turbulent combustion. They observed that most fluctuations of the reactive 22 scalars can be associated with the fluctuation of the mixture fraction.

2.4.2.2 Premixed combustion

In a premixed combustion configuration both fuel and oxidized are mixed at molecular level prior to entering combustion zone. A schematic representation of an idealized one-dimensional flame is shown in Fig. 2.7 This is following idealized representation is introduced by Zeldovich and Frank-Kamenetsky (ZFK) (see e.g. [70]) in their asymptotic analysis. One can see the development of the gas temperature T along the only considered axis z from minimal value T_0 (reactants) to maximal value T_{max} (products) and, consequently, the one-dimensional flame structure. Actually the flame front, if it is considered as an interval where significant temperature changes occur, consists of two main zones:

- Preheating zone where the diffusion of heat and mass proceeds very intensively while chemical reactions are not yet running
- Reaction zone where, in contrast to the preheating zone, chemical reaction rates rapidly grow up first and then go down so that chemistry dominates against diffusion

Behind the reaction zone a post flame region (or oxidation zone) is located where no significant heat is released and only some slow (in terms of kinetics) reactions occur at the high temperature achieved in the reaction zone. The fundamental issues of Zeldovich-Frank- Kamenetsky-von-Karman (ZFK) asymptotic theory is as follows:

- The reaction zone is located in the high temperature part of the flame and has a temperature nearly equal to T_{max}
- The thickness of the reaction zone is approximately one order of magnitude smaller than the thickness of the flame front
- The flame front propagates in the reactants' direction with velocity($\overrightarrow{s}$), which is proportional to the square root of from the product of the reaction rate following Eq. 2.53 at adiabatic flame temperature and thermal diffusivity as given by Eq. 2.55.

$$|\overrightarrow{s}|^2 \sim \frac{\lambda}{\rho C_p} e^{\left(\frac{E}{RT_{max}}\right)} \tag{2.55}$$

  this gives, consequently, the nature of the flame propagation coupled with the kinetics of the heat release and with heat conduction from the hot to the cold gas layers
- The maximal combustion temperature T_{max} is equal to the adiabatic temperature of the chemical reaction that, in turn, can be determined independently on the flame propagation theory from thermodynamic equilibrium.

In spite of lots of simplification and assumptions introduced in ZFK asymptotical thermal propagation theory, it helps to understand the fundamental mechanism. Namely that the flame propagation is caused by diffusive processes and the gradients, necessary for diffusion, are sustained by the chemical reaction. This fact is common for all premixed flames independently on the flow regime: laminar or turbulent. First, it is the laminar burning velocity (called by some authors the laminar flame speed) which is defined as a flow velocity necessary to keep a laminar premixed flame in the steady state (no propagation in reactants' direction). It is also directed normal to the flame front from products (burnt) to reactants (unburnt). The laminar burning velocity can be determined analytically under certain assumptions (ZFK theory [70], Williams [225] etc.). However, these assumptions lead to quantitatively poor results especially for rich flames. More accurate results may be obtained either from one-dimensional computations using detailed chemistry or from experiments. Actually the laminar burning velocity for a given fuel is only a function of the fuel/oxidizer ratio (equivalence ratio θ), pressure and the initial temperature of reactants. The laminar burning velocity decreases with increasing pressure and it increases with increasing temperature of the fresh gases.

In premixed combustion the fuel consumption and products formation take place in the thin reaction zone, but for the pollutant formation, both the reaction zone and the post flame region are important. Due to the fact that the post flame region is significantly larger than the reaction zone and consequently the residence time, which is much longer, the importance of this region for the "slowly" formed species (e.g. NOx) is even greater than that of the reaction zone.

2.4.2.3 Partially premixed combustion

The non-premixed and premixed regimes of combustion discussed in the previous sections are actually separated in terms of mixing. However, in technical applications, that

also include stationary gas turbines, there are very few situations when one of these combustion regimes appears in its pure form. More often a combination of non-premixed and premixed combustion modes takes place featuring the so-called partially premixed combustion phenomenon. The definition of partially premixed combustion given by Peters in [151] is as follows "If the fuel and oxidizer enter separately, but partially mix by turbulence before combustion, the turbulent flame propagates through a stratified mixture. Such a mode of combustion has traditionally been called partially premixed combustion".

In partially premixed flames the equivalence ratio θ of the fresh gas mixture directly in vicinity of the flame front is still located within the flammability limits but cannot be a priori specified like in perfectly premixed flames because of the additional mixing processes (not mandatory turbulent) appearing before combustion proceeds. Therefore, the equivalence ratio θ changes. These changes directly influence the flame propagation process. If the equivalence ratio varies only within the lean region ($z < z_{st}$), the complete fuel consumption occurs in the flame front. But if the mixture includes rich values of θ then the premixed flame is accompanied by an additional diffusion flame in the post flame region where the remaining fuel oxidizes. This type of flame is called triple flame. An example of a triple flame may be a lifted jet diffusion flame.

Depending on the nozzle exit velocity, the diffusion flame structure may disappear, i.e. at a sufficiently low nozzle exit velocity value a diffusion flame is attached to the nozzle. But increasing the exit velocity leads to stretching and finally disruption of the flame. Consequently, the flame lifts, the reactants mix above the nozzle without reaction to proceed, and a premixed flame stabilizes downstream within the jet. The stabilization appears at those points where the equilibrium between the flow velocity and the burning velocity (that depends on the local mixture) is achieved. In the region with rich (lean) mixture a rich premixed flame is stabilized. The fuel which is not consumed in the rich premixed flame diffuses across the flame into the post flame region and oxidizes building an additional diffusion flame along the stoichiometric mixture surfaces ($z_{st} = z$). Thus, three flame zones can be distinguished at one spatial location: lean premixed, rich premixed and diffusion flame. The location of the flame stabilization depends on the nozzle exit velocity and is characterized by the lift-off height. The lift-off height increases with increasing jet exit velocity but it cannot exceed a critical value at which the flame is completely blown out.

In real gas turbine combustors the situation is even more complicated. The flow is more complex, featuring different recirculation zones and gradients in different directions. The fuel is usually injected into a compact mixing chamber where it is mixed with the oxidizer. It is very important to accurately predict the mixing and flame stabilization processes for the construction of the burner. Partially premixed flames represent a very challenging example of highly complicated phenomena where fluid dynamics, mixing and combustion interact strongly influencing each other. Therefore, the importance of their understanding and possible prediction cannot be emphasized enough.

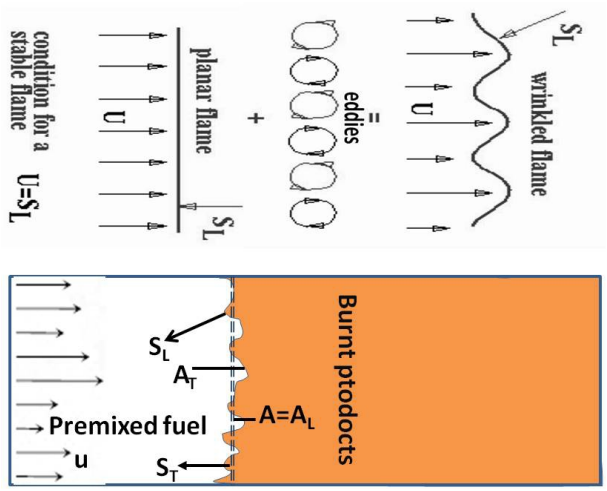

Figure 2.8: A schematic drawing of an idealized steady premixed flame in a duct

2.4.3 Combustion regimes

Similar to turbulent flows, combustion involves various lengths, velocity and time scales describing turbulence and chemical reactions. These scales are crucial in development of turbulent combustion models and applications. The relevant turbulent time and length scales are presented, followed by an overview of the relevant chemical time and length scales for laminar premixed combustion. When these characteristic chemical time and length scales are compared to those of the turbulent flow in a regime diagram, different regimes of premixed turbulent combustion can be identified. Combustion takes place, in most combustion engines, within a turbulent flow field. The turbulence enhances combustion process and thereby it increases the reactants consumption rate and hence heat releasing rate, which are much larger than those of laminar combustion. This is advantageous as it allows for smaller combustions systems. In turbulent premixed combustion, the fresh premixed mixture enters into the mean turbulent flame zone in a direction normal to the mean front at a speed much higher than the laminar flame speed (S_L). This speed is defined as turbulent flame (burning) speed S_T. Fig. 2.8 shows an idealized steady premixed flame in a duct.

The definition of a turbulent burning velocity was introduced by Damköhler, who also introduced the concept of an instantaneous wrinkled turbulent flame surface, which for constant turbulence and combustion properties should have reached statistically a steady state. $\dot{w}_T$ equated the mass flux $\dot{m}$ of unburnt gas with the laminar burning velocity S_L through the turbulent flame surface area A_T to the mass flux through the cross sectional area A_L with the turbulent burning velocity S_T Fig. 2.8. Damköhler specified two different regimes of turbulent premixed combustion [163, 214, 151]: the small-intensity, large scale turbulence and the high intensity, small scale turbulence. For small-intensity, large scale turbulence, Damköhler proposed that

$$\frac{S_T}{S_L} = \frac{A_T}{A_L} \tag{2.56}$$

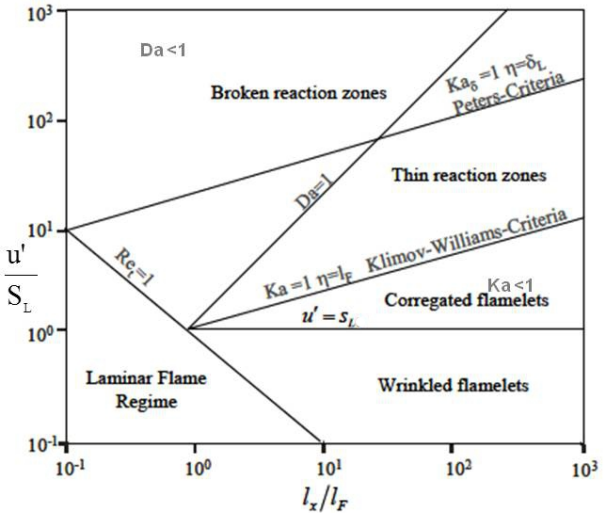

Figure 2.9: Premixed combustion regime diagram [151]

Damkohler also extended this by proposing the area ratio on the R.H.S. of Eq. 2.56 follow

$$\frac{A_T}{A_L} \propto 1 + \left(\frac{u'}{S_L}\right) \tag{2.57}$$

Thus turbulent flame speed can be expressed as

$$S_T \sim S_L + u' \tag{2.58}$$

For high-intensity, small scale turbulence, assuming that turbulence only modifies the transport between the reaction zone and the unburnt zone with an enhanced equivalent diffusivity to replace the molecular kinematic viscosity. From the scaling relation for the laminar flame speed and turbulent flame speed are:

$$S_T \sim \left(\frac{\nu}{t_F}\right)^{(1/2)} \tag{2.59}$$

$$S_T \sim \left(\frac{\nu_t}{t_F}\right)^{(1/2)} \tag{2.60}$$

where ν, ν_t and t_F are the molecular, turbulent kinematic viscosity and chemical time scale, respectively. From Eq. 2.59 and 2.60, a relation between S_T and S_T is obtained as

$$\frac{S_T}{S_L} \sim \left(\frac{\nu_t}{\nu}\right)^{(1/2)} \tag{2.61}$$

In literature different combustion regimes were identified which are based on both turbulent and chemical time scales. Peters [151, 20] identified the small-intensity, large scale and the high-intensity, small scale turbulence, with the corrugated flamelets regime and thin reaction zone regime (see Fig. 2.9), respectively. For small-intensity turbulence, the Kolmogorov scale is larger than the flame thickness, and the interaction between the flame front and the turbulence field is purely kinematic, i.e. turbulence can wrinkle the flame

but cannot disturb its local structure. For high-intensity turbulence, the Kolmogorov eddy scale is smaller than the preheat zone; hence, it can enter into the preheat zone, and enhances the transport of radicals and heat between the reaction zone and the unburnt gas. A large number of experiments for measuring the turbulent flame speed have been conducted with different combustion configurations, such as the Bunsen flame, counter-flow flame, swirling flame and so on. Review articles on the turbulent flame speed are available in the literature, e.g. [23]. It is found that, at low turbulence intensity, the turbulent flame speed increases almost linearly with the turbulence level. If the turbulence levels are higher than some critical value, the turbulent flame speed, however, only increases slightly, and even quenching of the combustion may happen. This effect is known as turbulent flame speed bending in combustion literature [23]. In order to distinguish the influence of different turbulence levels on the turbulent combustion, it is useful to classify the turbulent combustion into different regimes. To do this, a few dimensionless parameters are first introduced. To simplify the analysis, equal diffusivity for all reactive scalars are assumed. The flame thickness (l_F) and chemical reaction time scale (l_F) are defined as follows:

$$t_F = \frac{l_F}{S_L} = \frac{D}{S_L^2} \text{ where } l_F = \frac{D}{S_L} \tag{2.62}$$

where D is mass diffusivity. Then, the turbulent Reynolds number Re_t is expressed in terms of the turbulent fluctuation u' and turbulent integral length scale $L_I(= l_x)$ as

$$Re_t = \frac{u' L_I}{S_L l_F} \tag{2.63}$$

The Damköhler number Da which is the ratios of turbulent integral time scale τ_I to the reaction time scale t_f is defined as:

$$Da = \frac{\tau_I}{t_f} = \frac{L_I}{u'} \frac{S_L}{l_F} \tag{2.64}$$

The Karlovitz number is the ratio between the reaction time scale and Kolmogorov scale is defined as (see also Eq. 2.29):

$$Ka = \frac{t_f}{\tau_k} = \frac{u'(L_K)}{L_K} \frac{l_F}{S_L} = \sqrt{\frac{\varepsilon}{\nu}} \frac{S_L}{l_F} \tag{2.65}$$

From Eq. 2.63, 2.64 and Eq. 2.65, the turbulent Reynolds number can be correlated as:

$$Re_t = Da^2 Ka^2 \tag{2.66}$$

The turbulent premixed combustion regime is plotted in Fig. 2.9. The area below $Re_t = 1$ line corresponds to the laminar flame regime. Below the $u' = S_L$ line is the wrinkled flamelet regime where the velocity of the largest eddy is less than the laminar flame speed. The regime bounded by $Ka = 1$ and $u' = S_L$ lines is called the corrugated flamelet regime and the flame thickness l_F is thinner than the Kolmogorov length scale (L_K). The turbulence eddies can only wrinkle but cannot penetrate into the flame front. The region between $Ka_\delta = 1$ ($Ka = 100$) and $Ka = 1$ corresponds to thin reaction zone; in this region L_K is equal to the inner layer thickness. In this region the Kolmogorov eddies can enter into the preheat zone but cannot penetrate into the reaction zone. Thus,

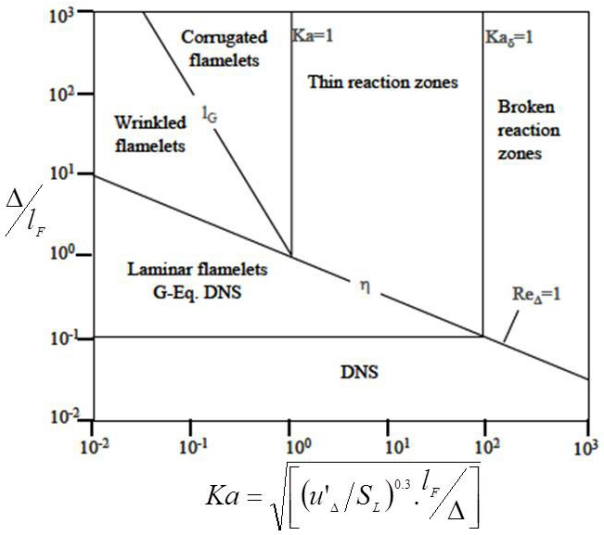

Figure 2.10: Premixed combustion regime in the LES context, while non-dimensional filter width is represented in terms of the Karlovitz number.[161, 58]

it is called thickened-wrinkled regime. The region above the line $Ka = 100$, lies the broken reaction zone, in which both the preheat zone and inner layer are disturbed by the turbulent eddies, where the thin flame assumption is no longer valid. This diagram is extended for LES by Pitsch et al. [161] and by Düsing et. al [58] and theses are formulated in terms of quantities and plotted for (Δ/l_F to Ka) at the filter level(Δ) in Fig. 2.10.

2.4.4 Reduction methods for combustion chemistry

Theoretically the combustion of natural gas involves many reactions and species. The popular detailed mechanism GRI-Mech 3.0 by [188] contain as many as 53 species with 325 elementary reactions. The species number and reaction steps increase rapidly with complicated chemical environments such as higher hydrocarbons/ignition/multiphase/soot. It requires very huge computational resources to work with these reaction mechanisms involving a few hundreds of species and reaction steps. This is inevitable because it needs to solve transport equations for all involved species. In addition, due to the wide range of chemical time scales (fast reactions take place within 10^{-8} seconds, whereas slow reactions can last up to 1 second) the resulting set of PDEs are extremely stiff and therefore difficult to solve. The applications of detailed mechanisms of these large mechanisms are mostly limited to zero and one dimensional cases and while three dimensional application cases are very rare. The reaction mechanisms comparatively with less number of reaction steps can be used to perform direct numerical simulation of turbulent combustion and considerable effort has been put into the development of numerical methods for solving such systems [110, 15, 137, 227, 50]. Presently, the availability of the large, fast and affordable computational resources allows the application of these methods for only to the selected academic problems. It is not an option for real time applications in the next 10 years in the LES framework also. As a result, there is a definite requirement for reduction techniques, which help to retain all the relevant information about important species and rate determining processes by reducing unnecessary information.

In the literature many works are available on reduction methods for chemistry. The classical approach for reducing the chemical reaction mechanism by reducing to a single step reaction between fuel and oxidizer forming the products; was proposed by Zeldovich and Frank-Kamentzki [231]. The necessary Arrhenius law reactions rates for reactions involved in these reaction mechanisms are fitted with the experimental data/detailed simulations to avoid the complexity to derive from the elementary kinetic data [221]. This limits the insight provided by these one step mechanisms to only the overall analysis, by ignoring many crucial physical phenomenon that takes place during the combustion. Therefore, more sophisticated reduction techniques incorporate additional chemical kinetic details. The very small time scales of combustion chemistry allow decoupling combustion chemistry from other processes with larger time scales. The most of the reduction strategies are based on this assumption. This can be achieved systematically via steady-state or partial-equilibrium [150, 151]. The reduction strategies cannot be achieved by following universal principle. Thus they cannot be automated. One need to understand chemical kinetics involved in detail to reduce them typically below 10 reaction steps, thus reduced mechanisms are specific to the selected applications.

The reduction mechanisms in recent times are becoming very popular industrially. But as the stringent emission norms demand the capturing and retaining of in detail thermo-chemical information new methods were evolving. Maas and Pope [129] proposed Intrinsic Low-Dimensional Manifolds (ILDM) considering combustion as a movement along a trajectory through composition space. These trajectories are rapidly evolved to form low-dimensional manifolds starting from different initial conditions taking advantage of different time scales present in the combustion process. The slowest time scales govern the movement and thereby it reaches the chemical equilibrium. The manifold can be identified automatically by an Eigen value analysis of the Jacobean of the detailed mechanism. This results in the possibility of tabulation of chemical system as a function of a few reaction progress variables (RPV) across the manifold. Typically, a progress variable a combination of two species mass fractions, namely the mass fractions of CO_2 and H_2O are used. Although in principle linear combination of any available species mass fractions could be chosen. ILDM based reduced mechanisms have been applied successfully in the past to the computation of turbulent flames [132]. Following ILDM, the concept that a multi-dimensional flame can be represented by a set of one-dimensional flamelets, Giquel et al. [76] and independently van Oijen and de Goey [142, 36, 203] proposed to construct Flamelet-Generated Manifolds (FGM) by tabulating the chemical state from a series of one-dimensional flame simulations using a detailed mechanism at different conditions. In the simplest case, a single-progress variable can give all necessary thermo-chemical properties of the combustion system. The FGM approach also gives the advantage of retaining the effects from flow and turbulence.

2.4.5 Turbulent chemistry interactions

The combustion takes place in turbulent flow environment; which is challenging to understand and model it satisfactorily. The flames undergo rapid changes of many orders (e.g. number of reactions) at sub grid level (within a single CV), whereas in the

LES context the turbulent premixed flames completely changes from un-burnt to burnt within a single CV. To capture all chemical behaviors exactly, CV should be smaller than the molecular size of smallest molecule/radical which exist in the process. In CFD simulations of turbulent combustion, it is very apparent the mixing of different of species, radicals is influenced and controlled by turbulence of the flow. It is challenging to model the mixing of these anisotropic radicals, though some works in that direction are available in the literature [240, 238]. In the context of CFD combustion modeling, the mixing in the case of diffusion flames, fluctuations in the mixture fraction and equivalence ratio can be observed. Note that, in the premixed combustion configurations, the diffusion flame reactions also takes place in the shear layer between main jet and co-flow. Eq. 2.50, 2.52 and 2.53 are used to determine through kinetic theory the species source terms, density, viscosity etc. Filtered source terms cannot be assessed using the filtered concentrations and temperature, as the strong non-linearity of these functions exists.

$$\overline{\dot{w_\alpha}} \neq \dot{w_\alpha}\left(\overline{T}, \overline{Y_\propto}\right) \qquad \alpha = k \tag{2.67}$$

where T, Y and $\propto$ denotes respectively the temperature, concentration and the species. It is very difficult to expand the reaction rate into a Taylor-series based on the fluctuations of temperature and concentrations of the species. Therefore it is not viable a solution for the combustion driven systems. In recent time many works [208, 151] are focused to overcome this issue, initially with a special focus on the diffusion flames. The concepts of turbulent flame chemistry can be categorized into mainly three types:

1. Chemical time scales are much faster than the time scales of the turbulent flow $Da >> 1$ (see Eq. 2.64).
2. Physical view of the flame in geometrical perception [92, 17]
3. Local statistical analysis of the reactive flow [165, 134]

In the first category, mixing at the small scales takes place then followed by the rate determining step. Thus, the chemical source term can be parametrized by the turbulent mixing. The eddy-breakup and eddy-dissipation models were developed following this assumption which is more relevant to the premixed and partially premixed flames. Classical examples of this type of approach are the eddy-breakup and eddy-dissipation models which simply take the turbulent time scale as the relevant rate. These models are, however, not relevant for the diffusion flames.

The second category is a physical feature in the place of a geometrical view, called flamelet model. The flamelet models in general define the changes of physical quantities in the normal direction to the flame surface and flamelets are 1-dimensional laminar flames. In diffusion flames, the flame-normal coordinate is the mixture fraction ξ and turbulence is taken into account only through the probability density function (PDF) of ξ. The most familiar approach to model this PDF is from a number of its statistical moments, for example a $\beta - PDF$ parameterized by the mean and fluctuation of mixture fraction [92]. The conditional moment closure (CMC) [17], also belongs to the models based on a physical features of the flame. Instead of using conventional averaging, all quantities are conditioned on a particular value of mixture fraction, e.g. $\xi = \xi_{st}$. In order

to obtain reasonable accuracy, several equations must be solved to account for different values of the conditioning variable and the method is therefore quite expensive.

The third category to address turbulent chemistry interaction is based on local statistical analysis of the reactive flow. Once details of the joint PDF $P(T, Y_\alpha)$ is available, the filtered source term can be computed without any additional closure assumptions. The most well-known example is the transported PDF [165], which is based on solving an equation for the 1-point joint PDF of velocity and the reactive scalars. These are computationally very expensive due to their high-dimensionality. In addition, while the convective term appears also in a closed form in these equations, the diffusion here is described by a micromixing model. In theory, the PDF method can predict kinetic effects correctly, but the results are sensitive to the micromixing model used. A further method of this type is the linear eddy model (LEM) [134], which solves the unresolved mixing in a 1-dimensional sub domain making some assumptions about the influence of turbulent structures on the mixing process. This method is reasonably universal, but requires additional computational cost due to increased number of equations that need to be solved.

2.5 Non-adiabatic combustion

Non-adiabatic combustion is described when a flame reaction zone losses heat to the surroundings. This means the temperature achieved by the combustion cannot sustain anymore. The combustion phenomenon involving hundreds of species, thousands of reactions steps, flow, turbulence and mixing is highly influenced by the initial, final and intermediate temperatures in the reaction zone. Therefore, the study of this phenomenon is challenging.

In most of the practical applications combustion takes place in a closed vessel or at least flame experience the walls during the combustion process. The walls are challenging for modeling in CFD; because the velocity gradients are very steep and the modeling physics accurately is a very expensive task. In addition when flame comes into contact to the wall, the modeling becomes more challenging and difficult task. All combustion processes detailed in previous sections could experience walls in real applications. The walls are exposed from one side to the ambient temperatures or cool devises leading to lower temperatures on the flame side. This leads to very high steep gradients of the flame near the wall in case of the flame is in the vicinity. It is assumed that within 1 mm thickness temperature drops from adiabatic flame temperature to the wall temperature [163]. The flame behavior (combustion process) also depends on the local temperatures together with concentrations, degree of the mixing following Eq. 2.52, 2.53 and 2.54. The practical and most of academic applications avoid solving detailed chemical mechanism. Furthermore, it is difficult for modeling this complex combustion phenomena using classical combustion models. It is worth mentioning that the wall in combustion chamber could play an important role in a catalytic combustion for producing combustion stabilities, but this is not considered in this work. In this section an overview of flame wall interaction is presented.

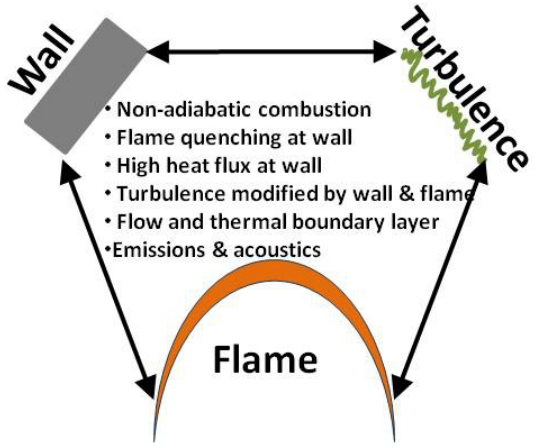

Figure 2.11: A schematic represenation flame wall interaction phenomenon [163]

2.5.1 Fundamentals of Flame wall interaction

The interaction of flame, wall and turbulence is a common phenomenon as detailed in section 1.1.2 and it can be represented as in Fig. 2.11. All these three aspects influence each other by:

- Wall could quench the flame and could modify the turbulence
- Flame modifies the turbulence and heats the wall
- Turbulence enhance both heat transfer the combustion phenomenon

These phenomenon is attributed to the formation of unburnt hydrocarbons (HC), flame quenching and the damages to the combustion walls [4], the major HC pollutant formation from crevice combustion [97] is also a part of FWI, which is not considered here. The two major highly technical combustion systems gas turbines and internal combustion engines (IC) are different in FWI prospects. In gas turbine mainly hot gases are interacting with the walls, whereas in IC engines part of the liquid fuel spay injected on the walls and piston need to be burnt. The combustion of fuel on the flame induces very high heat flux and flame also can quench leaving unburnt HC on the walls.

The CFD modeling of interactive, complex physics of FWI is necessary to design many combustion systems and it is challenging. The FWI modeling performed by flamelet turbulent combustion model and $\kappa\&\epsilon$ for flow was discussed by Poinsot and et al. [163]. The flame wall interaction basically classified into three categories for a premixed combustion namely *Head-on quenching (HOQ)*, *Side-wall quenching (SWQ)* and *Tube quenching* [163]. Please note that mine-lamp is based on the principle of flame quenching by walls, i.e. Tube quenching. The concept of flame wall interaction is not very well developed though in literature few works can be found with RANS and DNS models [164, 7, 26]. The modeling of combustion for FWI with LES is presented in chapters 3 and 5.

Chapter 3

LES of flow, mixing, combustion with and without heat loss

In this work Large Eddy Simulation (LES) is applied throughout the work, together with advanced SGS mixing models, ATF combustion models, Scale similarity reaction models and heat transfer models, where ever it is necessary. The details of these models are provided. The details of chemistry modeling and reaction models are discussed in tabulated chemistry chapter separately.

3.1 Filtering of variables for LES

The concept of classical LES formulation is that the large scales are spatially and temporally resolved by the numerical discretization while the small scales which cannot be resolved on the grid are described by a subgrid scales (SGS) model. Therefore, LES constitutes an approach on intermediate level between DNS and RANS. The small unresolved scales are usually referred to as the SGS while the resolved ones are named as the grid scales. The separation of large from small scales is attained by means of the spatial low pass filtering which is expressed by convolution of the equations with a filter function G, here for an arbitrary variable $\Phi(x,t)$ [121].

$$\overline{\Phi}(x,t) = \int_{-\infty}^{\infty} G(r)\,\Phi(x-r,t)\,dr \tag{3.1}$$

This type of an integral is called a convolution. $G(r)$ is a filter function that satisfies the normalized condition:

$$\overline{\Phi}(x,t) = \int_{-\infty}^{\infty} G(r)\,dr = 1 \tag{3.2}$$

The filter function has a typical filter width Δ which is chosen such that the separation is carried out within the inertial sub range of energy spectrum. The most commonly used filter functions are:

- The sharp Fourier cutoff filter (see e.g. [121, 166, 48]) defined in wave space as:

$$G(\kappa) = \begin{cases} 1 & \text{if} \quad \kappa < \pi/2 \\ 0 & \text{otherwise} \end{cases} \tag{3.3}$$

- The Gaussian filter:

$$G(r) = \sqrt{\frac{6}{\pi\Delta^2}} e^{\left(-\frac{6r^2}{\Delta^2}\right)} \tag{3.4}$$

- The box filter or top-hat filter:

$$G(r) = \begin{cases} 1/\Delta & \text{if} \quad |r| < \Delta/2 \\ 0 & \text{otherwise} \end{cases} \tag{3.5}$$

Since a finite-volume structured code was used for this work, the box filter is also appropriate and used here. With a finite volume discretization, filter G doesn't appear explicitly at all. The way the implicit filter works is to discard any scale smaller than grid size. The decomposed variable by filtering can be written as:

$$\Phi(x,t) = \bar{\Phi}(x,t) + \Phi'(x,t) \tag{3.6}$$

The difference between filtered quantity $\bar{\Phi}(x,t)$ and original variable (not filtered, $\Phi(x,t)$) is the fine structure $\Phi'(x,t)$, which contributes to SGS terms in LES transport equations.

Favre filtering The major difference of combustion from isothermal flow is that density varies by a factor of seven to ten between unburnt and burnt gases. In a turbulent flow, the density is therefore a fluctuating quantity and when filtering the governing equations according to Eq. 3.1, the density has to be decomposed into a filtered mean and a residual, $\rho = \bar{\rho} + \rho'$. Since in the equations density is multiplied with the transported quantity, the filtering variable brings new unknown correlations as:

$$\overline{\rho\Phi} = \overline{(\bar{\rho} + \rho')\left(\bar{\Phi} + \Phi'\right)} = \overline{\bar{\rho}\bar{\Phi}} + \overline{\bar{\rho}\Phi' + \rho'\bar{\Phi}} + \overline{\rho'\Phi'} \tag{3.7}$$

The unknown density correlations from Eq. 3.7 need to be correlated, which brings additional complexities into LES combustion modeling. This difficulty is avoided by using Favre or density-weighted filtering similar to Favre averaging known from the RANS context [62]. A density-weighted quantity is given by

$$\widetilde{\Phi} = \frac{\overline{\rho\Phi}}{\bar{\rho}} \Rightarrow \bar{\rho}\widetilde{\Phi} = \overline{\rho\Phi} \tag{3.8}$$

This density based averaging formulation allows defining the filtered equations basically to keep the same structure as in the case of constant density. It is common practice to model the combustion with the Favre-filtered correlations in exactly the same manner as for the case of flows with constant density.

3.2 Modeling technique

In the present work, a classical approach for LES is used according to [241]. To separate the large from small-scale structures in LES, filtering operations are applied to the governing equations as described in last section, which are the momentum equation (3.10) along with the continuity equation (3.9) used to describe the motion of low Mach number Newtonian fluids. In addition, the change of mixture fraction, ξ, caused by the turbulent convection and diffusion of a passive (or conserved) scalar is given by the transport equation (3.11).

$$\frac{\partial \bar{\rho}}{\partial t} + \frac{\partial \bar{\rho}\widetilde{u_i}}{\partial x_i} = 0 \tag{3.9}$$

$$\frac{\partial \bar{\rho}\widetilde{u_i}}{\partial t} + \frac{\partial \bar{\rho}\widetilde{u_i}\widetilde{u_j}}{\partial x_j} = \frac{\partial}{\partial x_j}\left[\bar{\rho}\widetilde{\nu}\left(\frac{\partial \widetilde{u_i}}{\partial x_j} + \frac{\partial \widetilde{u_j}}{\partial x_i}\right) - \frac{2}{3}\bar{\rho}\widetilde{\nu}\frac{\partial \widetilde{u_k}}{\partial x_k}\delta_{ij} - \bar{\rho}\tau_{ij}^{sgs}\right] - \frac{\partial \bar{p}}{\partial x_i} \tag{3.10}$$

$$\frac{\partial \bar{\rho}\widetilde{\xi}}{\partial t} + \frac{\partial \bar{\rho}\widetilde{u_i}\widetilde{\xi}}{\partial x_i} = \frac{\partial}{\partial x_i}\left(\bar{\rho}\widetilde{D_\xi}\frac{\partial \bar{\rho}\widetilde{\xi}}{\partial x_i}\right) - \frac{\partial \bar{\rho}J_i^{sgs}\left(\widetilde{\xi}\right)}{\partial x_i} \tag{3.11}$$

In equations (3.9)-(3.11) the quantity u_i (i=1, 2, 3) denotes the velocity components in x_i direction, ρ the density, p the hydrostatic pressure and δ_{ij} the Kronecker delta. The quantity ν is the molecular viscosity and D_ξ the molecular diffusivity coefficient. Quantities denoted as $\overline{(\bullet)}$ and $\widetilde{(\bullet)}$ are filtered and Favre-filtered quantities, respectively. To take into account chemical kinetic effects, the introduction of variables to track the reaction progress is useful. This is achieved by incorporating into the CFD, besides the mixture fraction equation already available, an additional transport equation for the reaction progress variable (RPV):

$$\frac{\partial \bar{\rho}\widetilde{Y_\alpha}}{\partial t} + \frac{\partial \bar{\rho}\widetilde{u_i}\widetilde{Y_\alpha}}{\partial x_i} = \frac{\partial}{\partial x_i}\left(\bar{\rho}\widetilde{D_{Y_\alpha}}\frac{\partial \bar{\rho}\widetilde{Y_\alpha}}{\partial x_i}\right) - \frac{\partial \bar{\rho}J_i^{sgs}}{\partial x_i} + \widetilde{\dot{w}_\alpha} \quad (\alpha = 1, 2, ..) \tag{3.12}$$

where $\widetilde{Y_\alpha}$ is the filtered concentration of the reaction progress variable α. The quantity D_{Y_α} denotes the molecular diffusivity coefficient. For the combustion process under investigation only one RPV has been defined ($\alpha = 1$) as:

$$Y \equiv Y_{RPV} = \frac{Y_{CO_2}}{M_{CO_2}} \tag{3.13}$$

where M denoted the molar mass of the species. The equations (3.9)-(3.12) govern the evolution of the large, energy-carrying scales of flow and mixing field. In flow and scalar field, the effect of the small scales appears through the SGS stress tensor and the SGS scalar flux vector,

$$J_i^{sgs} = \widetilde{u_i z} - \widetilde{u_i}\widetilde{z}; \quad z \equiv (Y, \xi) \tag{3.14}$$

$$\tau_{ij}^{sgs} = \widetilde{u_i u_j} - \widetilde{u_i}\widetilde{u_j} \tag{3.15}$$

respectively. The last term in equation (3.12) is the filtered chemical reaction rate that together with the quantities (3.14) and (3.15), must be modeled in order to obtain a closed system of equations (3.9)-(3.12).

The subgrid kinetic energy k^{SGS} is defined as $k^{SGS} = (\widetilde{u_i u_i} - \widetilde{u}_i\widetilde{u}_i)/2$. For solving passive scalar, it is necessary to introduce, analogously to k^{SGS}, the subgrid *scalar energy* also referred as the SGS scalar variance [198]. It is defined as:

$$f_z = \widetilde{z}\widetilde{z} - \tilde{z}\tilde{z} \tag{3.16}$$

The scalar variance is in turn governed by the transport equation

$$\frac{\partial f_z}{\partial t} + \frac{\partial \widetilde{u}_i f_z}{\partial x_i} = \frac{\partial}{\partial x_i}\left(D\frac{\partial f_z}{\partial x_i}\right) - \frac{\partial}{\partial x_i}\left(\widetilde{u_i z^2} - \widetilde{u}_i\widetilde{z^2}\right) - 2D\left(\widetilde{\frac{\partial z}{\partial x_i}\frac{\partial z}{\partial x_i}}\right) + 2D\frac{\partial \widetilde{z}}{\partial x_i}\frac{\partial \widetilde{z}}{\partial x_i} + 2\frac{\partial}{\partial x_i}\left(\widetilde{z}J^{sgs}_{i,z}\right) - 2J^{sgs}_{i,z}\frac{\partial \widetilde{z}}{\partial x_i} \tag{3.17}$$

The four unclosed terms on $R.H.S$ represent turbulent convection of scalar (term 2 in R.H.S), SGS dissipation of scalar (term 3), large scale diffusion (term 5) and production of large scales (term 6). Terms 5 and 6 can be closed by using SGS scalar flux models. Term 2 can be closed by using a series expansion or an appropriate model. The SGS scalar dissipation (term 3) defined as:

$$\widetilde{\chi} \equiv 2D\widetilde{\frac{\partial z}{\partial x_i}\frac{\partial z}{\partial x_i}} \tag{3.18}$$

which requires an additional model. The SGS scalar dissipation modeling is not an issue in this work. It will be nevertheless needed for determination of the scalar mixing as introduced earlier in this chapter. The section below therefore will only focus on SGS models both in the velocity and scalar field.

3.3 Modeling sub-grid scales of the flow

The filtered momentum Eq. 3.10 has unknown term τ^{sgs}_{ij} called SGS stresses, which represents unresolved scales by Eq. 3.15 is decomposed following [156] as:

$$\tau^{sgs}_{ij} = \widetilde{u_i u_j} - \widetilde{u}_i\widetilde{u}_j = L_{ij} + C_{ij} + R_{ij} \tag{3.19}$$

and

$$L_{ij} = \widetilde{\widetilde{u}_i\widetilde{u}_j} - \widetilde{u}_i\widetilde{u}_j, \quad C_{ij} = \widetilde{\widetilde{u}_i u'_j} - \widetilde{u'_i\widetilde{u}_j}, \quad R_{ij} = \widetilde{u'_i u'_j} \tag{3.20}$$

where

- $L_{ij}$is the Leonard stress : This term represents the subsgrid scales results from the interaction of resolved scales and these can be computed explicitly
- C_{ij} is the cross term: This contribution is from the interaction between the resolved and sub grid scales. The sub grid scales are unknown quantities here, hence modeling of this term is required

- R_{ij} is the SGS Reynolds stress: SGS Reynolds stresses represent interactions between unresolved scales. So, this also needs to be modeled.

For developing SGS models, some direction has been available in the literature from classical modeling of the Reynolds stresses. In the following classical SGS stress models will be outlined, which assume that the influence of the small structures can be described as a function of the large scale quantities. The simplest class of models consists of the linear models, which are based on the eddy viscosity approach. A very common model is the one developed by Smagorinsky [187]. It is one of the simple models available and applied successfully for wide range of applications by provided good numerical properties; however, it has a tendency to dissipate high amounts of turbulent kinetic energy. Another popular model is the Bardina model [11]. This scale similarity based model yields accurate SGS stresses. However Bardina's model does not dissipate sufficient turbulent kinetic energy, so simulation tends to be unstable. To overcome this problem, the model has often been combined with the *Smagorinsky* model, which leads to mixed model.

All models mentioned here are scaled by a model parameter. However, the ideal values of this parameter depend on the configuration and on the location in the flow. A recent development is that of the dynamic procedure originating from M. Germano [74] and Lilly [123], which can be used to automatically determine e.g. the Smagorinsky suited model parameter. The resulting approach is often referred as Germano model (or dynamic procedure). A further class of models comprises the nonlinear models. Advanced and complex algebraic stress models have been proposed by C. Speziale [193] and B. Kosovic [112] are available in literature, but not studied in this work. Menon et al. [135] proposed to solve an additional transport equation for determining turbulent kinetic energy k^{SGS}.

3.3.1 Eddy viscosity model

In eddy viscosity approach, it is assumed that small scale turbulence affects the flow field as the molecular viscosity. Therefore, the SGS term τ_{ij}^{SGS} may be modeled by adding a turbulent viscosity ν_t to the molecular viscosity ν, resulting in an effective viscosity $\nu_{ef} = \nu + \nu_t$. The ν is replaced by ν_t in Eq. 2.4 to find the SGS stress tensor τ_{ij}^{SGS} in the filtered Navier-Stokes Eq. 3.10 corresponds to applying the following model

$$\tau_{ij}^{SGS} = \rho\nu_t \left(\frac{\partial \widetilde{u_i}}{\partial x_j} + \frac{\partial \widetilde{u_j}}{\partial x_i} \right) - \frac{2}{3}\rho\nu_t \frac{\partial \widetilde{u_k}}{\partial x_k}\delta_{ij} \tag{3.21}$$

where the tensor τ_{ij}^{SGS} has been decomposed into a deviatoric part and a isotropic part. FASTEST-3D CFD code [218, 241] used here is based on a pressure correction scheme [147, 63] to determine the value of the pressure so that the equation of continuity is satisfied. This pressure correction is able to compute the sum of the pressure and the trace-term of the stress-tensor. Therefore, the pressure-parameter $\overline{P}$ is introduced as [85]:

$$\overline{P} = \overline{p} - \frac{1}{3}\overline{\rho}\tau_{kk}^{SGS} \tag{3.22}$$

Adding trace term from Eq. 3.22 in Eq. 3.21, one gets the following deviatoric τ_{ij}^{SGS*} as follows:

$$\tau_{ij}^{SGS*} = \tau_{ij}^{SGS} - \frac{1}{3}\overline{\rho}\tau_{kk}^{SGS} = \rho\nu_t\left(\frac{\partial\widetilde{u_i}}{\partial x_j} + \frac{\partial\widetilde{u_j}}{\partial x_i}\right) - \frac{2}{3}\rho\nu_t\frac{\partial\widetilde{u_k}}{\partial x_k}\delta_{ij} \tag{3.23}$$

The final favre averaged momentum equation for solving in LES is obtained by substituting equation 3.23 in Eq. 3.10. The the following sub sections formulation of the models required for ν_t are discussed.

3.3.1.1 Smagorinsky model

The solving of farvre filtered momentum Eq. 3.10 including τ_{ij}^{SGS} as described in Eq. 3.23 requires an approximation for the turbulent viscosity ν_t. One of the first and most successful approximations by Smagorinsky [187] is as follows:

$$\nu_t = (C_s\Delta)^2\,|\widetilde{S}| \quad \text{with} \quad |\widetilde{S}| = \left(2\widetilde{S}_{ij}\widetilde{S}_{ij}\right)^{\frac{1}{2}} \tag{3.24}$$

where Δ is the filter width and C_s is model coefficient. The Smagorinsky model gives relation between the eddy viscosity and the large-scale strain-rate tensor as

$$\widetilde{S}_{ij} = \frac{1}{2}\left(\frac{\partial\widetilde{u_i}}{\partial x_j} + \frac{\partial\widetilde{u_j}}{\partial x_i}\right) \tag{3.25}$$

The Smagorinsky model uses a typical length scale $C_s\Delta$ and a typical time scale (determined by the contraction of the deformation velocity tensor) to compute the turbulent viscosity. The Smagorinsky parameter C_s contained therein can vary between 0.065 and 0.2 and it primarily depends on the type of flow as well as on the filter width. Since the parameter enters the model quadratically, the model expression can vary by one order of magnitude depending on the choice of C_s. Still, with a proper choice of C_s reasonable results can be obtained for simple flows, but when complex flows are considered, the Smagorinsky model envisage inadequately. The most important drawback of this model is that it is purely dissipative and therefore is unable to predict the backscatter effects described earlier. The model is also not able to differentiate between shear connected to turbulence and shear due to mean gradients in the velocity field. This poses a problem especially in boundary layers, which always have a laminar sublayer near to the wall. The turbulent viscosity ν_t should therefore tend towards zero when approaching the wall. Near the wall steep velocity gradients are present due to the boundary layer presence, in this region the Smagorinsky model predicts high levels of turbulence.

3.3.1.2 Dynamic procedure for Smagorinsky model

In Smagorinsky approximation the model coefficient needs to be estimated or chosen prior to the LES simulation as the constant is not universal. Germano [74] proposed a dynamic procedure for the calculation of the model coefficient. In dynamic models, the coefficient of the model is determined from the flow parameters rather than a priori input as in the standard Smagorinsky model. This is achieved by defining a test filter $\widehat{\Delta}$ with a width larger than the grid filter-width ($\sim \widehat{\Delta}/\Delta > 1$). This test filter eliminate the smallest resolved scales and can be used to define a test filter stress

$$B_{ij} = \widehat{\widetilde{u_i}\widetilde{u_j}} - \widehat{\widetilde{u}}_i\widehat{\widetilde{u}}_j = T_{ij} - \widehat{\tau_{ij}^{SGS}} \tag{3.26}$$

where resolved turbulent stresses B_{ij} (the contribution from the region between test-filter and grid-filter scale), the SGS stresses τ_{ij}^{SGS} the subtest stresses (test filter stress) $T_{ij} = \widehat{\widetilde{u_i}\widetilde{u_j}} - \widehat{\widetilde{u}}_i\widehat{\widetilde{u}}_j$, which are obtained by applying the test filter of characteristic width $\widehat{\Delta}$, to the filtered Navier-Stokes equation. Consider now an eddy viscosity model to parameterize both subgrid and subtest filter stresses, of the form (Υ_{ij} and γ_{ij} following Eq. 3.23 and 3.24 with test-filter and grid-filter)

$$T_{ij} = -2C_d\Upsilon_{ij} \quad \text{with} \quad \tau_{ij}^{SGS} = -2C_d\gamma_{ij} \tag{3.27}$$

By substituting Eq. 3.27 into Eq. 3.26, the identity can be satisfied only approximately, since the stresses are replaced by modeling assumptions, and the system is overdetermined (five independent equations are available to determine a single coefficient). Lilly [123] proposed that the error incurred when a single coefficient is used should be minimized in a least-squares sense. The error is

$$e_{ij} = B_{ij} - T_{ij} + \tau_{ij}^{SGS} = B_{ij} + 2C_dM_{ij} \tag{3.28}$$

with $M_{ij} = \Upsilon_{ij} - \widehat{\gamma_{ij}}$. The least squares minimization procedure requires

$$\frac{\partial\langle e_{ij}e_{ij}}{\partial C_d} = 2\left\langle e_{ij}\frac{\partial e_{ij}}{\partial C_d}\right\rangle = 0 \tag{3.29}$$

where the $\langle\rangle$ brackets indicate an appropriate ensembled average. This leads to

$$\langle(B_{ij} + 2C_dM_{ij})\,M_{ij}\rangle \tag{3.30}$$

and giving

$$C_d = -\frac{1}{2}\frac{B_{ij}M_{ij}}{M_{ij}M_{ij}} \tag{3.31}$$

An eddy viscosity form model adequately approximates the interaction between given turbulent scales and distinctly smaller scales, in which the main function of the SGS is to eliminate energy from the grid scale, but it is inadequate for representing the backward scatter of SGS energy into the grid scale. Another drawback is the alignment of τ_{ij}^{SGS} and $\widetilde{S}_{ij}$ which is not confirmed experimentally [37]. All Smagorinsky based models also assume the equilibrium between production and dissipation of kinetic energy in small scales which is difficult to be met in complex configurations. Nevertheless, they appear to be satisfactorily implemented in a number of engineering flows. To overcome the shortcomings, related to the alignment assumption in these models, the so called scale similarity based models, the nonlinear gradient model have been suggested.

3.3.1.3 Scale similarity SGS model

One of other SGS model for the eddy viscosity is the scale-similarity model which is based on the hypothesis that the smallest grid scale and the largest SGS are similar. Scale-similarity models employ multiple filtering operations to identify the smallest resolved scales as:

$$\tau_{ij}^{SGS} = C_{ss}\left(\widehat{\widetilde{u_i}\widetilde{u_j}} - \widehat{\widetilde{u}}_i\widehat{\widetilde{u}}_j\right) \tag{3.32}$$

where C_{ss} is the model coefficient. This model has been shown to be the most active in the interaction with the unresolved sub grid scales. These models can provide backscatter in a numerically stable and physically realistic manner, and predict SGS stresses in regions that are well correlated with the locations where large Reynolds stress occurs. There are many modifications of scale similarity model (e.g. [43, 180]). For example, the mixed models include an eddy-viscosity part as well as a scale-similar contribution in order to overcome the drawback inherent to the scale similarity model, which is that the predicted magnitude of the backward scatter contribution is larger than the exact DNS predicted value [90].

Besides these classical models mentioned above, the new developed models tried to overcome the local equilibrium assumption. For this end one equation model and anisotropy model try to model the unclosed term in more physically consistent way. Second order SGS models have also been proposed, (see Fureby et al. [73], Davidson [48] and Horiuti [83]). However, because of difficulties of implementation and cost on computation, these higher order models didn't gain wide applications for implementation. A recent overview on SGS stress tensor modeling can be found in [179]. The Smagorinsky-model with dynamic procedure according to Germano et al. [74] is applied to determine the subgrid scale stresses. In order to stabilize the model, the modification proposed by Sagaut [178] is applied. In addition a clipping approach will reset negative Germano coefficient to zero to avoid destabilizing values of the model coefficient. It is known that wall-adaptive SGS models have been proposed recently, like the wall adapting laminar eddy (WALE) model [199] or the Vreman model with and without dynamic procedure [100, 146, 13]. Some hybrid LES/RANS approaches are also available [199, 72]. Neverthless no special wall-treatment is included in the subgrid-scale model applied in this work. We rather rely on the ability of the dynamic procedure to capture the correct asymptotic behavior of the turbulent flow when approaching the wall as discussed in detail by Wegner [218].

3.4 Modeling of scalar sub-grid scales

In this work the one of the key issues addressed in modeling is of SGS scalar flux with advanced models. The high Schmidt number flows carry considerable energies to sub grid scales as shown in Fig. 2.5. The other focus of the work here is the combustion. Especially premixed combustion flame thickness assumed to be infinitely small, makes necessary to model the mixing of scalars at sub grid scales for predicting accurate flame front and tracking it. The SGS scalar flux represented by Eq. 3.14 contributes for the scalar energy from the small scales (smaller than the filter scale) in the scalar transport Eqs. 3.11, 3.12 and these small scales are modeled using the details from resolved scales [85].

3.4.1 Classical eddy difusivity SGS scalar flux model

Many LES simulations in both academic and industrial applications employ a standard gradient diffusion hypothesis [60], as it is simple to model. In eddy diffusivity models SGS fluxes are parameterized as proportional to the resolved scalar gradient [187]:

$$J_i^{SGS} = -D_{ed}\frac{\partial \widetilde{z}}{\partial x_i} = (C_{s,z}\Delta)^2 \left|\widetilde{S}\right| \tag{3.33}$$

where D_{ed} is model coefficient also known as turbulent diffusivity and from Eq. 3.33 and 3.24

$$C_s = C_{s,z}/Sc_t \tag{3.34}$$

Turbulent diffusivity is defines as ratio of turbulent viscosity ν_t to the turbulent Schmidt/Pranftl number as:

$$D_{ed} = \frac{\nu_t}{Sc_t} \tag{3.35}$$

In previous sections ν_t is defined as a fluid property derived from the flow field details. The turbulent Schmidt number in Eq. 3.35 was mainly treated as a constant in many works in literature [220, 113, 195, 85, 219]. The turbulent Schmidt number value also taken in the same order of normal Schmidt number as it is tough to determine or measure. For example in case for air flow, the experiment has shown that typical values of the turbulent Schmidt number should be $Sc_t \sim 0.5 - 0.7$ and most accepted value is 0.7, while for the water flow, a constant turbulent Schmidt number is hard to be achieved.

3.4.2 Eddy diffusivity SGS scalar flux model with dynamic procedure

In the model for calculating Sc_t dynamic procedure is used, which in an analogous to the so called dynamic procedure for the flow field by [74, 123]. This methodology uses the information from the resolved scalar field to optimize the value of the free parameter as a function of time and position. The turbulent Schmidt number can therefore be calculated by applying a test filter with filter width $\widehat{\Delta}$. The dynamic procedure in the scalar field following from the velocity field from equations 3.34, 3.35 and 3.31 results in the turbulent Schmidt number as:

$$\frac{1}{Sc_t} = \frac{1}{2C_d}\frac{F_i H_i}{H_i H_i} = \frac{M_{ij}M_{ij}}{H_i H_i} \tag{3.36}$$

where

$$H_i = \left(\widehat{\Delta^2 |\widetilde{S}| \frac{\partial \widetilde{z}}{\partial x_i}}\right) - \widehat{\Delta}^2 |\widehat{\widetilde{S}}| \frac{\partial \widehat{\widetilde{z}}}{\partial x_i} \quad \text{and} F_i = \widehat{\widetilde{u}_i \widetilde{z}} - \widehat{\widetilde{u}_i}\widehat{\widetilde{z}} \tag{3.37}$$

The application of the dynamic procedure for calculating turbulent Schmidt number Sc_t in scalar field has not yet become common, but some applications can be found in the literature [30]. The assumption based on the scale similarity assumption may lead to unstable behavior of the model. So Porté-Agel et al. [167] have proposed a generalized scale-dependent dynamic procedure and compared it to the traditional dynamic models in LES. The results from this model were encouraging. In this work, a classical dynamic procedure is implemented to calculate the turbulent Schmidt number in various configurations (see also [85, 236]). The gradient assumption (or isotropic eddy diffusivity assumption) has the same disadvantages as the Boussinesq approximation for flow field. So, such an eddy-diffusivity model is not able to predict realistic values of all components of the scalar flux, since it assumes the SGS scalar flux to be aligned with the resolved scalar gradient.

This may be valid if the scalar flux vector is collinear to the scalar gradient. The scalar variance at the filter scales can only be dissipated by the subgrid scales, and this model is regarded as being fully dissipative.

3.4.3 Scale similarity SGS scalar flux model

The scale similarity SGS model was originally developed for flow field. The same approach is adapted for scalar field, the SGS contribution is assumed to be similar, in position and order of magnitude, to the contribution evaluated at the resolved quantities. The procedure is as following. A test filtering operation is introduced with filter size $\widehat{\Delta}$. Based on the assumption of scale invariance, the SGS scalar flux is proportional to the flux on the test filter level as:

$$J_i^{SGS} = D_{ss}\left(\widehat{\widetilde{u}_i\widetilde{z}} - \widehat{\widetilde{u}}_i\widehat{\widetilde{z}}\right) \tag{3.38}$$

where D_ss is a model coefficient, which can be a constant depending on configurations or calculated by a dynamic procedure as well. The improvement on this SGS models mostly focuses on the choice of test filters and the modification on the model coefficient. In literature, the available test simulations reported that the similarity model alone does not dissipate enough scalar variance and typically leads to inaccurate results [91]. Therefore, *mixed models* are developed with a combination of the eddy diffusivity model.

3.4.4 SGS scalar flux mixed model

The mixed model concept for SGS scalar fluxes comes from Classical eddy diffusivity SGS scalar flux model and Scale similarity SGS scalar flux models. A priori assessment of a well implemented mixed model is presented by Jaberi et al. [91].

$$J_i^{SGS} = -D_{ed}\frac{\partial\widetilde{z}}{\partial x_i} + D_{ss}\left(\widehat{\widetilde{u}_i\widetilde{z}} - \widehat{\widetilde{u}}_i\widehat{\widetilde{z}}\right) \tag{3.39}$$

Moreover the coefficient in above model can also be obtained using dynamic-diffusivity model as described by 3.31. To simplify, most simulations choose the coefficient of the scale similarity part equal to one [198]. The model is therefore called as mixed, one parameter model as:

$$J_i^{SGS} = -D_{ed}\frac{\partial\widetilde{z}}{\partial x_i} + 1.0\left(\widehat{\widetilde{u}_i\widetilde{z}} - \widehat{\widetilde{u}}_i\widehat{\widetilde{z}}\right) \tag{3.40}$$

These models presented for SGS scalar flux are based on isotropic behavior of scalar fluxes. The modeled SGS scalar flux in the i_{th} direction is proportional to the derivative of the resolved scalar in the respective direction. However, the new research findings notice that the skewness of scalar increments (and derivatives) are inherently anisotropic quantities, and are not suitable indicators of the tendency towards isotropy [98].

In recent times various SGS scalar flux models have been proposed including the probability function, the linear eddy model and diverse algebraic models. Focus on the latter, new models have been suggested besides the linear eddy diffusivity model going from the serial decomposition closures and nonlinear gradient models to the one equation transport model. For complex configurations the attention on describing the SGS scalar fluxes with

anisotropic behavior and the new developed models are inclined to anisotropic forms. The models developed were validated and implemented for non-reactive flows [85]. In this work these models were extended to complex reactive configuration, including both premixed and non-premixed combustion.

3.4.5 Non-linear anisotropy SGS scalar flux model

The energy of SGS scales for both flow and scalars fields are realized through large scales of corresponding fields. The energy is then transferred in a cascade manner to the smaller and ever smaller scales and eventually dissipated by the smallest structures of Kolmogorov scales. In LES, it is assumed to have the filtering cutoff in the inertial sub-range of the energy spectra. The SGS scale itself would neither generate nor destroy but transfers turbulent kinetic energy in both directions, i.e forward and backward. Turning to turbulent scalar fluxes, analogous interchanges exist between the large and small scales. The transport equation for the SGS scalar flux following RANS turbulent kinetic energy equation can be written as [149].

$$\frac{\partial J_i^{SGS}}{\partial t} + \frac{\partial \widetilde{u_j} J_i^{SGS}}{\partial x_j} = P_{i,z} + G_{i,z} + D_{i,z} + D_{i,z}^v + D_{i,z}^P - \varepsilon_{i,z}^v \tag{3.41}$$

where the right-hand side includes subsequently the shear production ($P_{i,z}$), buoyancy production ($G_{i,z}$), the SGS diffusion ($D_{i,z}$), the viscous diffusion ($D_{i,z}^v$), the pressure transport ($D_{i,z}^p$) and viscous dissipation ($\varepsilon_{i,z}^v$). The production term in the transport equation takes the following form

$$P_{i,z} = -J_j^{SGS} \frac{\partial \widetilde{u_i}}{\partial x_j} - \tau_{ij}^{SGS} \frac{\partial \widetilde{z}}{\partial x_j} \tag{3.42}$$

$$G_{i,z} = -\beta_{th} g_i \left(\widetilde{z z} - \tilde{z}\tilde{z} \right) \tag{3.43}$$

where β_{th} is thermal expansion coefficient and g_i is gravitation force in i_{th} direction. The production term of ($\Psi_{i,z}^{SGS} = P_{i,z} + G_{i,z}$) SGS scalar flux transport equation is represented by the actual SGS scalar fluxes dissipation, whereas in RANS context it the shear production ($P_{i,z}$). Buoyancy production ($G_{i,z}$) assumed to be negligible compared shear production in this work. If $J_i^{SGS} > 0$, this SGS dissipation indicates the net scalar fluxes exchange of forwards ($\Psi_{i,z}^{SGS} > 0$) and backwards ($\Psi_{i,z}^{SGS} < 0$) transfer between resolved large-scale and SGS scalar structures. If $J_i^{SGS} < 0$, forward (backward) transfer corresponds to $\Psi_{i,z}^{SGS} < 0 (\Psi_{i,z}^{SGS} > 0)$. It is thus reasonable to assume that the SGS scalar flux is proportional to this net scalar flux exchange. An alignment between J_j^{SGS} and $\Psi_{i,z}^{SGS}$ can then be directly invoked as follows:

$$J_i^{SGS} = -D_z T_{SGS} P_{i,z} = -D_z T_{SGS} \left(J_j^{SGS} \frac{\partial \widetilde{u_i}}{\partial x_j} + \tau_{ij}^{SGS} \frac{\partial \widetilde{z}}{\partial x_j} \right) \tag{3.44}$$

where D_z is an adjustable parameter and T_{SGS} is an appropriate SGS time scale. This equation forms an implicit algebraic formulation for the SGS scalar flux vector, J_i^{SGS}. However, singularities can occur for certain types of behavior in the large-scale velocity and scalar gradient. A simplified form of the equation by only taking the deviatoric part

of SGS stress tensor, τ_{ij}^{SGS*} and the large-scale scalar gradients is considered by Peng et al. [149]. This leads to

$$J_i^{SGS} = -D_z T_{SGS} \tau_{ij}^{SGS*} \frac{\partial \widetilde{z}}{\partial x_j} \tag{3.45}$$

where

$$\tau_{ij}^{SGS*} = \tau_{ij}^{SGS} - \frac{1}{3}\delta_{ij}\tau_{kk}^{SGS} = -2\nu_t \widetilde{S_{ij}} \tag{3.46}$$

Formulating the SGS time scale in terms of the filter size, and the SGS viscosity as $T_{SGS} \sim \Delta^2/\nu_t$, it becomes

$$J_i^{SGS} = -D_{ij}^{an} \frac{\partial \widetilde{z}}{\partial x_j} \quad \text{where} \quad D_{ij}^{an} = D_\beta T_{SGS} \tau_{ij}^{SGS} \tag{3.47}$$

D_{ij}^{an} is the model coefficient that can be determined using a dynamic procedure. The proposed scalar model invokes a tensor diffusivity and takes into account the scalar gradients in all directions for each scalar flux component, The model is able to sustain the streamwise SGS scalar flux through a cross-stream large-scale scalar gradient in presence of SGS shear stresses, even when the scale gradient is vanished in the streamwise direction. This model is a first step to use tensor diffusivity. This model is partly similar to the scale similarity model which is subject to a Taylor expansion for the filtering operation. This model was examined in LES for a buoyant flow in an infinite vertical channel with two different headed side walls. It was shown that the proposed nonlinear model could reproduce reasonable results as compared with isotropic SGS diffusivity model and DNS data [149]. The recent works demonstrated shortcomings of the model (see e.g. [107, 71]). The new formulation of SGS scalar flux model is expressed as an explicit anisotropy-resolving algebraic model derived from the transport equation of the SGS scalar flux vector, such that the irreversibility requirements of the second law of thermodynamics are automatically fulfilled by the suggested parameterization [240, 238, 244, 234, 237]

$$J_i^{SGS} = -D_{ed}\frac{\partial \widetilde{z}}{\partial x_i} - D_{dev} T_{SGS} \tau_{ij}^{SGS_{dev}} \frac{\partial \widetilde{z}}{\partial x_j} + D_\lambda \left(T_{SGS} \tau_{ij}^{SGS} \frac{\partial \widetilde{z}}{\partial x_k} \frac{\partial \widetilde{z}}{\partial x_k} \right) \frac{\partial \widetilde{z}}{\partial x_j} \tag{3.48}$$

where D_- are the model coefficients that may depend on the invariants of τ_{ij}^{SGS} and $\frac{\partial \widetilde{z}}{\partial x_j}$. This expression includes explicitly the filtered scalar dissipation rate in the last term. More details can be found in [240]. In its simple form, the chosen new model combines the conventional linear eddy diffusivity model (EDM) with an additional term. This second term couples the (deviatoric) SGS stress tensor and the gradient of the filtered scalar field. The newly developed model [240] includes an additional term validated model Explicit algebraic anisotropy SGS scalar flux model is discussed in the next subsection.

3.4.6 Explicit algebraic anisotropy SGS scalar flux model

The SGS scalar flux models discussed and presented in previous sections are having limitations in predicting with a scalar or isotropic eddy diffusivity hypothesis. The linearity

also excludes any dependence on system rotation in the scalar flux relation. Furthermore, the assumption of alignment between the scalar flux vector and the mean filtered scalar gradient is often not well satisfied in real flows (see e.g. [223, 107]. In contrast to Peng et al. [149] who assumed, the alignment of scalar flux vector J_i^{SGS} and the production, the idea of constructing a more general valid expression for the scalar flux vector is here in an approach similar to that for explicit algebraic SGS stress tensor following the explicit algebraic Reynolds stress modeling (EARSM) or explicit algebraic scalar flux modeling (EASFM) in RANS following [176, 230, 85, 117, 192].

- The first step is here to consider a filtered transport equation for the scalar flux vector, Eq. 3.41.
- In contrast to Peng et al. [149], here the weak equilibrium assumption is made and accounts for neglecting advection minus the SGS diffusion of the scalar flux vector in the transport equation. This is well satisfied for instance, for the case of homogeneous shear flow with an imposed mean scale gradient.
- The production vector term is explicit in the SGS stress tensor and scalar flux vector, but one needs to specify a model for the pressure-scalar gradient correlation and the destruction rate vector.

The model can be very complex. So, here taking advantage from the RANS modeling from [176, 230, 85] and an expression had chosen from Yun [230], rewritten for non-filtered quantities. One obtains then implicit expression for scalar flux vector. From this expression one can now derive the solution for the explicit J_i^{SGS} in terms of the original scalar flux vector in the form

$$D_{ij}^{an} = D_\beta T_{SGS} \tau_{ij}^{SGS} \tag{3.49}$$

where D_{ij}^{an} is anisotropic diffusivity, D_β is an adjustable parameter and T_{SGS} is appropriate SGS time scale. It generalizes the model by Peng et al. [149]. Further consideration of the Eq. 3.49 consists in decomposing according to Eq. 3.21, into a deviatoric part and an isotropic part. This results in the expression

$$J_i^{SGS} = D_\beta^1 \frac{\partial \widetilde{z}}{\partial x_i} + D_\beta^2 \tau_{ij}^{SGS*} \frac{\partial \widetilde{z}}{\partial x_j} \tag{3.50}$$

D_β^1 and D_β^2 are adjustable parameters. The above Eq. 3.50 is the general model consists of two parts: linear part one, which corresponds to the linear eddy diffusivity methods, and an anisotropic part two, which includes the nonlinear, anisotropic contribution. When the SGS time scalar are formulated in terms of the filter size and the SGS viscosity following Smagorinsky, and the linear part is modeled according to equations 3.33 and 3.36, giving

$$J_i^{SGS} = \frac{C_s}{Sc_t} \Delta^2 |\widetilde{S}| \frac{\partial \widetilde{z}}{\partial x_i} + D_{an} \Delta^2 \widetilde{S_{ij}} \frac{\partial \widetilde{z}}{\partial x_j} \tag{3.51}$$

where $D_{an} (= D_\beta^2)$ is the anisotropic model coefficient. A dynamic procedure is applied to calculate model coefficient D_{an}. It is accomplished by defining a test filter (denoted by a caret), whose width $\widehat{\Delta}$ is larger than the grid filter-width Δ. The dynamic adjustment of the model coefficients is based on the similar theory as proposed by Germano [74] and

the major steps are presented here. According the model the SGS scalar flux in Eq. 3.51, on the test filter level is:

$$I = \widehat{\widetilde{u_i}\widetilde{z}} - \widehat{\widetilde{u}_i}\widehat{\widetilde{z}} = \frac{C_s}{Sc_t}\widehat{\Delta}^2|\widehat{\widetilde{S}}|\frac{\partial\widehat{\widetilde{z}}}{\partial x_i} + D_{an}\widehat{\Delta}^2\widehat{\widetilde{S_{ij}}}\frac{\partial\widehat{\widetilde{z}}}{\partial x_j} \tag{3.52}$$

The SGS scalar flux overlaps a test filter and results in

$$\Pi = \widehat{\widetilde{u_i}\widetilde{z}} - \widehat{\widetilde{u}_i}\widehat{\widetilde{z}} = \frac{C_s}{Sc_t}\widehat{\Delta^2|\widetilde{S}|\frac{\partial\widetilde{z}}{\partial x_i}} + D_{an}\widehat{\Delta}^2\widehat{\widetilde{S_{ij}}}\frac{\partial\widehat{\widetilde{z}}}{\partial x_j} \tag{3.53}$$

To determine D_{an}, the error expression is adopted following [123] as:

$$e_i = \widehat{\widetilde{u_i}\widetilde{z}} - \widehat{\widetilde{u}_i}\widehat{\widetilde{z}} - \left(\frac{C_s}{Sc_t}\widehat{\Delta}^2|\widehat{\widetilde{S}}|\frac{\partial\widehat{\widetilde{z}}}{\partial x_i} + D_{an}\widehat{\Delta}^2\widehat{\widetilde{S_{ij}}}\frac{\partial\widehat{\widetilde{z}}}{\partial x_j}\right) + \left(\frac{C_s}{Sc_t}\widehat{\Delta^2|\widetilde{S}|\frac{\partial\widetilde{z}}{\partial x_i}} + D_{an}\widehat{\Delta}^2\widehat{\widetilde{S_{ij}}}\frac{\partial\widehat{\widetilde{z}}}{\partial x_j}\right) \tag{3.54}$$

To simplify the expression, define H_{1i}, H_{2i} and F_i following Eq. 3.37 for each direction component as:

$$H_{1i} = \widehat{\Delta^2|\widetilde{S}|\frac{\partial\widetilde{z}}{\partial x_i}} - \widehat{\Delta}^2|\widehat{\widetilde{S}}|\frac{\partial\widehat{\widetilde{z}}}{\partial x_i} \tag{3.55}$$

and

$$H_{2i} = \widehat{\Delta^2\widetilde{S_{ij}}\frac{\partial\widetilde{z}}{\partial x_j}} - \widehat{\Delta}^2\widehat{\widetilde{S_{ij}}}\frac{\partial\widehat{\widetilde{z}}}{\partial x_j} \tag{3.56}$$

Now, the Eq. 3.56 can be written as:

$$e_i = F_i - \frac{C_s}{Sc_t}H_{1i} + D_{an}H_{2i} \tag{3.57}$$

Following Lilly [123] the error incurred when a single coefficient is used be minimized in a least-squares sense, by giving

$$\frac{\partial\left\langle e_i e_i\right\rangle}{\partial D_{an}} = 2\left\langle e_i\frac{\partial e_i}{\partial D^{an}}\right\rangle = 0 \tag{3.58}$$

Finally, the model coefficient can be calculated by

$$D^{an} = \frac{\left(F_i - \frac{C_s}{Sc_t}H_{1i}\right)H_{2i}}{H_{1i}H_{2i}} \tag{3.59}$$

The newly developed SGS models have been implemented in the code FASTEST-3D for simulating reactive flows, validated and studied for a selected complex configurations.

3.5 Modeling of LES combustion

For solving combustion with LES, the filtered species and energy equations need to be closed. This requires models which require a significant modeling effort. The combustion phenomenon as discussed in previous chapter is governed by turbulence, mixing, heat

Table 3.1: Classification of LES combustion modeling

Model type	Modeling	Combustion Type
Geomtric	G-field	Premixed
	Turbulent flame speed closure	Premixed
	Flame surface density	All types of combustion
	Flame wrinkling	All types of combustion
	Thickened flame	All types of combustion
Statistical	Presumed FDF/PDF	Non-Premixed/Premixed/All
	Conditional Filtered Moment Closure (CMC)	Non-Premixed/Premixed/All
	Linear Eddy Model (LEM)	All types of combustion
	Transported FDF/PDF	Non-Premixed/Premixed/All

transfer, chemistry; combustion regimes (see Fig. 2.9, 2.10), spray dynamics, geometrical aspects of the combustion systems and etc. The combustion models which were developed in the RANS context need to be adopted for LES formulation, which is not a straightforward task. In literature many LES based combustion models were developed and successfully applied for both academic and industrial applications. The recent reviews on state of the art LES combustion were carried out by Veynante et al. [208] and Gicquel et al. [75]. The very common LES combustion models are summarized in [162, 160, 233].

Ideally for solving combustion with LES and reduction chemistry as detailed in sections 2.4.5, one needs to solve Eq. 3.9, 3.10, 3.11, 3.12, and 3.80. In solving adiabatic combustion Eq. 3.80 is ignored. Nevertheless, one needs to model the reaction source term in Eq. 3.12 and also the molecular viscosity, density and other thermo-chemical properties need to be determined. Here tabulated chemistry approach is used for this purpose and discussed in detail in chapter 5.

3.5.1 Artificially thickened flame model

In combustion systems turbulence and chemistry interaction should be modeled precisely. Moreover in turbulent premixed combustion is very challenging, due to the fact that the thermo-chemical variables change very sharply through the flame profile, which is typically very thin [93]. The best model is which can track the all thermo-chemical instances within this thin reaction zone also in time. This could be achieved only when there are sufficiently enough grid points in the flame front, which is very hard-hitting task; as the number of required grid points goes up many hundreds of times compared to that of simple LES flow calculations. One of the practical solution for solving premixed combustion on a coarser grid compared to that flame thickness is artificially thickened flame model (ATF). This model is applied for FWI study of this work. In the thickened flame model, the computed flame front structure is artificially locally thickened in such a way that it can be resolved on a relatively coarse LES mesh, but such that the flame

speed remains unaltered. Butler and O'Rourke [29] were the first authors to propose the idea of capturing a propagating premixed flame on a coarser grid. The basic idea with this approach is that the flame is artificially thickened to include several computational cells and by adjusting the diffusivity to maintain the same laminar flame speed S_L^0. From the theory of laminar premixed flames, it is well established that the laminar flame speed (S_L^0) and the laminar flame thickness (δ_L^0) are related through the relationship as:

$$t_L = \frac{\delta_L^0}{S_L^0} \tag{3.60}$$

$$S_L^0 \propto \sqrt{D\dot{w}} \qquad \texttt{and} \quad \delta_L^0 \propto \frac{D}{S_L^0} = \sqrt{\frac{D}{\dot{w}}} \tag{3.61}$$

Where t_L is chemical time scale, D is the molecular diffusivity and $\dot{w}$ the mean reaction rate. Thus, an increase in flame thickness by a factor $\mathcal{F}$ with a constant flame speed, can be achieved by multiplying the molecular diffusivity by $\mathcal{F}$, and the reaction rate $\dot{w}$ by $\mathcal{F}$ as:

$$\frac{\dot{w}}{\mathcal{F}} \tag{3.62}$$

It should be pointed out that, in the context of laminar flames, O'Rourke & Bracco [29] originally introduced a coordinate transformation to thicken the flame front, which leads to the modification of all the diffusive terms in the governing equations, including the transport of momentum. However, as outlined in Colin et al. [42], no modification is applied to the transport of momentum in the context of turbulent combustion. The thickening of the flame by a factor of $\mathcal{F}$ modifies the interaction between turbulence and chemistry, represented by the Damköhler number, Da, where it is decreased by a factor $\mathcal{F}$ and becomes $Da/\mathcal{F}$. As the Da is decreased, the thickened flame becomes less sensitive to turbulent motions. Therefore, an efficiency factor, Ξ, is introduced to account for the resulting decrease in the Damköhler number (by $Da/\mathcal{F}$) and incorporate the influences of the unresolved turbulent field on the chemical kinetics [42]. Using the efficiency function, the resulting filtered balance equation for RPV (Eq. 3.12) in the modified form becomes:

$$\frac{\partial \bar{\rho}\widetilde{Y_\alpha}}{\partial t} + \frac{\partial \bar{\rho}\widetilde{u_i}\widetilde{Y_\alpha}}{\partial x_i} = \frac{\partial}{\partial x_i}\left(\bar{\rho}\mathcal{F}\Xi\widetilde{D_{Y_\alpha}}\frac{\partial \bar{\rho}\widetilde{Y_\alpha}}{\partial x_i}\right) - (1-\Omega)\frac{\partial \bar{\rho}J_i^{sgs}}{\partial x_i} + \frac{\Xi}{\mathcal{F}}\widetilde{\dot{w}_\alpha}\ (\alpha = 1, 2, ..)\,, \tag{3.63}$$

The mixture fraction Eq. 3.11 also needs to be thickened in order to keep both ξ and Y_α consistent in physical space and the modified mixture fraction equation is :

$$\frac{\partial \bar{\rho}\widetilde{\xi}}{\partial t} + \frac{\partial \bar{\rho}\widetilde{u_i}\widetilde{\xi}}{\partial x_i} = \frac{\partial}{\partial x_i}\left(\bar{\rho}\mathcal{F}\Xi\widetilde{D_\xi}\frac{\partial \bar{\rho}\widetilde{\xi}}{\partial x_i}\right) - (1-\Omega)\frac{\partial \bar{\rho}J_i^{sgs}}{\partial x_i} \tag{3.64}$$

The *thickening* procedure in ATF formulation multiplies the diffusivity term by a factor $\mathcal{F}$ which has the effect of augmenting the diffusivity. Therefore, the gradient approximation for the unresolved fluxes is multiplied by $(1-\Omega)$ [49] explicitly in the mixture fraction and reaction progress variable equations. The final tranport equation propagates with a modified flame thickness $\delta_L^m = \delta_L^0\mathcal{F}$ with turbulent flame speeds of $S_T = \Xi S_L$. The flame sensor and Flame thickness factors used in this work are discussed briefly here.

Flame sensor The idea of the ATF combustion modeling is to distribute the (thin) flame front on many grid points of a coarser gird. The diffusion coefficient of the transport equation is thickened, even where the flame is not present, leading to source term is absent. So, to avoid the flame structure gets distorted a flame sensor is introduced. This allows thickening factor is active only in the active flame region. The flame sensor was defined by Schmitt et al. [182] in terms of RPV source term, but in this work following Durand and Polifke et al. [55] is used, which is defined in terms of RPV itself as:

$$\Omega = a_{\Omega}^{p}1\left[Y^{*}(1-Y^{*})\right]^{b_{\Omega}^{p}1} \tag{3.65}$$

where a_Ω, b_Ω and $p1$ are model constants, Y^* (see chapter 5) is normalized reaction progress variable. Durand and Polifke et al. [55] had proposed $a_\Omega = 16$, $b_\Omega = 2$, $p1 = 1$ in addition a value of $p1 = 2$ is also considered and details are presented in the chapter 8.

Flame thickening factor Flame thickening factor $\mathcal{F}$, is the value by which flame is thickened on physical space, and keeping all thermo-chemical properties intact. The thickening approach has drawback as the increased thermal and molecular mass diffusivity can severely affect the mixing process in the whole domain. Increasing the diffusivity of these properties only in the flame front region is enough for the purpose of flame thickening. Therefore, *dynamic flame thickening* (DFT) techniques were proposed to track the flame front and increase the diffusion only in the flame region [55, 243, 182], which also takes into the local mesh size.

$$\mathcal{F} = 1 + (\mathcal{F}_{max} - 1)\Omega \tag{3.66}$$

$\mathcal{F}_{max}$ is maximum thickening factor in dynamic formulation of $\mathcal{F}$. The consistency of this approach was discussed by Kuenne et al. [113] also presented the $\mathcal{F} = 5$ as an maximum appropriate value and used in this work. Irannezhad et al. [89] used $\mathcal{F} = 10$ in simulation of a lean premixed low swirl methane-air flame. Roux et al. [173] proposed $\mathcal{F}$ in terms of grid points required in flame front, local mesh size and the laminar flame speed. Now, the efficiency function is explained in the following paragraph.

Efficiency function One of the main advantage of the ATF model is introducing of efficiency function Ξ, which is defined by the dimensionless wrinkling factor E. The Ξ retrieves the sub-grid scale wrinkling, so the variances of the mixture fraction and (or) the RPV are not necessary to transport or model algebraically. In this work the efficiency functions derived by Colin et al. [42] as well as Charlette et al. [34] are used and analyzed, which were developed from the DNS of flame vortex interaction to characterize the unresolved flame surface.

Primitive model for efficiency The factor E is the ratio of the flame surface to its projection in the direction of flame propagation. The efficiency function, Ξ, is written as a function of the local filter size ($\Delta_e \approx 10\Delta_x$ (actual grid size)), local sub-grid scale turbulent velocity (u'_{Δ_e}), laminar flame speed (S_L^0), and the thickness of the laminar and the artificially thickened flame (δ_L^0, δ_L^m). Colin et al. [42] proposed the following expressions for modeling the efficiency function.

$$\Xi = \frac{E\left(\delta_L^0\right)}{E\left(\delta_L^m\right)} = \frac{1+\beta\Gamma\left(\frac{\Delta_e}{\delta_L^0}, \frac{u'_{\Delta_e}}{S_L^0}\right)\frac{u'_{\Delta_e}}{S_L^0}}{1+\beta\Gamma\left(\frac{\Delta_e}{\delta_L^m}, \frac{u'_{\Delta_e}}{S_L^0}\right)\frac{u'_{\Delta_e}}{S_L^0}} \tag{3.67}$$

$$\beta = \frac{2 \quad ln(2)}{3C_{ms}\left(Re_t^{1/2}-1\right)} \quad C_{ms} = 0.28, \quad Re_t = \frac{u'l_t}{\nu_t} \tag{3.68}$$

where Re_t is the turbulent Reynolds number. The local filter size Δ_e is defined as:

$$\Delta_e = \delta_L^m = \delta_L^0 \mathcal{F} \tag{3.69}$$

The function Γ which represents the integration of the effective strain rate induced by all scales affected due to artificial thickening is defines as:

$$\Gamma = \left(\frac{\Delta_e}{\delta_L^{0,m}}, \frac{u'_{\Delta_e}}{S_L^0}\right) = 0.75exp\left[-1.2\left(\frac{u'_{\Delta_e}}{S_L^0}\right)^{-0.3}\right]\left(\frac{\Delta_e}{\delta_L^{0,m}}\right)^{2/3} \tag{3.70}$$

The sub-grid scale turbulent velocity is evaluated as $u'_{\Delta_e} = 2\Delta_x^3|\nabla \times (\nabla^2 \overrightarrow{u})\,|$ and Δ_x is the grid size on a similarity assumption. This formulation for sub-grid scale velocity estimation is free from dilatation representing appropriate filter for required length scales for flame vertex interactions. Usually, Δ_e differs from Δ_x, and it has been recommended that values for Δ_e be at least $10\Delta_x$ [42].

Power-law efficiency Charlette et al. [34] proposed a model for the wrinkling factor with a power-law relationship defined as ratio of inner (Δ) and outer (η_c) cutoff scales as :

$$\Xi = \left(1+\frac{\Delta}{\eta_c}\right)^{\beta} \tag{3.71}$$

This represents required range of length scales for modeling the turbulence and chemistry interaction estimated from DNS simulation over a homogeneous and isotropic turbulence spectrum giving model that by the Charlette et al. [34].

$$\Xi\left(\frac{\Delta}{\delta_L^0}, \frac{u'_\Delta}{S_L^0}, Re_\Delta\right) = \left(1+min\left[\frac{\Delta}{\delta_L^0}, \Gamma\frac{u'_\Delta}{S_L^0}\right]\right)^{\beta} \tag{3.72}$$

and

$$\Gamma\left(\frac{\Delta_e}{\delta_L^0}, \frac{u'_{\Delta_e}}{S_L^0}, Re_\Delta\right) = \left[\left(\left(f_u^{-a}+f_\Delta^{-a}\right)^{-1/a}\right)^{-b}+f_{Re}^{-b}\right]^{-1/b} \tag{3.73}$$

where the function Γ takes into account the net straining effect of all relevant turbulent scales smaller than Δ. Re_Δ is the sub grid scale Reynolds number and β is a model parameter. Other variables in Eq. 3.73 are fitted as:

$$f_u = 4\left(\frac{27C_k}{110}\right)^{1/2}\left(\frac{18C_k}{55}\right)\left(\frac{u'_\Delta}{S_L^0}\right)^2 \tag{3.74}$$

$$f_{\Delta} = \left[\frac{27C_k\pi^{4/3}}{110} \times \left(\left(\frac{\Delta}{\delta_l^0}\right)^{4/3} - 1\right)\right]^{0.5} \tag{3.75}$$

$$f_{Re} = \left[\frac{9}{55} exp\left(-\frac{3}{2}C_k\pi^{4/3}Re_{\Delta}^{-1}\right)\right]^{0.5} Re_{\Delta}^{0.5} \tag{3.76}$$

$$a = 0.6 + 0.2exp\left[\left(-0.1\frac{u'_{\Delta}}{S_L^0}\right) - \left(-0.01\frac{\Delta}{\delta_L^0}\right)\right] \quad b = 1.4 \tag{3.77}$$

Where $C_k = 1.5$ is the Kolmogorov constant, Δ =is the filter size and since for laminar flames $\delta_L^0 S_L^0/\nu = 4$ [34, 42] $Re_{\delta} = 4(\Delta/\delta_L^0)(u'_{\Delta}/s_l^0)$ is the sub-grid turbulent Reynolds number. The velocity fluctuations u'_{Δ} are obtained following Colin et al. [42] and the exponent is set to $\beta = 0.5$ according to the non-dynamic formulation of the model. The simulations in chapter 8 are carried out following Wang et al.[211], where in Eq. 3.72 $\frac{\Delta}{\delta_L^0}$ is replaced by $(\frac{\Delta}{\delta_L^0} - 1)$ to maximize the wrinkling factor Ξ by fractal mode.

Mixture fraction variance The mixture fraction variance has pivotal role in combustion systems, especially in RANS context. The mixture fraction variance is present where there is a change of mixture fraction value at a physical location in time. This is crucial in determining combustion in much industrial application, where the combustion takes place in all forms like premixed, non-premixed, diffusion and stratification. It is well argued that mixture fraction variance in premixed combustion is not vital in main reaction region of interest, except where it mixed with co-flow. In general, the SGS variance of mixture fraction from LES calculations can be obtained using several methods. One technique would be to derive and solve a separate transport equation for mixture fraction variance. This is the method is widely used in RANS context and this can be extended to LES [101]. Nevertheless, the most common approach in LES is to employ an algebraic closure for $\widetilde{\xi''^2}$. This can be acceptable by the same theory that applied in modeling of the sub grid scale stress and some works literature showed its credibility [241, 238, 218]. The well established SGS variance of a scalar proposed by Cook et al. [44] is based of scale similarity between the sub grid and the resolved distribution of the scalar.

$$\widetilde{\xi''^2} \approx C_{sim}\left(\widehat{\left(\widetilde{\xi}\right)^2} - \left(\widehat{\widetilde{\xi}}\right)^2\right) \tag{3.78}$$

Assuming an equilibrium between production and dissipation the Eq. 3.78 becomes :

$$\widetilde{\xi''^2} \approx C_{eq}\Delta^2\left(\frac{\partial\widetilde{\xi}}{\partial x_i}\frac{\partial\widetilde{\xi}}{\partial x_i}\right) \tag{3.79}$$

Branley et al. [24] have suggested a value of $C_{eq} = 0.2$ and for specicial application of a turbulent hydrogen diffusion flame $C_{eq} = 0.1$. In this work $C_{eq} = 0.15$ is considered. In flame wall interaction non-adiabtic case simulation performed based ATF model didn't use this variance theory as ATF model takes care of this aspect as detailed in previous section.

3.6 Modeling of LES with heat loss

The evaluation of the enthalpy phenomenon in combustion CFD modeling is carried out in this work by accounting for the heat loss and the associated flame stabilization. The total enthalpy (h) is considered and defined as sum of heat of formation and sensible heat. The single phase combustion considered here allows the source term of enthalpy to be avoided in its transport equation. As described in section 2.1.3, other transport processes that occur due to the body-forces, volume forces or temperature gradients [18, 57, 243] are neglected here. In addition unity Lewis number is assumed in solving the 3D simulations. The resulted Eq. 2.17 is filtered to incorporate it into the CFD frame work. The following total enthalpy (3.80) equation as a first approximation assuming unity Lewis number and unity thickening factor has been applied in its filtered form:

$$\frac{\partial \bar{\rho}\widetilde{h}}{\partial t} + \frac{\partial \bar{\rho}\widetilde{u_i}\widetilde{h}}{\partial x_i} = \frac{\partial}{\partial x_i}\left(\frac{\mu}{Pr}\frac{\partial \widetilde{h}}{\partial x_i}\right) - \frac{\partial \bar{\rho} J_i^{sgs}}{\partial x_i}, \qquad J_i^{sgs,h} = \frac{\nu_t}{\sigma_t}\frac{\partial \widetilde{h}}{\partial x_i} \tag{3.80}$$

where μ is the viscosity and Pr the Prandtl number, $J_i^{sgs,h}$ is the subgrid scalar flux of the enthalpy equations. A LES modeling without thickening in the enthalpy equation appears to be appropriate for the region of interest under investigation for configuration presented in chapter 8. However, within the shear layer between the co-flow and the fuel jet a thickening in the enthalpy equation is critical. Especially it is very challenging near the non-adiabatic wall due to the presence of steep temperature gradients that can be strongly influenced and thereby lead to erroneous heat flux values, though the flame speed could be retrieved correctly. Note that an accurate estimation of heat flux near the wall while resolving the flame simultaneously is challenging for the investigation of FWI by means of LES. In the present work all non-adiabatic simulations are carried out without thickening in the enthalpy equation.

3.7 Modeling of LES with heat loss for non-unity Lewis effects

Combustion process involves both heat and mass transfer. Each species of the combustion process has its own mass transfer and heat transfer coefficients; and they are variables and strongly depended on the surrounding physical conditions such as temperature and composition. Accounting for all physics involved is necessary to capture precisely the combustion phenomenon. However, it is limited because of the requirement of solving hundreds species transport equations involved in combustion process. Thus majority of the works especially for three-dimensional modeling laboratory and industrial problems consider all species diffuse in the same way (unity Lewis number), the value of the mixture fraction does not depend on the element considered. Linan et al. [124] have extended the mixture fraction concept for non-unity Lewis numbers flows but rarely used.

The Lewis number (Le) is a dimensionless number which characterizes fluid flows where there is simultaneous heat and mass transfer by convection. It is defined as the ratio of

thermal diffusivity to mass diffusivity and also could be defined as the ratios the Schmidt number to Prandtl number as:

$$Le = \frac{D_{th}}{D_m} = \frac{\lambda}{\rho D_{ma} c_p} \tag{3.81}$$

$$Le = \frac{Sc}{Pr} \tag{3.82}$$

where D_{th} the thermal diffusivity, D_m the mass diffusivity, λ the thermal conductivity, D_{ma} the mixture-averaged diffusion coefficient, c_p the specific heat capacity at constant pressure, Sc the Schmidt number and Pr Prandtl number.

By using this Lewis number the species diffusion fluxes can be expressed as:

$$\rho U_\alpha Y_\alpha^{mf} = -\frac{\lambda}{Le_\alpha c_p} \frac{\partial Y_\alpha^{mf}}{\partial x_i} \tag{3.83}$$

U_α is diffusion velocity defined by Stefan-Maxwell equation, Y_α^{mf} species α mass fraction and Le_α Lewis number species α. Haghighi [79] has demonstrated taking advantage of mixture averaged diffusion coefficients for consideration of non-unity Lewis (NUL) number in the combustion modeling is vital to predict flame-wall interaction physics accurately. For more details on theory and background on non-unity Lewis reader could refer to works of Haghighi [79] and Oijen van J.A. [143]

Consideration of NUL modifies transport equations Eq. 3.63, Eq. 3.64, Eq. 3.80. In this work equations are thickened for RPV and mixture fraction transport equations. Therefore resulting equations with non-unity Lewis number should be also thickened. Here modified equations of reaction progress variable, mixture fraction and enthalpy are presented below following the work of Oijen [143].

$$\frac{\partial \bar{\rho} \widetilde{Y_\alpha}}{\partial t} + \frac{\partial \bar{\rho} \widetilde{u_i} \widetilde{Y_\alpha}}{\partial x_i} = \frac{\partial}{\partial x_i} \left(\bar{\rho} \mathcal{F} \Xi \frac{\widetilde{D_{Y_\alpha}}}{Le_\alpha} \frac{\partial \bar{\rho} \widetilde{Y_\alpha}}{\partial x_i} \right) - (1 - \Omega) \frac{\partial \bar{\rho} J_i^{sgs}}{\partial x_i} + \frac{\Xi}{\mathcal{F}} \widetilde{\dot{w}_\alpha} \; (\alpha = 1, 2, ..) \,, \tag{3.84}$$

Eq. 3.84 is new RPV equation it resulted by dividing the diffusion coefficient by Lewis number of the corresponding species α.

$$\frac{\partial \bar{\rho} \widetilde{\xi}}{\partial t} + \frac{\partial \bar{\rho} \widetilde{u_i} \widetilde{\xi}}{\partial x_i} = \frac{\partial}{\partial x_i} \left(\bar{\rho} \mathcal{F} \Xi \widetilde{D_\xi} \frac{\partial \bar{\rho} \widetilde{\xi}}{\partial x_i} \right) + \frac{\partial}{\partial x_i} \left(\frac{\mu}{Pr} \sum_{\alpha=1}^{N_\alpha} \left(\frac{1}{Le_\alpha} - 1 \right) \frac{\Xi}{\mathcal{F}} \widetilde{\dot{w}_\alpha} \frac{\partial Y_\alpha^{mf}}{\partial x_i} \right) - (1 - \Omega) \frac{\partial \bar{\rho} J_i^{sgs}}{\partial x_i} \tag{3.85}$$

Non-unity Lewis based ATF mixture fraction Eq. 3.85 includes now an additional term to accommodate the RPV source term generated from various reaction steps and to account for the concentrations variation due to diffusion velocities. Total enthalpy equation needs to be modified to account non-unity Lewis number effects. Total enthalpy doesn't change in pre-flame or post-flame regions in the adiabatic combustion process. However, different mass diffusion coefficients of species and their thermal diffusion velocities allows to travel both thermal scalar and species at different speeds resulting the enthalpy change

across the flame. To account for these effects Eq. 3.86 needs to be used for solving total enthalpy.

$$\frac{\partial \bar{\rho}\widetilde{h}}{\partial t} + \frac{\partial \bar{\rho}\widetilde{u}_i\widetilde{h}}{\partial x_i} = \frac{\partial}{\partial x_i}\left(\frac{\mu}{Pr}\frac{\partial \widetilde{h}}{\partial x_i}\right) + \frac{\partial}{\partial x_i}\left(\frac{\mu}{Pr}\sum_{\alpha=1}^{N_\alpha}\left(\frac{1}{Le_\alpha}-1\right)h_\alpha\frac{\partial Y_\alpha^{mf}}{\partial x_i}\right) - \frac{\partial \bar{\rho}J_i^{sgs}}{\partial x_i} \quad (3.86)$$

where h_α is total enthalpy of species α. In this work FASTEST-3D CFD solver used considered unity Lewis number equation as non-unity Lewis work is not in the scope of present work.

Chapter 4

Numerical method

Three different CFD codes were used extensively in the present work. Two of these three CFD codes were used exclusively for carrying out one dimensional (1D) simulations of combustion with detailed chemistry on a DNS grid, the other code being a three dimensional (3D) multi-physics code. DNS based combustion simulations with detailed chemistry codes exclusively employed for 1D simulations are Cantera [32] and CHEM1D [36]. The FASTEST3D CFD code was employed for all 3D simulations work. Besides, the ANSYS CFX [8] software also used partly in the work for validation and verification purpose to determine the boundary conditions (see section 6.5) employed on a perforated plate for turbulence generation in chapter 8, but excluded in the discussion.

In any CFD simulation, system of ordinary and partial differential conservation equations for various physics involved should be solved on a physical domain and in time space. And at the same time both time and length scales of various physics involved should be taken care. They are non-linear, coupled and complex. It was well established that, Navier-Stokes equations describe the flow of a Newtonian fluid accurately. In most cases, even the simplified equations cannot be solved analytically. For this purpose one has to use numerical methods. The starting point of any numerical method is the mathematical equations. They have to be discretized and solved numerically. Among different discretization methods, Finite Difference FD), Finite Volume (FV) and Finite Element (FE) are widely used in CFD and FEM. In finite volume method, generally two types of discretization of physical domain are common, namely structured grid and unstructured grid. Discretization of a physical domain yields a large system of non-linear algebraic equations, which need to be solved by using numerical methods.

It is necessary to get insight into the combustion processes in detail to get optimized design and operating paradigm. Therefore, first the actual physics is converted into mathematical equation through theoretical studies. Then this theoretical work is transformed into the numerical framework. The obtained equations in theoretical studies are discretized using various appropriate and suitable schemes. Software CFD codes will be developed by implementing the respective algorithms developed for solving the discretized equation. The CFD codes will be simulated on computers to get required in depth understanding of the systems in an efficient manner.

First, a very short overview of numerical techniques used in 1D codes provided then followed by an extended over view of numerical methods employed in the FASTEST3D.

CHEM1D code uses an exponential second order finite-volume discretization in space and the resulting system is solved using a fully implicit, modified Newton technique [189]. Adaptive gridding is implemented to increase the resolution around the flame front. A fully second order backwards differencing scheme based implicit solver CHEM1D [36] with adaptive time stepping is used to solve the equations.

Cantera employs finite difference spectral element method for flow equations to form systems of non-linear algebraic equations. It uses hybrid Newtonian, pseudo-time-stepping algorithm for time discretization. The grid refines /coarsenes adaptively to resolve the flow. The unnecessary points will be discarded when it resolves beyond the requirement [32, 190].

FASTEST-3D was originally developed by Durst and Schäfer [56] and was employed for this purpose. This code solves the incompressible Navier-Stokes equations using a finite-volume approach on block-structured, boundary-fitted, cell-centered collocated grids. It was extended for combustion and explicit time stepping in the framework of the collaborative research project SFB-568 at EKT (`http://www.ekt.tu-darmstadt.de/`, see also [115, 1, 230, 242, 245, 244, 247, 234, 237, 235, 239]). The basic features of this code are:

- Navier -Stokes equations are discretized using finite volume approach. The discretization is based on structured hexahedral volumes (ICEMCFD [9] can be used for this purpose)
- Uses basis vectors Cartesian coordinate system [174, 63]
- Boundary-fitted non-orthogonal block-structured grid system [63]
- Block-structured grid interfaces are connected, matching and continuous
- Collocated variable arrangement (Fig. 4.3)
- Parallelization is based on domain decomposition in space using the MPI message (Fig. 6.1)
- Implicit and semi-implicit temporal treatment and first (upwind) and second order (central difference) with TVD schemes discretisation schemes
- Strongly implicit/ explicit procedure for the iterative solution of the linearised equation system
- For the present work only the fully implicit scheme with second order discretisation was used for non-combustion systems and explicit time stepping for combustion systems for time discretizaion

The discretization schemes, solution procedure, boundary conditions and parallelization strategy are presented in this chapter. Reader who is interested in CFD code development and analysis of detailed numerical methods and error evaluation

can refer to the books of M. Peric & J.H. Ferziger [63] and Patankar [147]. Some special issues such as pressure correlation, TVD (total variation diminishing) scheme etc. have been studied extensively in [51]. A special attention is given to implicit and explicit time dicretization, and the time derivative of density which is crucial for combustion simulations. The focus also has given on boundary conditions applied in this work.

4.1 Finite volume method

The finite volume method is a technique for representing and evaluating of partial differential equations in the form of algebraic equations. To use the finite volume methods, the solution domain is subdivided into a finite number of small control volumes (CV) called grids. In contrast to the finite difference (FD) method, finite volume (FV) methods define the control volume boundaries, not the computational nodes. In the Fig .4.1, typical 3D Cartesian (the coordinates in a three dimensional system are of the form (x, y, z)) control volumes are shown with the notation used in this work. The CV surface can be subdivided into six plane surfaces, denoted by lower case letters corresponding to their directions (e, w, n, s, t, and b) with respect to the central node (P). Taking into account the non-orthogonality of the grids used, it is plausible to use in each CV and on each CV face a local coordinate system and then to transform the operators (derivatives) from local into the global (Cartesian) coordinate system. In the FASTEST-3D code a hexahedron control volume is used. The derivative of field variable F with respect to Cartesian coordinates can be expressed in terms of the local coordinates with a transformation matrix (the transformation method can refer to [115]). Every hexahedral control volume contains grid points and a central point, representing the mean over the full control volume (Mid-point rule). The standard Cartesian coordinates are used below for denotation. This method is based on the resolution of governing equations in the integral form given by the Eq. 4.1:

$$\int_V \frac{\partial}{\partial t}(\rho\psi)dV + \int_V \frac{\partial}{\partial x_i}(\rho u_i\psi)dV = \int_V \frac{\partial}{\partial x_i}\left(\Gamma_\psi \frac{\partial \psi}{\partial x_i}\right)dV + \int_V S_\psi dV \qquad (4.1)$$

The quantity ψ represents a conserved variable (velocity component, scalar, etc.), Γ_ψ notes the diffusivity coefficient, S_ψ the sum of all source terms and V the volume of the considered cell. The volume integrals are transformed to area integrals using Gauss' Law:

$$\int_V \frac{\partial}{\partial t}(\rho\psi)dV + \int_\sigma \left(\rho u_i\psi - \Gamma_\psi \frac{\partial \psi}{\partial x_i}\right) n_i d\sigma = \int_V S_\psi dV, \qquad (4.2)$$

where σ represents the surface confining the volume V (of the cell) and n_i the unit vector normal to the surface σ. The Eq. 4.2 is applied for each control volume (CV) of the numerical grid which defines the computational domain. These CVs are the discrete locations at which the variables need to be calculated (Fig. 4.1, 4.2 and Fig. 4.4). The possibility of storage of the flow information associated with each CV is categorizing the discretization scheme into two different arrangements, namely: collocated grid and staggered grid. A typical CV and the notation used for a Cartesian 3D grid are shown Fig. 4.1 and Fig. 4.2:

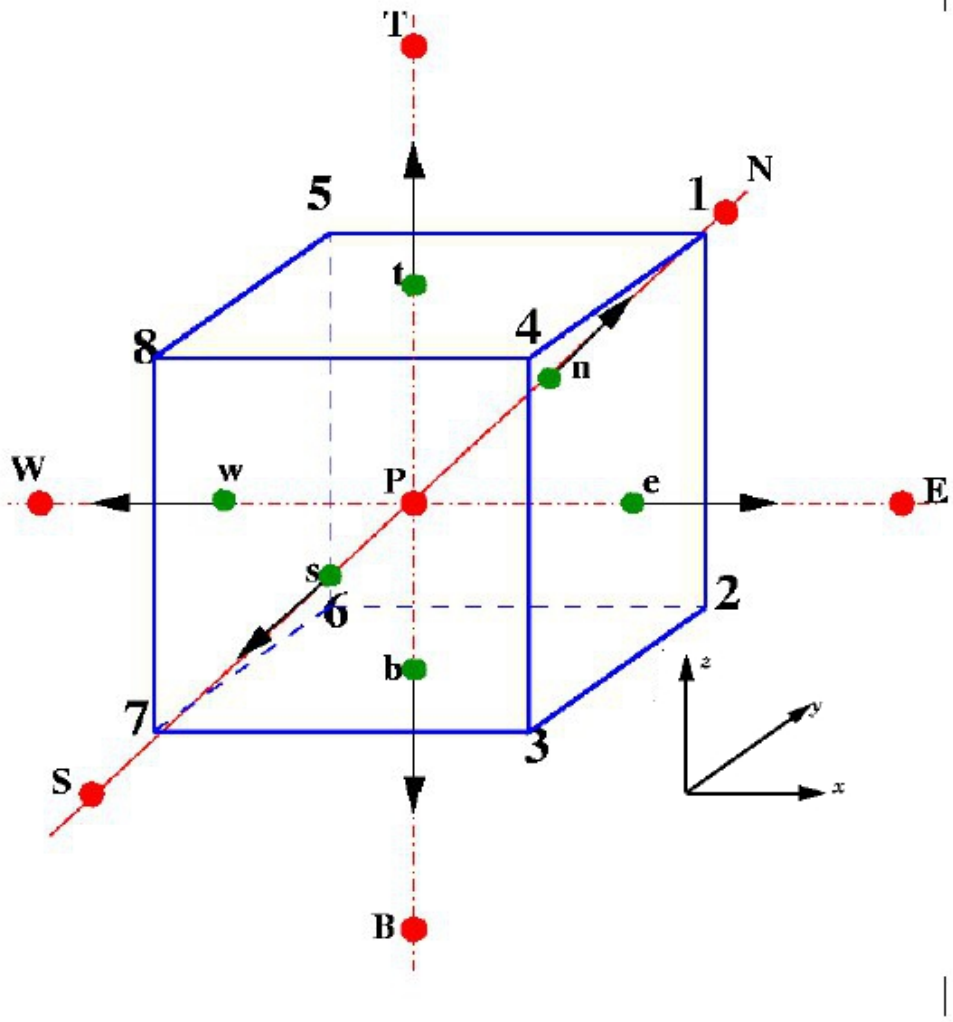

Figure 4.1: A typical CV and the notation used for a Cartesian 3D grid [63, 181, 115]

Collocated grid: This type of grids are used in this work. These are one in which the pressure and velocity variables share the same grid (Fig. 4.3 left). Thus all variables are stored on the same grid point and the same control volume is used for all variables. It is the preferred method for non-orthogonal coordinates. The implementations of collocated grids on non-orthogonal co-ordinates require regularization to prevent the formation of oscillations because of pressure velocity decoupling [63, 147].

Staggered grid: The scalar variables (pressure, density, total enthalpy, scalar, etc.) are stored in the center of the grid, whereas the normal components of the momentum (velocity) are located at the midpoints of the cell faces (Fig. 4.3 right). Using a staggered grid is the most common way to avoid the pressure-velocity decoupling and thus avoid pressure oscillations [63, 147].

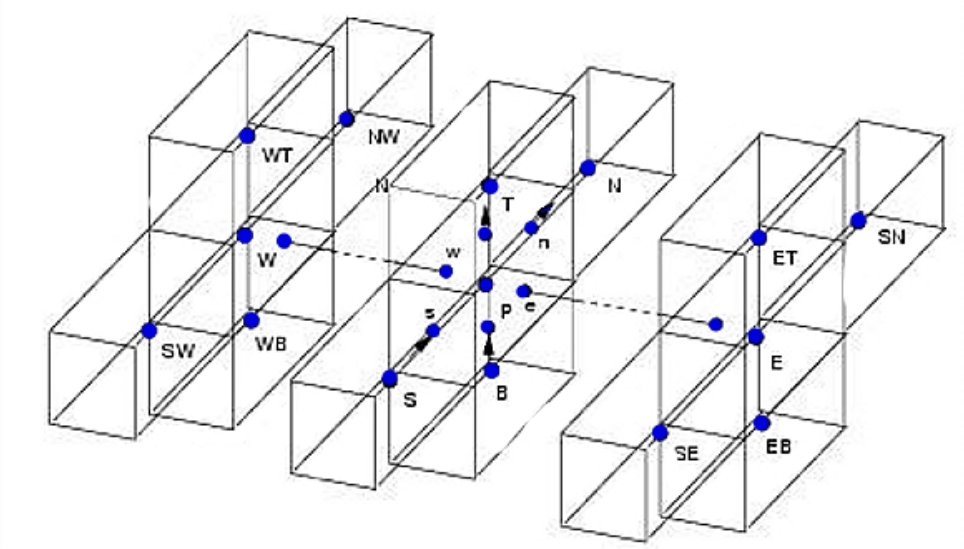

Figure 4.2: Topology and control volume notification[39, 1]

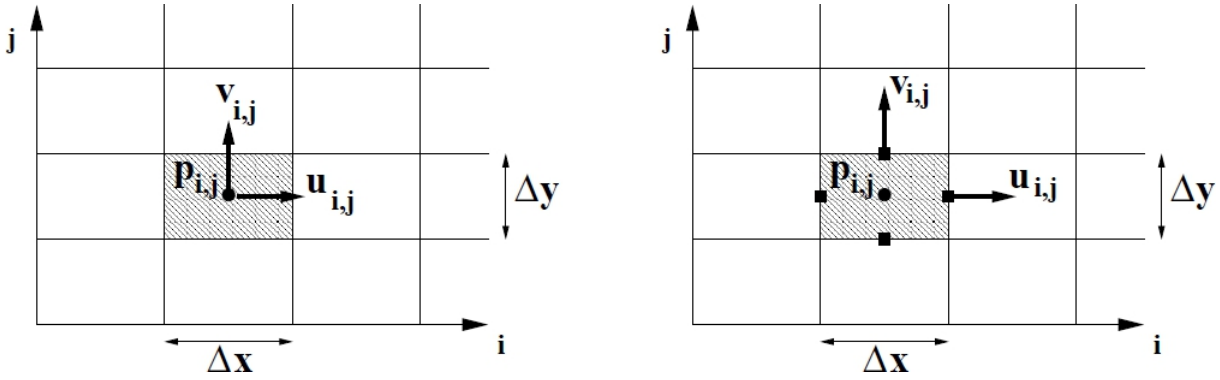

Figure 4.3: Variables arrangement on staggered and collocated grid [63, 181, 115]

Now consider a hexahedral control volume with central point denoted as P, having six neighbor CVs: E (east), W (west), N (north), S (south), T (top) and B (bottom) (see Fig. 4.2) and sharing common faces with neighbors: e, w, n, s, t and b, respectively. The final objective within finite volume method is to transform the integral differential equation (4.2) into an algebraic equation of the following form:

$$\underbrace{A_p\psi_p - \sum_{Nb} A_{Nb}\psi_{Nb}}_{\text{implicit part}} = \underbrace{S_p}_{\text{explicit part}} \tag{4.3}$$

Here, the subscript Nb corresponds to the 6 neighbor CVs: W, E, S, N, B, T and A_p, A_{Nb} denote the coefficients belonging to the dependent variable values ψ_p, ψ_{Nb} in the point P, Nb derived from the discretization. All the remaining terms resulting from the discretization that can not be included into the implicit part of Eq. 4.3 are treated explicitly and put into the source term S_p on the RHS.

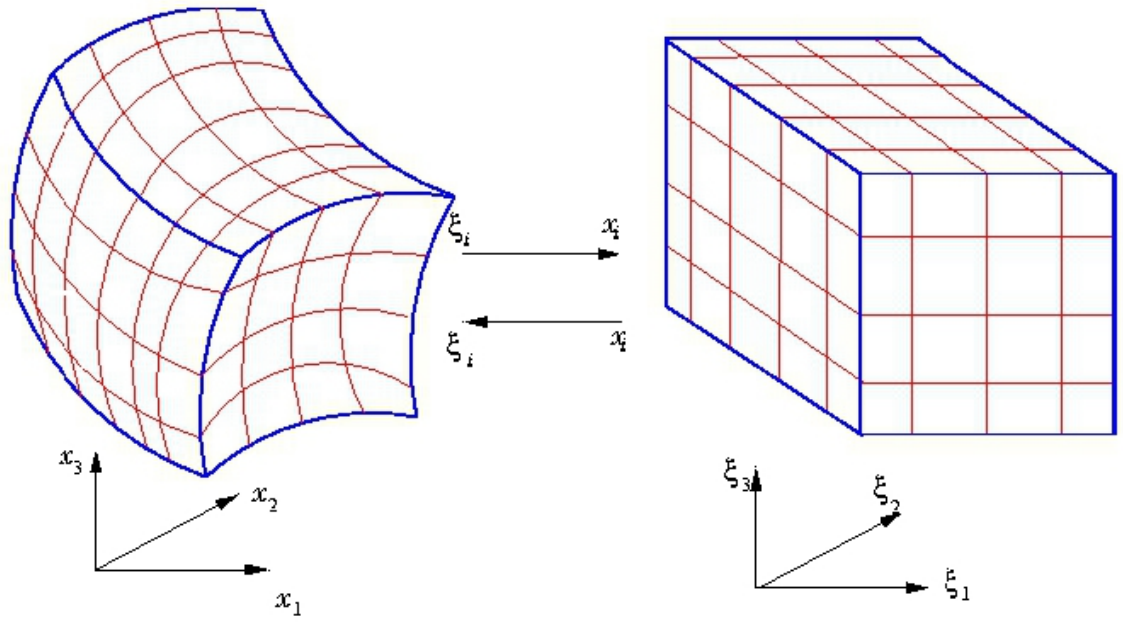

Figure 4.4: Coordinate system transormation [63, 181, 115]

4.2 Coordinate transformation

The grids used in the FASTEST3D frame work are primarily non-orthogonal. This is because block structured grids are body fitted. However it is possible to use a local co-ordinate system on all faces of each CV to retain the orthgonality. Subsequently local co-ordinate system derivatives will be transformed to global Cartesian co-ordinate system. Here the basis vectors of the local coordinate system are obtained by connecting the CV center with the CV's faces centers. In Fig. 4.1 a local coordinate system arranged in the CV central point is shown.

The transformation of equations for a complex domain in the Cateresian space $x_{1,2,3}$ to a simple orthogonal domain of computational space ξ_i is for simplifying discretization (see Fig. 4.4). The local coordinates are denoted as (ξ_1, ξ_2, ξ_3) while global (Cartesian) coordinates are denoted as (x_1, x_2, x_3). The resulting transformed matrix in the local coordinate system is represented by matrix 4.4.

$$A = \begin{pmatrix} \frac{\partial x_1}{\partial \xi_1} & \frac{\partial x_1}{\partial \xi_2} & \frac{\partial x_1}{\partial \xi_3} \\ \frac{\partial x_2}{\partial \xi_1} & \frac{\partial x_2}{\partial \xi_2} & \frac{\partial x_2}{\partial \xi_3} \\ \frac{\partial x_3}{\partial \xi_1} & \frac{\partial x_3}{\partial \xi_2} & \frac{\partial x_3}{\partial \xi_3} \end{pmatrix} \tag{4.4}$$

In local co-ordinate system the derivative of the any field variables ψ with regard to Cartesian coordinates is :

$$\frac{\partial \psi}{\partial x_i} = \frac{\partial \psi}{\partial \xi_i} \frac{\partial \xi_i}{\partial x_i} \tag{4.5}$$

Following the linear algebraic relation (Eq. 4.6):

$$A^{-1} = \frac{1}{J}(A_{adj})^T \tag{4.6}$$

The local to global inverse transformation matrix, A^{-1} is obtained as:

$$A^{-1} = \begin{pmatrix} \frac{\partial \xi_1}{\partial x_1} & \frac{\partial \xi_1}{\partial x_2} & \frac{\partial \xi_1}{\partial x_3} \\ \frac{\partial \xi_2}{\partial x_1} & \frac{\partial \xi_2}{\partial x_2} & \frac{\partial \xi_2}{\partial x_3} \\ \frac{\partial \xi_3}{\partial x_1} & \frac{\partial \xi_3}{\partial x_2} & \frac{\partial \xi_3}{\partial x_3} \end{pmatrix} \tag{4.7}$$

here Determinant of A is the Jacobean (J) and A_{Adj} is the transpose adjoint matrix of A . i.e.

$$\frac{\partial \xi_j}{\partial x_j} = \frac{1}{J}\left[adj\left(\frac{\partial x_j}{\partial}\xi_i\right)\right]^T = \frac{1}{J}B_{ij} \tag{4.8}$$

By substituting Eq. 4.8 in Eq. 4.5 one obtains:

$$\frac{\partial \psi}{\partial x_i} = \frac{1}{J}B_{ij} \tag{4.9}$$

whereas B_{ij} is the elements from matrix B and it is given by

$$B = \begin{pmatrix} \frac{\partial x_2}{\partial \xi_2}\frac{\partial x_3}{\partial \xi_3} - \frac{\partial x_2}{\partial \xi_3}\frac{\partial x_3}{\partial \xi_2} & \frac{\partial x_1}{\partial \xi_3}\frac{\partial x_3}{\partial \xi_2} - \frac{\partial x_1}{\partial \xi_2}\frac{\partial x_3}{\partial \xi_3} & \frac{\partial x_1}{\partial \xi_2}\frac{\partial x_2}{\partial \xi_3} - \frac{\partial x_1}{\partial \xi_3}\frac{\partial x_2}{\partial \xi_2} \\ \frac{\partial x_2}{\partial \xi_3}\frac{\partial x_3}{\partial \xi_1} - \frac{\partial x_2}{\partial \xi_1}\frac{\partial x_3}{\partial \xi_3} & \frac{\partial x_1}{\partial \xi_1}\frac{\partial x_3}{\partial \xi_3} - \frac{\partial x_1}{\partial \xi_3}\frac{\partial x_3}{\partial \xi_1} & \frac{\partial x_1}{\partial \xi_3}\frac{\partial x_2}{\partial \xi_1} - \frac{\partial x_1}{\partial \xi_1}\frac{\partial x_2}{\partial \xi_3} \\ \frac{\partial x_2}{\partial \xi_1}\frac{\partial x_3}{\partial \xi_2} - \frac{\partial x_2}{\partial \xi_2}\frac{\partial x_3}{\partial \xi_1} & \frac{\partial x_1}{\partial \xi_2}\frac{\partial x_3}{\partial \xi_1} - \frac{\partial x_1}{\partial \xi_1}\frac{\partial x_3}{\partial \xi_2} & \frac{\partial x_1}{\partial \xi_1}\frac{\partial x_2}{\partial \xi_2} - \frac{\partial x_1}{\partial \xi_2}\frac{\partial x_2}{\partial \xi_1} \end{pmatrix} \tag{4.10}$$

Now by replacing the differential operator Eq. 4.9 into Eq. 4.2 results in:

$$\int_V \frac{\partial}{\partial t}(\rho\psi)dV + \int_\sigma \left(\rho u_i \psi - \Gamma_\psi \frac{\partial \psi}{\partial x_i}\right) n_i d\sigma = \int_V S_\psi dV \tag{4.11}$$

4.3 Discretization of the convective, diffusion and accumulation (time) terms

Any discretization methods adapted in CFD methods will yield only the discrete solution. This, in turn, disallows in finding the exact solution of the governing transport equations. This gives rise to two types of errors one being truncation (truncation of Taylor series expansion [63, 147]) error and other one is the solution error. In general, the unsteady transport equation consists of four terms namely time term (accumulation), convective, diffusive and source terms. In addition time derivative of the density needs to be addressed separately in combustion problems. In this section, the numerical approach adapted for addressing these issues are discussed. The discretized methods implemented here are based on the works of Schäfer following [119, 181]. The discussion here separated into parts one into spatial discretization other one is temporal.

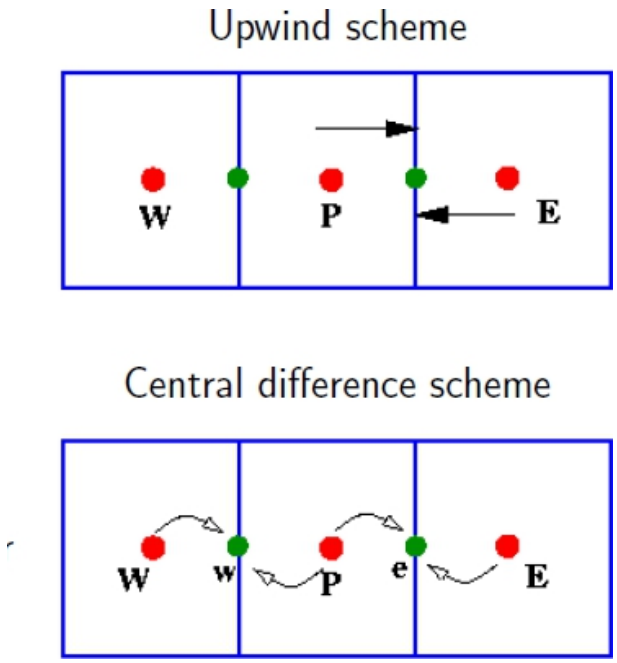

Figure 4.5: Central Differencing Scheme (bottom), Upwind Differencing Scheme (top)[63, 115]

4.3.1 Spacial discretizaion

4.3.1.1 Convective fluxes

The surface integrals are evaluated individually for each face. Since the procedure is identical for each of the faces only the east face in an exemplary manner in the following derivations is considered. The discretization of the convective term is given by:

$$\int_\sigma \rho u_i \psi n_i d\sigma = \sum_{k=e,w,n,x} a_k \sigma_k = (\rho u\psi)_e \sigma_e - (\rho u\psi)_w \sigma_w + (\rho u\psi)_n \sigma_n - (\rho u\psi)_s \sigma_s + (\rho u\psi)_t \sigma_t - (\rho u\psi)_b \sigma_b \quad (4.12)$$

For approximating the value ψ at the faces e, w, n s, t and b, three basic discretization schemes are available, i.e Central Differencing Scheme, Upwind Differencing Scheme and The Flux Blending method.

The first common way is to use linear interpolation **Central Differencing Scheme (CDS)**. The value of ψ (e.g. at the east face) is estimated using the neighbor nodes P and E (Fig. 4.5 bottom).

$$\psi_e = f_x \psi_E + (1 + f_x)\psi_p, \quad (4.13)$$

where f_x is the interpolation function, and for a constant mesh spacing $f_x = 0.5$. The central differencing scheme has a second order accuracy. One can prove this by applying the Taylor series expansion on the point P. The accuracy is proportional to the square of grid width; i.e. if the number of cells within one direction is doubled, the error will be divided by a factor of 4.

The Upwind Differencing Scheme (UDS) assumes that the neighboring cell value for ψ will be convected across the boundary(Fig. 4.5 top):

$$\psi_e = \begin{cases} \psi_p & \text{if} \quad u_e \geq 0 \\ \psi_E & \text{if} \quad u_e < 0 \end{cases} \tag{4.14}$$

The main drawback of the upwind scheme is that it is inaccurate and very diffusive, because it is of first order.

The Flux Blending switches between the two, according to the relative size of the convective and diffusive fluxes across the cell face. By resulting in oscillation, one can combine UDC and CDS to calculate the value at the faces e:

$$\psi_e = \underbrace{\psi_e^{UDS}}_{I} + \underbrace{\gamma(\psi_e^{CDS} - \psi_e^{CDS})}_{II}, \tag{4.15}$$

where $0 \leq \gamma \leq 1$ is factor which scales the manner of flux blending. For $\gamma = 1$, the interpolation is pure CDS whereas for $\gamma = 1$, the interpolation is pure Upwind. Part I of Eq. 4.15 is treated implicitly whereas part II is treated explicitly. The flux blending scheme is a good control tool to achieve an optimum between stability and accuracy.

4.3.1.2 Diffusive fluxes

Similar to that of the convective term discretization of the diffusive fluxes is the sum of the fluxes across all faces of an individual control volume. So, the diffusive part, a centered difference for the discretization of the normal gradient of the flux on the control volumes faces is used. Thus the diffusive part is discretized by:

$$\left(\frac{\partial \psi}{\partial x}\right)_e = \frac{\psi_E - \psi_P}{x_E - x_P}, \tag{4.16}$$

In the frame of this work, all above mentioned schemes for the interpolation of scalar (e.g. ψ_E) at the control volume faces have been applied on different configurations. These numerical schemes reflect the way how information is transported through the faces. It is dependent on the ratio between convection and diffusion, i.e. the Peclet number, which is defined by:

$$Pe = \frac{\rho u_i \Delta x_i}{\Gamma} \tag{4.17}$$

If the Peclet number is small, the transport is dominated by diffusion, which transports information equally in all directions. Contrarily if the Peclet number is large, information is transported in the direction of the velocity field. Having a large Pe is undesired, since it influences the solution convergence very much. The numerical results may contain oscillations due to the fact that while computing the convective term at the note P only the values at E (east) and W (west) nodes are used, but not at the P node. Thus, ψ_P can take any value, i.e. oscillations are allowed. Please refer [119, 119, 181] for more details on the implementation diffusive fluxes in FASTEST3D.

Total variation diminishing TVD MULI (multi-linear interpolation procedure) [119, 119, 181, 218] which has two additional terms compared to Eq. 4.13 is more accurate than CDS schemes. However, the interpolation factors $\gamma_{e,w}$ in Eq. 4.15 are only functions of the grid, which are suitable for flow variables. The MULI which is a CDS don't have numerical dissipation behavior resulting a strong oscillations for scalar quantity (e.g mixture fraction and reaction progress variable); in the presence of steep gradients (between fuel and oxidant streams). This would not only cause violation of physical realizability-limits for these quantities, but since density is obtained from these scalars through the non-linear functional relation-ships of transport equations, it would also oscillate severely and the solution would be completely erroneous.

Numerical dissipation need to be introduced to obtain smooth and bounded solutions of the scalars. This can be achieved with total variation diminishing TVD schemes. Originally developed for the purpose of capturing shocks in simulation of compressible flow, they have been successfully employed to scalar transport in LES (e.g. [218, 102, 217]). From the large class of TVD schemes a so-called flux limiter formulation was implemented in FASTEST3D. These schemes which have been summarized share with the UDS the fact that the discretization depends on the direction of the flow at the cell face. Fig. 4.6 shows the computational molecule consisting of three CV's that will be used for the computation ψ. The three points that will be used are called the upwind, center and downwind point shortly referred to as U, C, D. In a general notation the face value is approximated as:

$$\psi_e^{TVD} \approx \psi_e^{TVD} + \frac{1}{2} B(r) \left(\psi_C - \psi_D\right) \tag{4.18}$$

where B is flux limiter which is a function of solution ratio r, which is defined as the ratio of the gradient of ψ between the downwind and the upwind side.

$$r = \frac{\psi_D - \psi_C}{|x_{i,D} - x_{i,C}|} \frac{|x_{i,C} - x_{i,U}|}{\psi_C - \psi_U} \tag{4.19}$$

In this work for FASTEST3D, CHAM limiter function was used. This allows using of a high order accuracy with little numerical dissipation in regions of smooth ψ. Furthermore, introducing just enough artificial dissipation to prevent oscillations when the sensor r detects the presence of a jump in ψ approaching from the upstream direction. CHARM limiter reduces to the UDS at a jump, but is of $\wp(3)$ when r is positive.

$$B(r) = \begin{cases} 0 & r \leq 0 \\ r \bullet \frac{(3r+1)}{(r+1)^2} & r > 0 \end{cases} \tag{4.20}$$

This formulation generates low numerical dissipation and constantly produces bounded, non-oscillatory results. Compared to other limiters which are piecewise linear functions, CHARM has the advantage of being smooth except at $r = 0$ over other limiters which are piecewise linear functions. This is advantageous for the convergence behavior of the iterative solution methods.

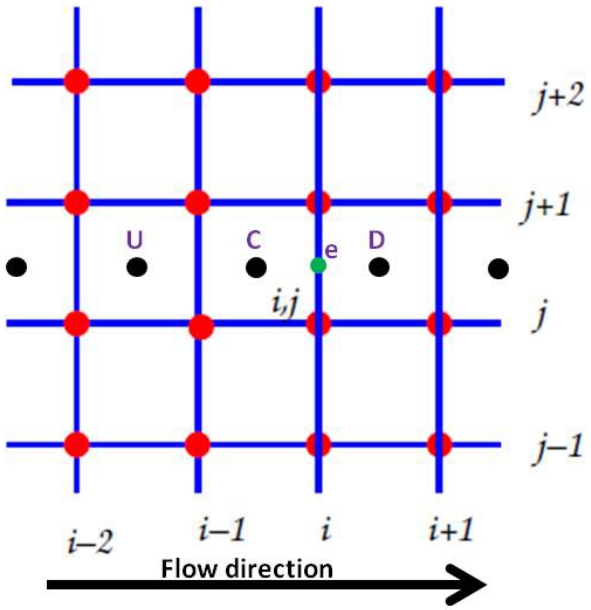

Figure 4.6: Labelling neighouring cells for TVD

Source term discretization: The source term contributions in the governing equations are may be from gravity, production or annihilation of reaction progress variable and due to mass source in multiphase simulations. These source terms are integrated over corresponding control volume of the particular cell accordingly, by evaluating them in the cell center P and multiplying the source term with the volume of CV, δV as:

$$\int_V S dV = S_P \delta V_P \quad (S_P = \rho_P g_i, \dot{w_P}) \tag{4.21}$$

Cell gradient for SGS variance The required approximation of gradients in the cell centers for the pressure gradient in the momentum equations and the model expressions for the SGS stress τ_i^{sgs}, the SGS variance of mixture fraction $\widetilde{f''^2}$ and it's scalar dissipation are computed using the local coordinate system, before transforming into to Cartesian coordinates. See Wegner [218] for more details on claculation of cell gradients and on filter width and test filtering operator employed in this work (FASTEST3D).

4.3.2 Time dependent discretization

In CFD, a combination of the Navier-Stokes equations and Continuity Equations result in a system of Differential Algebraic Equations (DAE) due to the discretizaion, but not in ODE (Ordinary differential equation). Dealing a DAE is different than dealing an ODE. All LES simulations are unsteady simulations. For obtaining the solution for Navier-stokes discretization has to be carried out also for time, in addition to space as detailed in previous section. The transient term also known as accumulation term in conservation equations, is a change at a point in time. The discretization of the transient terms is usually called temporal discretization or discretization in time. The temporal

Table 4.1: Advantages of implicit and explicit time integration methods

	Explicit	**Implicit**
Stability	conditionally stable	inherently stable
Time-step size	limited	not limited
Algebraic system of equations	no (only pressure)	yes
Preference	highly unsteady flows	steady flows
Programming effort	moderate	high
Implicit solvers can be optimized with fast solvers such as multigrid		
Explicit methods must fulfill CFL criteria i.e. $\frac{U\Delta t}{\Delta x} < 1$		

discretization is directly influences the stability of simulations and accuracy of the results.

The majority of existing time integrators in literature are called "linear methods". The main three approaches of linear methods are:

- Multistep methods
  - Adams-Bashforth
  - Adams-Moulton
  - BDF (Backward Differentiation Formulation)
- Multistage methods (Runge-Kutta methods, both explicit and implicit)
- Multiderivative methods (Taylor-Series methods)
- Combination of above methods

Kempf [102] presented detailed analysis of time discretization specific to combustion application (see also [218, 63]). In the FASTEST3D framework two different time stepping procedures are available and will be presented here. The implemented time discretizations within the used code FASTEST3D are: First Order Forward Implicit (FOFI), Second Order Forward Implicit (SOFI), Crank Nicolson (CN), and Runge Kutta (RK) [63] methods. In Table 4.1 the advantages of implicit and explicit methods are presented.

The time-dependent transport equations for the quantity ψ should be integrated in time. The discretized Eq. 4.22 for one dimensional convective diffusive problem is:

$$\frac{\psi_P^{n+1} - \psi_P^n}{\Delta t} = -u\frac{\psi_P^n - \psi_W^n}{2\Delta x} + \Gamma\frac{\psi_P^n - \psi_W^n - 2\psi_P^n}{(\Delta x)^2} \tag{4.22}$$

All of the terms in Eq. 4.22 are known from the spatial discretization that has been described in the previous section, except the time derivative of the transported quantity ψ_P. The right hand side of equation 4.22 and are now referred to as the fluxes $F(\psi, t)$. It is represented by Eq. 4.23:

$$\frac{\psi_P^{n+1} - \psi_P^n}{\Delta t} = F(\psi_P, t) \tag{4.23}$$

In equations 4.22 and 4.23 the ψ_P^{n+1} which is present time step (n+1) value of ψ can be calculated from the available information from previous time step and time step size (Δt) as given in Eq. 4.24. This scheme is called Euler-Explicit Scheme, which has only first order accuracy and not stable with Navier stokes equation.

$$\psi_P^{n+1} \approx \psi_P^n + \Delta t F\left(\psi_P, t\right) \tag{4.24}$$

From equations 4.22 and 4.23, one can define the Courant-Friedrichs-Lewy (CFL) number. Thus one can also make an instruction for the explicit time discretization method which is valid for RK-method:

$$CFL = \left| u \frac{\Delta t}{\Delta x} \right| \leq 1, \tag{4.25}$$

this requires:

$$\Delta t \leq \frac{\Delta x}{u}. \tag{4.26}$$

A stable first order scheme can be obtained by time discretization based on backward time stepping $F\left(\psi_P, t\right)$ in Eq. 4.24, i.e. discretizing at the new time step $n+1$, by using $F\left(\psi_P, t + \Delta t\right)$ instead of $F\left(\psi_P, t\right)$. This is called *Euler-Implicit* (also known as FOFI method) method scheme, which is stable for larger scales can be represnetd by:

$$\frac{\partial \psi^{n+1}}{\partial t} \approx \frac{\psi^{n+1} - \psi^n}{\Delta t_n} = F\left(\psi_P^{n+1}, t + \Delta t\right) \tag{4.27}$$

For the computing time dependent non-combustion configuration as reported by Pantangi et al. [240] the FOFI method was chosen. The advantage of using this scheme (fully-implicit technique) is that there is no restriction on time-steps (the implicit Euler method allows arbitrarily large time steps to be taken). However the first order implicit method is no more accurate than the explicit Euler method [218, 63, 102, 181]. The disadvantage is the first order truncation error in time. The *Crank-Nicolson method* solves both the accuracy and the stability problem. It is based on central differencing and hence it is second-order accurate in time. The approximation of the time derivative is done on the time point $t_{n+1/2}$ as follows:

$$\frac{\partial \psi^{n+1}}{\partial t} \approx \frac{\psi^{n+1} - \psi^n}{\Delta t_n} = \frac{F\left(\psi_P^{n+1}, t + \Delta t\right) + F\left(\psi_P, t\right)}{2} \tag{4.28}$$

and which gives:

$$\psi^{n+1} \approx \psi^n + \Delta t_n \frac{1}{2}\left(F\left(\psi_P^{n+1}, t + \Delta t\right) + F\left(\psi_P, t\right)\right) \tag{4.29}$$

Wegner [218] found that, combustion flow simulations oscillate in scalar equation with the Crank-Nicolson scheme. This in turn effecting the velocity field through the density variation caused by the scalar oscillations. To overcome these problems reacting flows without density variation are simulated by this scheme (see [240]).

For solving combustion problems with density variation an explicit time stepping approach is adopted in this work. The explicit scheme as defined by Eq. 4.23 is not

stable for solving governing transport equations. This can overcome by incorporating additional sub steps into the explicit scheme. For this purpose *a three stage Runge-Kutta* explicit time stepping method is adopted in this work for combustion based simulations.

Time Derivative of Density of combustion flow is vital in achieving the mass conservation of the continuity equation and it is also crucial for stability of the simulation as it influences directly the pressure correction equation as detailed in the next section. The appropriate choice for its approximation depends on the time-integration scheme used for the flow equations and has a great impact on the stability of the final algorithm; Cook and Riley [45] found a second order explicit approximation (see [218]) to work best in the context of a 3rd−order Adams−Bashforth time integration. Cook and Riley [45] reported drawbacks of using purely explicit schemes for in the maximum density ratio locations, in LES context. Multi-stage explicit schemes (for e.g. see [68, 102]) using a Runge-Kutta time-marching method or semi-implicit schemes [155] seem to be more suitable for this purpose. Wegner [218] found the temporal change approximated by:

$$\left.\frac{\partial \rho}{\partial t}\right|^{n+1} \approx \frac{\rho^{n+1} - \rho^{n}}{\Delta t} \tag{4.30}$$

is very suitable for simulating combustion simulation and this formulation is used in this work for simulating combustion flows with FASTEST3D.

4.4 Pressure velocity coupling

The fluid flows are classified into two types based on the speed of the flow for developing CFD codes, i.e. compressible and incompressible flows. If the ratio of the speed of the flow to the speed of sound speed less than Mach 0.3 then the flow considered as a incompressible otherwise compressible flows. Fig. 4.7 shows Mach number values and the corresponding flow regimes. To predict flows at different Mach number regimes, many flow solvers have been developed. Most solvers deal with incompressible or compressible flow regimes only. For instance, if incompressible solvers are used to predict the flow in compressible regime or vice versa, predicted values become unrealistic and solution becomes totally wrong. The mathematical character is the major difference between incompressible and compressible flow equations. Compressible steady flow equations are hyperbolic which means flow characteristics travel at finite propagation speeds. On the contrary, incompressible steady flow equations have a mixed parabolic/elliptic character.

In this work only low Mach number flows, i.e, incompressible flows are considered. Hydrodynamic pressure is vital in these type of flows and which is a driving force in the momentum equations. The 3D-incompressible flow is described numerically by three equations of momentum and the continuity. Thus we have four unknowns (u, v, w, and P) and four equations (3 for momentum + 1 for continuity). Pressure is decoupled from the density due to the assumption of low Mach-number, so equation of state is not required to solve as in the case of the compressible solver. In general incompressible flow solvers are pressure based and compressible solvers are density based, but not always

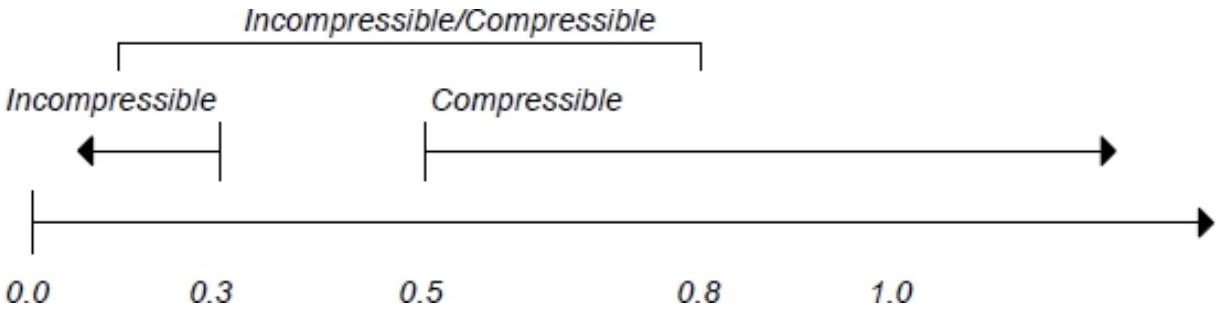

Figure 4.7: Mach number values and the corresponding flow regimes

true. However, the continuity equation does not contain an independent unknown since the density is already given by the combustion model and is obtained from the look-up tables. As Ferziger and Perîc [63] point out, the mass balance is rather a kinematic constraint on the velocity field than a dynamic equation and can therefore be used to construct a pressure field such that mass continuity is satisfied. Many methods are available in the literature to realize the pressure-velocity coupling which are commonly called projection methods or pressure correction schemes and in general solve a Poisson equation for the pressure or a pressure correction. In FASTEST, the Semi Implicit Method for Pressure Linked Equation (SIMPLE) algorithm of Patankar [147] is used.

The SIMPLE algorithm is preceded as follows: first the momentum equations are solved, using an "old" pressure to give u^*, v^*, and w^*. Below only the x-direction with the velocity component u^* is considered, the other two directions can be treated in the same way. The discretized governing Eq. 4.3 in its steady state form for the u^* velocity component is given by:

$$a_e u_e^* = \sum_{nb} a_{nb} u_{nb}^* + S_{\tilde{u}} + (P_W^* - P_P^*)\sigma_e, \tag{4.31}$$

where $S_{\tilde{u}}$ represents a source term, $\sigma_e\,(\Delta V/\partial x_i)$ the control volume surface in the east face, $(P_W^* - P_P^*)\sigma_e$ is the pressure gradient, and a_{nb} are the discretization coefficients related to all faces. By introducing corresctions in pressure, velocity and mass:

$$u_i^{n+1} = u_i^* + u_i^{cor} \tag{4.32}$$

$$P^{n+1} = P^* + P^{cor} \tag{4.33}$$

$$m^{n+1} = m^* + m^{cor} \tag{4.34}$$

where u_i^* have been obtained from the momentum equations, and p^* was obtained from the previous iteration, m^* is caluculated based on density, velocity from previous iteration together with CV's face area u_i^{cor} and P^{cor} are the velocity and pressure correction respectively. Now, velocities u_i^{n+1} are used (corrected) to solve the continuity equation

$$\left(\rho\frac{\Delta V}{\Delta t}\right) + \sum_i (\rho u^{n+1}\sigma)_i = 0 \tag{4.35}$$

First term of L.H.S in Eq. 4.35 is the discretized form time derivative of density. By substituting Eq. 4.32 in continuity above Eq. 4.35, gives :

$$\underbrace{\left(\rho\frac{\Delta V}{\Delta t}\right)+\sum_i(\rho u^*\sigma)_i}_{\acute{b}}+\sum_i(\rho u^{cor}\sigma)_i=0 \tag{4.36}$$

where $\acute{b}$ is the virtual mass source, which will disappear as the convergence is achieved during the iterations. Then rewriting the momentum Eq. 4.31 to obtain a relation between u_i^{n+1} and P^{cor} .

$$a_e u_e^{n+1}=\sum_{nb}a_{nb}u_{nb}^{n+1}+S_u+(P_W^{n+1}-P_P^{n+1})\sigma_e, \tag{4.37}$$

where nb denotes the neighboring faces. Subtracting Eq. 4.31 from Eq. 4.37 a relation between u_i^{cor} and P^{cor} is obtained as follows:

$$a_P u_P^{cor}=\underbrace{\sum_{nb}a_{nb}u_{nb}^{cor}}_{\approx 0}+(P_W^{cor}-P_P^{cor})\sigma_e, \tag{4.38}$$

since the velocity corrections in the neighbor nodes u_{nb}^{cor} are not yet known, they must be aproximated following some criteria. A typical approach for pressure-correction methods is that now the first term in R.H.S of Eq. 4.38, which still contains the unknown velocity corrections in the neighboring points of P, are suitably approximated. There are different possibilities for this, the simplest of which is to simply neglect this term $\sum_{nb}a_{nb}u_{nb}^{cor}\approx 0$. This is well-justified, since the correction u_{nb}^{cor} vanishes during the iteration procedure. This approach yields the SIMPLE method (Semi-Implicit Method for Pressure-Linked Equations) proposed by Patankar und Spalding [147]. The resulting equation from Eq. 4.38 is:

$$u_P^{cor}=\frac{1}{a_P}(P_W^{cor}-P_P^{cor})\sigma_e, \tag{4.39}$$

By inserting this expression for u_P^{cor} into Eq. 4.36 one obtains a Poisson equation for the pressure correction.

$$\sum_i\left(\rho\frac{1}{a_P}(P_W^{cor}-P_P^{cor})\sigma^2\right)_i=-\acute{b} \tag{4.40}$$

The right hand side of this equation differs from that of the pressure correction equation of the standard SIMPLE since $\acute{b}$ contains the time derivative of density in addition to the divergence of the predicted velocity. After solving Eq. 4.40 the pressure correction can be used to compute the velocity correction from Eq. 4.39 . By adding the respective corrections, the final pressure and velocity are obtained from equations 4.32, 4.33 and 4.34. On a staggered grid arrangement, the Poisson Eq. 4.40 can be discretized and solved in a straight-forward manner. In this work the central discretizations is used for approximating the divergence operator in the continuity equation. The cell center gradient of pressure determined similar to MULI, which is based on a Taylor-series by deducing a discrete system for the pressure correction following Lehnhuser [119]. So,

since a collocated variable arrangement is used in FASTEST, its discretization needs some special care.

$$a_P P_P^{cor} + \sum_{nb} a_{nb} P_{nb}^{cor} = -\acute{b} \quad \text{(nb= EE, WW, NN, SS, TT, BB are second immediate neighboring points of P)} \tag{4.41}$$

in which the immediate neighbors of point P (i.e. E,W,N,S,T,B) have been canceled out, resulting strong grid-scale oscillations in the pressure field due to an absence of ellipticity at the grid scale in equation 4.41 [10]. The first approach is to recover the grid-scale ellipticity of the discrete pressure correction equation was introduced by Rhie and Chow [171]. This approach which is based on pressure-weighted interpolation (also referred as selective interpolation, momentum interpolation method), is very widely accepted in the literature and used in extensively in numerous CFD codes. The same interpolation method is implemented in the FASTEST3D CFD code and more details on interpolation of cell face velocities and predicted cell face velocities are detailed by Wegner [218]. Thus momentum weighter interpolation techqniue for the velocities, for equidistant grids Rhie and Chow [171] suggested:

$$u_e^* = \frac{1}{2}\left(\widehat{u_W^*} - \widehat{u_P^*}\right) + \frac{A_f \sigma_e}{a_{nb}} \left(P_W^{cor} - P_P^{cor}\right) \tag{4.42}$$

The "Pseudo velocities" $\widehat{u_i^*}$ are derived from the momentum balance equation by neglecting the influenec of the pressure gradient.

$$\widehat{u_W^*} = u_W^* - \frac{A_f \sigma_e}{a_{nb}} \left(P_W - P_P\right) \tag{4.43}$$

This procedure allows to counter the problem of strong grid-scale oscillations in the pressure field arising from pressure velocity decoupling on collocated grid. The combustion simulations are accompanied by density change, especially across the flame front. The change in density could be in order of 10 and this could take place in a single CV only. The mass flux calculation across the cell face requires the estimation of density by same interpolation practice as for the convective term of the combustion scalars, i.e. the TVD scheme. This is the only approach for obtaining an essential, stable and conservative scheme. The mass flux calculated from the pressure-weighted face velocity Eq. 4.47, is given by:

$$\dot{m}_e = \rho_e^{TVD} u_e^{n+1} \sigma_e \tag{4.44}$$

Thus virtual mass source (appearing from algorithm used, but not real source) is calculated by:

$$-\acute{b} = \left(\rho \frac{\Delta V}{\Delta t}\right) + \sum_{nb} \dot{m}_e \tag{4.45}$$

Using CDS approximation for the cell face gradient of p and the MULI scheme for the interpolated velocity one obtains a pressure correction equation has the preferred property of being elliptic on the grid-scales. This is represented by:

$$a_P P_P^{cor} + \sum_{nb} a_{nb} P_{nb}^{cor} = -\acute{b} \quad \text{(nb= E,W,N,S,T,B are first immediate neighboring points of P)} \quad (4.46)$$

Once pressure is updated as $P^{n+1} = P^* + P^{cor}$ and $(P_W^{cor} - P_P^{cor})$ is calculated, then new corrected velocities can be computed following equation momentum correction Eq. 4.38 and mass flux correction Eq. 4.45 as follows:

$$u_e^{n+1} = u_e^* - \frac{\sigma_e}{a_e - \sum_{nb} a_{nb}} P_W^{cor} - P_P^{cor} \quad (4.47)$$

The Eq. 4.47 includes the term $\sum_{nb} a_{nb}$, which is unknown and therefore it will be set to zero in the frame of the SIMPLE method [147] and in FASTEST3D it is implemented by complimenting by explicit projection method introduced by Chorin [38] . Other pressure correction method (SIMPLEC) [147] assumes that $\sum_{nb} a_{nb} u_{nb}^{cor} = \sum_{nb} a_{nb} u_e^{cor}$ in Eq. 4.38 to get the Eq. 4.47.

The solution procedure using the SIMPLE method can be summarized as follows:

- Guess the pressure p^* (or take it from previous step)
- Solve the Navier-Stokes equations and get u_i^*
- Solve the pressure correction p^{cor} (Eq. 4.46)
- Update the pressure (Eq. 4.33)
- Correct the velocities and mass flux (Eqs. 4.38, 4.47 and 4.45)
- Repeat Steps 2-5 till convergence.

Chapter 5

Tabulated chemistry

The availability of high performance computational resources (HPCR) is still expensive for investigating combustion systems numerically. The advancement and application of HPCR in general are not suitable for industrial problems with detailed chemistry, involving hundreds of species and thousands of reaction steps [228, 188]. The reduced reaction mechanism can't capture all intermediate species in detail [228] for comprehensive combustion analysis. In recent times, for many academic and industrial problems [241] the Tabulated chemistry [204, 241, 66, 172, 113] is emerging as an alternative for detailed chemistry based simulations. In this section a brief overview of FGM tabulation method for non-adiabatic combustion is presented and then followed by its validation against 1D DNS simulations.

5.1 Three dimensional tabulated chemistry (FGM)

The FGM tabulation concept is based on solving one dimensional laminar steady state flame called flamelet (unsteady for diffusion flames [204]) by means of detailed chemistry for complete mixture fraction range(0-1) [205]. Flame Prolongation based ILDM (or FPI) tabulated chemistry approach developed independently by Gicquel et al. [76] is in accordance with FGM. Here 1D flames are computed in the flammability region, here by means of CHEM1D [36] with detailed mechanisms. A suitable reaction progress variable (RPV) is predetermined from the literature for the specific reaction mechanism of a specific fuel mixture. Once RPV is known, then each flamelet's thermo-chemical properties from fresh gas to complete burnt gas can be parametrized as a function of a unique RPV for a combination of single mixture fraction enthalpy. In this study flamelets are constructed using both Lewis unity and also accounting differential diffusion and analyzed its effect in 3D LES simulations. For adiabatic combustion, a look-up chemistry table is constructed according to the FGM tabulation approach [204, 241, 66, 172, 113] with two co-ordinates (mixture fraction, reaction progress variable). Thus, all chemical species involved in the detailed kinetics scheme, the temperature, and the thermo-chemical data are tabulated in terms of these two coordinates (ξ, Y). If φ denotes any thermo-chemical scalar; where species mass fraction, density, viscosity, RPV and source rate are denoted by Y_α, ρ, μ, $\dot{w}$ respectively (where α is species indices) etc., then for a constant enthalpy combustion (adiabatic combustion):

$$\varphi = \varphi(\xi, Y) \qquad \varphi = Y_\alpha, \mu, \rho, \widetilde{\dot{w}_\alpha} \text{ etc.} \tag{5.1}$$

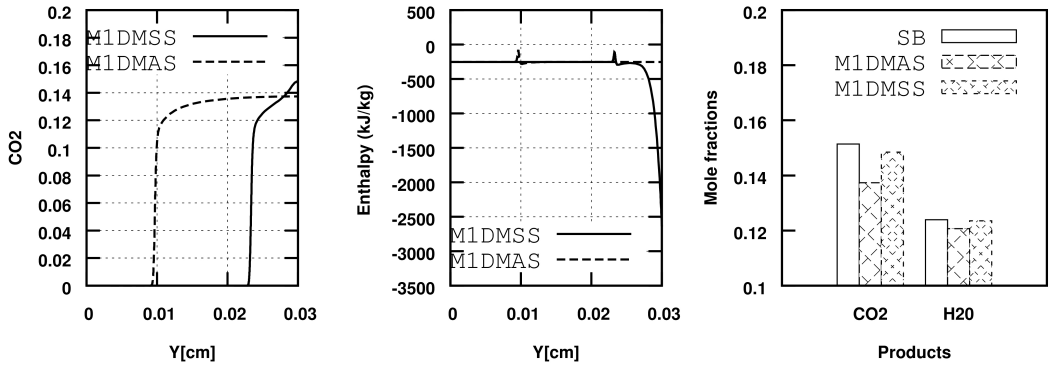

Figure 5.1: Maximum CO_2 and H_2O mass fractions achieved by simple balance, adibataic and non-adibatic combustion

In an adiabatic combustion enthalpy remains constant when Lewis number considered is equal to unity. Due to differential diffusion effects enthalpy changes in the flame front as shown in Fig. 5.1 (middle) for an adiabatic combustion. The change of enthalpy in the flame front arises in adiabatic combustion as the species diffusion co-efficients are different for each chemical species/radicals present. Thereby the enthalpy associated with the the species travels with varied speeds. In reality the enthalpy doesn't change in adiabatic system in a global closed systems perspective. However the enthalpy could change by other means during the combustion. For example, the evaporation in spray combustion contributes to local enthalpy change in the combustion systems and in the flame region due to the enthalpy consumed for evaporation of the spray. The other physical phenomenon contributing to enthalpy change is during the flame interacting with cooled wall.

5.2 Non-adiabatic combustion

FWI is very obvious situation in many industrial applications as detailed in section 1.1.2. Thus tabulated chemistry is also appropriate when enthalpy is considered as a third co-ordinate for tabulation thermo-chemical properties of combustion. Enthalpy inclusion in tabulated chemistry produced encouraged results [65, 66, 136]. Please note that, enthalpy change due to mixing between different mixtures fractions with same inlet temperatures are already taken care by adiabatic FGM table as defined by Eq. 5.1. The influence of enthalpy on combustion processes and on its associated processes is very crucial in determining both design and operating parameters of combustion systems.

A short overview is presented here to get a first impression on the differences between adiabatic and non-adiabatic combustion flames. For this study, three cases are considered for a comparison; a simple one step reaction balance (SB), a one dimensional (1D) adiabatic case (M1DMAS), and a 1D stagnation flame (M1DMSS) which is non-adiabatic, more details of the case setup are provided in Table. 5.1. The CO_2 mass fraction compared in Fig. 5.1 (left) in the physical domain shows enthalpy is influencing its formation even though initial mixture fraction, inlet temperatures are same for both cases. The higher CO_2 is predicted in stagnation flame case. The peaks in CO_2 from

Table 5.1: 1D DNS/ 0D cases (^{s} = Stagnation flame, ^{a} = Free propagating adiabatic flame)

	Fuel	**1D 0D**	Lewis No.	ϕ	Inlet T[K]	Wall T[K]
$M1DMSL^s$	CH_4	1D	Mix. Avg.	0.83	300	600
$M1DMSS^s$	CH_4	1D	Mix. Avg.	1.0	300	600
$M1DMSR^s$	CH_4	1D	Mix. Avg.	1.2	300	600
$H1DMSS^s$	nC_7H_{16}	1D	Mix. Avg.	1.0	373	600
SB	CH_4	0D		1.0	300	
$M1DMAS^a$	CH_4	1D	Mix. Avg.	1.0	300	

both cases in Fig. 5.1 (middle) are attributed to the differential diffusion effect. The final products of CO_2 and H_2O are compared in Fig. 5.1 (right) indicates that the compositions calculated from simple mass fraction balance are higher than M1DAS and M1DSS. The conversion levels of final products (of CO_2 and H_2O) achieved by non-adiabatic case are higher than M1DSS and close to the simple balance calculations. This demonstrates the combustion physics is very different from the adiabatic case to the non-adiabatic case. Therefore, it is attention-grabbing to see if same FGM tabulation strategy of adiabatic combustion can be extended to the non-adiabatic case by adding only additional enthalpy co-ordinate, which is discussed in section 5.3.

Enthalpy inclusion is vital in determining combustion properties for FWI. To include enthalpy in FGM table one needs three types of flamelets, namely the adiabatic flamelets at different inlet temperatures, secondly the burner stabilized and the extrapolated flamelets in flame quenching region. The change in enthalpy at each mixture fraction can be achieved by changing inlet temperature, here from 600 K to 300 K (373 K for n-heptane) with 10 K temperature step size. The burner stabilized flamelets are generated by passing fuel through the inlet of porous burner at different inlet velocities starting from laminar flame speed for a particular mixture fraction until the inlet velocity reaches the lower velocity where flame starts to unstable. Beyond this lower inlet velocity a flame could not be ignited with physical conditions available.

The inlet temperature for each mixture fraction for all burner stabilized flamelets is fixed at the lowest adiabatic inlet temperature, i.e here 300 K. The lowest temperature should be chosen such that the real combustion system where the final non-adiabatic FGM table will used cannot experience any temperature below the *lowest temperature*. The quenching region which are present below the lowest possible inlet velocity are generated by extrapolation following Fiorina et al. [65]. Details of method adopted in this work is presented later in section 5.2.1. The final FGM table is constructed following Ketelheun et al. [104]. In the following sub section an analysis is carried out on FGM tabulation suitability for simulating non-adiabatic combustion.

5.2.1 Construction of non-adiabatic FGM table

CHEM1D solves the 1D flame in physical space system for various inlet condition. For example for adiabatic premixed FGM table, flamelets are constructed by changing the inlets mixture fraction. However these flamelets can not be used as chemistry table by CFD solver. Therefore FGM table is constructed by following ILDM approach of differentiating between variable which are independent chemical reaction (e.g species mass fraction) and dependent variables(e.g mass fraction chemical elements, pressure and enthalpy). The reaction control variable is the one which can describe the combustion process from unburnt to burnt is chosen as RPV, while the composition of the chemical equilibrium mixture is completely determined by the values of the conserved variables. The complete set of 1D flamelets are now transformed into a FGM table as described in detail by Oijen [204]. Then the FGM table is coupled with CFD solver for complex configurations as represented by Fig. 5.4.

Different types 1D flamelets are required for the construction of FGM tables. Flowchart in Fig. 5.2 provides the the method adopted to generate all required flamelets for non-adiabatic FGM table. The main steps involves:

- Adiabatic flamelets for various mixture fraction of fuel and air in flammability region
- At each mixture fraction adiabatic flamelets for various inlet temperatures are constructed in the flammability region
- The burner stabilized flamelets are constructed at various inlet velocities
- Extrapolated flamelets for each mixture fraction beyond flammability limits
- Extrapolated flamelets for lower enthalpy to achieve the minimum possible configuration temperature for all mixture fractions and RPVs

CHEM1D solves the 1D flame in physical co-ordinate systems. These flamelets are used to construct to form multi dimensional FGM table. The basic assumption in construction of 1D flamelets is such that all enthalpies and mixture compositions of the configuration that will be simulated could be retrieved correctly. These flamelets will be transformed into the space of RPV, mixture fraction and enthalpy as described in Fig. 5.3b. However as shown in the Fig. 5.3a; BST flamelets at lowest velocity could be exposed to lower temperatures than achievable by CHEM1D in actual non-adiabatic applications. Thus lower enthalpies could be possible than that of BST flamelets at the lowest inlet velocity (Below this inlet fuel velocity flame cannot be stable or flammable). The missing enthalpies beyond flammable region at lower temperatures were constructed by search method by Fiorina [65] and Ketelheun et al. [104] for appropriate species, temperature. Please note that the cooling of the burnt or unburnt products don't change the configuration of species concentrations. However search method to construct missing BST flames is not suitable when there is not unique solution available for example in case flamelets simulated using mixture averaged diffusion co-efficient (non-unity Lewis number). Please note that adibataic laminar flame speed obtained by non-unity Lewis number approach is higher than that of with unity Lewis number. In the present work both unity Lewis number and non-unity Lewis based flamelets used and separately for constructing two types of FGM tables. The lower enthalpies at extreme end are determined by using 8

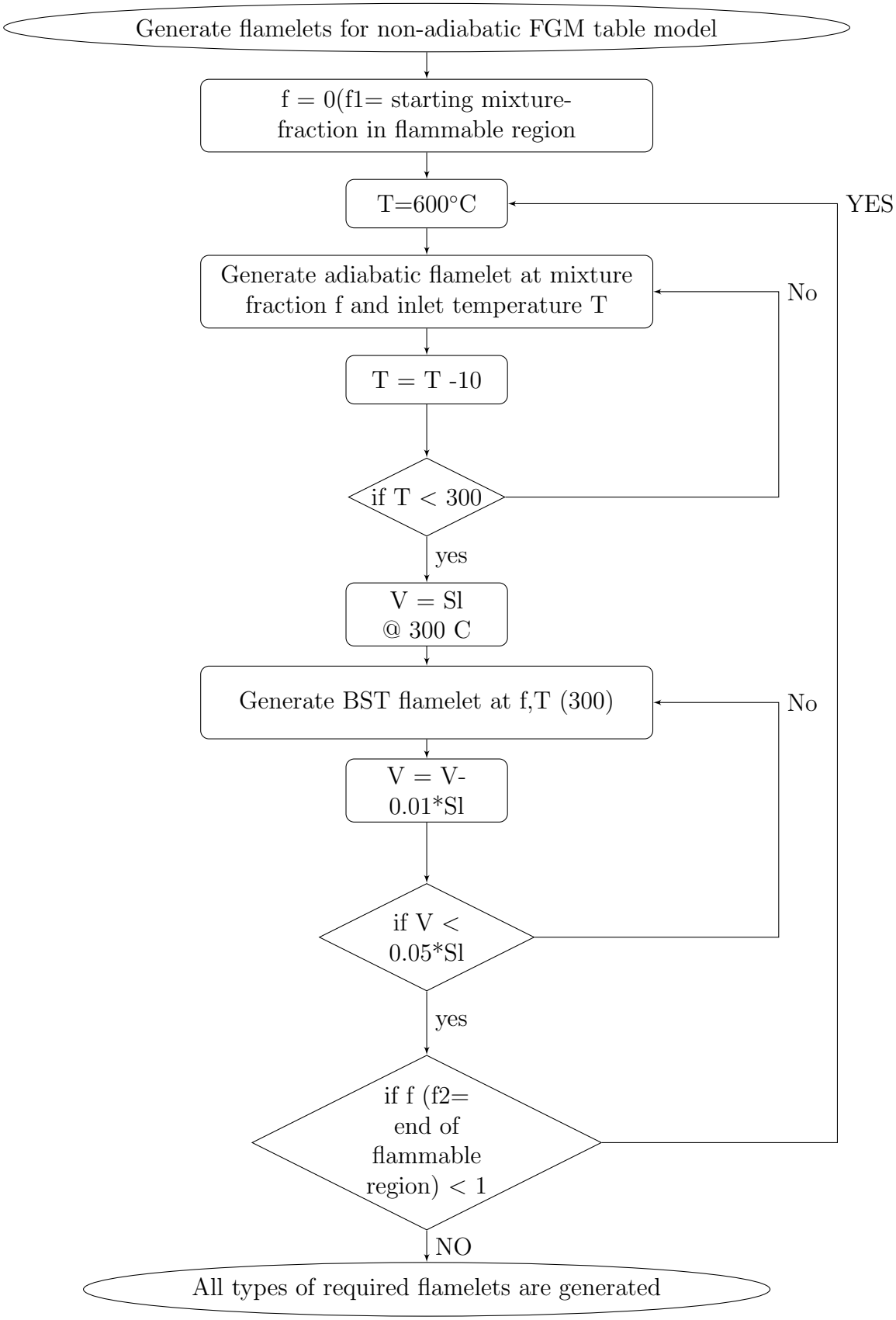

Figure 5.2: Procedure for generating various flamelets required for non-adiabatic FGM table

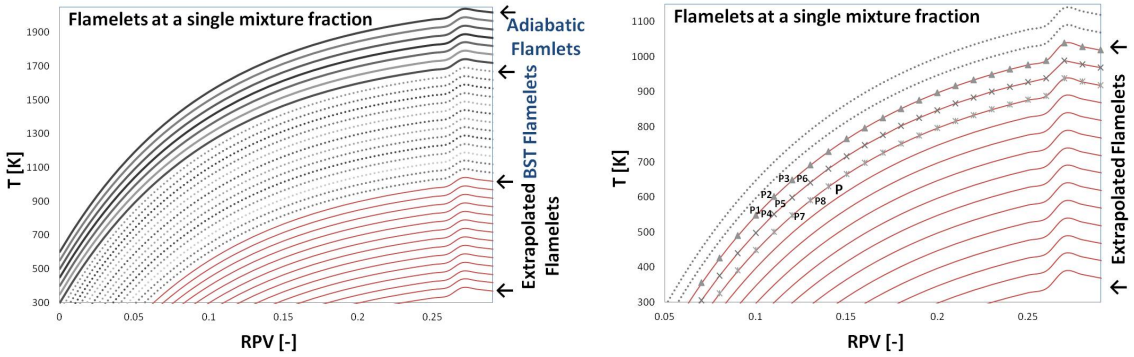

(a) Adiabatic, BST and extrapolated flamelets for a single mixture fraction

(b) Eighth point weighted extrapolation for BST flamelets

Figure 5.3: Representation of 1D Flamelets transformed into independent combustion variables space

nearest neighbor point weighted average extrapolation approach. This allows unique and thermo-chemical consistent solution. The extrapolation approach for constructing FGM table in this work are successfully validated and verified with the works of Fiorina [65] and Ketelheun et al. [104]. Further in this work new approach of FGM table construction is adopted.

5.2.2 FGM and LES CFD solver coupling

Combustion by FASTEST 3D solver is carried out by coupling it with FGM look-up table. The flow chart represented by Fig. 5.4 illustrates the FASTEST3D coupling with FGM table.

5.3 Validation of enthalpy based FGM table

The non-adiabatic FGM look-up tables were proven as an effective combustion modeling tool for academic combustion configurations [66, 136]. The success of chemical lookup tables is the choice of RPV for adiabatic combustion table. In literature recent works can be found which are dedicated for finding the optimized RPV for a given reaction mechanism [141, 87] for adiabatic configuration. An ideal optimized RPV should evolve monotonically from fresh gasses to burnt gasses, such that all thermo-chemical properties for any unique mixture fraction can be tabulated by RPV. The definition of RPV is defined is not unique[87], but more commonly used are combustion of mass fractions or mole fraction of final products, but sometimes also taking intermediate species into account. Here in this work, different RPVs are defined and analyzed. In the present work six definitions of RPV as listed in Table 5.2 are analyzed for tabulating enthalpy based chemistry lookup FGM table. Here firstly, the basic difference between adiabatic and non-adiabatic combustion is presented, followed by the predictability of thermo-chemical properties by RPV. Then species considered for defining RPV are analyzed, and concluded by indicating the performance of different RPVs. Here for this study, two fuels are considered with GRI mechanism [188] including 53 species and 325 reactions and with an 88-species skeletal mechanism with 387 elementary reactions [228] were used for methane and for n-heptane

respectively. N-heptane is considered in addition to methane as it is widely used a fuel in spray combustion. An inlet temperature of 373 K for n-heptane was considered, which is just above the vaporization temperature. This was done in order to avoid the two phase enthalpy change in 1D flame simulations. In order to find the behaviors of combustion in lean, stoichiometric and rich combustion zones ϕ= 0.83, 1.0 and 1.2 were considered for methane, where as for n-heptane only ϕ= 1.0 was investigated. The non-adiabatic FGM tables are constructed with all six RPVs defined in Table 5.2 as a three co-ordinate table in mixture fraction, RPV and enthalpy dimensions. All thermo-chemical data is represented by

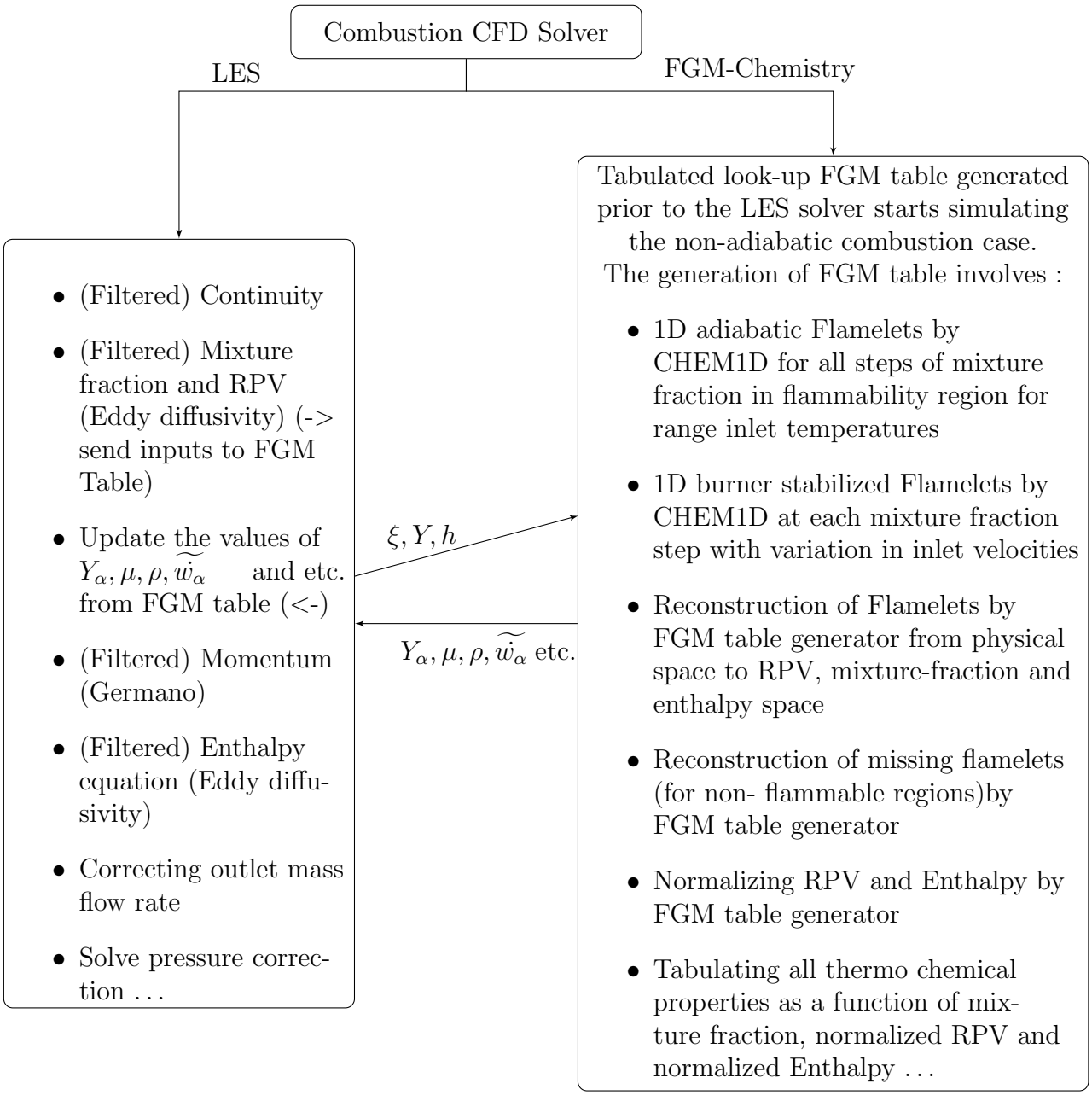

Figure 5.4: LES solver coupling with FGM table for non-adiabatic case

Table 5.2: RPV Definitions

	RPV	
RPV1	$\frac{Y_{CO_2}}{M_{CO_2}}$	
RPV2	$\frac{Y_{CO_2}}{M_{CO_2}} + \frac{Y_{H_2O}}{M_{H_2O}}$	[87]
RPV3	$\frac{Y_{CO_2}}{M_{CO_2}} + \frac{Y_{H_2O}}{M_{H_2O}} + \frac{Y_{H_2}}{M_{H_2}}$	[87]
RPV4	$\frac{Y_{CO_2}}{M_{CO_2}} + \frac{Y_{H_2O}}{M_{H_2O}} + \frac{Y_{H_2}}{M_{H_2}} + \frac{Y_{CO}}{M_{CO}}$	[87]
RPV5	$\frac{Y_{CO_2}}{M_{CO_2}} + \frac{Y_{CO}}{M_{CO}}$	[14]
RPV6	$\frac{Y_{CO_2}}{M_{CO_2}} + \frac{Y_{CO}}{M_{CO}} + \frac{Y_{HO_2}}{M_{HO_2}}$	[14]

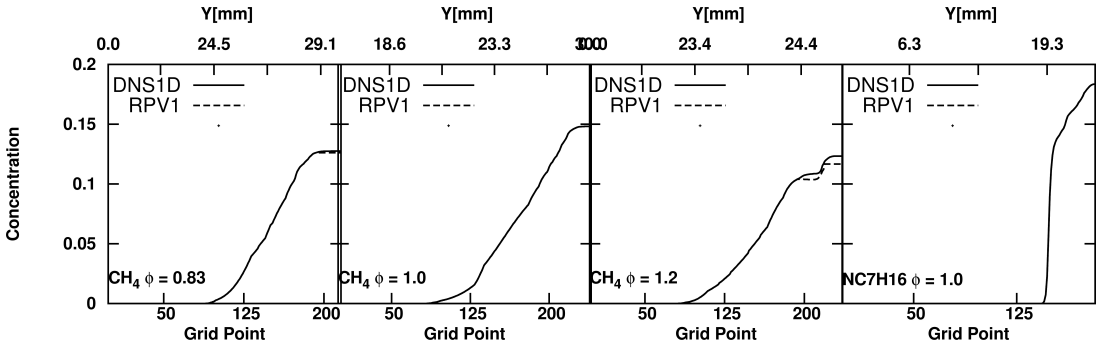

Figure 5.5: CO_2 mass fraction profiles in physical space of grid number obtained from RPV1 based FGM table for methane(ϕ=0.83,1.0,1.2) and n-heptane (ϕ=1.0) and compared wuth 1D DNS Cantera simulations

$$\varphi = \varphi\left(\xi, Y, h\right) \qquad \varphi = Y_\alpha, \mu, \rho, \widetilde{\dot{w}_\alpha} \text{ and etc.} \tag{5.2}$$

The validation is carried for both fuels using 1D DNS calculations with detailed chemistry. Here an independent 1D CFD code Cantera [32] was chosen. Cantera is an object-oriented, open source suite of software tools for reacting flow problems involving chemical kinetics, thermodynamics and transport processes [32, 215, 59]. A wall cooled axi-symmetric stagnation flame at atmospheric pressure has chosen with an inlet velocity of 3.0 m/s, which corresponds to Reynolds number (N_{Re}) 5000 for methane fuel at ϕ=1.0 with fuel inlet diameter of 30 mm. Distance between burner exit to the cooled wall at 600 K is fixed at 30 mm. All four stagnation flames listed in Table. 5.1 were simulated using Cantera, similar stagnation flame studies can be found with Cantera in [215, 59]. Stagnation flames are suitable for this study as the flame is detached from the nozzle and stabilized at the cold wall. This allows the influence of enthalpy loss on the flame front as shown in Fig. 5.1.

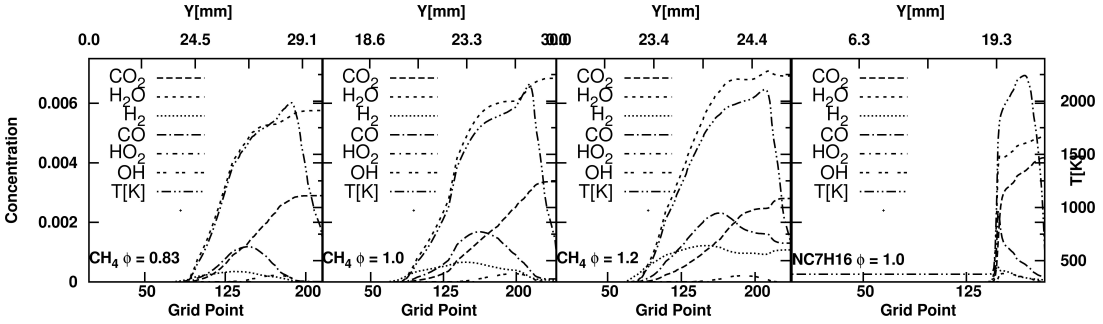

Figure 5.6: Temperature and mass fraction profiles of CO,OH,CH3,H20 in physical space of grid number obtained from 1D DNS Cantera simulations for methane(ϕ=0.83,1.0,1.2) and n-heptane (ϕ=1.0)

Note that for each definition of RPV a complete new FGM table needs to be generated from same set of flamelets. Four different 1D DNS steady state axi-symmetric stagnation flames with detailed chemistry were simulated (see Table. 5.1) with Cantera freeware and differential diffusion effect was taken into account. Each of the simulated 1D case has complete thermo-chemical information at each grid point. The RPV and enthalpy data from the 1D Cantera simulation were taken and normalized with corresponding equilibrium values as given here below for RPV. In its non-dimensional form, the variable enthalpy is defined as

$$H^*(\xi) = \frac{\widetilde{h}(\xi) - \widetilde{h}_{min}(\xi)}{\widetilde{h}_{max}(\xi) - \widetilde{h}_{min}(\xi)} \tag{5.3}$$

and the normalized RPV is defined as :

$$Y^*(\xi, H^*) = \frac{\widetilde{Y}_{CO_2}(\xi, H^*) - \widetilde{Y}_{CO_2 min}(\xi, H^*)}{\widetilde{Y}_{CO_2 max}(\xi, H^*) - \widetilde{Y}_{CO_2 min}(\xi, H^*)} \tag{5.4}$$

where h is the actual total enthalpy resulting from sum of heat of formation and sensible heat, h_{max} the adiabatic enthalpy for specific ξ and h_{min} the enthalpy of the burnt products corresponding to ξ, when brought to ambient temperature T_{min}=298 K. Y_{CO_2}, $Y_{CO_2 min}$ and $Y_{CO_2 max}$ are respectively actual concentration, concentration in fresh gasses and equilibrium concentration of CO_2 for a given mixture fraction and enthalpy. A detailed description of the non-adiabatic FGM table generation can be found in [65], (see also [3, 172, 205]). Both Y^* and H^* were used to access the FGM table for corresponding thermo-chemical data. Now, for each grid point thermo-chemical data is available from 1D DNS calculations and FGM table. This analysis is carried out for all four stagnation flames and for 6 RPVs defined.

CO_2 mass fractions for all four cases were plotted from both DNS simulations and corresposnding data from FGM table in Fig. 5.5. Abscissa at bottom was taken as grid point number (X1) from 1D DNS case to get better insight in the flame front and corresponding physical distance was shown on top abscissa(X2). The species considered for RPV and compared variable was CO_2 in Fig. 5.5. The concentrations of CO_2 from both chemical look table were matching well with the 1D DNS detailed chemistry simulations from Cantera in all four cases considered. Minor deviations were observed for the rich combustion case in non-adiabatic region in Fig. 5.5. (Second from right). CO_2

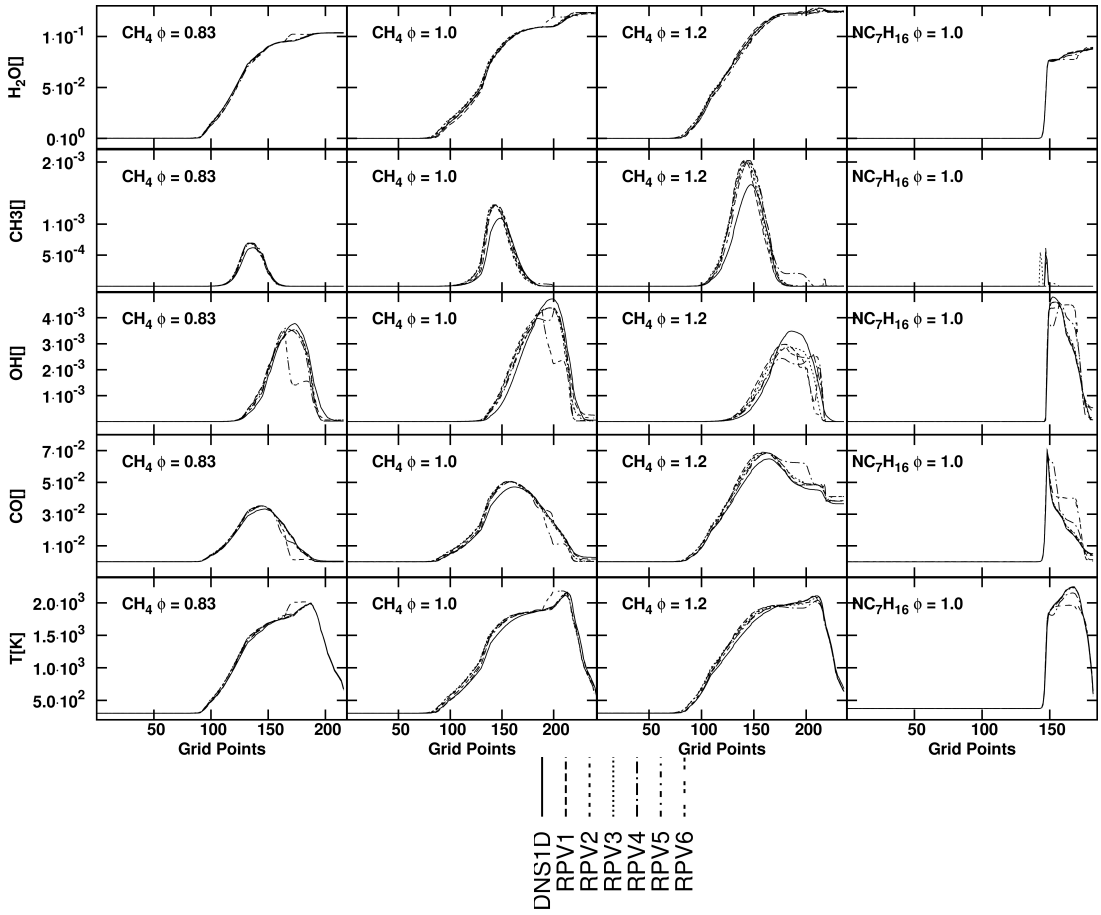

Figure 5.7: Validation of non-adiabatic FGM tabulation: Temperature, mass fraction profiles of CO,OH,CH3,H20 in physical space of grid number obtained from various definitions of RPVs in tabulating FGM look-up table for methane(ϕ=0.83,1.0,1.2) and n-heptane (ϕ=1.0) compared against 1D DNS Cantera simulations

was monotonic in physical space except in rich methane case. Position of flame starting was different in physical space for all methane flames were started around same grid point. The flame brush gradient with respect to grid points was getting steeper in lean regions. Flame starting was taking more grid points at $\phi = 1.0$ before flame accelerating. Flame was starting much earlier in n-heptane case then burning to final products, the conversion was not finished completely even at the cold wall. Maximum conversion was achieved earlier in lean case. Flame was resolved for methane case in around 120 controls volumes (CVs). A step behavior for ϕ=1.0 was observed near the cold wall in conversion to final products. The non-adiabatic combustion was exhibiting different combustion phenomenon in different regions. The non-adiabatic FGM table could capture the DNS results very accurately both trend and magnitude for CO_2 mass fraction, though minor deviations were observed in rich region. These predictions were encouraging as one of the primary species in non-adiabatic combustion was retrieved accurately from FGM table. In many combustion applications very strong stratification occurs. The combustion is very sensitive to equivalence ratio. So, it was very interesting to find the suitable RPV for non-adiabatic configurations. The various species and their combinations are used in defining RPV are listed in Table 5.2. The species in the definition of RPV used are

CO_2, H_2O, H_2, OH, CO, and HO_2 were analyzed together with the temperature in Fig. 5.6. The second ordinate (Y2) on right side in Fig. 5.6 is temperature in K and other axes were same as in Fig. 5.5. In all four investigated cases, CO_2 were monotonically increasing in physical space. Second variable H_2O was increasing monotonically for $\phi =$ 0.83, 1 including a step increase at the wall; but in rich case it was displayed a bumpy nature in the vicinity of the wall.

The concentrations of the intermediate species forming are very minor in the lean combustion and stoichiometric case. CO and H_2 and OH concentrations were in significant concentrations, OH is found to be present only in very few CVs. In rich case both H_2 and CO were not consumed completely and especially H_2 exhibiting partially monotonic nature in physical space. The temperature profiles are plotted to represent the influence of heat loss on different species. Overall CO_2, H_2O, and H_2 showing better monotonic nature than others. Definition of RPV is critical especially in rich regions, so definition of RPV can't be universal in all combustion regions as stratification is very crucial which deliver all three regions of combustions. The chosen combinations of RPV are analyzed in Fig. 5.7.

Profiles from 1D DNS simulations and corresponding values from non-adiabatic FGM table for temperature, selected intermediate species and H_2O are compared for understanding more in detail. This comparison study was carried out for all six RPVs, for both fuels, for $\phi=$ 0.83, 1.0, 1.2. All definitions of RPVs considered were able to capture correct flame starting position, annihilating positions and their thickness of the flame front correctly. Magnitude of the species from FGM table was mainly over predicting for intermediate species. Note that these intermediate species profiles were very different in physical space. The scale of mass fraction for each species was different as shown Fig. 5.7. Temperature profiles were well predicted. Inclusion of CO in RPV definition led to inaccurate prediction of trend and magnitude of various profiles as shown in Fig. 5.7. The values obtained from the FGM lookup table for rich combustion, especially for intermediate species OH were very sensitive to RPV definition. Intermediate species CH_3 from FGM table over predicting, and it was getting more poorer from lean to rich regions. The corresponding temperature profiles, H_2O are agreeing well with 1D DNS calculations. It is interesting to note that formation and annihilation of CH_3 was not being influenced by the enthalpy change in present configuration. Its predictions are encouraging in n-heptane case. RPV1, RPV2 and RPV3 were better combinations for retrieving thermo chemical data from n-heptane non-adiabatic FGM table. The definition of RPV is very vital in tabulated chemistry and more importantly in non-adiabatic combustion. Tabulated chemistry with three co-ordinates of ξ, RPV and enthalpy are suitable for calculating the non-adiabatic combustion problems such as spray combustion, differential diffusion FWI. Non-adiabatic FGM tabulation method adopted in study was able produce very good predictions chemistry and thermal data. In the next section modeling, setup and simulation of a 3D impinging premixed flame water cooled wall was simulated using enthalpy based FGM table.

on mixture

Chapter 6

LES solution procedure

6.1 Boundary conditions

The CFD simulations solve the governing equations through the divergence expressions employed to discretize them. Thus linear systems of equations are solved from the obtained algebraic relations between the unknown values in neighboring control volumes. The boundary CVs don't have any neighbors, which makes it necessary to treat them in such a way that, no additional unknowns are introduced into the linear systems of equations. This is achieved by incorporating the boundary conditions of the physical system under consideration in a appropriate manner into the expressions for the fluxes across the boundary faces. This results in additional contributions to the source term $\acute{b}_P$ of the CV's at the boundary. In addition, the boundary conditions have to be specified in a way that satisfies the overall conservation of all quantities in the computational domain.

The imposition of exact boundary and initial conditions is necessary for a unique solution of the underlying partial differential equations [63]. Boundary conditions are those which are imposed by nature and must be satisfied by every Navier-Stokes fluid. They are at the inlet, outlet, wall, symmetry and periodicitylimit. For transient problems, the initial conditions are also to be defined at the time point $t_0 = 0$s. There are two kinds of boundary conditions. When the specified value is directly imposed on the boundary, it is classified as Dirichlet boundary condition (e.g. inlet, wall) and when the boundary values are presented as gradient forms, they are Neumann boundary conditions (e.g. symmetry or flux boundary).

6.1.1 Inlet boundary conditions

The inlet boundary conditions for the velocity components (momentum) as well as other scalar variables like temperature and concentration are set by means of Dirichlet boundary condition in the LES context. This is the simplest method to deal with the inflow conditions. The value of the unknown is prescribed on each inlet CV face by providing fixed values.

Flow: The inlet boundary conditions for the velocity components (momentum) are set by means of Dirichlet boundary condition. In many industrial applications the flows are turbulent, which means at each cell face in time the velocity will be fluctuating in time. Though the time averaged mean velocity for stationary flows is constant. The

simplest method is Dirichlet boundary condition to deal with the inflow conditions. However this approach can lead to large coherent structures instead of turbulence. This type of treatment neglects the turbulent fluctuations but reasonable if the inflow is far upstream of the area of interest or if all the relevant fluctuations develop inside the computational domain. In other situations, it is necessary to introduce artificial inflow boundary conditions for capturing fluctuations. In principle there is no difference from the point of view of the discretization and the use of the artificial inflow turbulence from the conventional boundary conditions. The method of Klein et al. [108] could be implemented directly into the flow solver or through an external software called the inflow generator. This inflow generator produces three-dimensional frozen turbulence based on the prescribed statistics on a Cartesian grid. This frozen turbulence is then transferred to the inlet plane of the LES calculation using Taylor's hypothesis that turbulent structures are transported with the mean convective velocity of the flow without being altered. Thus, as simulation time advances, the 3D-field produced by the inflow generator is scanned perpendicular to the inflow direction and values for each CV face are obtained by tri-linear interpolation of the inflow data. Since the inflow values obtained in this way do not guarantee a constant mass flow into the domain, the desired mass flow was prescribed in addition and the inflow values were multiplied with a correction factor such that this mass conservation was attained. In the present work turbulent inflow conditions were achieved by implementing a perforated plate in the upstream of inlet nozzle as in experimental setup (see Section 6.5).

Scalars: Various scalars need to be solved in reacting and combustion problems, which is the case here. In this work mainly three types of scalars were used, namely mixture fraction, reaction progress variable (RPV) and enthalpy. The details of how each of scalars were treated are provided here below.

Mixture fraction:is one of the crucial scalar in reacting flows and combustion, which provides great insight into the composition of the fluid at any physical point in the computational domain. The mixture fraction definition is already provided in theory chapter. The mixture fraction at inflow boundary varies between zero and one, depending on the stream composition. Fluctuations in mixture fraction at inlet boundary is not having importance as it remains constant in time at a particular cell face.

Reaction progress variable (RPV): plays a vital role in reactive flows, which gives the progress of various chemical reactions in computational domain. It is in general zero at all inlet boundary faces, except in the case where the part of products are premixed with fresh inlet streams.

Enthalpy:is not significant in isothermal reacting and adiabatic combustion problems. The main reason being, it is not necessary to solve the enthalpy equation. In case of non-adiabatic combustion simulation, the temperature at inlet boundary conditions are supplied, in which enthalpy is being solved. In this work, total enthalpy is solved for accounting for non-adiabatic combustion phenomenon. So, it is necessary to convert the prescribed temperature into the total enthalpy as defined in chapter tabulated chemistry. CFD solver obtains total enthalpy as a function of the temperature from the second FGM table which is separately generated for treating boundaries and applied through

Dirichlet boundary conditions.

6.1.2 Outlet boundary conditions

Outflow boundary conditions are resultant of the inlet, other boundary conditions and the physical phenomenon that takes place in computational domain. So, it is a solution and it is not known a priori and a different type of boundary condition has to be employed than for the inlets. The simplest and most wide-spread way in CFD is the use of a Neumann condition which prescribes the gradient of the solution on the boundary. This gradient in normal direction (n)is usually assumed to be zero, meaning that the value of the unknown Φ in the center of the boundary CV is equal to the value on the face.

$$\frac{\partial \Phi}{\partial n} = 0 \tag{6.1}$$

For the scalar quantities (mixture fraction, progress variable and enthalpy) this condition was employed in all simulations. In LES however, the use of this procedure can lead to the problem by disturbing with large scale structures of vorticies leaving the computational domain. The convective outflow condition for the velocity is an alternative for overcoming the limitation of zero gradients out flow boundary condition. The convective boundary condition implemented in FASTEST3D is given by:

$$\frac{\partial \Phi}{\partial t} + U_c \frac{\partial \Phi}{\partial n} = 0 \tag{6.2}$$

In equation Eq. 6.2, U_c is convective velocity and it should be supplied in prior. The choice of U_c should be approximated and it can be supplied as a profile or as constant global value. Application of conditions Eq. 6.1 or Eq. 6.2 in general does not lead to velocity components on the outflow such that the global mass balance is fulfilled. This is achieved by satisfying the general continuity written here in terms of the sum of incoming and outgoing mass fluxes $\dot{m_{in}}, \dot{m_{out}}$ over all boundaries and the time derivative of density integrated over the domain $\frac{dM}{dt}$ is defined as:

$$\frac{dM}{dt} = \dot{m_{in}} - \dot{m_{out}} \tag{6.3}$$

In treating above relation (Eq. 6.3) a special care must be taken, while the sum of the mass fluxes on the inlet $\dot{m_{in}}$ is known, the mass fluxes on the out flow boundary are taken as provisional values computed from a provisional set of velocities $u^*_{i,out}$ on the outlet after solution of the momentum equations. The outlet velocities are therefore corrected by scaling them according to the equation Eq. 6.4 straight away by satisfying them.

$$u_{i,out} = u^*_{i,out} \left(\frac{\dot{m_{in}} - \frac{dM}{dt}}{\dot{m_{out}}} \right) \tag{6.4}$$

6.1.3 Wall boundary conditions

Velocity components: The velocities in grid nodes conjoined with the wall are set equal to the wall movement. In the frame of this work they are set to zero in the tangential (t_i)

as well as in the normal direction (n_i), because the wall is fixed (Eq. 6.5). This condition is also valid for all turbulent quantities (in RANS context).

$$u_i|_{wall} n_i = 0 \tag{6.5}$$

$$u_i|_{wall} \mathfrak{t}_i = 0 \tag{6.6}$$

In the near wall region a boundary layer is formed and the velocity profile slowly increases until it reaches the outer flow velocity. In order to capture this damping effect, wall functions are available in the FASTEST3D for the velocity components, the turbulent kinetic energy, Reynolds stress components, and the dissipation rate, but not used in the work in LES context. This is valid as the CV sizes are small enough in boundary layer to capture all necessary scales that are relevant for the flow near the wall. In industrial applications it may be necessary to use wall models to avoid huge number of CVs despite the availability of fast and massive computational resources but it is limited for a very few selected cases. The reader interested in the details of wall models in FASTEST3D can refer to the work of Wahid [1].

The mixture fraction, RPV scalars at wall follow the velocity components and their gradient is zero at the wall also in the context of this work where the wall is considered having zero velocity and chemically inert. In the present work, the von Neumann zero gradient boundary conditions are applied for both these scalars. This leads to same physical value of the scalar on the wall to the corresponding value of it in first neighboring CV to the wall.

The enthalpy scalar in adiabatic (or isothermal) case at the wall follow the velocity components and they can not change at the wall similar to mixture fraction and RPV.

The FWI configuration studied here is a non-adiabatic configuration. The wall here is no more follows the zero gradient approach, therefore Dirichlet boundary conditions are applied. As discussed in tabulated chemistry chapter, the fixed temperature is imposed at the wall. The fixed temperature imposed on the wall is converted to total enthalpy utilizing inverse FGM table specifically generated for treating boundaries through the scalar information and temperature boundary values.

6.1.4 Symmetry boundary conditions

Symmetry boundaries can be used to reduce the size of the problem. If we know that there is a plane where the flow field is symmetric then instead of simulating the whole configuration, we can set the appropriate boundary conditions and reduce the problem size. The symmetry boundary conditions are set by following the von Neumann zero gradient boundary conditions.

6.1.5 Periodic boundary conditions

The periodic boundary conditions (between boundary I and II) make the variables at the boundary I equal the variables at the boundary II conforming to the following equation.

$$\psi(\vec{r}) = \psi(\vec{r} + \vec{L}), \tag{6.7}$$

where $\vec{r}$ is the position vector and $\vec{L}$ is the periodic length vector of the domain considered. The periodic boundary condition corresponds to zero flux. Making the boundaries periodic, this will make the inflow through one of the boundaries equal the outflow through the other.

6.2 Solver

Solution of the linear equation system

The discretization of the governing equations summarized in chapter 4 by means of the finite volume procedure and explained together with the applied boundary conditions results in a system of linear algebraic equations each having a form. This system can be written in matrix notation as

$$A\underline{\Psi} = \underline{S} \tag{6.8}$$

where A is the square coefficient matrix [85] built from the coefficients of the linear equations Eq. 4.3 for each CV, $\underline{\Psi}$ is a vector containing the values of the variable Ψ in each CV and $\underline{S}$ is the vector containing the terms on the RHS of Eq. 4.3

The system Eq. 6.8 has to be solved by means of an efficient solution method. The coefficient matrix A resulting from Eq. 4.3 is sparse, i.e. most of its elements are zero and the non-zero elements lie on a small number of well-defined diagonals (in FASTEST-3D seven diagonals). Advantage should be taken from this structure. Since direct methods like Gauss elimination or LU decomposition do not take this advantage, being quite costly, and since discretization errors are normally much larger than the computer accuracy, there is a clear reason to apply an iterative method. Furthermore, the fully implicitly discretized momentum equations are actually non-linear and can not be solved by means of a direct method. The details of their linearization are discussed in the following section. In an iterative method some initial solution is guessed and then systematically improved. One would have after n iterations an approximate solution of Eq. 6.8, $\underline{\Psi}^n$, that is not the exact one. The non-zero residual vector $\underline{r}^n$ (a difference between the left and the right hand side of Eq. 6.8 satisfies the expression

$$A\underline{\Psi}^n = \underline{S} - \underline{r}^n \tag{6.9}$$

An iterative scheme for the linear system, that should drive the residual to zero, can be written as

$$M(\underline{\Psi}^{n+1} - \underline{\Psi}^n) = B - (M - N)\underline{\Psi}^n \tag{6.10}$$

$$M(\underline{\Psi}^{n+1} - \underline{\Psi}^n) = B - (M - N)\underline{\Psi}^n \tag{6.11}$$

or

$$M(\underline{\delta}^n) = \underline{r}^n \tag{6.12}$$

Here, $\underline{\Psi}^{n+1} - \underline{\Psi}^n$ is the correction vector which is simultaneously an approximation to the convergence error. Once the computation of $N\underline{\Psi}^n$ is inexpensive and the solution of Eq. 6.11 converges rapidly the optimal iterative method is found. For rapid convergence in the solution of Eq. 6.11 the matrix M must be as good an approximation to A as possible. For that purpose the *strongly implicit procedure* (SIP) [39], originally proposed by Stone [196] and further developed for the seven diagonal coefficient matrix by Leister and Peric [120], is applied in FASTEST-3D. In this method the matrix M is chosen to be equal to the incomplete LU decomposition (ILU):

$$M = LU = A + N \tag{6.13}$$

In the ILU decomposition the procedure is the same as in standard LU factorization. But for each zero element of the original matrix A a corresponding element of the lower triangular matrix L or the upper triangular matrix U is set to zero too. Even though L and U have the non-zero elements only on the same diagonals as A (W, E, S, N, B, T, P), their product LU has additional non-zero diagonals (SE, NW, *etc.*). Stone [196] found that convergence can be improved by allowing N to have non-zero elements on the diagonals corresponding to all non-zero diagonals of LU. The elements of the matrix N must be defined so that the elements of vector $N\underline{\Psi} \approx 0$ and that the matrix M to be the best approximation to A. This means that the contribution of the terms on the 'additional' diagonals (SE, NW, *etc.*) in N must be nearly cancelled by the contribution of other diagonals (W, E, S, N, B, T, P). Expecting the solution of the elliptic partial differential equations to be smooth, Stone [196] approximated the unknown function values in 'additional' nodes in terms of the known function values at nodes corresponding to the diagonals of A. Finally, one proceeds as follows. Having a matrix A the elements of N can be found. The elements of M, which are the sum of A and N, do not need to be computed. Instead, the elements of L and U are found in sequential order for the given A and N. Once the elements of L and U are known, the inner iterations begin. The system Eq. 6.12 can be rewritten as

$$LU\underline{\delta}^n = \underline{r}^n \tag{6.14}$$

$$U\underline{\delta}^n = L^{-1}\underline{r}^n = \underline{R}^n. \tag{6.15}$$

Using the advantage of LU decomposition the elements of the vector $\underline{R}^n$ are computed first using Eq. 6.15 by marching in the order of increasing CV's index (forward substitution). Then the elements of the correction vector $\underline{\delta}^n$ are calculated by marching in the order of decreasing CV's index (backward substitution). In addition to that the variable values in the CVs are updated following $\Psi^{n+1} + \underline{\Psi}^n = \underline{\delta}^n$. The iterations proceed until the sum over all elements of the residual vector $\underline{r}^n$ becomes lower than prescribed tolerance.

Solution of steady and unsteady problems

In steady computations a steady state solution of the governing equation system is sought. In this case the time history is of no interest. One can either neglect the unsteady

terms in the governing equations or iterate until the steady equations are satisfied, or march in time without requiring full satisfaction of the equations at each time step. The iterations within one time step or during steady computations, in which the coefficient matrices and source vectors in Eq. 4.3 are updated, are called outer iterations in order to distinguish them from the inner iterations performed on the linear systems Eq. 4.3 with fixed coefficients (in the SIP solver). The changes in variables after each outer iteration may be significant and particularly at the beginning where they may cause instabilities. In order to reduce this effect the under-relaxation of the variables is applied:

$$\psi^m = \psi^{m+1} + \alpha_\psi(\psi^m - \psi^{m-1}) \tag{6.16}$$

where ψ^m and ψ^{m-1} are the values of the variable ψ after m^{th} and (m^{-1})st outer iteration, ψ^{new} new is the result of solution of equation Eq. 4.3 and the under-relaxation factor α_ψ satisfies $0 < \alpha_\psi \leq 1$. Wegner [218] presented solution procedure in FASTEST3D for one time step and also reader can refer to Kuenne et al. [113] for substep strategy for the scalar transport applied within a 3-stage Runge-Kutta scheme implemented in FASTSET and used in this work. It is worth noting that, although the converged solution does not depend procedure by solving the equations for the combustion scalars and use their new values to update all transport coefficients and the time derivative of density. Since the latter plays a central role in the momentum and pressure correction equations, it seems to be good to update it as soon as possible. In order to prevent divergence of the outer iterations due to large changes in some of the quantities, the under relaxation technique of Patankar (1980) was employed for the scalars and velocity (Eq. 6.16) and pressure by adding only part of pressure equation [218]. In unsteady computations (URANS, LES) the time accuracy is required in order to resolve in time e.g. some periodical process. In this case the iterations must be continued within each time step until the entire system of the governing equations is satisfied to within a narrow tolerance.

6.3 Time-Averaging Procedure

Simulation carried out by LES produces an instantaneous data in time for all variables that are being solved and also not solved (dependent variables) by transport equations (species from FGM table, algebraically calculated values from solved variables and etc.) at each physical position (x, y, z) of the simulated domain. Engineers are generally interested in statistically time averaged quantities, more ever it is more convenient to compare simulated results against the experimental findings. For obtaining the statistical results, a time-averaging process and a measure for monitoring convergence of the time-average are needed. Supposing averaging has been performed from time t_0 to time t_1, this time-averaging process depends on both the total sampling time interval and the spatial coordinates:

$$\langle \psi\,(x,y,z)\rangle = \frac{1}{(t_1 - t_0)} \int_{t_0}^{t_1} \psi\,(x,y,z,t)\,dt \tag{6.17}$$

The accuracy of the statistical result depends on two parameters namely *time step width* and *time independent sampling*.

Time step width: Similar to the discretization in space, the discretization in time affects accuracy. Normally, reduced time interval allows for an accurate solution, like the smaller cells resulting in improved precision. With explicit methods a limited time step width is thus a precondition to obtain a stable scheme. So called Courant, Friedrich and Levy criteria "CFL-condition" is in general used to evaluate the time interval as defined by equations Eq. 4.25 and Eq. 4.26. This means within one time step, information may only travel to the neighboring cell but no further. In this work CFL <1 (~ 0.3) is chosen for define the time step width.

Time independent sampling: Once simulation starts, we need to decide how often a sampling data has to be read out. The aim is to ensure sampling data to be statistically time independent. This may be clarified by the autocorrelation function. At one special position, the time autocorrelation function $R_A^T(t)$ of a continuous real function $\psi(t)$ is defined by

$$R_A^T(t) = \lim_{\Delta t \to \infty} \frac{1}{2\Delta t} \int_{-\Delta t}^{\Delta t} \psi(\tau)\psi(t+\tau)d\tau \tag{6.18}$$

where Δt is the time interval. The correlation between two events separated in time diminishes as the interval increases. In analyzing statistical results of a spatially developing flow we should average long enough in time to guarantee a proper estimate of the average solution and its physical properties. It is difficult to quantify the criteria. Throughout the simulations in the thesis, the averaging process has always started at time when the flow becomes fully turbulent, and ends at the time when the results presented do not change significantly when the averaging is ended at a later moment in time.

6.4 Parallelization

The majority of simulations carried out here was too large to fit on a normal PC or would have taken too long in doing so, the computations were performed in parallel. This domain (`domain decomposition`) is split up in as many parts as there are processors to run the simulation on. This is conveniently done via the block-structure of the grid, simply assigning each block to a processor and /or sometimes distributing same block onto multiple processors (see Fig. 6.1). In doing so, the geometrical blocks created in the grid-generation process can be subdivided into several parallel blocks which can help to achieve better load-balancing. Note that, when a same block in distributed onto n number of processors, then that block is divided into the number of processors on which it being simulated. In the solution procedure, the unknowns have to be exchanged between the blocks. This is done via message passing using the well-known MPI library. The data are provided to the other block by a row of help control volumes called ghost cells. This code has been already used to study numerically a series of laboratory classical flames and generic combustors fueled by methane, pre-vaporised kerosene for single phase cases ([241, 218, 238, 113]), as well as acetone and ethanol for spray cases (e.g. [40]) using FGM method for combustion. Computations reported in the present paper were carried out for three flow troughs prior to collecting of statistics and four flow troughs

Recommended

```
### processor info
1 1 1 : 1          ;proc. in i, j, k dir., new processor (block 1)
1 1 1 : 2          ;proc. in i, j, k dir., new processor (block 2)
1 1 1 : 3          ;proc. in i, j, k dir., new processor (block 3)

### processor info
1 1 1 : 1          ;proc. in i, j, k dir., new processor (block 1)
1 1 1 : 1          ;proc. in i, j, k dir., new processor (block 2)
2 1 1 : 2 3        ;proc. in i, j, k dir., new processor (block 3)
```

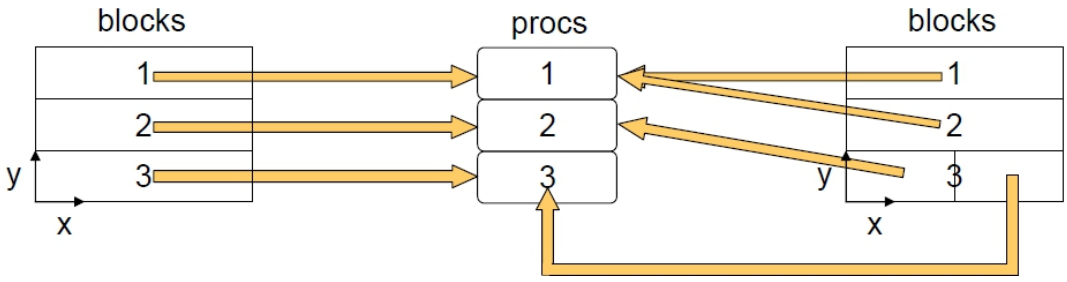

Figure 6.1: Recommended parallelization of block structured mesh in the FASTEST3D [115]

for obtaining time averaged values.

6.5 Study of boundary conditions in perforated nozzle

An analysis was carried out to analyze the difficulty in bringing real physical boundary conditions in experiments into the numerical setup [183]. It was explained in the previous section that the boundary conditions are very crucial in numerical calculations, where the calculation domain is limited contrary to its experimental/real physical domain. The capability of CFD tools and methods can be enhanced by providing correct boundary conditions. Especially the complex CFD model development, validation and verification for physical processes such as combustion require more accurate boundary conditions. The application of a perforated plate to generate turbulence in the nozzle for combustion experiments is one of the common practices to generate turbulence. It was found from various numerical studies [195, 243] the Reynolds number conditions supplied from the experiments [19, 186] could not produce the corresponding measured velocity fields. The attempt was made to find the reason behind the difference between the measured and numerical results velocity fields for same Reynolds number [183]. Here the generation of mesh for perforated plate was carried out by more convenient and suitable unstructured mesh. The commercial multi physics and geometric flexible CFD software [8] was used for this investigation.

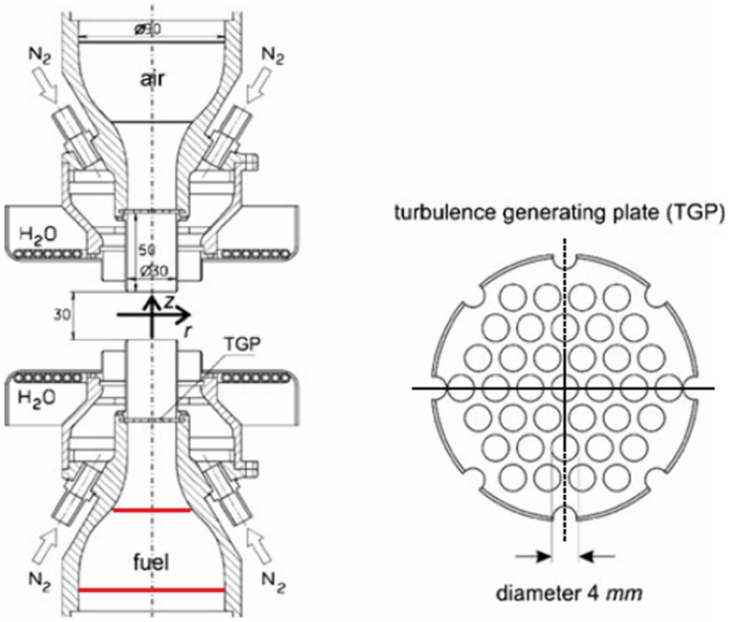

Figure 6.2: Opposed jet configuration including the perforated plate(TGP): Red line indicated mesh used for reducing the boundary layer and for obtaining uniform flow in the upstream of the TGP

Configuration: The configuration used here was the nozzle part flow from the Pantangi et al. [243]. For this study, experimental boundary details were adapted from Boehm et al. [19]; as the detailed measurements were available within the nozzle. The study is carried out for both opposed jet (see Fig. 6.2) and single jet non-reactive flows, various Reynolds numbers, considering plenum part and meshes in plenum. In all cases the inlet flow boundary was placed far away from the turbulent generator (perforated plate (see Fig. 6.2)) in the upstream direction. In depth study was carried out assuming the measurements from experiment were accurate. CFD model was setup with available inputs from experimental measurement for inlet boundaries to determine flow field to validate, verify the model and thereby predicting the flow field. Flow field velocity and their fluctuation predicted by CFD solver couldnt match with the measured data. This is done to reveal the possible erroneous set up of the numerical setup (see also [183]). Any valid physical or numerical evidence couldnt be established for quantifying difference between measured and predicted flow profiles. This leads to the possibility of the methods adapted for determining the Reynolds number from the flow meters data and analytical methods in measurements as a rationale. The advanced measuring methods were in general were used only in the main combustion field. Therefore, corrected boundary conditions which were measured by conventional methods may be not appropriate for using in the development of precise CFD model development.

Effective diameter: the boundary conditions can be supplied by means of artificial turbulence for this configuration or by implementing all geometrical features of the configurations. In both cases it is necessary to get minimum details from the experiment and then they can be adapted. The methods here adapted were to take all possible geometrical features into the numerical setup. This is not always possible with all solvers such as FASTSET3D, which is based on block structured mesh solver. In order to use the

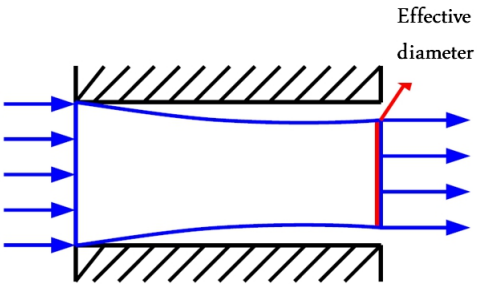

Figure 6.3: The representation of boundary layer development and effective diameter at the exit of TGP plate

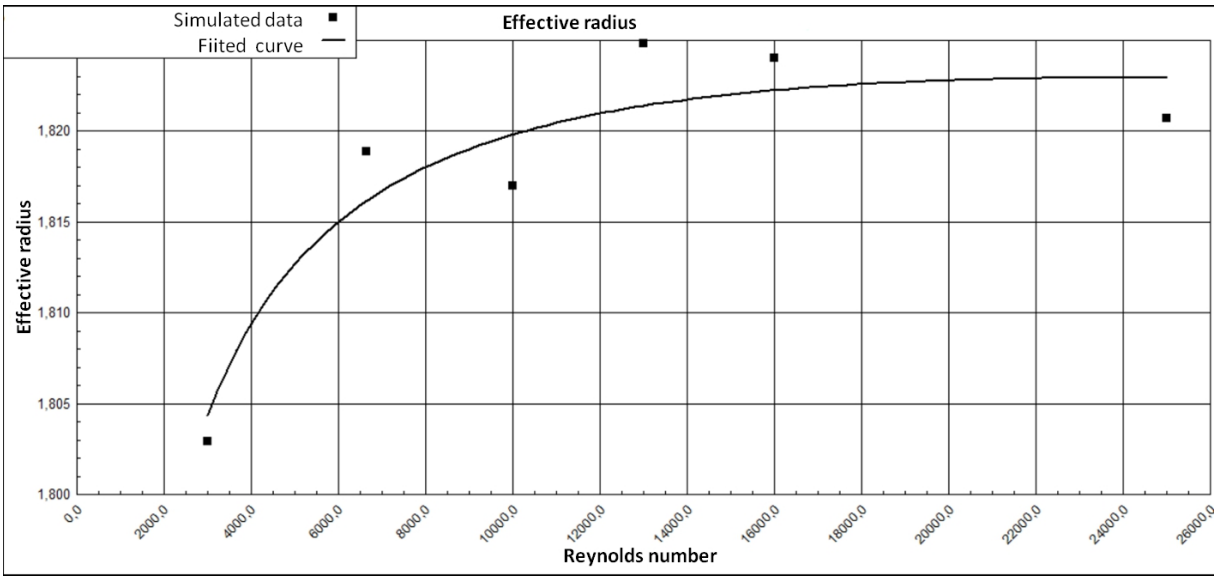

Figure 6.4: The effective hole diameter calculated as function of Reynolds number for the single jet flow

original features in block structured mesh solvers and also to avoid the complex meshing of numerous small holes; a study is carried out to find the effective diameter at the exit of the perforated plate (TGP).

The perforated plate considered here is having many holes with a 2mm radius each. The effective radius is plotted in Fig. 6.4 show the strong boundary layer formation within $\sim$ 1.65 mm thickness of TGP plate at lower Reynolds numbers. The boundary layer is getting thinner parabolically as the Reynolds number is changing from 3000 to 16000 and then boundary layer is remaining almost constant for higher Reynolds numbers.

Applications

Chapter 7

Combustion processes of complex fuels

In this work LES code was developed as detailed in the previous chapters to describe the mixing in reactive flows and non-adiabatic combustion physics more precisely taking advantage of advanced sub-grid scalar flux models and non-adiabatic FGM tables.

Developed models were validated for reactive sub grid scalar (SGS) mixing, non-premixed, premixed combustion in both adiabatic and non-adiabatic configurations. In this chapter, LES based non-adiabatic combustion models are applied for two complex combustion configurations namely rod-stabilized V-flame and pre-vaporized kerosene. First a SGS sub-grid scalar flux model is validated for premixed V-flame configuration while the FGM combustion model is extended to complex fuel pre-vaporized kerosene. These results are reported in [238, 241].

7.1 Premixed combustion of rod stabilized V-flame

A V-shape flame is generated when a premixed flame is stabilized on a hot wire or a rod [207]. In a laminar flow environment, the reaction layer propagates against the incoming fluid and a premixed V-shape flame is built. In the case of a turbulent flow, the two wings of the flame are wrinkled by velocity fluctuations and the V-flame is obtained in mean. Hertzberg et al. [81] had demonstrated that vortex shedding accompanied by high periodic fluctuation intensities stabilizes the lean to very mild bar and rod stabilized premixed flames but not evidently for a richer rod-stabilized case. Recently Domingo et al. [53] have pointed that the flame stabilized by the rod could take benefit from the recirculation of hot products behind the obstacle, while the flame stabilized on a hot wire is initiated by the energy released by the wire. Thereby localized burning kernel serves to stabilize a premixed flame that develops downstream. Besides 2D DNS [53] and 3D DNS [15] calculations for low Reynolds number configurations, LES of V-flame are very rare. Manickam et al. [130] applied an algebraic flame surface wrinkling model to study rod stabilized flames. They compared the performance of a RNG k-Epsilon RANS model and LES applying a standard Smagorinsky using the commercial code Fluent [67] to address the flow past the rod cylinder along with the effects such as vortex shedding, lift and drag forces. The SGS scalar flux has been described by a classical linear gradient approximation.

In the literature sub grid-scale (SGS) model assessment was mainly achieved through comparisons with Direct Numerical Simulation (DNS) results limited to low Reynolds numbers. Based on a comprehensive, highly resolved experimental database of SGS and mean scalar field quantities [127, 154], an assessment of a new anisotropic SGS scalar flux model is carried out in a non-reacting free jet and a rod stabilized premixed methane V-flame configuration characterized by high Reynolds numbers for which DNS-data are not available. For that purpose, Large Eddy Simulations are performed using the dynamic Smagorinsky SGS model for the flow field. The new anisotropic SGS scalar flux model used to describe the turbulent scalar flux combines the conventional linear eddy diffusivity model with an additional contribution that couples in a thermodynamically consistent way the deviatoric SGS stress tensor and the gradient of the filtered scalar field. The combustion is modeled by a detailed tabulated chemistry based method following the flamelet generated manifold (FGM) approach. To assess the prediction capability of the anisotropic SGS scalar flux model, LES achievements are compared against the highly resolved experimental data available and other simulation results performed under use of existing SGS scalar flux models. The behavior of SGS scalar fluxes is especially analyzed. It turns out that the new anisotropic model retrieves the overall expected features of the SGS scalar fluxes at both resolved and SGS levels and in both non-reacting and reacting premixed environments. It also allows achieving LES results for the flow and scalar field that are in better agreement with experimental data.

7.1.1 Configuration and boundary conditions

The configuration under study corresponds to that experimentally investigated by Pfadler et al. [127, 154] who carried out experiments with a rod stabilized flame at atmospheric pressure. Here, perfectly premixed fuel and air are supplied to 48 mm diameter tube, where 10 mm above the exit a 1.6 mm rod is situated for flame stabilization. A 150 mm diameter co-flow with low velocity of 0.3 m/s prevents environmental influence in the measurement region. A turbulence grid with hexagonally oriented holes being situated 100 mm upstream of the exit produces nearly homogeneous turbulence conditions. The burner set up and geometry is sketched in Fig. 7.1.

Two-dimensional instantaneous velocity information can be obtained with particle image velocimetry (PIV). For that the flow field is seeded with small tracer particles (TiO2, d_{mean} = 1 micrometer), which follow the turbulent flow adequately. Stereo PIV measurements of all three velocity components in the measurement plane were possible with two PIV cameras. For the measurement of the three-dimensional rate-of-strain tensor, a dual plane approach was used, consisting of two complete stereo PIV systems. The details of the complex system (synchronization procedure, data storage, validation and evaluation) are described by Pfadler et al. [127, 154, 152].

The flame characterized by Reynolds numbers of 10,188 is investigated here. All the flame parameters are summarized in Table 7.1. For representing this geometry numerically, the turbulence grid with circularly oriented 86 holes was included in the computational domain (see Fig. 7.2 along with the pipe (see sectional view in Fig. 7.3).

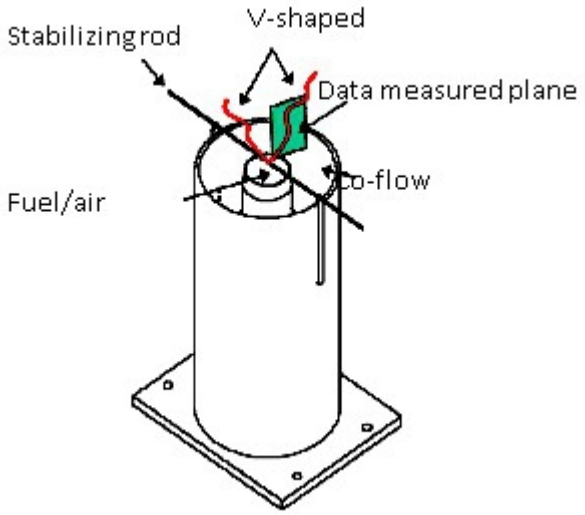

Figure 7.1: Burner set up

Description of parameter	Unit	Details
Fuel mixture	Methane& air	Stoichiometry 0.8
Bulk velocity	$U\,[m/s]$	3.50
Turbulent rms velocity	$U^{'}\,[m/s]$	0.55
Reynolds number	$Re\,[--]$	10,188
Turbulent Reynolds number	$Re_t\,[--]$	148
Unburnt density	$[kg/m3]$	1.10
Burnt density	$[kg/m3]$	0.17
Laminar burning velocity	$S_L\,[m/s]$	0.27

Table 7.1: Boundary conditions

This consists of 206 structured blocks featuring an O-type structure. The total amount of grid points on the fine grid is 1.3 million. The block structured mesh was constructed with ICEMCFD [67, 8] and elliptical smoothening is carried out on it for getting better convergence. All simulations were ran on 8 processors. The domain is extended with coarse mesh radially beyond co-flow region to accommodate numerical instabilities due to the limitations of availability of pressure boundary conditions at outlet.

As inlet boundary conditions, the mass flows from the experiment were prescribed using laminar unperturbed profiles. A laminar inlet profile is sufficient for such a simulation since the flow field is dominated by the intense shear of the jets produced by the turbulent grid at upstream. The co-flow air stream was assumed to be homogeneous. Again, a constant mean value was prescribed for the velocity of 0.3 m/s. Thickness of 1 mm for the nozzle separating the fuel jet and the co-flow is considered as in experiments. Mixture fraction of fuel at fuel inlet is specified as 0.0445, which corresponds to the premixed methane fuel (stoichiometry of 0.8), and for co-flow as zero. Outlet boundary

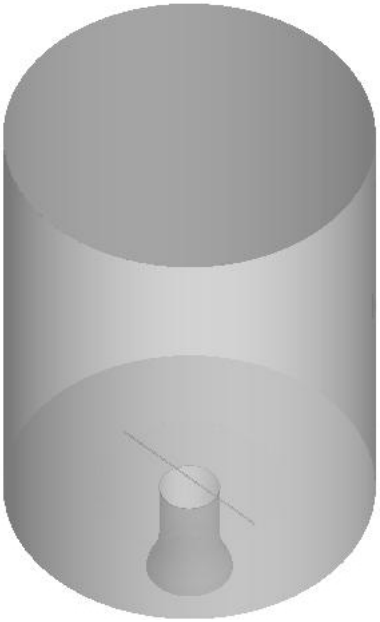

Figure 7.2: Simulated domain with nozzle and flame stabilizing rod

at top is given as convective boundary and other regions with open boundaries are described as slip wall with zero velocity.

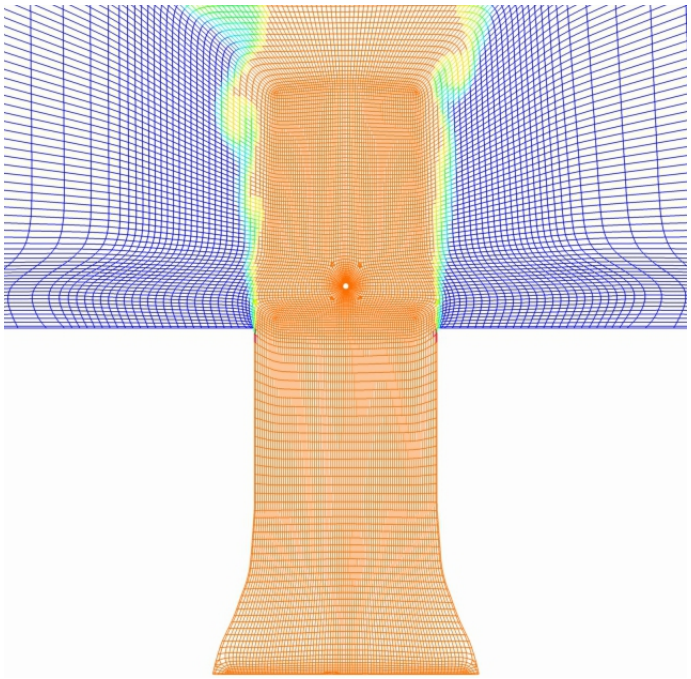

Figure 7.3: Representation of mesh on a plane across the stabilization rod and passing through centre line of the nozzle with super imposed by instantaneous mixture fractip

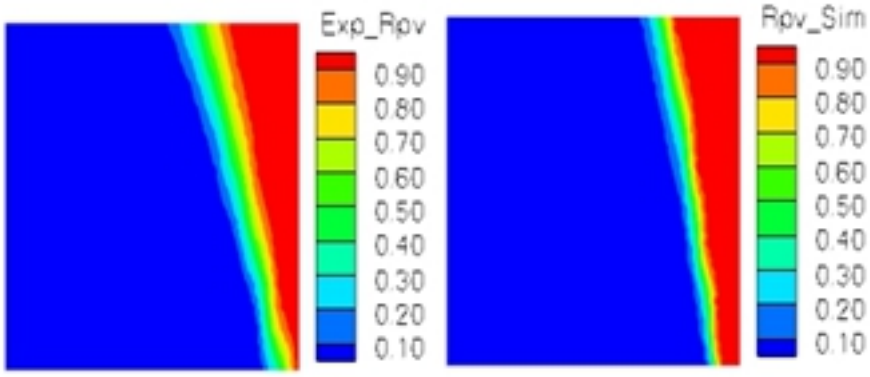

Figure 7.4: Experimentally measured reaction progress variable (left), numerically obtained reaction progress variable (right)

7.1.2 Results and discussions

First a qualitative insight will be given before going to quantitative comparisons. Experiments measured the temperature as progress variable and in FGM based approaches the RPV is based on the concentration of specie(s). Temperatures and other species (like CO, OH, CO2 and etc) concentrations are obtained as only a post process variable from beta integrated FGM table rather than a transported quantities. The experimental measured area (EMA) data is available on one side of the V-flame, reaching from the axis to a radius of 17 mm and in height from 4.5 to 22.5 mm above the stabilization rod (see Fig. 7.1). All field data from simulations are compared against experiments in the EMA region until otherwise it is specified. The time averaged reaction progress variable based on temperature in both experiment and simulations plotted in Fig. 7.4 shows the well predictability of the model used. Here it is worth mentioning that the flame front from Fig. 7.4 is away from the mixing zone (in Fig. 7.2, Fig. 7.3) between co-flow and main fuel jet, which clearly points out that the co-flow is not influencing the flame behavior in the vicinity of the stabilization rod. Iso-surfaces of instantaneous temperature gradient shown in Fig. 7.5 (left) clearly predict that the flame is stabilized on the rod and the V-shape of the flame is recovered well. It shows in addition the highly turbulent nature of the flame front. The instantaneous RPV source term, which is being used in simulations are plotted in Fig. 7.5 (left), outlines the reaction zone of the flame. This reaction zone is very thin which makes the combustion modeling very challenging as the fuel is transformed completely from burnt to un-burnt within a control volume. So, it may be very interesting to see the models for the sub-grid scales in detail as discussed later in this section.

With respect to quantitative predictions, the mean axial and radial velocity profiles at 2 mm downstream from the nozzle exit are plotted; Fig. 7.6 recovers well the experimental data provided as inlet conditions. To get further overview of the model capability and more insights into the predictions of SGS quantities, flow and combustion properties such as mean axial and radial velocities, normalized RPV and their fluctuations as well as axial and radial SGS fluxes in the EMA region are plotted in Fig. 7.7. For an easier interpretation of the results, let us mention that FGM model solves absolute reaction progress variable whereas experimental data is available as normalized temperature based RPV. To bring similarity between them RPV from simulations are

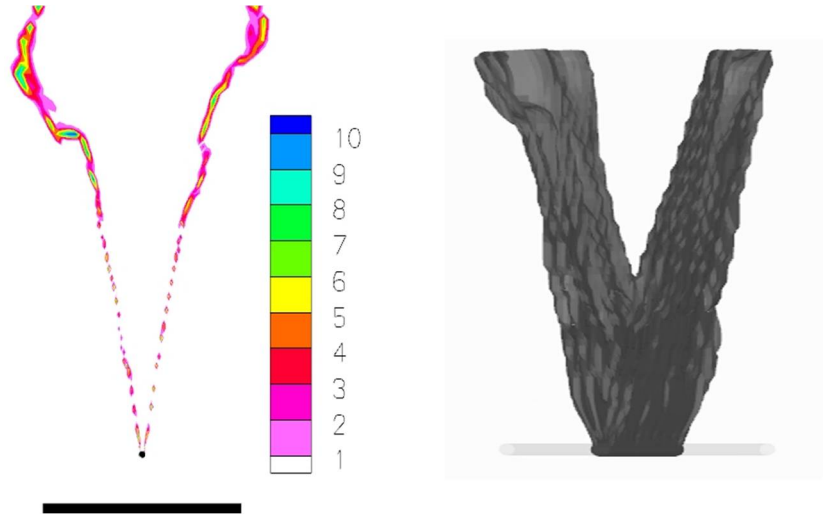

Figure 7.5: Reaction progress variable source term (left) and Temperature gradient (right)

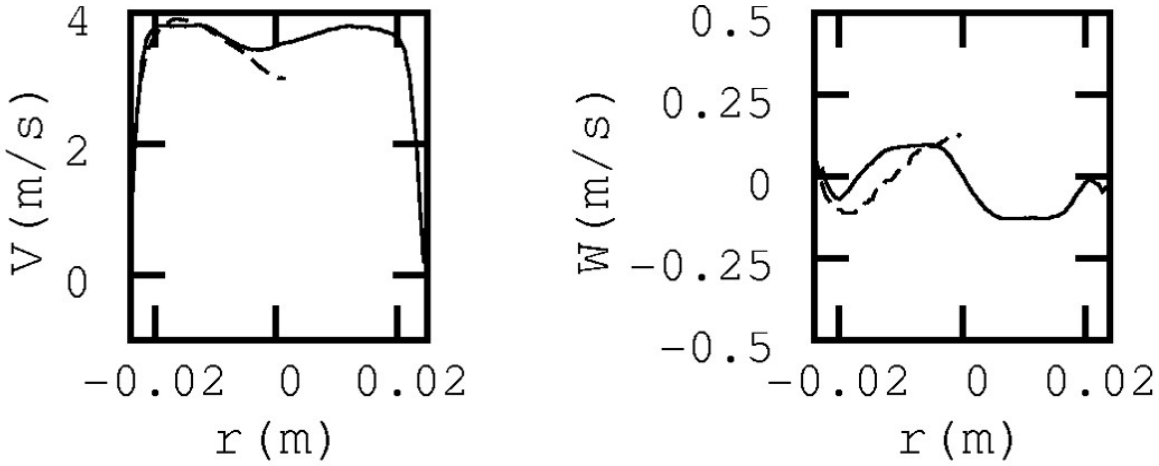

Figure 7.6: Comparison of measurements against numerically obtained corresponding data: Axial velocity(left), right: radial velocity (right) (Num-solid line, experimental-dashed line)

normalized based on equilibrium value corresponding to mixture fraction values. Since the reaction zone is very thin in this configuration and Lewis number is unity for the fuel under investigation, it can be assumed that both RPV from experiments and simulations are comparable, and an assessment of the model capability is thus possible. If the model predicts perfectly the experimental findings, then all points should fall on 45^o line. As they deviate from that line model prediction capability goes down. Note that each point on the scatter plot corresponds to one measurement (and numerical).

Measured axial mean velocities in the EMA region are very well captured by model except at lower velocity values. Similar deviation can be found at higher axial and radial velocity fluctuations, but they are much higher compared to that of mean velocities. Mean radial velocities are well predicted, their fluctuations deviate strongly, and again at higher velocities simulations are under predicted. These deviations, among others can be attributed to the laminar fuel inlet boundary conditions used since the turbulence

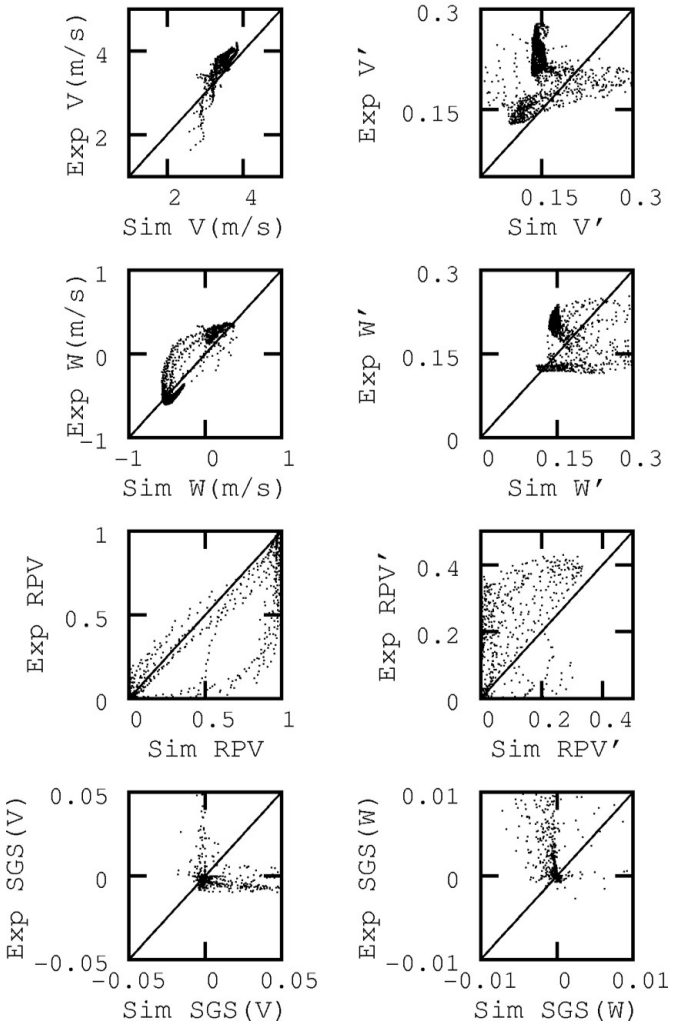

Figure 7.7: Comparison of numerical simulations (x-axis) against experiments (y-axis) in form of scatter plots : First from top: Axial velocity (left)Axial velocity locations(right), Second from top: Radial velocity (left) Radial velocity fluctuations (right), Third from top: RPV (left) RPV fluctuations (right), Bottom: Axial SGS fluxes(left) and Radial SGS fluxes(right)

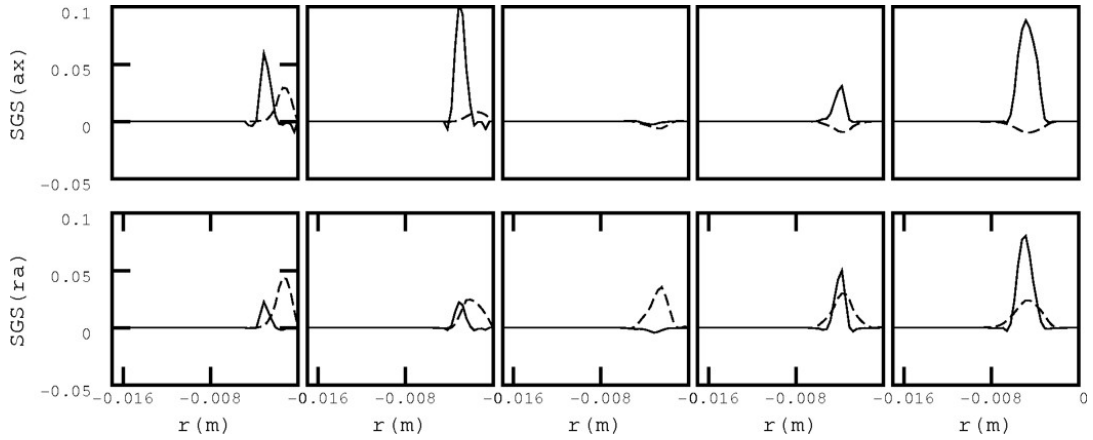

Figure 7.8: Comparison of axial (top) and radial (bottom) SGS flux experimentally measures (dashed line) against the numerically obtained (solid line) at four different locations above the flame stabilization rod

generated by shear alone is not sufficient to capture the whole EMA range.

The FGM based CFD model predicts the reaction zone in a reasonable agreement within the EMA region, though in few EMA locations the model delivers over predictions. Similar and opposite trends are also observed in RPV fluctuations.

To assess the used classical eddy viscosity SGS scalar flux model, a comparison of the axial and radial scalar fluxes are carried out. It turns out that axial and radial SGS fluxes are comparable only when they are very small, Otherwise large deviations are observed. These deviations of numerical predictions can be linked to flow field and (or) combustion field predictions. It is worth mentioning that the thickness of the flame is influenced by sub grid scale fluxes, and it is very much important especially in the context of premixed combustion and variable turbulent Schmidt number to concentrate on this aspect.

In Fig. 7.8 radial profiles of axial and radial SGS fluxes are plotted and compared against experimental data at four upstream locations 17.9 mm, 19.4 mm, 23.1 mm, 26.07 mm and 30 mm from exit of nozzle respectively. Though scatter plots show great deviation in predicting SGS fluxes, comparison on radial profiles gives better comparability. The trend and peak locations of SGS fluxes are either shifted or predicted in opposite way, and the absolute values do not agree with experimental findings. This clearly demonstrates the weakness of the linear diffusivity SGS scalar flux model in predicting scalar transport and mixing within reaction zones in which anisotropy processes strongly affect the behavior of the flame. To improve the prediction capability, new models need to be integrated as suggested by Sadiki et al. [176, 86].

7.1.3 Combustion modeling with advanced SGS scalar flux models

Three different SGS scalar flux models (the standard eddy diffusivity model (EDM), the Clark model [41] and the new anisotropic model) are evaluated on the V-Flame methane-air premixed combustion configuration. In Fig. 7.9, correlations from the EDM, Clark and Anisotropic model are plotted against the experimental data. This analysis was discussed in more detail by Pfadler et al. [127, 154, 152]. The EDM model fails for the description of the SGS scalar flux in the investigated flame while the Clark model shows a totally different behavior. Even though, the sign of the SGS scalar flux is mostly fitting in all cases, the model predicts too low flux values. For the anisotropy model the linear gradient diffusion term seems to be dominant, leading to a slight strong deviation between model and directly measured scalar flux. The second term in the anisotropic model is evaluated separately. It behaves relatively better than the Clark model with the chosen fixed pre-constant.

This result underlines the importance of the third contribution term in Eq. 3.48 that was not accounted for in Eq. 3.51. This term, that clearly includes the scalar dissipation rate into the model, is expected to balance the influence of the linear gradient term. Its role has to be investigated in more details in future works.

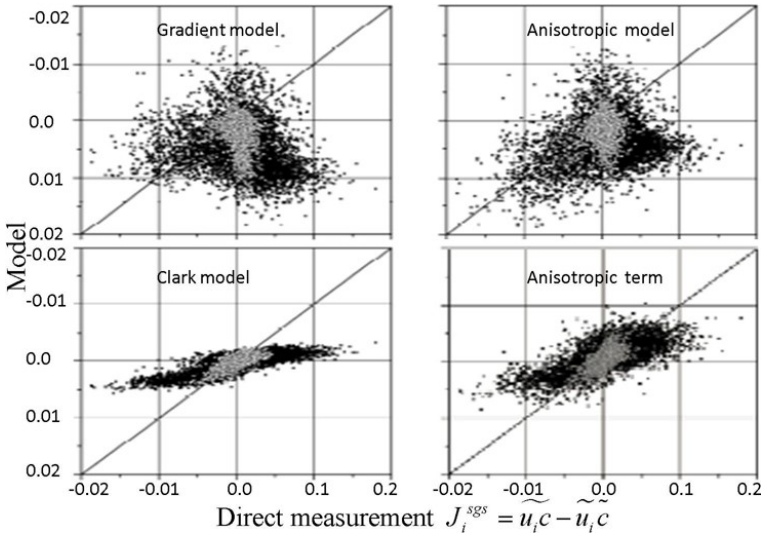

Figure 7.9: Correlation plots between directly measured SGS flux (x-axis) and modelled SGS-flux (y-axis, with different analytical models). Diagonal line indicates perfect correlation. All fluxes are in m/s. Gray symbols: < 0.5 (< 0.13), black symbols: > 0.5 (> 0.13) [127, 154, 152]

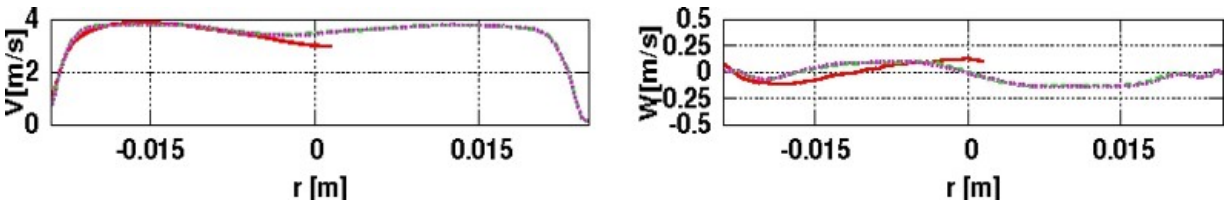

Figure 7.10: Time averaged mean axial (left), radial (right) velocity. Experimental results(.....), EDM (.....), Dynamic EDM (.....), Anisotropic (.....) at y = 0.002 m

Numerical results obtained by applying the EDM and the anisotropic model are now analyzed and compared against experimental data available. First insight on the capability of the models under consideration in predicting the flow field is demonstrated, before discussing the combustion and SGS scalar flux fields' predictability. Radial profiles of velocity are available only at one location in the domain at 2 mm downstream from the exit of the nozzle. The radial velocity profiles of mean axial and mean radial

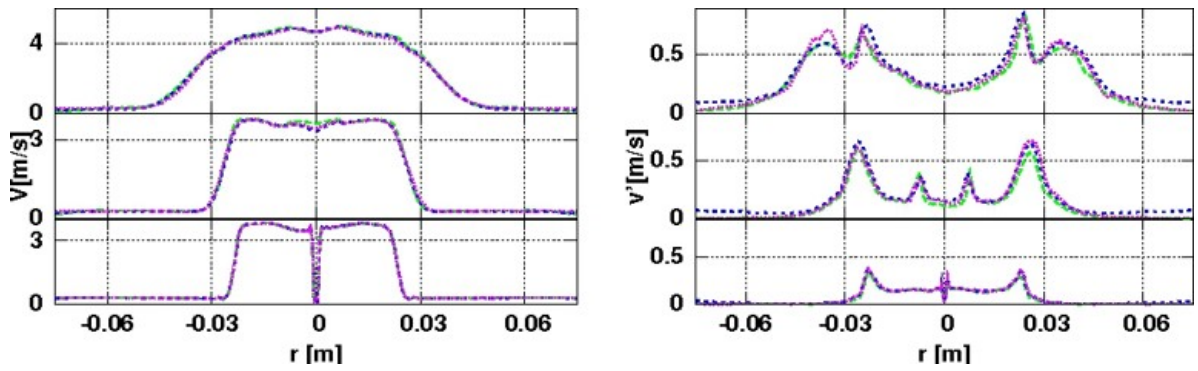

Figure 7.11: Time averaged mean axial velocity (left); fluctuations (right) EDM (.....), Dynamic EDM (.....), Anisotropic (.....) at y = 0.012 m (bottom), y = 0.05 m (middle), y = 0.1 m (top)

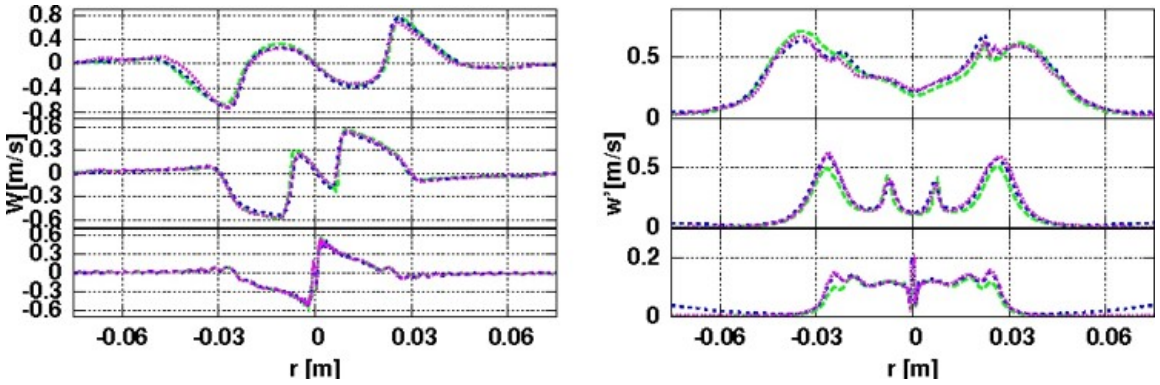

Figure 7.12: Time averaged mean radial velocity (left); fluctuations (right) EDM (.....), Dynamic EDM (.....), Anisotropic (.....) at y = 0.012 m (bottom), y = 0.05 m(middle), y = 0.1 m (top)

velocities are compared against the experimental data in Fig. 7.10. All models could allow capturing the experimental data well. Radial velocity profiles of mean axial, mean radial velocities and their fluctuations obtained from three models are compared against each other at 0.012 m (just above the V-flame stabilization rod), 0.05 m and 0.1 m downstream locations from the exit of nozzle in Fig. 7.11 and Fig. 7.12. The SGS scalar flux model does not influence the flow field directly, though it can alter flow field due to the density dependency. In Fig. 7.11 (left-bottom), axial velocities at 0.012 mm from the exit of nozzle in the downstream show that stagnation zone above the rod is formed, which is crucial for flame stabilization. Stagnation zone formed above the rod is very thin and in the order of one millimeter. All three models could capture well this stagnation zone. The temperature of the flame stabilization rod is not important in stabilizing the flame. To capture well these phenomenon total 25 nodes were placed on the circumference of the flame stabilization rod. Stagnation zone in the downstream at y = 0.05 m (left-middle) and y = 0.1 m (left-top) are disappeared. Though all models are predicting axial velocities in agreement with other models, the anisotropic model estimated the slower disappearance of stagnation zone at y = 0.05 m over others. From Fig. 7.11 (left-top) it is evident that the fuel jet started spreading out at y = 0.1 m. Axial velocity fluctuations are shown in Fig. 7.11 (right). In all three locations two main peaks are observed, one at the shear layer between the fuel jet and co-flow and in the other at the flame front. In other locations axial velocity fluctuations are small. It can also be observed that shear layer and the flame front are very close to each other at y = 0.1 m. Magnitudes of axial velocity fluctuations are found to increasing downstream from y = 0.012 m to y = 0.05 m. In general all three models are predicting the axial velocity and its fluctuations similarly.

Radial velocity and its fluctuations are having similar behavior like axial velocity component (see Fig. 7.12). Maximum radial velocity in the flame zone is found at centre in upstream region and is moving away from centre in downstream. Non-zero radial velocities are found at radial distance greater than co-flow radius at y = 0.1 m predicting the spread of fuel jet radially. Though all three models are predicting similar profiles, predictions from EDM are marginally different. In particular, the radial velocity fluctuation, which is crucial in determining the flame thickness, is predicted differently by the EDM.

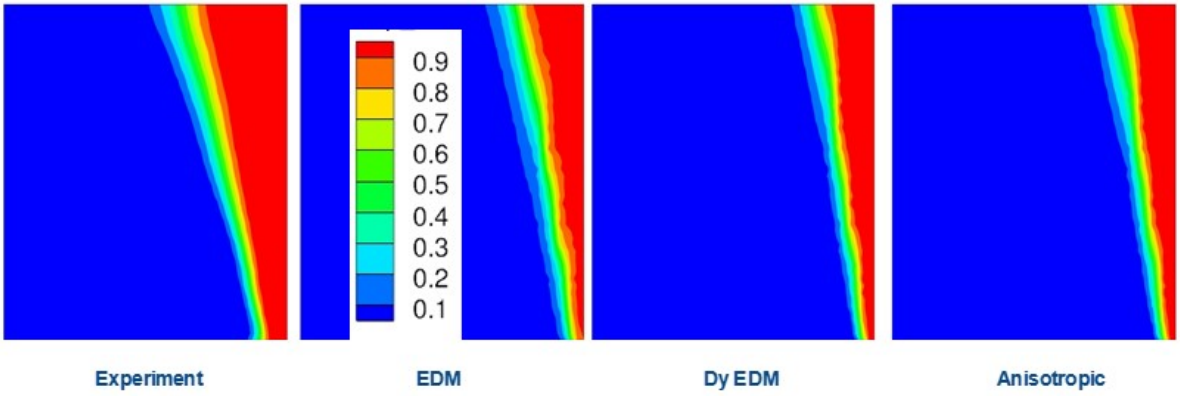

Figure 7.13: RPV from Experiment (left), Eddy diffusivity model (second from left), Dynamic eddy diffusivity model (third from left)anisotropic(right)

In the experiments temperature is measured as the progress variable and in FGM based approach the RPV is based on the concentration of specie(s). Temperatures and other species (like CO, OH, CO_2 and etc) concentrations are obtained only as postprocess variables from the beta integrated FGM table rather than as transported quantities. The detailed experimental data in the experimental measured area (EMA) is available on one side of the V-flame, reaching from the axis to a radius of 17 mm and in height from 4.5 to 22.5 mm above the stabilization rod. The time averaged reaction progress variable derived from temperature in both experiment and simulations plotted in Fig. 7.13 shows the well predictability of the model used. Here it is worth mentioning that the flame front from Fig. 7.13 is away from the mixing zone between co-flow and main fuel jet, which clearly points out that the co-flow, is not influencing the flame behavior in the vicinity of the stabilization rod. All models are shown similar flame angle and location as in experiments. The anisotropic model and the dynamic EDM achieve better flame prediction especially near the flame stabilization rod. Iso-surfaces of instantaneous temperature gradient in Fig. 7.5 (right) clearly show that the flame is stabilized on the rod and the V-shape of the flame is recovered well. The highly turbulent nature of the flame front can also be observed. The instantaneous RPV source term which is plotted in Fig. 7.5 (left), outlines the reaction zone of the flame. This reaction zone is very thin and makes the combustion modeling very challenging as the fuel is transformed completely from unburnt to burnt within a control volume. So, it is very interesting to investigate the models for the sub-grid scales of mixing transport in detail as discussed later in this section.

To get further insight of the model capability the radial profiles of mean combustion properties such as temperature, temperature fluctuations, reaction source and reaction source fluctuation are plotted in Fig. 7.14 and Fig. 7.15. Temperature profiles allow locating the flame position. Fig. 7.14 shows the thickness of the temperature profile getting thicker along the downstream direction of the domain, which characterizes the V-flame shape. Maximum temperature for this configuration is about 2000 K. The temperature is suddenly jumped from inlet fuel jet temperature to the adiabatic flame temperature in about 1 mm as seen in Fig. 7.14 (left). All three models under

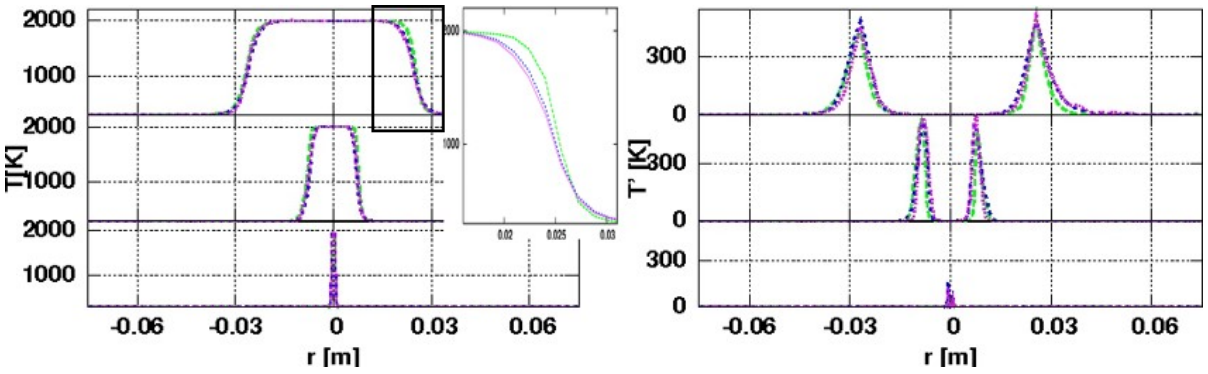

Figure 7.14: RPV from Experiment (left), Eddy diffusivity model (second from left), Dynamic eddy diffusivity model(third from left) Anisotropic model(right)

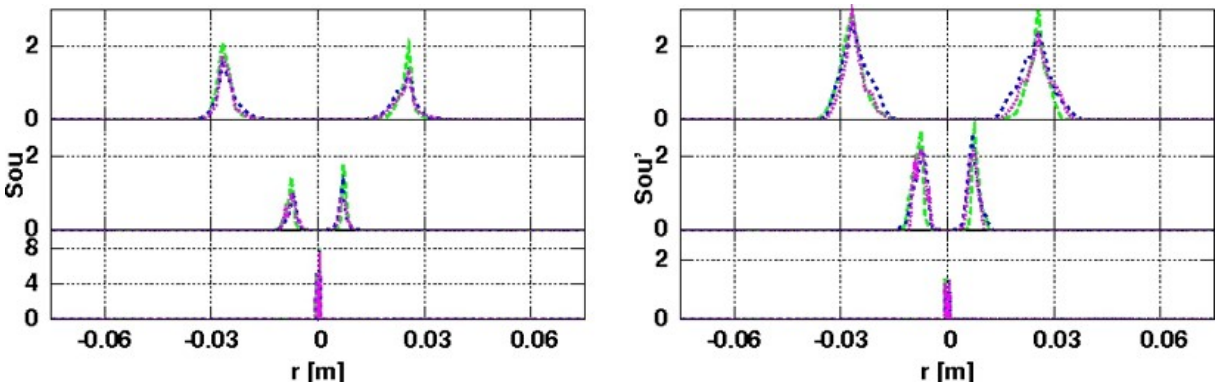

Figure 7.15: RPV from Experiment (left), Eddy diffusivity model (second from left), Dynamic eddy diffusivity model (third from left) Anisotropic model(right)

investigation predict the flame location similarly. The model using a dynamical procedure for computing the model coefficient estimates blunt jump rather than sharp jump as in the EDM (see Fig. 7.14, top left zoomed). Experimental investigation showed that the flame brush is thicker, which is better captured by both models. This indicates a dynamic computation of the diffusion coefficient is playing an important role in determining the flame front more exactly. Time averaged temperature fluctuations as plotted in Fig. 7.14 (right) show the same trend like that of the radial profiles at all three locations. Time averaged values of temperature are as high as 600 K and thicker, which indicates the flame is fluctuating in space especially more in downstream direction. Temperature fluctuation predictions from the dynamic model are higher and wider than of those of the classical EDM. This is especially pronounced by the anisotropic model.

Let us now focus on SGS scalar fluxes behavior. SGS scalar fluxes in the EMA region are plotted in Fig. 7.16. For an easier interpretation of the results, let us mention that the FGM model solves absolute reaction progress variable whereas experimental data is available as normalized temperature based RPV. To bring similarity between them RPV from simulations are normalized based on equilibrium value corresponding to mixture fraction values. Since the reaction zone is very thin in this configuration and a Lewis number is assumed unity for the fuel under investigation, it can be expected that both RPV from experiments and simulations are comparable, and an assessment of the model

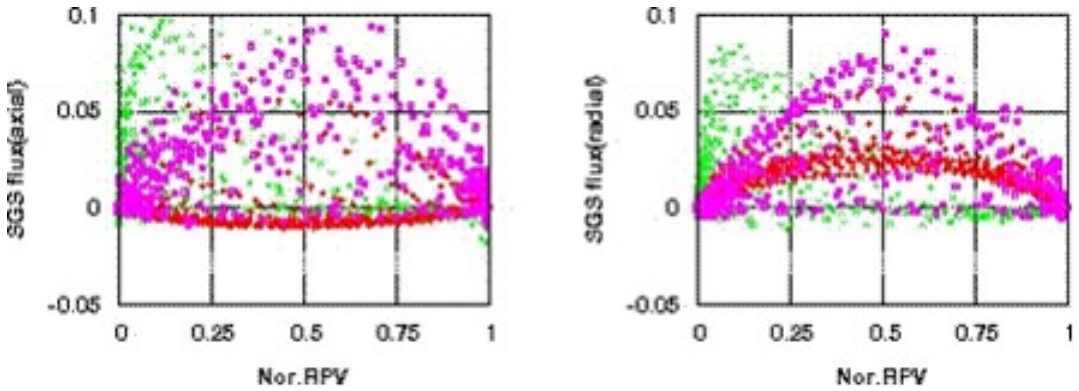

Figure 7.16: RPV SGS scalar flux axial (left), adial (right) in normalized RPV space, Experimental (red, EDM (green, Anisotropic model (pink)

capability is possible. The RPV source terms and their fluctuations plotted in Fig. 7.15 show that EDM predicts higher values than the Dynamic EDM and Anisotropic models.

To assess further results from the classical eddy viscosity SGS scalar flux model and the new anisotropic model, a comparison of the axial and radial scalar fluxes of RPV are carried out against the experimental data in Fig. 7.16. The SGS scalar flux change in physical co-ordinates may not be able to give more insight as the flame is changing from burnt to unburnt in a single cell. To overcome this difficulty in understanding the model capability, SGS scalar fluxes in EMA region are plotted in the normalized reaction progress variable space which represents the flame brush. Whereas the SGS fluxes in the flame brush is having better range of variation.

The EDM predicts higher magnitude SGS scalar fluxes near unburnt location, while the anisotropic model predicts the higher magnitude of SGS fluxes in middle of flame brush as in experiments. The EDM is not able to predict both the trend and magnitude of the experimental findings. Though anisotropic model could not capture magnitude of the SGS scalar flux accurately, the trends are captured well in mixture normalized progress variable space. These observations substantiate the argument that the thickness of the flame is influenced by SGS fluxes, and it is important especially in the context of premixed combustion and variable turbulent Schmidt number to well addresses on this aspect.

To analyze the results in more detail, the radial profiles of axial and radial SGS fluxes are plotted and compared against experimental data at two axial locations from the exit of 17.9 mm and 19.4 mm nozzle, respectively, in Fig. 7.17. These radial profiles of SGS fluxes are plotted against the normalized progress variable. These profiles are deduced from the area scatter data from Fig. 7.16. The trend and peak locations of SGS fluxes from EDM model are either shifted or predicted in opposite way, and the absolute values do not agree with experimental findings. This clearly demonstrates the limitation of the linear diffusivity SGS scalar flux model in predicting scalar transport and mixing within reaction zones in which anisotropy processes strongly affect the behavior of the flame. The results from the anisotropic model capture the trend of the experimental findings and also one of the radial or axial SGS flux magnitude. The new model predictions are encouraging and need to be considered for obtaining better predictions of scalar field

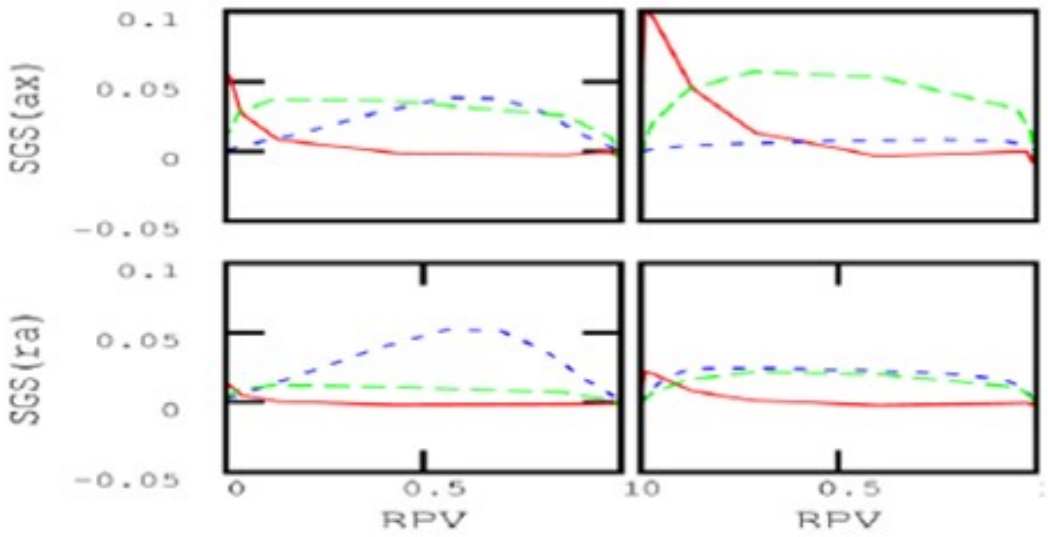

Figure 7.17: SGS scalar flux components (top: axial; bottom: radial) as function of reaction progress variable (distance from nozzle exit: 17.9 mm left, 19.4 mm right): Red: gradient ansatz, Green: anisotropic model and Blue: Experiment

behavior.

7.1.4 Conclusion

The ability of LES to correctly describe turbulent premixed combustion has been appraised on a rod stabilized unconfined flame. The technique combines the flamelet generated manifold (FGM) tabulated chemistry approach with LES. In addition FGM table considered here also accounts for the variable local equivalence ratio due to a possible entrainment of the environment air through a mixture fraction variable. LES results of the rod stabilized flame compared well with experimental data for both flow field quantities and species concentrations.

Further, a new anisotropic SGS scalar flux model has been assessed using highly resolved experimental measurements in both non-reacting and reacting premixed configurations characterized by high Reynolds numbers for which DNS-data are not available. The behavior of SGS scalar fluxes was especially analyzed. Besides experimental data, LES results obtained by the use of other existing SGS scalar flux models have been considered. In both configurations, the new anisotropy model showed a better predicting ability for both the SGS and the resolved quantities than the classical eddy diffusivity model with or without a dynamic computation for the model co-efficient. The new anisotropic model also allowed achieving LES results for the flow and scalar field that are in a better agreement with experimental data than that from EDM based models. Computational cost for same grid resolution is not substantially different (around +1%) in both reacting and non-reacting environments with advanced SGS scalar flux models implemented in this work.

7.2 Non-premixed prevaporized kerosene combustion in a swirl SSC

In order to demonstrate the feasibility of LES model to complex flows of practical applications, a realistic single sector combustor (SSC) as experimentally investigated in the frame work of TIMECOP-AE project is used. This combustion chamber is fuelled with pre-vaporized kerosene fuel using a nozzle fired at 0.4 and 0.6 MPa. It features a strong unsteady swirling flow with recirculation and breakdowns of large scales vertical structures, turbulent mixing, combustion, conjugate heat and mass transfer and pollutant formation. These complex interacting processes make predictions of such a system very complicated and challenging even if only part of the phenomena is considered.

7.2.1 Configuration and boundary conditions

The aim of the experiments conducted in the frame of TIMECOP-AE was to replace natural gas used in previous test cases [94] by pre-vaporized liquid kerosene. A set-up designed by DLR (Deutsches Zentrum für Luft- und Raumfahrt) was used for the fuel supply, where liquid kerosene was vaporized at a minimum temperature of 673 K in a flowing system. To achieve comparable conditions for mixing and combustion with previous methane based studies [218, 94] a primary combustion chamber pressure of at least 0.4 MPa was necessary to supply sufficient momentum for the fuel-jet in the actual test cases. It consists of a squared cross section single sector combustor (SSC) as depicted in Fig. 7.18, where combustion air was supplied through a swirl nozzle. It is optically accessible from three sides in order to allow various modern optical laser diagnostics. The test rig can withstand an operating pressure of up to 2 MPa and can be operated with a combustion air flow up to 1.3 kg/s and cooling air flow rates of up to 3.0 kg/s. The maximum heating temperature of the combustion air is 850 K. Similar to the previous combustion chamber, the fused silica windows of the combustion chamber are cooled by guided cooling air, which is let into the hot exhaust before leaving the combustor through a throttling nozzle. In order to keep further disturbances of the chemical and physical reactions inside the combustion chamber small, no secondary air was used (Fig. 7.18) in the experiments. Note that the combustion air inlet supplies the swirler/injector part, while a window air inlet provides fresh gas through films on the front combustion chamber wall. This air entering the main combustion chamber is needed during the experiment to avoid any soot deposition on the windows impacting the optical quality. In computations the window air was not included. The SSC test rig pressure is controlled by the amount of cooling air let into the system. In the present test case, dilution of hot gases by cold air is not considered for both experimental and numerical studies.

Flow fields and flame stabilization were investigated using state-of-the-art Laser Doppler velocimetry (LDV) and planar laser-induced fluorescence (PLIF) methods. This paper focuses on validation of the model implemented in the in-house CFD code FASTEST-3D and does not give details of the spectroscopic part of the measurements, consisting of kerosene LIF, OH-LIF and chemiluminescence measurements at three different operating points. In fact, the fired nozzle was operated at 0.4, 0.6 and 0.9 MPa, with an air mass flow of 77, 114 and 170 g/s heated up to 623 K, cor-

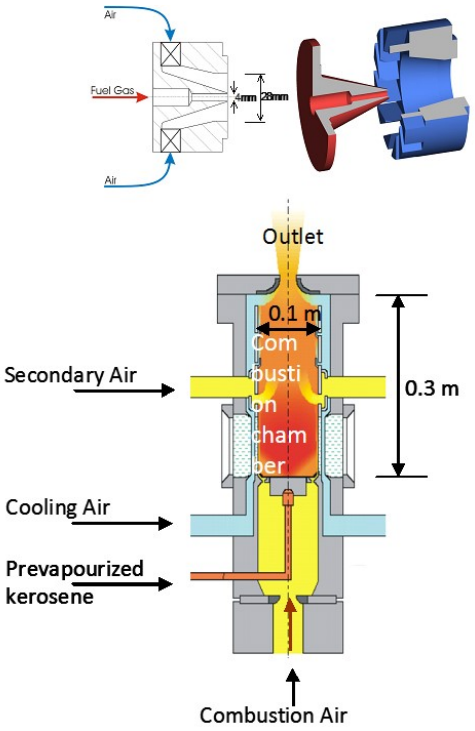

Figure 7.18: Experimental setup (bottom) and swirled nozzle (top)

responding to a pressure drop across the nozzle of 3.4% for all three investigated test cases.

The global equivalence ratio was set to $\phi = 0.9$ which is equal to an Air Fuel Ratio (AFR) of 18.6. As a result, a comprehensive database including, the velocity flow fields and the characteristic parameters of the flame derived from the spectroscopic measurements has been provided. This database is suitable for model validation and numerical simulation. For the present investigations, the test case corresponding to a combustion chamber pressure of 0.6 MPa is considered. Table. 7.2 summarizes the corresponding operating conditions.

To simulate the configuration as shown in Fig. 7.18 the computational domain in Fig. 7.19 is considered. It includes the combustion chamber and the swirl nozzle represented by a mesh consisting of 137 grid blocks featuring an O-type structure. The total number of grid points is 2.0 millions. The resulting mesh is able to resolve more than 85% of total kinetic energy of the flow field in accordance to the so-called Pope-criteria (see in [93]). All simulations were run on sixteen processors.

As inlet boundary conditions, the mass flows from the experiment were prescribed using laminar unperturbed profiles. A laminar inlet profile used was sufficient for such a simulation as measurements from experiments show that flow field is dominated by the intense recirculation of the swirl flow and not by the inlet turbulence [218].

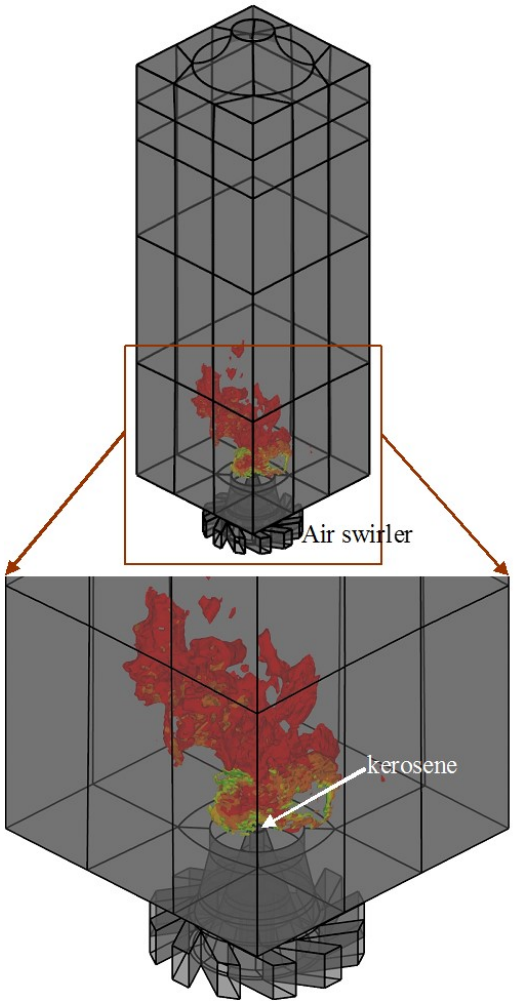

Figure 7.19: Computational domain with instantaneous isosurfaces of the reaction source term

Table 7.2: Operating conditions for 4 bar and 6 bar cases

Description of parameter	Details
Nozzle swirl number (geometrical)	1.2
Combustor pressure [MPa]	0.4, 0.6
Fuel	Pre-vaporized kerosene Jet-A1(Experiments)
	80% n-decane and 20% n-propylbenzene (FGM)
Kerosene mass flow rate(g/s)	4.16, 6.12
Fuel temperature [K]	673
Oxidant	Air
Mass flow of Oxidant [g/s]	77, 114
Oxidant Temperature [K]	623
Equivalent ratio	0.9
Thermal Power (kW)	174, 250
AFR (Air Fuel Ratio)	18.6

7.2.2 Results and discussions

In this section we present some numerical results obtained for the kerosene pre-vaporized combustion for the 0.6 MPa case. Flow field results will be discussed first, followed by an analysis of some flame characteristics.

The time averaged velocity magnitude and streamlines resulting from the simulation are shown in Fig. 7.20. Negative velocities are seen on top of kerosene jet and also surrounding it, leading to limit the kerosene fuel jet penetration depth within few millimeters from the exit of the nozzle. Negative velocities are also observed in the air swirler side near exit of the nozzle. This is leading to a partial infiltration of kerosene into the nozzle. The main feature of the flow is the spreading of the flow, surrounding a reverse flow area reaching back to the stagnation point. The recirculation zone along the centerline reaches down to a stagnation point at x, y, z = 0, 0, 6 mm and grows from a diameter of 8 mm at x = 10 mm to a diameter of 16mm at x = 20mm away from the nozzle. This can also be seen in Figs. 4 and 5. The recirculation zone is typical for highly swirling flows and results from a positive axial pressure gradient that is associated with the vortex breakdown phenomenon. The highest positive (negative) axial velocity occurred at x, y, z = 0, 12, 5 mm (0, 0, 20) mm, where a velocity of 76 m/s (-18 m/s) was measured. The highest radial velocity was 31 m/s at x, y, z = 0, -18, 15 mm, whereas the highest tangential velocity reached up to 59 m/s at x, y, z = 0, -12, 5 mm. As pointed out above this observation can also be made from Fig. 7.21 and 7.22 in which velocity profiles and turbulent kinetic energies are plotted at different axial positions from the nozzle exit (x = 5 and x = 10 mm in Fig. 7.21 and; x = 15 and x = 20 mm in Fig. 7.22). All three components of the velocities and the turbulent kinetic energy predicted by the LES are in good agreement with the experimental data. The axial velocity component is becoming strongly negative from x = 5 mm to x = 20 mm away from nozzle exit. This indicates the presence of a recirculation zone, which is necessary for flame stabilization. In this respect, the instantaneous RPV source term, the CO mass fraction and the temperature plotted in Fig. 7.23 (top) and time averaged values of the RPV source term, the RPV source variance and the temperature in Fig. 7.23 (bottom) allow to give a first impression of the flame characteristics.

The instantaneous RPV source term in Fig. 7.23a is located in the main reaction zone. The flame seems to stand above the nozzle featuring a lifted flame in agreement with experiments. However it can be observed from the averaged reaction progress variable source term plotted (Fig. 7.23e) that the flame is attached to the nozzle, though the value of the RPV source term remains very low. This suggests that the flame may be fluctuating between an attached and a lifted regime. In non-premixed swirled combustion as investigated in [218] the flame was found to be lifted while exhibiting a partially premixed nature. The RPV source term variance plotted in Fig. 7.23f looks like two thin leafs starting from the swirled nozzle tip. It is worth noting that the reaction progress variable is strongly influenced by the swirl flow. This causes the strong change of the RPV in the mixing layer of the swirled air flow and the fuel. Especially it is observed that higher values of the RPV variances are disappearing above distances x = 10 mm away from the nozzle exit.

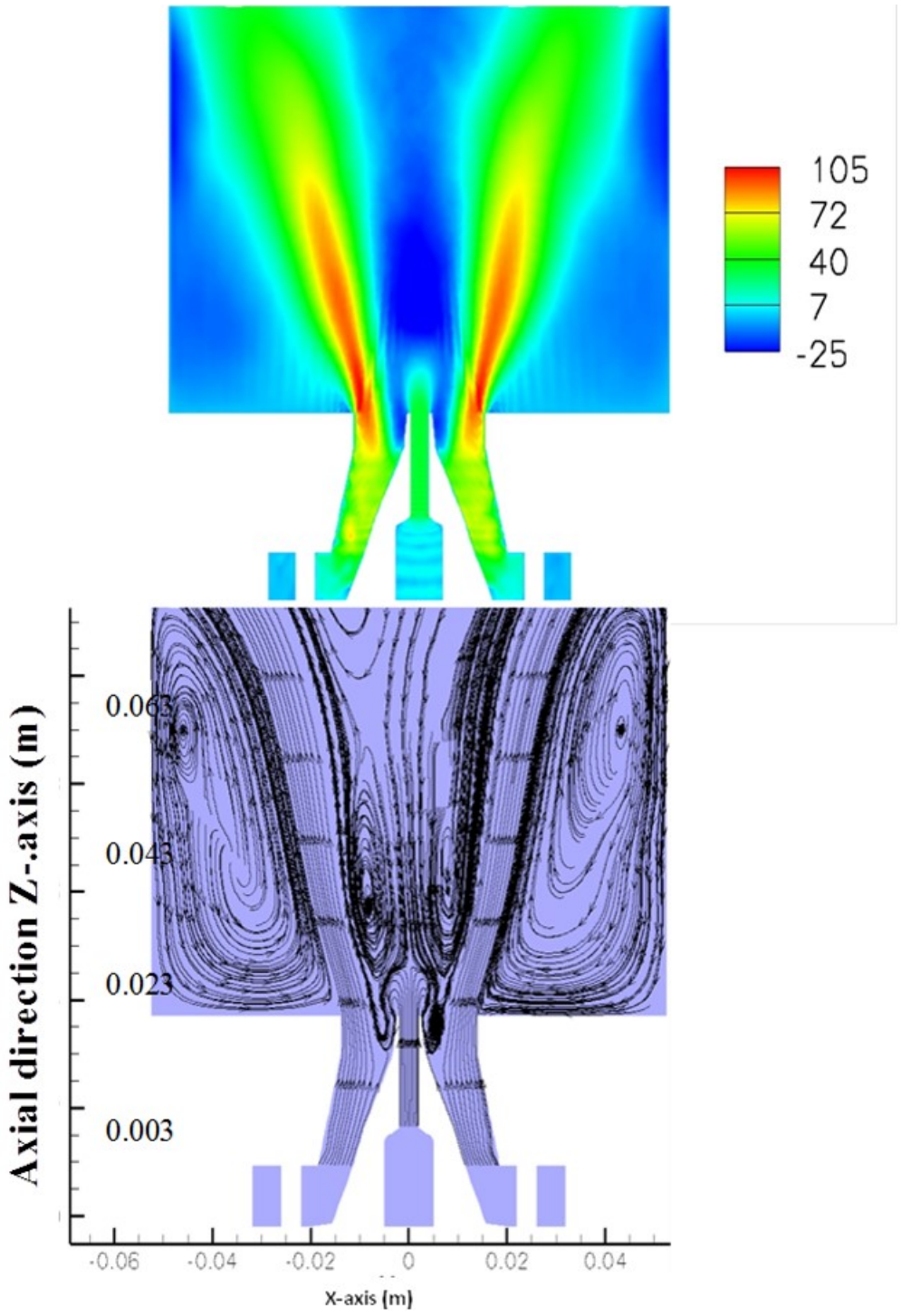

Figure 7.20: Time averaged axial velocity magnitude (m/s) (top) and time averaged velocity streamlines computed from LES (bottom)

A high concentration of CO in the reaction zone is observed in Fig. 7.23b. Most of the CO is combusting further downstream to limit the reaction zone within the vicinity of the nozzle. This is strongly influenced by the swirled air. The maximum instantaneous temperature in the reaction zone is found to be 2250 K (Fig. 7.23c). This maximum temperature is found at stoichiometric mixture fraction region. Averaged and instantaneous temperature contours in Fig. 7.23c and f, respectively, confirm that the main reaction zone of the flame is lifted. Streamline plots derived from experimental

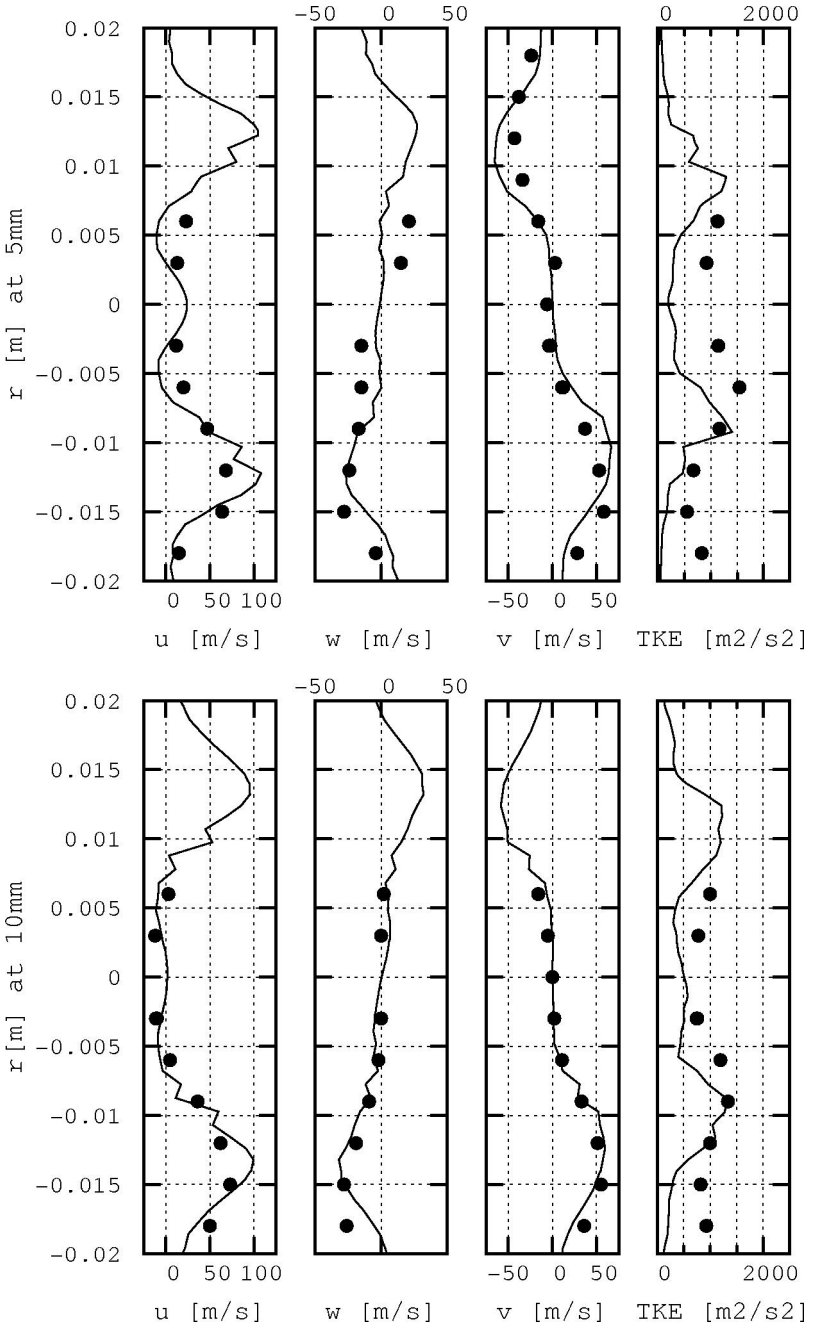

Figure 7.21: Radial profiles of time averaged axial (u), radial (w) and tangential (v) velocity components and turbulent kinetic energy (TKE) at 5 mm (top) and 10 mm from the exit of the nozzle (_simulated , • Exp)

LDV data as well as from numerical simulation show the existence of a recirculation zone responsible for stabilization of the flame and a fluctuating stagnation point near the nozzle, causing the flame position to also fluctuate between a lifted to an attached behavior.

A comparison of predicted mass fraction of OH species and kerosene by LES against pixel intensity from experiments is shown in Fig. 7.24 for the main reaction zone

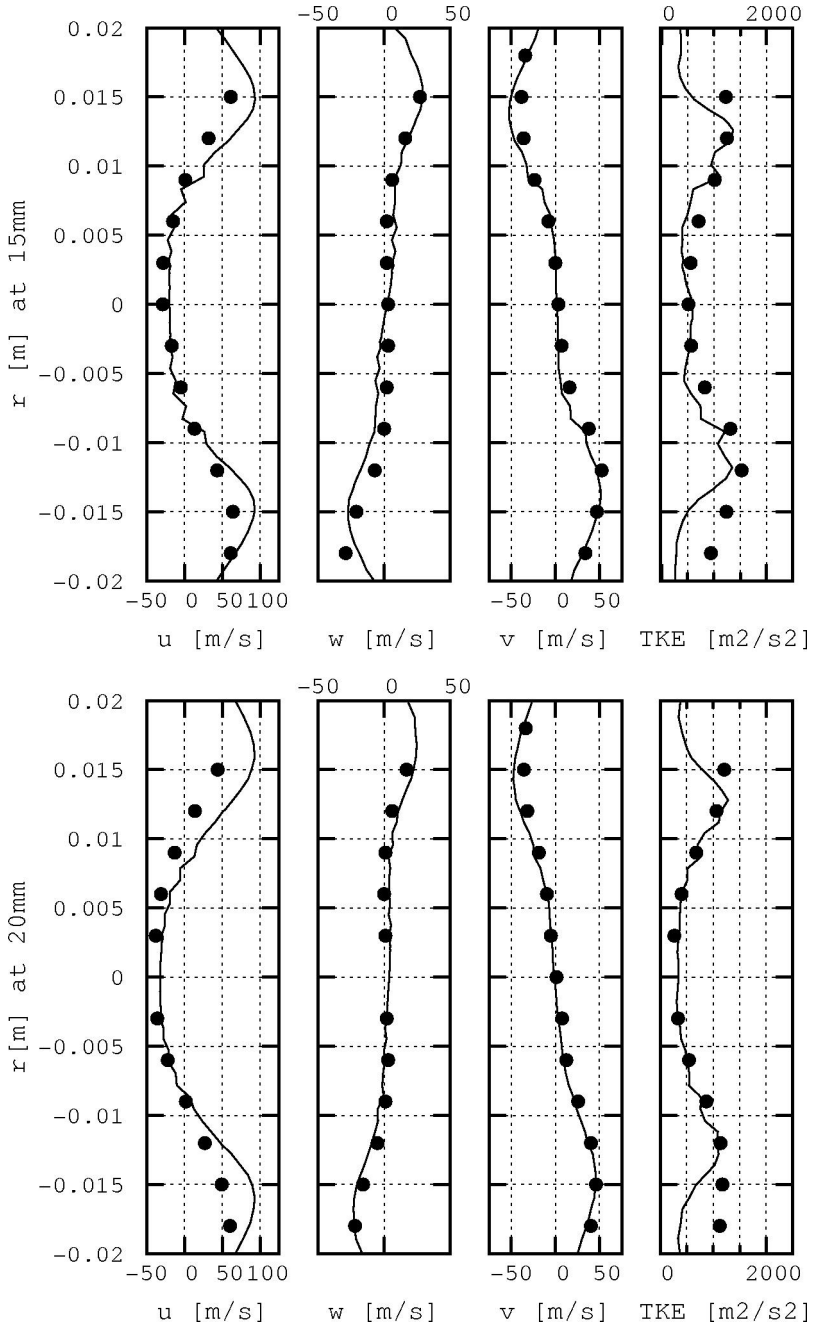

Figure 7.22: : Radial profiles of time averaged axial (u), radial (w) and tangential (v) velocity components and turbulent kinetic energy (TKE) at 15 mm (top) and 20 mm from the exit of the nozzle (_simulated , • Exp)

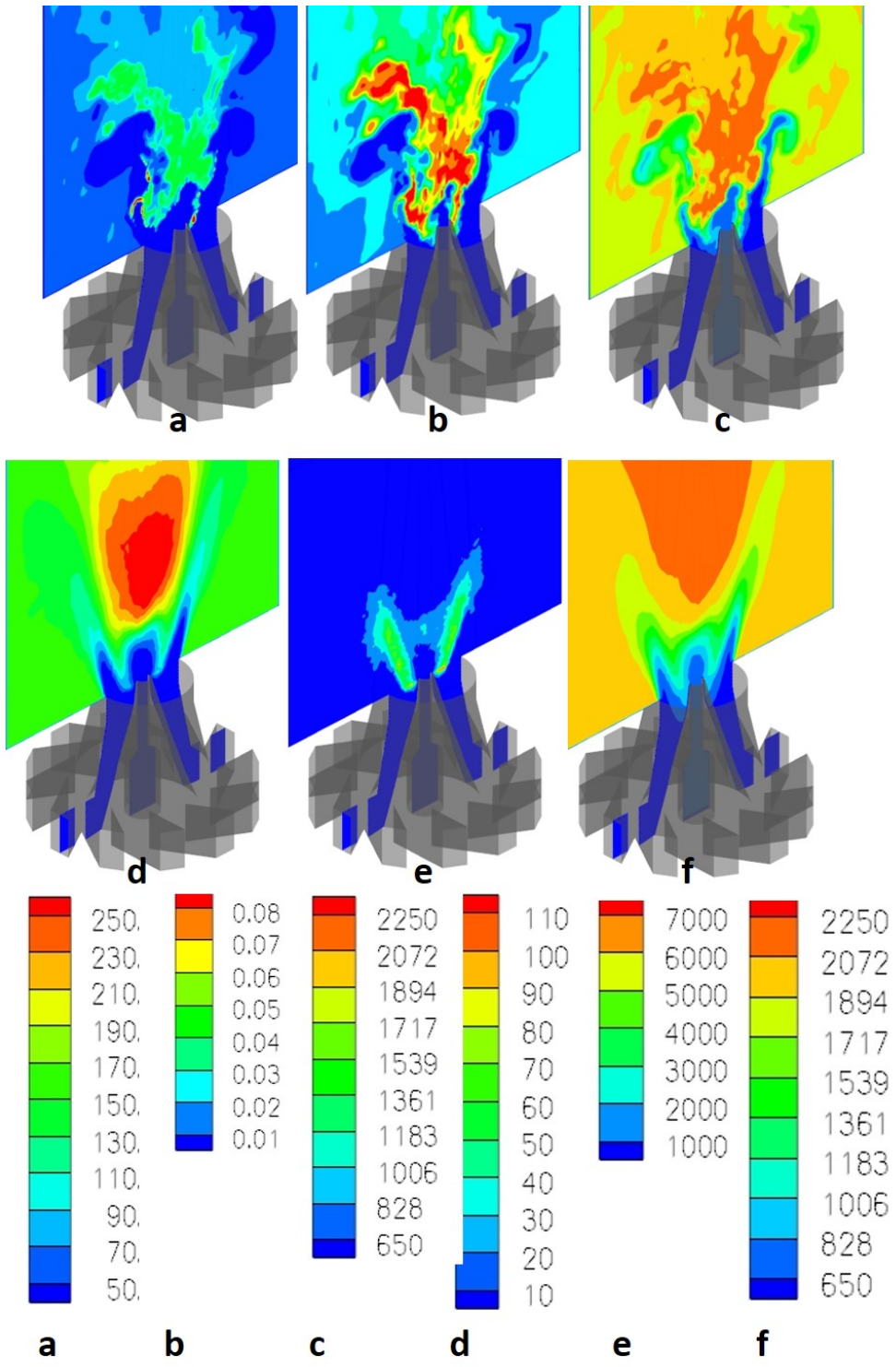

Figure 7.23: Contour plots of instantaneous (top) and time averaged (bottom) a) RPV source (kg/m3-s) b) CO mass fraction c) temperature (K) d) source term (kg/m3-s) e) RPV resolved source variance f) temperature (K) on a plane passing through the center of nozzle

region. The different red line contours of Fig. 7.24 (top) show the distributions of averaged OH measured in experiments. Gray line contours of Fig. 7.24 (bottom), with corresponding percentage of time averaged maximum OH mass fraction are estimated by LES. Experiments show the maximum OH concentration on top the fuel jet. This is also confirmed by LES. In general, though OH mass fractions from the LES calculations are qualitatively comparable with those from experiments, they differ from each other

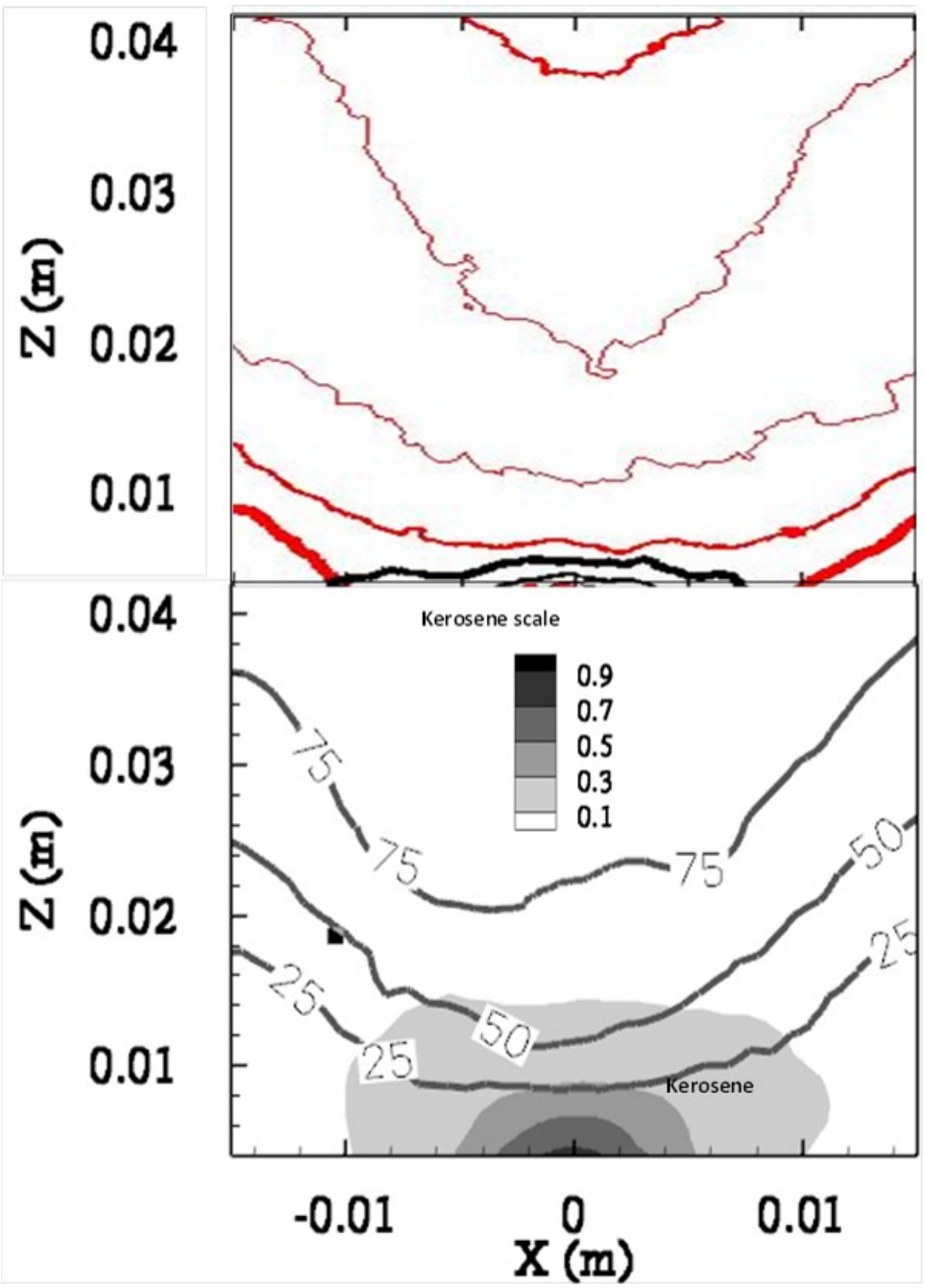

Figure 7.24: Qualitative representaion of OH concentration and kerosene. Top: Experiment (bold contour: 25% of maximum; middle contour: 50% of maximum; light contour: 75% of maximum). Bottom: simulation

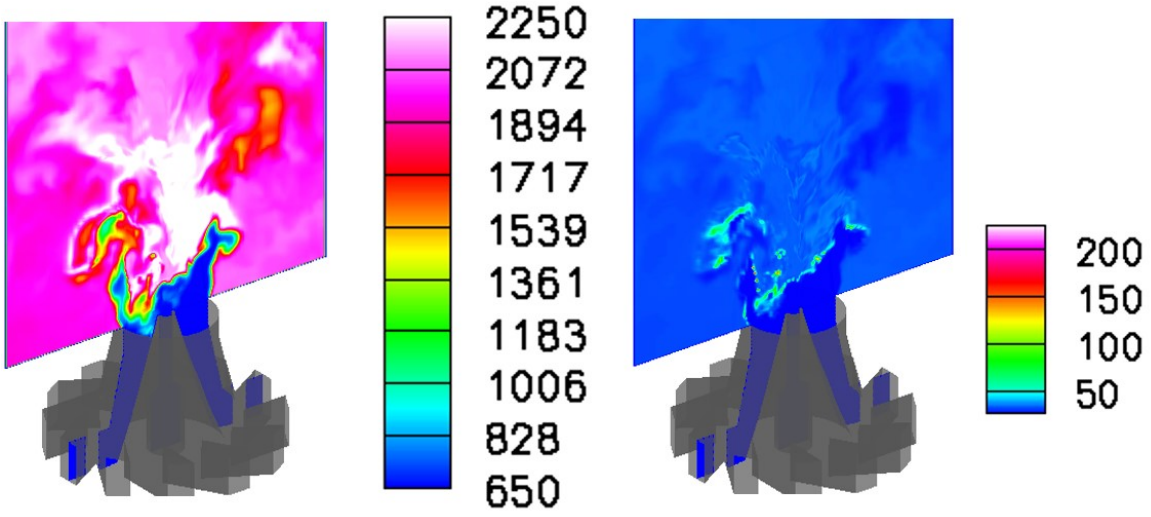

Figure 7.25: Temperature (K) (top) RPV source term (kg/m^3-s) (bottom) on a plane passing through the center of nozzle - 4 bar case

by a few millimeters in physical space. One of the reasons may be the window air effect that was not included in computations. In particular the greater part of the vaporized kerosene (dark lines in Fig. 7.24 (top)) that is located in the vicinity of the nozzle is captured by the LES (gray scale contours of Fig. 7.24 (bottom)) with a slight deviation. For 4 bar pre-vaporized kerosene combustion, radial profiles of time averaged axial velocities and turbulent kinetic energy are plotted in Fig. 7.26. Negative axial velocity is increasing in Fig. 7.26 from 5 mm from the exit of the nozzle to the 20 mm. This indicates the presence of a recirculation zone, which is necessary for flame stabilization. Fuel jet penetration is restricting the back flow at 5 mm. All three components of the velocities and the turbulent kinetic energy predicted by the LES are in good agreement with the experimental data. The axial velocity component is becoming strongly negative from x = 5 mm to x = 20 mm away from nozzle exit. The instantaneous temperature and RPV source term on plane passing through center of nozzle are plotted in Fig. 7.25. RPV source term represents the main reaction zone in the combustion chamber; here main reaction zone is lifted, but temperature profile shows that flame is attached to the nozzle. This concluded here flame is exhibiting partially premixed combustion, which was also observed in experiments. Due to the lack of detailed experimental data regarding the other species concentration and a temperature distribution an appropriate assessment of the model with respect to this prediction could not be provided.

7.2.2.1 Energy spectrum

For the 4 bar test case time series were recorded at three radial position at z = 5 mm. Fig. 7.27 (left) show power spectral densities deduced from temporal correlations (via FFT) for axial and radial positions of 5, 10 mm from the center nozzle exit. The peak frequency was approximately at 1450 Hz. Second peak is recoded at 2932 Hz. These experimental findings are captured well by the simulations results (Fig. 7.27 (right)), both peak frequencies from experimental findings are reproduced by the simulation.

The recirculation zone is typical for highly swirling flows and results from a positive axial pressure gradient that is associated with the vortex breakdown phenomenon. Investigation of advanced dynamic EDM and anisotropic SGS scalar flux models were extended to complex fuels pre-vapourized kerosene.

In depth analysis was carried out to investigate predictability of the new advanced SGS models [234] for complex fuel combustion physics. Results obtained with SGS

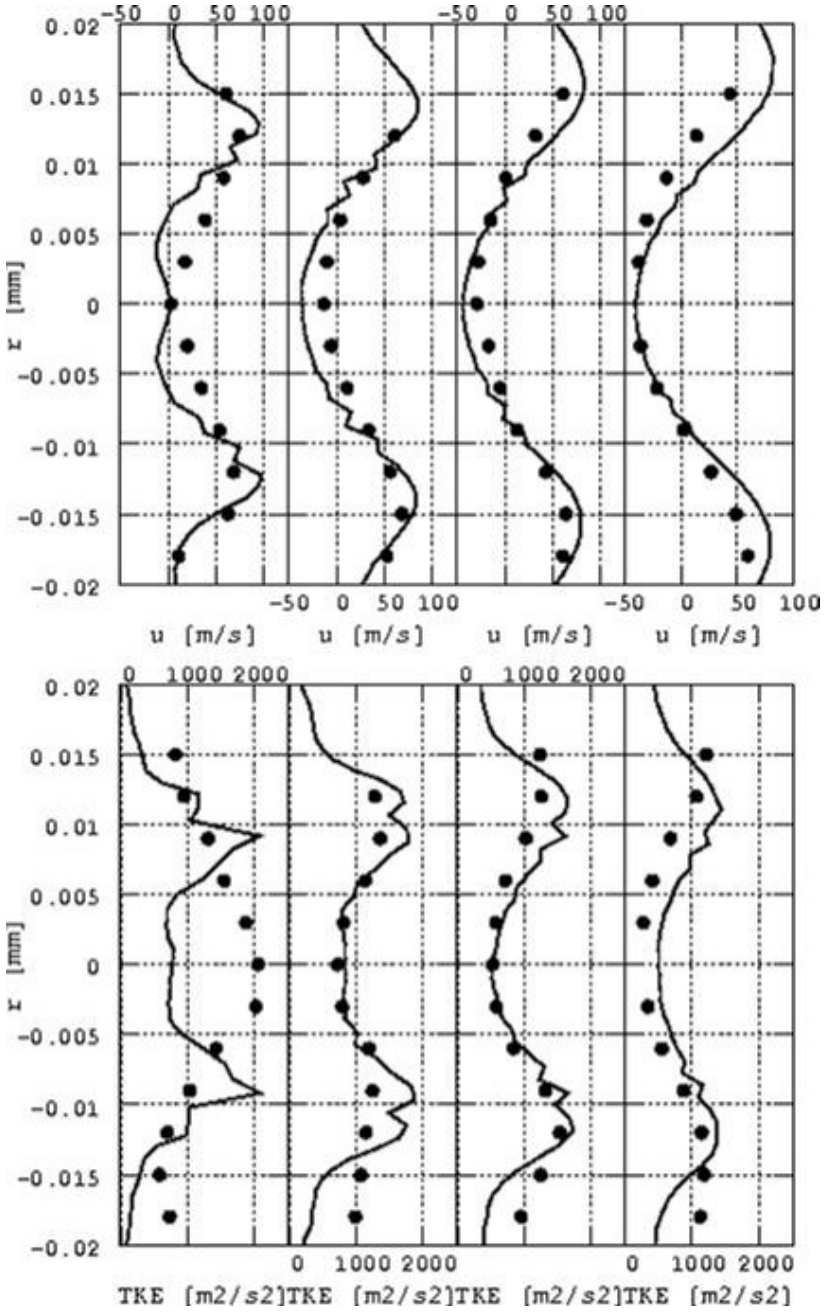

Figure 7.26: Radial profiles of time averaged axial (u)(top) and turbulent kinetic energy (TKE)(bottom) at 5, 10, 15 and 20 mm (left to right) from the exit of the nozzle (_simulated , • Exp) - 4 bar case

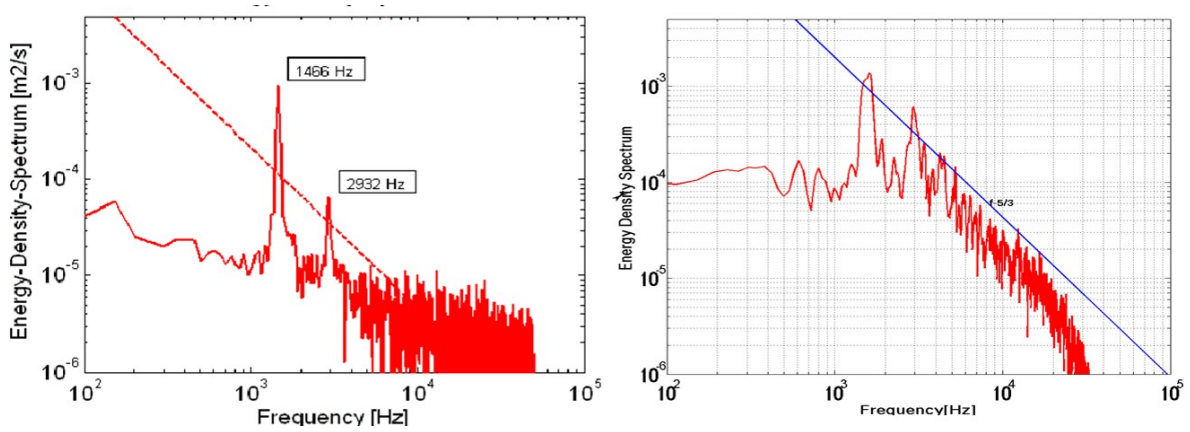

Figure 7.27: Power spectral density Experimental (left) Numerical(right) dashed line(left), blue line(right) denotes a -5/3 slope - 4 bar case

models especially anisotropic model were encouraging as newly implemented models were able to capture reaction region more precisely than conventional models. However the lack of SGS scalar flux experimental data at sub-grid level limited to provide greater insight into the influence of new SGS scalar flux models on scalar field predictions.

7.2.3 Conclusions

An LES based advanced combustion model for a reliable description of combustion processes in a gas turbine combustion chamber has been developed and implemented in the FASTEST-3D code. The numerical approach including a FGM method based combustion model was successfully assessed with respect to its prediction capability of the flow and combustion characteristics. In particular the complex flow field properties in the SSC are captured well. However, it could be pointed out that turbulent kinetic energy at 5 mm from exit of the nozzle is not in agreement with the experimental data. The results further show that the flame is not always attached to nozzle and appears to fluctuate in time.

Chapter 8

Complex combustion process with heat loss

In this chapter application of the combustion modeling near wall combustion is discussed. The near wall combustion as described earlier involves many phenomenon happening at same time, like flame development, flame quenching, heat loss, boundary layer formation and its influence on other physics as represented by Fig. 2.11. Some parts of results presented here were reported in [243, 245, 242].

8.1 Flame wall interactions - Non-adiabatic configuration

Recently FGM based combustion modeling was extended to "stratified premixed cooled flames" by Donini et al. [54] for 2D geometrical configuration successfully. In the present work application of FGM based LES combustion modeling for non-adiabatic combustion is extended to 3D premixed laboratory complex flame configuration. In the next sections of the chapter geometrical setup, numerical setup of the configuration will be described. These will be followed by the verification and validation of the model implemented.

8.2 Experimental setup

The experimental configuration chosen for the FWI study is shown in Fig. 8.1. Therby a premixed fuel of methane/air is supplied through the center pipe of the nozzle, which has a diameter of 30 mm. This fuel jet nozzle is surrounded by a concentric nitrogen flow with a diameter of 60 mm. Nitrogen is chosen as a co-flow as it can restrict oxidant entrainment from the ambient air into the reaction zone. Impinging wall is of convex shape on impinging side. This shape has been chosen in order to provide an optical accessibility of the complete surface area of the impinging wall.

Temperatures and CO profiles have been measured simultaneously using $CARS$ thermometry and 2-photon LIF as described in [131]. All three velocity-components have been measured with 2D3C-PIV at 10 KHz repetition rate using a frequency doubled Nd:YLF laser with 1.4 mJ/pulse. The Mie scattering of the seeded TiO2 particles was detected by 2 CMOS cameras arranged in the Scheimpflug condition with a field of view of 30x30 mm^2. Data were processed using the commercial code (LaVision Davis 7) using

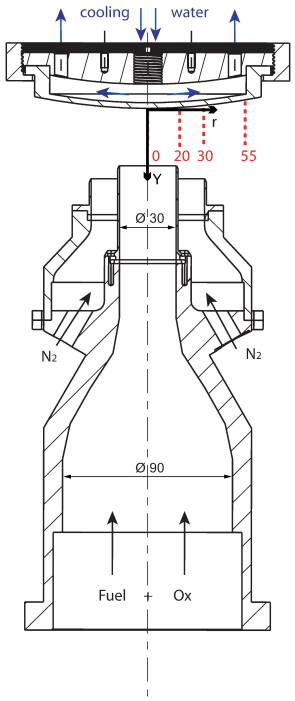

Figure 8.1: Schematic representation of the experimental setup.

a multi pass method. The final interrogation area of 16x16 pixel with 75 % overlap resulted in a spatial resolution of 600 μm/pixel.

A turbulent grid generator is placed in the upstream at 50 mm from the nozzle exit to introduce disturbances into the main fuel jet. Both side and bottom boundaries are open to the ambient, whereas a suction is provided on the top of the water cooled impinging wall. Experiments were carried out for Reynolds number of 5000 in the range suggested in [185] for IC engine flow conditions. More details of the experimental setup and parameters investigated are described in [131, 186].

8.3 Computational setup

Near wall modeling for very large Reynolds number flows are very well investigated in the literature [93, 199, 146, 72] mostly focused on aerodynamic engineering applications. Criteria to define mesh resolution near wall region were therefore developed for different physical phenomenon. Froehlich et al. [72] discussed the grid resolution, especially in the streamwise direction around the mean separation position in non-reacting periodic-hill flow configurations. They found that the grid resolution has a very strong influence on the reattachment behavior and hence on the whole flow predictions. The application of the no-slip condition even if the wall-nearest grid nodes are within the semi-viscous sublayer, in the range $5 < y^+ < 15$, can cause substantial errors at the wall at which separation occurs in conjunction with poor streamwise resolution. Besides the WALE [199] model, a modified eddy-viscosity model was proposed by Vreman [100, 210] and applied in large-eddy simulation of turbulent shear flows. This model is well suited

for engineering flows to handle not only turbulent but also transitional flow regime phenomena.

In this study, the grid resolution near the wall region is investigated in reacting configurations in which thermal, combustion and flow boundary layers develop. To model these different boundary layers efficiently, the grid resolution should be addressed with respect to the actual Reynolds number. Relying on IC-engine experiences where the Reynolds number based on ICE cylinder diameter fall in the range of 1000 to 10000 and assuming that the turbulent Reynolds number (Re_t) in IC engine is as high as 500, the investigated configuration with a Reynolds number of 5000 could likely feature a turbulent Reynolds number of 50. In order to match the turbulent Reynolds number of the same order of the IC engine Re_t the main jet Reynolds number flow has to be increased up to 50000. Thus, three configurations with Re = 5000, 25000 and 50000, respectively, are investigated, where an intermediate value of $Re = 25000$ has been introduced for comparison purposes. The corresponding operating conditions are summarized in Table 8.3. According to experiments, the investigated configuration features inlet boundaries of a premixed fuel-inlet (CH_4, O_2, N_2), a co-flow (N_2) and open boundary conditions which allow entrainment of ambient air (O_2, N_2) due to the suction provided on the top of the water-cooled impinging wall. Solving only one mixture fraction is not really appropriate to completely describe the actual composition resulting from these three different inlets. Multiple mixture fractions simulation which may be suitable are very rare in the flamelet and FGM based combustion modeling. Some attempts are reported in [80, 206]. In section 8.5 FGM table is generated for complete range of mixture fraction (0 - 1.0). Since the main region of interest in the configuration under investigation is premixed in nature, only one mixture fraction is rather defined in the first part (see section 8.4.2) of the study, so that the complexity of defining a second mixture fraction and constructing corresponding flamelets and FGM table is avoided accordingly. The single mixture fraction is restricted to define the ambient air as the pure nitrogen only. This approximation is reasonable as the lateral mixing of the ambient air with the premixed jet and the co-flow is not interacting in the region of interest. Therefore in a first step of the development of the non-adiabatic FGM table, it is made simpler to only consider two mixture fractions of $\xi = 0.27$ and 0. The resulting non-adiabatic FGM table is generated by interpolating to other intermediate mixture fractions using the standard thermochemistry analysis [52, 125, 103] to capture non-linear behavior of density, temperature, and species mixture fractions according to

$$\frac{0.27}{\widetilde{\phi}\left(\xi, Y, h\right)} = \frac{0.27 - \widetilde{\xi}}{\widetilde{\phi}\left(\xi_{=0.0}, Y, h\right)} + \frac{\widetilde{\xi}}{\widetilde{\phi}\left(\xi_{=0.27}, Y, h\right)} \tag{8.1}$$

The boundary conditions used for the FGM table generation are listed in Tables 8.1 and 8.2. Following [113], the FGM tabulated chemistry is integrated into the LES framework that includes an artificially thickened flame (ATF) model to track the premixed combustion with air entrainment. Details of this modeling can also be found for example in [42] and [34]. For the self-consistency of the thesis, its main features outlined here. The principle of this approach is based on coordinate transformations applied to both scalar equations (3.64) and (3.63) to thicken the flame front and thereby make it resolvable on "coarse grids". The flame is then thickened by multiplying the diffusion term and dividing the reaction rate by the so called thickening factor. To ensure that the pure mixing is accurately predicted and not modified by the thickening,

a dynamic thickening is considered according to Kuenne et al. [114], while achieving a correct laminar flame propagation speed. The thickening is applied only to the flame front employing a flame sensor. However, the interaction between the flame front and the turbulent flow field is rather modified by the thickening procedure. This yields a decreased sensitivity of the flame to the vortices, which normally causes increased flame wrinkling. Therefore, an efficiency function has been introduced to compensate for the lost flame surface induced by thickening, and to account for unresolved flame wrinkling produced by turbulence [34].

Fig. 8.2 shows the computational domain that represents the experimental set up under study. It includes the main fuel-jet and the nitrogen co-flow together with the separation pipe thickness. To address the first aspect related to the grid resolution required near the wall two different grids are used, namely a mesh with 4.2 millions and 0.5 million control volumes (see Fig. 8.3). These grids have been elliptically smoothed to obtain a better orthogonality. Both grids have been refined towards the near nozzle entrance and at impinging wall regions whereas they get coarser in other regions with increasing distance from these locations to limit the total CVs (Control Volumes). In the fine mesh case 9 CVs are present within the one millimeter distance from the impinging wall at center, whereas 5 CVs are located in the coarse mesh case. Mesh sizes are distributed isotropically in all directions. The actual turbulence generating plate (TGP, perforated plate) as used in experiments is integrated in the numerical setup. All 37 holes on perforated plate are hexagonally arranged, each hole having a diameter of 4 mm. The resulting blockage is about 45% [131, 186, 19]. The TGP diameter is larger than that of the fuel nozzle, resulting in a partial blockage of some holes as shown in Fig. 8.4 (left). All these features are implemented to capture more accurately the flow inlet boundary conditions.

Iso-surfaces of Cartesian velocities V_y(axial velocity), U_x and W_y of the flow in the nozzle are plotted in Fig. 8.4. The TGP influence on the flow in the nozzle can be observed from such iso-surfaces. In fact, the numerous small jets are breaking up, interacting each other and producing strong turbulence near the exit of the TGP. Imposing the synthetic turbulence at the inlet is not necessary as strong turbulence is generated in all directions by interacting jets. More accurate results can be produced by taking into account the contraction at the exit diameter of holes on the TGP resulting from boundary layer and contraction effects on the flow.

The four regions in the nozzle flow namely the initial jet development, the jets interaction and breakup, the turbulence decay and homogenization are observed. The velocity iso-surfaces in Fig. 8.4 further indicate the development of boundary layers in the nozzle along with the contraction effect. The jets are traveling downstream combustion region and may interact with the flame near the wall in the reacting case. Experimental measurements are not available to validate these cases quantitatively. Nevertheless, qualitative comparisons of predictions from the simulated isothermal premixed impinging fuel jet with the experimental measurements for the isothermal air flow of the opposed jet configuration [19] are provided. The impinging distance in the opposed jet configuration is 15 mm, whereas it is 30 mm in the present configuration. These two differences could lead to significant differences between the two cases. However this comparison will give

Table 8.1: Boundary conditions for FGM and FASTEST under adiabatic conditions.

	FASTEST Mixture Fraction	
Fuel/Reactant	$\xi = 0.27$	$CH_4 = 0.055$ $O_2 = 0.21942$ $N_2 = 0.72558$
Co-flow/oxidant	$\xi = 0.0$	$CH_4 = 0.0$ $O_2 = 0.002$ $N_2 = 0.998$
Dimensions	$\xi = 201$, $Y^* = 101$,$H^* = 1$,$\xi'' = 11$,$Y'' = 1$, $H'' = 1$	

an insight into the flow prediction capabilities in the nozzle. Please note that both simulated and experimental cases are with the same $Re = 5000$. The radial profiles of the axial velocities and their predictions at an upstream distance from the nozzle exit of 20, 30, 35, 40 and 47 are plotted in Fig. 8.5. A very good agreement is achieved for axial velocities in the upstream near the TGP, but they deviate in the upstream region. This is due to a faster deceleration of velocities in experiments resulting from shorter impinging distance. The overall axial velocity profiles could capture the trend very well at all locations in the nozzle. RMS velocities from simulations reproduce the trend in the upstream region and agree well with experiments near the nozzle exit (d = 20). The analysis of the flow field in the combustion region is provided later.

The configuration under study is not confined, the exhaust suction enhances the entrainment of the ambient air into the domain. This entrainment is taken into account by applying appropriate boundary conditions as suggested by Muhamed et al. [139]. The mixture fraction is prescribed for both fuel inlet and co-flow. The wall is treated as adiabatic in cold flow simulations. In the reacting case a non-adiabatic impinging wall is considered with radial temperature profiles according to experimental investigations (Fig. 8.23). All the details of the configurations investigated are provided in Tables 8.3 and 8.4, respectively. Especially Table 8.4 summarizes all the investigated cases categorized with respect to grid resolution, Reynolds numbers, adiabaticity and combustion (reacting or non-reacting).

Table 8.2: Boundary Conditions for FGM and FASTEST under non-adiabatic conditions.

	FASTEST Mixture Fraction	
Fuel/Reactant	$\xi = 0.27$	$CH_4 = 0.055$ $O_2 = 0.21942$ $N_2 = 0.72558$
Co-flow/oxidant	$\xi = 0.0$	$CH_4 = 0.0$ $O_2 = 0.002$ $N_2 = 0.998$
Dimensions	$\xi = 2, Y^* = 101, H^* = 201, \xi'' = 1,\ Y'' = 1, H'' = 1$	

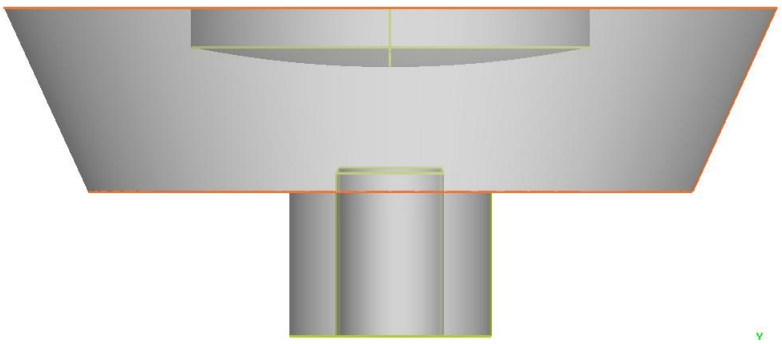

Figure 8.2: Computational domain including the nozzle and the impinging wall.

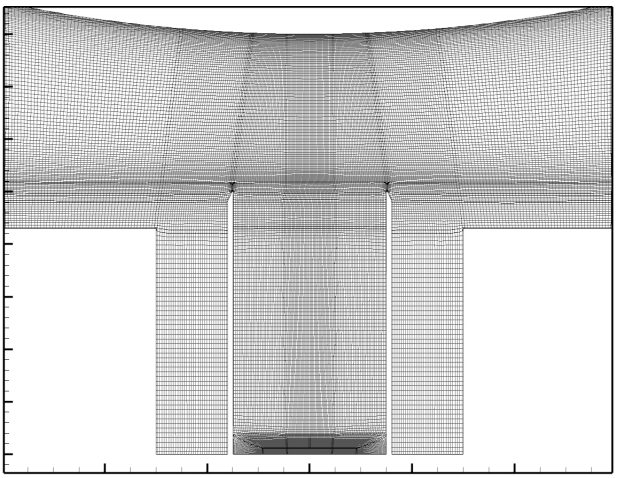

Figure 8.3: Schematic representation of the mesh on a plane passing through the nozzle. This mesh is constructed using block structured grid with 4.2 million CVs.

Table 8.3: Operating conditions.

Description of parameter	Unit	Details
Fuel Jet Reynolds number	Re[–]	5000, 25000, 50000
Fuel		Methane and Air
Combustion		Premixed
Phi		1.0
Co-flow		Nitrogen
Co-flow velocity	m/s	0.1, 0.25, 0.5
Fuel Jet Dia	m	30 mm
Co-flow Jet Dia	m	60 mm
Impinging Distance	mm	30 mm

Table 8.4: Investigated cases.

Parameter Case Name	Cold React	Fine Coarse Mesh	Adiabatic Non-adiabatic	Reynolds No.
CFA05	Cold	Fine	Adiabatic	5000
CFA25	Cold	Fine	Adiabatic	25000
CFA50	Cold	Fine	Adiabatic	50000
CCA05	Cold	Coarse	Adiabatic	5000
CCA50	Cold	Coarse	Adiabatic	50000
RFA05	React	Fine	Adiabatic	5000
RCA05	React	Coarse	Adiabatic	5000
RFA05N	React	Fine	Non-adiabatic table under adiabatic conditions	5000
RCN05	React	Coarse	Non-adiabatic	5000
RFN05/F5	React	Fine	Non-adiabatic	5000

8.4 Results and Discussions

8.4.1 Near wall resolution under isothermal conditions (Non-reacting results)

The averaged distance of the nearest point to the wall corresponds to $y^+ = 1.0$ and 1.5, respectively, for fine and coarse meshes as shown in Fig. 8.6. In the area of interest (r/D<1.0) both are in an acceptable range according to LES criteria for attached flows as estimated by Piomelli [159]. The mesh resolution in terms of y^+ on fine mesh for both Reynolds number of 25000 and 50000 is below 5 in the main region of interest. On coarse mesh it is higher than 5 for $Re = 50000$. This shows the fine mesh is capable of resolving the fluid boundary layer reasonably for all three Reynolds numbers investigated here. The mesh resolution quality can also be estimated by comparing the ratio of the mesh size Δ

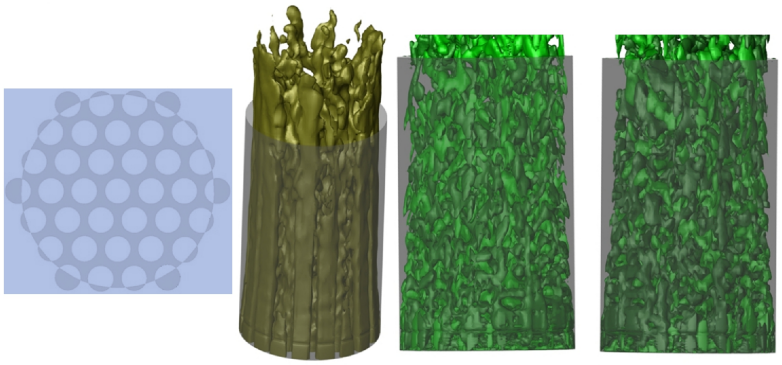

Figure 8.4: The original perforated plate used in simulation include the blockage on holes (which are beyond 30 mm diameter, left). Grey contours represent fuel nozzle geometry. Iso-surfaces of axial velocities Vy (second from left) and Cartesian velocities Ux (third from from left), Wz (right) at 3.0 m/s , ±0.15m/s and ±0.15m/s, respectively.

to the Kolmogorov length scale η

$$\eta = \frac{\nu^3}{\varepsilon} \tag{8.2}$$

where ν is the molecular viscosity and ε the turbulent dissipation rate. Pope [166] has shown that for an isotropic turbulence a grid spacing of 12η is needed to resolve the major part of the turbulence dissipation. Even though the turbulence is not isotropic, this approximation is used here for first assessments. The ratio Δ/η is plotted in Fig. 8.7 for the case with $Re = 5000$ on fine mesh (CFA05) on the plane passing through the fuel jet core. The value of Δ/η is very small near the impinging wall and almost below 12 away from the wall showing that the applied mesh is likely fine enough to capture the most energy carrying scales.

Instantaneous velocity contours of the axial and radial velocities are plotted on a plane passing through the center of the nozzle in Fig. 8.8. Instantaneous axial velocity contours show that many small jets which are generated by the turbulent grid placed in the nozzle are interacting very rapidly each other. These jets are very turbulent in nature and disappear before reaching the impinging wall. The radial velocities are developing within the nozzle due to the shear, while the axial velocity components are converting to radial velocities near the impinging wall.

The axial profiles of the time-averaged axial velocity and their fluctuations are plotted in Fig. 8.9 in comparison with the experimental data for the non-reacting case at three radial positions r = 0, 1 and 5 mm. Note that the experimental data are available only for $Re = 5000$. The velocity data from both experiments and simulations are normalized by the fuel jet bulk velocity. Especially normalized time-averaged axial velocity fluctuations on the fine mesh (CFA05) for $Re = 5000$ are matching well with the experimental prediction everywhere along the axis. On the coarse mesh case (CCA05) the agreement with experiment is observed only near the wall region while underpredicting the results away from the wall. This shows that the mesh resolution near the impinging wall is reasonable in both mesh resolution cases. For higher Reynolds number (CFA25, CFA50, CCA50) the near wall fluctuation shows steeper gradient than for low Reynolds number

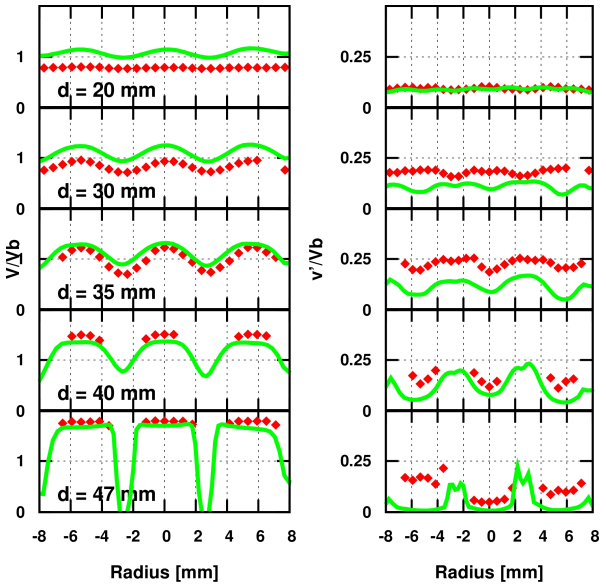

Figure 8.5: Profiles of normalized axial velocities and their fluctuations at upstream distances from the fuel nozzle exit d = 20, 30, 35, 40 and 47 mm. (CFA05 = —, Exp = ♦ [19].

cases (CFA05, CCA05).

The impinging wall acts as obstruction for the jet and causes all axial velocity components to convert into the radial velocity components. The time-averaged axial profiles of radial velocities in Fig. 8.10 predicted at radial position r = 0 mm are almost zero though there is a small tendency of the flow to follow different radial directions. The radial velocities are developing at r = 1 mm and then accelerating at r = 5 mm in agreement with experimental findings. The radial velocity fluctuations at three locations for the CFA05 case are well predicted by simulation, whereas the coarse mesh simulation (CCA05) captures near wall behavior of the radial velocity fluctuation well.

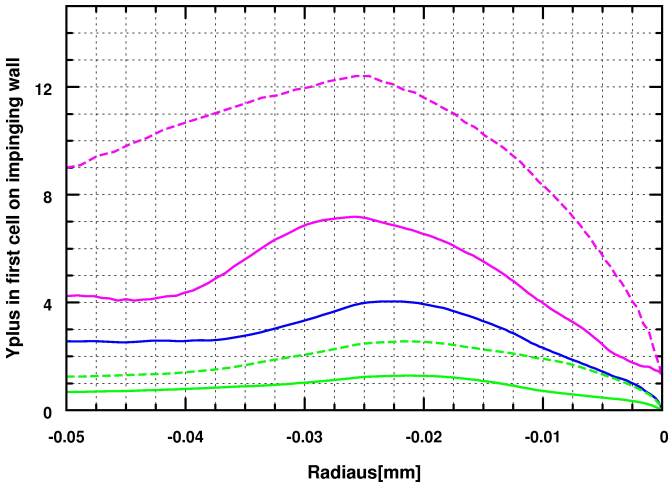

Figure 8.6: y^+ value in the first cell on the wall along the impinging wall stream-wise direction, green line = CFA05, green dashed line = CCA05, blue line = CFA25, pink line = CFA50, pink dashed line = CCA50.

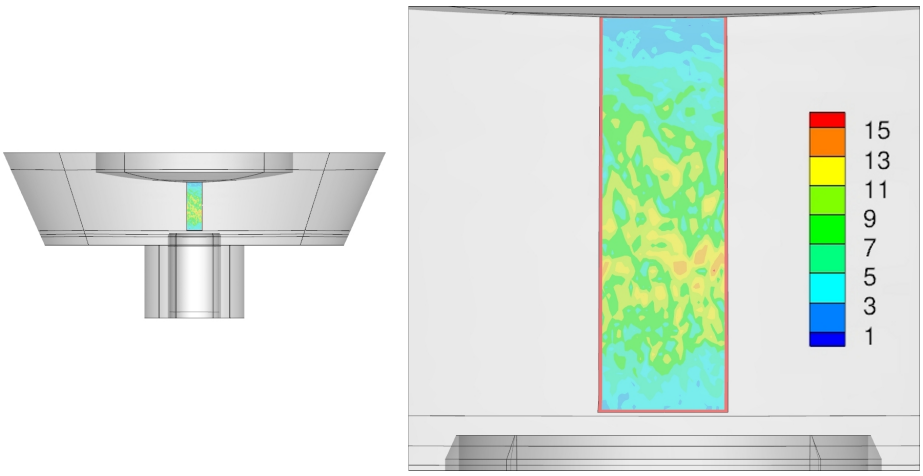

Figure 8.7: $\triangle/\eta$ on a plane passing through the center of the nozzle in the main fuel jet core (zoomed in right figure).

Figure 8.8: Instantaneous axial velocity (left in m/s) and radial velocity (right m/s) contours on a plane passing through the center of the nozzle.

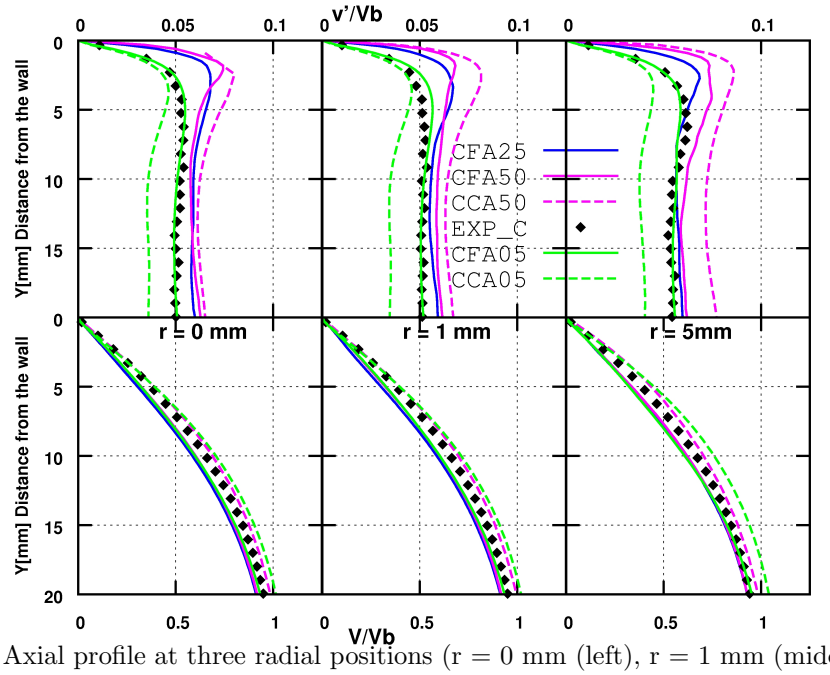

Figure 8.9: Axial profile at three radial positions (r = 0 mm (left), r = 1 mm (middle) and r = 5 mm (right)) of axial velocities (bottom) and their fluctuations (top) normalized by bulk velocity of non-reacting cases [green line = CFA05, green dashed line = CCA05, blue line = CFA25, pink line = CFA50, pink dashed line = CCA50, ♦ = Experiment (Non-reacting case)].

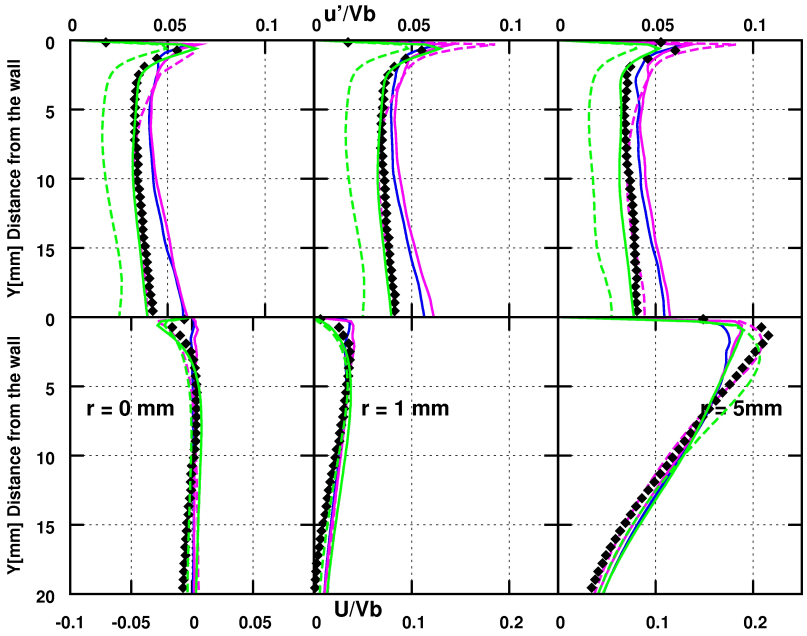

Figure 8.10: Axial profile at three radial positions (r = 0 mm (left), r = 1 mm (middle) and r = 5 mm (right)) of radial velocities (bottom) and their fluctuations (top) normalized by bulk velocity of non-reacting cases [green line = CFA05, green dashed line = CCA05, blue line = CFA25, pink line = CFA50, pink dased line = CCA50, ♦ = Experiment (Non-reacting case)].

In all the cases under study, the simulation could capture the trend on both mesh cases. These findings indicate the mesh resolution near the wall is adequate for all the cases investigated here without using any specific wall boundary treatment. Nevertheless, the fine resolution which keeps y^+ in the order of 1 and $\Delta/\ \eta$ less than 12 near the wall for low Reynolds number flows seems to be sufficient to resolve the flow boundary layer.

8.4.2 Reacting cases

As reported in [232] and pointed out above, basically five types of flames are possible for an impinging premixed fuel jet on water cooled wall, namely the ring flame, the conic flame, the disc flame, the envelop flame and the cool central core flame. The radial flow velocity plays a crucial role in determining this flame shape. If the main flame jet velocity is sufficiently high, the flame detaches the nozzle and stabilizes near the impinging wall forming a disk flame. The latter can be established for wide range of bulk stretch and equivalence ratio based on the flame initiation position. In the present study the flame initiated forms a disk shape flame [131].

Numerically two reacting cases are discussed here. The first one consists of a fuel jet impinging on an adiabatic wall and the second considers a water cooled non-adiabatic wall for the fuel jet $Re = 5000$, for which experimental data are available. Both cases are simulated on both coarse and fine meshes, respectively. For adiabatic simulations, the FGM table based on adiabatic flamelets and boundary conditions as detailed in Table 8.1

is used. Thereby methane and oxygen are given as a fuel inlet at mixture fraction equal to unity. In the present investigated configuration, the maximum mixture fraction is equal to 0.27. The choice of a mixture fraction equal to unity for a premixed fuel composition ($\phi = 1.0$) was not made to avoid the presence of mixture fraction equal to unity, especially on the impinging wall where the flame may be present producing a high heat flux. This is necessary to prevent the use of exclusively extreme end co-ordinate values of the FGM table in the mixture fraction space and thereby to make interpolation simple while ensuring an easier treatment of the scalars boundaries on the impinging wall during the 3D-CFD simulations. This approach brings requirements of more refinement in the mixture fraction co-ordinate in comparison to the case in which the mixture fraction $\xi = 1.0$ is used as a premixed composition of the fuel jet. Note that this table can definetely be used in the case an oxy-fuel combustion is investigated with $\xi = 1.0$ at fuel inlet and nitrogen as the co-flow. For non-adiabatic simulations, FGM tables used are constructed based on both variable enthalpy, burner stabilized flamelets and boundary conditions as listed in Table 8.2. Let us recall that the FGM tables are coupled to LES solver that includes the ATF combustion model as outlined in previous chapters (See Chapter 3).

First, a verification study is carried out in the following subsection to find out the deducability of the adiabatic table from the non-adiabatic one under adiabatic conditions. Then, an assessment of the simulation results obtained by applying the non-adiabatic table is presented.

8.4.2.1 Verification of the non-adiabatic table

1D Case: This verification study is first performed for 1D (one-dimensional) case. Thereby a 1D unsteady premixed combustion case is simulated with FASTEST-3D using the non-adiabatic table by imposing adiabatic boundary conditions for equivalence ratio 1.0. For this study, ξ and Y^* are used to obtain corresponding density, RPV source term, species mass fraction, temperature and molecular viscosity from the adiabatic table. So, for any combination of ξ and Y^* thermochemical properties from both adiabatic and non-adiabatic tables are obtained. This analysis avoids the influence of flow field and physical space and time discretization effects on thermochemical properties. In these 1D cases $\xi = 0.055$ and h (premixed fuel enthalpy at 300 K) remains constant. RPV changes along the flame in space. The temperature, RPV source, density and mass fractions of CO, OH and CH_4 are plotted in Y^* space in Fig. 8.11. Thereby the results obtained using adiabatic and non-adiabatic FGM tables are compared. In particular, predictions from non-adiabatic tables under adiabatic condition are reproduced very well by adiabatic simulations including the adiabatic table, except very minor deviations in the beginning of the flame for RPV source and OH concentrations.

3D Case: Once coupled with the flow field along with the ATF combustion model a 3D case is performed with both adiabatic and non-adiabatic tables under adiabatic conditions. The adiabatic simulation RFA05 is simulated using an adiabatic FGM table, whereas RFA05N is simulated applying a non-adiabatic FGM table. In simulating RFA05N, equations for continuity, momentum, mixture fraction, RPV and enthalpy are solved, while the wall boundaries are treated as adiabatic similar to RFA05. The case

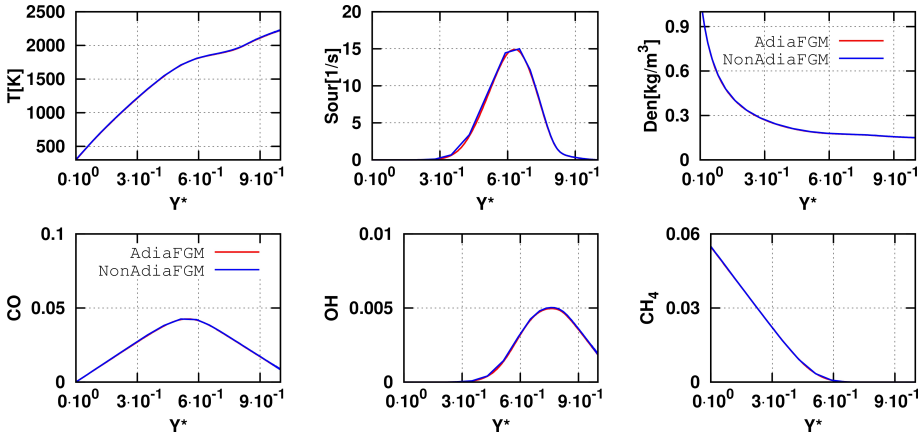

Figure 8.11: Comparison of temperature $[K]$ (top-left), RPV source $[1/s]$ (top-middle), density (kg/m^3)(top-right) and concentrations of CO (bottom-left), OH (bottom-middle) and CH_4(bottom-right) from 1D adiabatic premixed simulations at equivalence ratio 1.0. Red line are results obtained from adiabatic table and blue line results are obtained using non-adiabatic FGM table.

RCA05 is simulated in order to provide the grid sensitivity in adiabatic case. Results obtained from cases RFA05, RCA05 and RFA05N are analyzed in terms of velocities, temperature and CO concentrations.

Time-averaged mean axial velocity and its fluctuations predicted by adiabatic simulation using both adiabatic (RFA05) and non-adiabatic (RFA05N) tables are presented in Fig. 8.12. The mean axial velocity and its fluctuations from both simulations agree well with each other for the fine mesh cases. The coarse mesh results (RCA05) are deviating from the two fine mesh simulations. The time-averaged mean radial velocity and its fluctuations in cases RCA05, RFA05 and RFA05N are plotted in Fig. 8.13. Though overall matching between RFA05 and RFA05N for both mean and fluctuations is noticed, some minor deviations are observed at the flame starting position. However, such deviations are less than 2% in most of the locations and therefore not substantial. The axial profiles of the time-averaged mean CO mass fraction and its fluctuation at radial locations of 0 mm and 20 mm plotted in Fig. 8.14 show that predictions from RFA05N are comparable in magnitude and trend with the results for the case RFA05. Minor deviations in the physical space are nonetheless observed. The coarse mesh simulations are deviating from the fine mesh results, especially for velocity fluctuations. A similar behavior is observed for axial profiles of time-averaged mean temperature plotted in Fig. 8.15. In general, the flame starting position from RFA05N is differed less than 1mm from that of RFA05, though the magnitude and the trend are well comparable. The minor deviations between the profiles of RFA05 and RFA05N may be due to the interpolation methods between different enthalpies in non-adiabatic FGM table, the resolution of the RPV in FGM tables and the combustion modeling effects.

Nevertheless, from the analysis of the 1D case it is demonstrated that the non-adiabatic FGM table can be reduced to an adiabatic table very accurately. In the following section only results from non-adiabatic simulations are now analyzed and compared with experimental data.

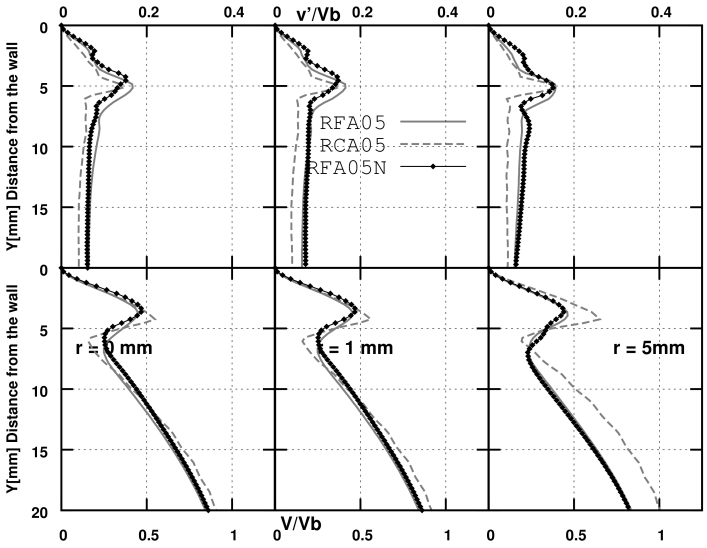

Figure 8.12: Reacting adiabatic cases: Axial profile at three radial positions (r = 0 mm (left), r = 1 mm (middle) and r = 5 mm (right)) of time-averaged axial velocities (bottom) and their fluctuations (top) normalized by bulk velocity of reacting cases, ♦ = Experimental reacting case.

8.4.2.2 Validation of the non-adiabatic simulations

Qualitative analysis

Firstly the qualitative analysis is presented, then some quantitative evaluations are provided. Instantaneous enthalpy contours from the case RFN05 on a plane passing through the center of the nozzle are plotted in Fig. 8.16 (left). Thereby, the line contours of RPV source $[1/s]$ are superimposed on enthalpy contours. The enthalpy remains constant in the main premixed fuel jet and also in the co-flow (which is clipped here). The enthalpy change is observed mainly in two regions, near the wall and in the mixing layer. The enthalpy change near the impinging wall is due to heat losses. In the mixing layer, the enthalpy change is attributed to the mixing of the co-flow with the fuel jet upstream near the nozzle and the hot products near the wall and at the outlet. The flame shape and position are represented by the RPV source term. The flame is wrinkled and present along the wall and also in the mixing layer. Fig. 8.16 (right) is a magnified view of the selected area of Fig. **??** (left). In Fig. 8.16 (right) the flame is present in the non-adiabatic zone, especially near the wall, which shows that the flame is interacting with the wall due to heat losses; it is wrinkled. So, this case is suitable for studying the flame wall interaction combustion modeling. In Fig. 8.17 iso-surface of the OH mass fraction at 0.012 colored by temperature scale (in K) and clipped mixture fraction on a plane passing through the center of the nozzle is shown (Fig. 8.17, left). A magnified view of the selected area is displayed in Fig. 8.17 (right). The flame features disk shape and the wrinkling of the flame can be observed. From the mixture fraction contours and OH iso-surface it can be seen the main part of the flame is represented in a single mixture fraction region, though the flame is present in the mixing layer.

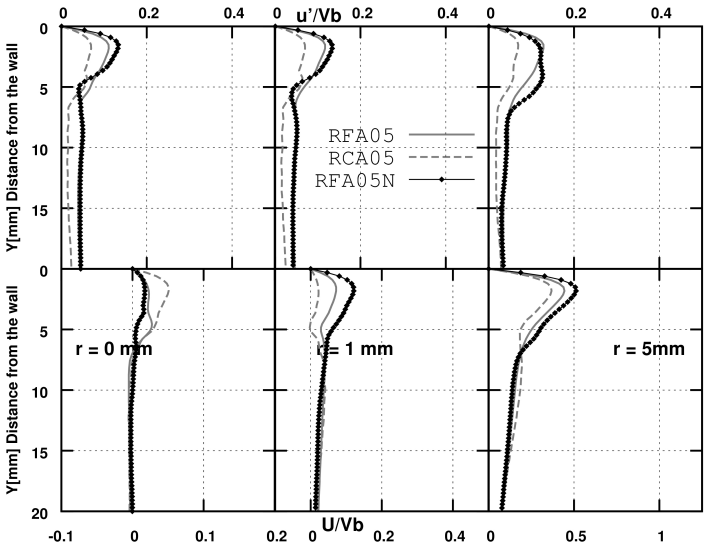

Figure 8.13: Reacting adiabatic cases: Axial profile at three radial positions (r = 0 mm (left), r = 1 mm (middle) and r = 5 mm (right)) of radial velocities (bottom) and their fluctuations (top) normalized by bulk velocity.

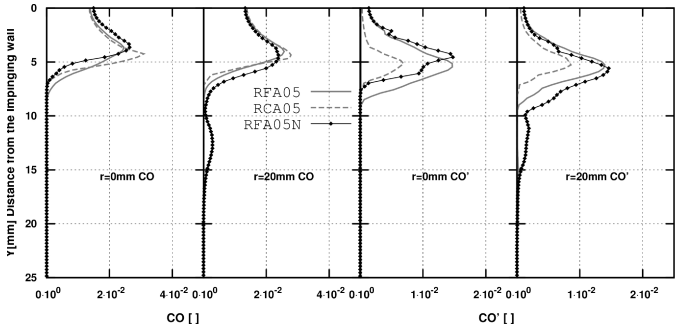

Figure 8.14: Reacting adiabatic cases: Axial profile at two radial positions (r = 0 mm, r = 20 mm) of averaged CO species mass fraction (First two from left) and their fluctuations (last two from right).

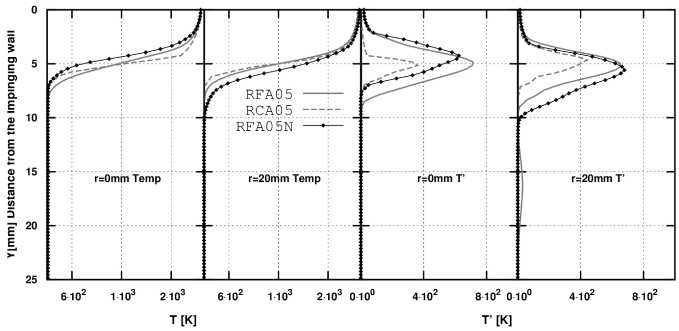

Figure 8.15: Reacting adiabatic cases: Axial profile at two radial positions (r = 0 mm, r = 20 mm) of averaged temperature (First two from left) and their fluctuations (last two from right).

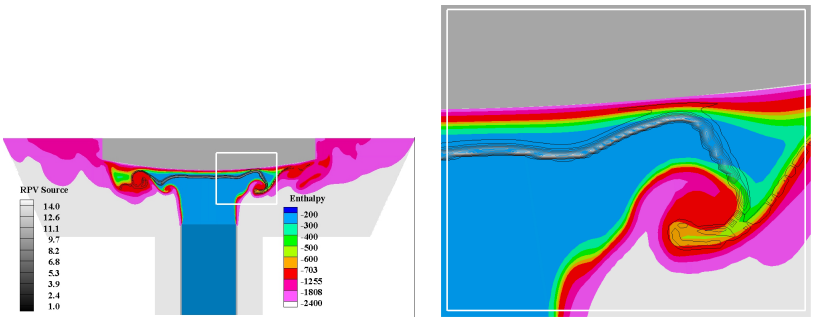

Figure 8.16: Instantaneous enthalpy contours superimposed by line contours of RPV source term (left), a magnified view of the selected area (right)for case RFN05.

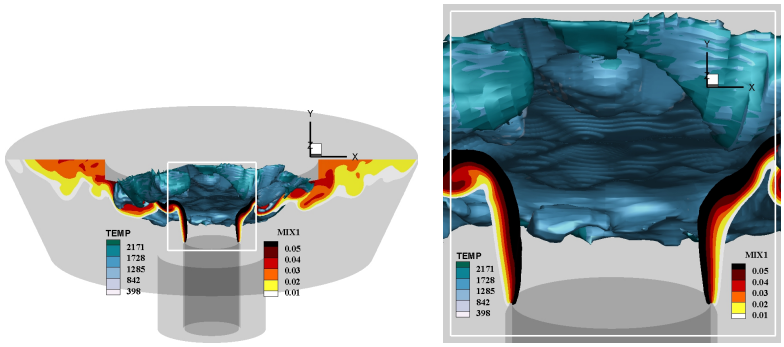

Figure 8.17: Instantaneous iso-surface of OH mass fraction at 0.012 colored by temperature scale (in K) and clipped mixture fraction on a plane passing through center of plane (left) and magnified view of the selected area (right).

Reaction source term contours are plotted in Fig. 8.18 on a plane passing through the center of the nozzle for all four reacting cases (see Table 8.4). The reaction source term, that represents the flame front position, is showing the formation of the disk shape flame. The reaction source term shape, magnitude and location are varying with different mesh resolutions and wall adiabaticity. Under adiabatic conditions the flame features similar shape, thickness, location and magnitude of the reaction source term in both fine and coarse meshes. Thereby the stagnation regions and hot products at the wall are stabilizing the flame. The flame front in the non-adiabatic case is shorter in breadth, marginally shifted toward the downstream region and thereby closer to the wall than that of adiabatic case. The coarse mesh is predicting a thinner flame with a higher magnitude of the RPV source than the finer mesh case. The reaction source term from the FGM table in both cases are of similar order of magnitude, but the time-averaged source term under adiabatic conditions appear lower. In adiabatic cases, the flame is almost perpendicular to the nozzle, while forming convex disk following impinging wall shape. The time-averaged RPV source term in the non-adiabatic case is tending to form a concave shape, especially at the boundaries of the flame disk. This can be attributed to the flame interaction with cold walls and shear layer in mixing regions.

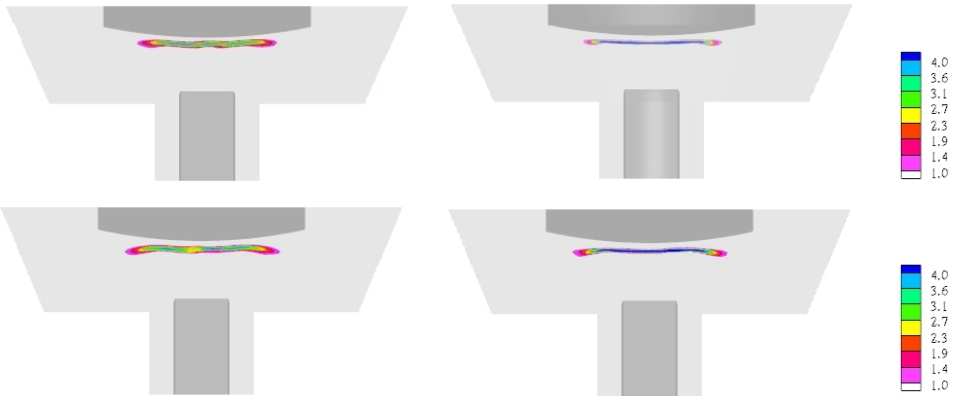

Figure 8.18: Time averaged reaction progress variable source term: Top Left-RFN05, Top Right-RCN05, Bottom Left-RFA05N, Bottom Right-RCA05.

Quantitative analysis

The mean axial profiles starting from the impinging wall for axial velocities and their fluctuations are shown in Fig. 8.19 and corresponding radial velocities are shown in Fig. 8.20. Axial mean velocities are decreasing from the nozzle towards the flame front. They are increasing at the flame front, further decreasing behind the flame front and becoming zero at the wall. RFN05 captures well experimental measurements of axial velocity magnitudes, trends and locations in both acceleration and deceleration regions. Velocity gradients at the wall in deceleration regions in non-adiabatic cases are higher than in adiabatic cases. The mean axial velocities are not influenced by the wall adiabaticity substantially. They are dominated by the stagnation zone induced by the impinging wall. Axial velocity fluctuations from RFN05 agree well with the experimental data and capture satisfactorily the second peak in the vicinity of the impinging wall. The coarse mesh simulation RCN05 could capture the trends of the profiles and locations, but not the magnitude of the measured data. The case under investigation is very sensitive to the mesh resolution for both flow and scalar fields. Time averaged mean radial velocities from RFN05 are matching well the experimental findings, even though some deviations are observed at r = 1 mm. Experimental measurements of radial velocity fluctuations are reproduced by the RFN05 case, but the adiabatic case results miss the profile trend at the location r = 5 mm. The radial velocity deceleration zone is much thinner than the axial velocity deceleration region. The coarse mesh case RCN05 could not reproduce the magnitudes of the experimental radial velocities and their fluctuations. It may be interesting to clarify the effect of heat losses on velocities profiles independently from other effects such as impinging flow. However the chosen boundary conditions do not allow for such a study.

Note that for the same resolution, the flow field results from both adiabatic simulations using a non-adiabatic table (RFA05N) are similar to that of using adiabatic table (RFN05). The FGM approach allows a getting detailed mass fraction of species, temperature and other thermochemical properties which are available in the chemical reaction mechanism used. To analyze the capability of the model implemented, comparisons of scalar quantities are provided. The time-averaged mass fractions of CO and their

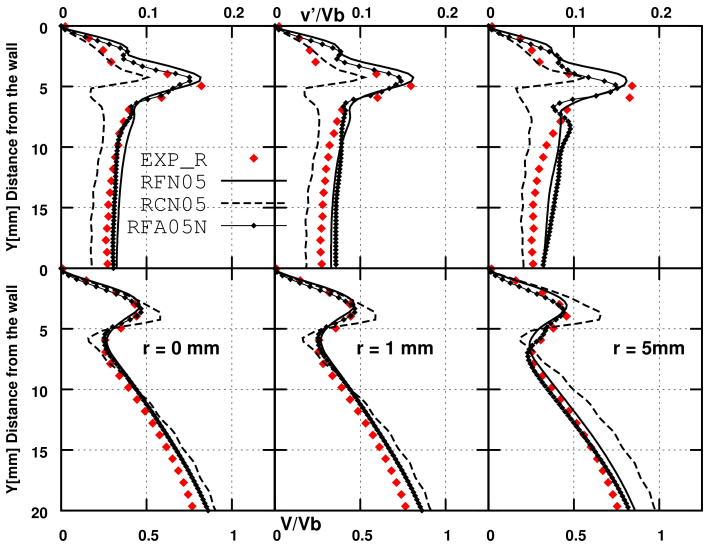

Figure 8.19: Axial profile at three radial positions (r = 0 mm (left), r = 1 mm (middle) and r = 5 mm (right)) of time-averaged axial velocities (bottom) and their fluctuations (top) normalized by the bulk velocity of reacting cases, ♦ = Experimental reacting cas.e

fluctuations are plotted for all four reacting cases in Fig. 8.21 at the radial positions r = 0 mm and 20 mm. The RFN05 case predicts well the mass fractions CO from measurements both in the flame, behind the flame and at the wall. At the center of axis the CO starting position is differed by few millimeters. This behavior at the beginning of flame is also observed in the CO mass fraction variance. This discrepancy needs further investigations. In the adiabatic case higher CO mass fractions are observed near the wall, featuring lower conversion of CO at the adiabatic flame temperature. The CO mass fraction variance at r = 20 mm is different from a non-adiabatic case in all regions of the flame.The mean temperature and its variance are shown in Fig. 8.22. The dependency of the adiabatic results (RFN05N) on mesh for the temperature is replicated here. The flame position in terms of temperature is captured well at both radial positions. The temperature drop due to heat losses on the water cooled wall is predicted well in both RFN05 and RCN05 cases. In particular, the mean temperature fluctuations in Fig. 8.22 (right) show that the trend can be captured better in the RFN05 case, though the peak positions are different. Interestingly the first peak of the temperature fluctuations next to the wall is captured well. The RFA05N adiabatic case temperature at the wall remained at adiabatic temperature as expected and its fluctuation at the wall is reaching a zero value. High fluctuations of CO mass fraction and temperature in experiments and simulation for the RFN05 case show that the flame is wrinkled, fluctuating rapidly and moving from upstream to near wall within the reaction zone.

It can also be clearly pointed out that for the same resolution the scalar field results with the non-adiabatic table (RFN05) agree better with experiments than that those obtained by using the RFA05N adiabatic case.

A further analysis is carried out here to evaluate the heat transfer prediction capability of the combustion LES tool. A one-dimensional heat flux in the wall is given by the

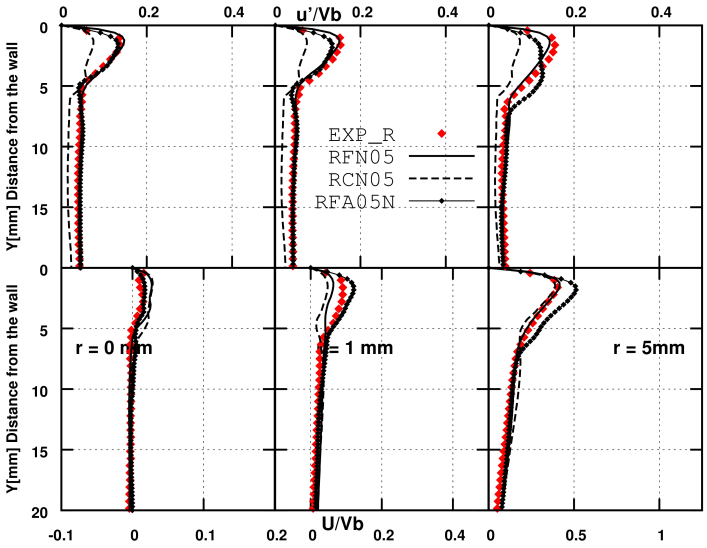

Figure 8.20: Reacting cases: Axial profile at three radial positions (r = 0 mm (left), r = 1 mm (middle) and r = 5 mm (right)) of radial velocities (bottom) and their fluctuations (top) normalized by the bulk velocity.

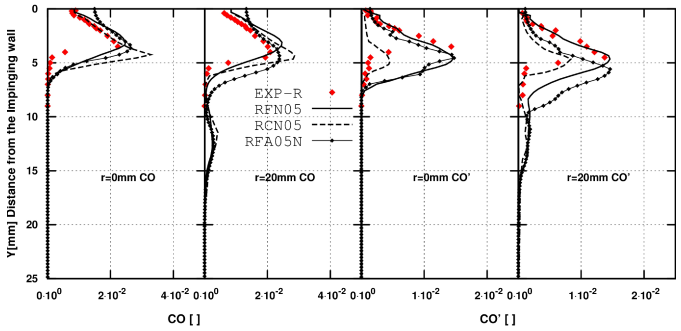

Figure 8.21: Reacting cases: Axial profile at two radial positions (r = 0 mm, r = 20 mm) of averaged *CO* species mass fraction (First two from left) and their fluctuations (last two from right).

Fourier Law of heat conduction as

$$\frac{\dot{q}}{A} = \lambda \frac{dT}{dY} \tag{8.3}$$

where $\dot{q}$ is the heat flux, A heat transfer area, λ the conductivity of the medium and dT/dY the temperature gradient in the medium. The conductivity λ of the gas phase next to the wall and the quartz wall are taken equal to 0.05368 and 1.66 (W/m-K) [184] respectively, in accordance with composition and material properties. In experimental measurements, the temperature gradient is calculated by dividing the difference in the temperature of the two surfaces of the wall by the thickness of the wall (i.e. here 0.003 m). In the simulation, the temperature gradients are calculated by finding the difference between the flame-side surface temperature and the gas temperature closest to the wall. dY is not a constant value as the mesh size may change along the radial position. This is accounted for, in calculating the heat flux of simulations. The obtained heat flux from both measurements (on the impinging disk) and CFD simulations (from the gas side) are plotted in Fig. 8.23 together with the temperature boundary profile imposed on the disk.

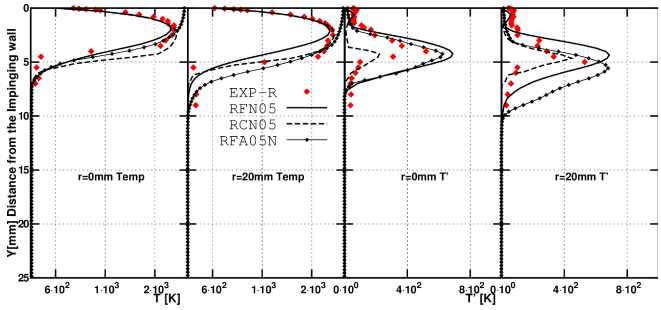

Figure 8.22: Reacting cases: Axial profile at two radial positions (r = 0 mm, r = 20 mm) of averaged temperature (First two from left) and their fluctuations (last two from right).

The implemented FGM based non-adiabatic combustion model captures quantitatively the trend in the center of the impinging disk and in regions beyond 20 mm radius. However, it marginally underpredicts the measured data between the radial positions 5 to 20 mm. The underprediction may be due to the neglecting of the radiation, a thickening in the enthalpy equation, or to a consideration of a constant thermal conductivity in the gas phase. Some issues in measurements of the surface temperature, which is very difficult to capture, could also contribute to these deviations. The heat flux into the wall is following the trend of the imposed temperature (see Fig. 8.23). The heat flux analysis on the impinging wall based on an overall heat transfer coefficient is presented for a better understanding.

$$\texttt{Heat flux} = \frac{\dot{q}}{A} = \lambda \frac{dT}{dY} = \lambda \frac{T_s - T_w}{dY} = U_0 \left(T_f - T_s\right) \tag{8.4}$$

where T_f = adiabatic (or maximum) flame temperature at the corresponding radial position, T_s = wall temperature on the gas side, T_w wall temperature on the water cooled side, U_o = heat transfer coefficient.

Here four 1D flames are considered at r = 0, 20, 30 and 40. Each 1D flame is schematically sketched by the representation in Fig. 8.24. The measured data of temperature on the water side wall temperature, the flame side wall temperature, the maximum temperature at each radial position and the wall thermal conductivity are available from the experimental measurements. The heat transfer coefficient is determined by substituting both the temperature and the conductivity data in the above equation (Eq. 8.4) and shown in Fig. 8.25. Thus the heat transfer coefficient is obtained using the above relation at these four radial positions. A correlation of U_o is obtained as a function of the impinging disk's radius and plotted in Fig. 8.25. Now, it can be assumed that U_o includes the effects from the both convective and the radiative heat transfers. The same U_o is used for calculating the heat flux from the gas phase in simulations. T_f is determined as the maximum temperature of 1D flame on that particular radial position from a simulation corresponding to a 3D case. The heat flux from measurements and the heat flux obtained from the simulations using a heat transfer coefficient are plotted in Fig. 8.25. The heat flux estimated from simulations on the impinging wall are very closely matching with experimental values, though some deviations are observed beyond the radial position of 30 mm.

Even though the heat flux predictions are encouraging a deeper investigation is required in the future by consistently incorporating radiation models in the CFD. In the next section a brief analysis of thermal and flow boundary layers is carried out.

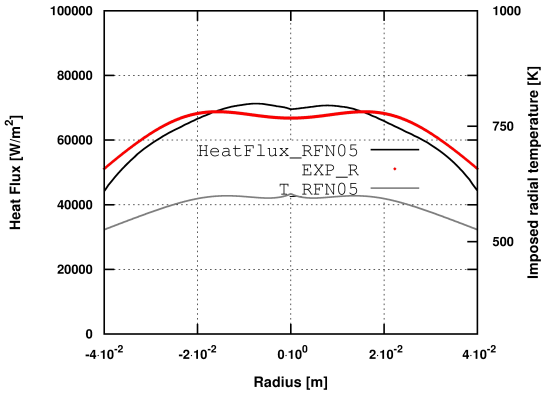

Figure 8.23: Radial heat flux on impinging wall, radial temperature profile imposed on the impinging wall in CFD simulations for RFN05 case. (measured heat flux = ♦ , simulated heat flux = — , Temperature profile imposed = —).

Figure 8.24: Schematic representation of a 1D premixed stagnation point flame on the water cooled non-adiabatic wall (thick orange line represents temperature profile).

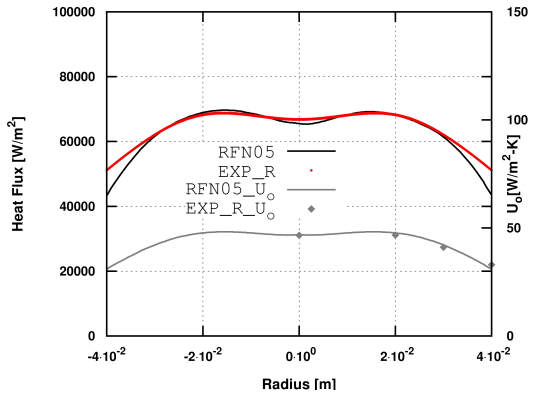

Figure 8.25: Radial profiles heat flux on impinging wall, radial temperature profile imposed on impinging wall in CFD simulations for RFN05 case. Results are obtained using heat transfer coefficient (measured heat flux = ♦ , simulated heat flux = — , Heat transfer coefficient = —, (Calculated heat transfer coefficient from measured data = ♦).

8.4.3 Outline of thermal and flow boundary layer analysis

The Prandtl number which is the ratio of the viscous diffusion rate to the thermal diffusion rate plays an important role in determining the thermal and fluid boundary layers. On a flat plate, the fluids with Prandtl number below 1 develop a thermal boundary layer which is thicker than that of flow boundary layer. This thermal boundary layer is thinner than the fluid boundary layer for Prandtl number greater than 1 as analyzed in [61]. Focused on the RFN05 case, both the thermal and fluid boundary layer profiles are plotted in Fig. 8.26. Thereby radial velocities normalized by the mean bulk velocity of the fuel jet are plotted at the radial positions r = 1, 5, 10, 15 and 20 mm in the axial direction starting from the impinging wall. The temperatures are normalized by the adiabatic flame temperature and the cold flow jet temperature according to the relation

$$T_N = \frac{T_a - T}{T_a - T_f} \tag{8.5}$$

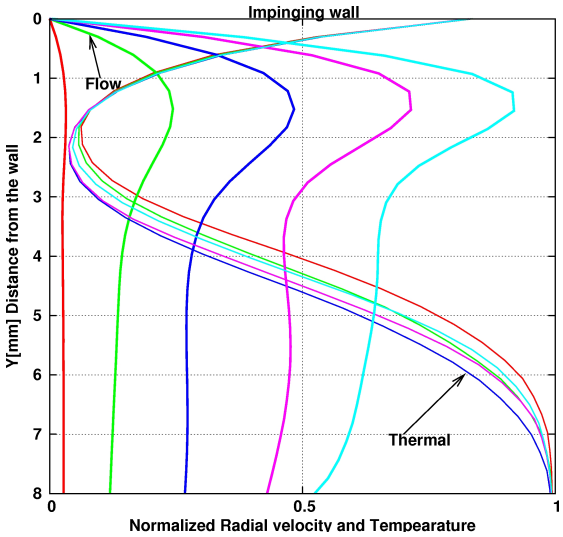

Figure 8.26: Axial profiles of flow and thermal boundary layers comparison from case RFN05 on radial positions of r = 1 mm (red), r = 5 mm (green) , r = 10 mm (blue) , r = 15 mm (pink) and r = 20 mm (aqua). Note that local gas temperature (T) at T_N = 1 corresponds to premixed fuel jet temperature and at T_N=0 to adiabatic flame temperature.

where T_N is the normalized temperature, T_a the adiabatic flame temperature, T the local temperature and T_f the fuel jet temperature. The investigated configuration RFN05 case is characterized by a Prandtl number below one. It turns out that the boundary layer is always very thin compared to that of the flat plate, especially around the impinging core. The flow boundary layer lies between 1 to 1.8 mm. This boundary layer is getting steeper away from the center due to the impinging jet. The thermal boundary layer is almost constant at 2 mm at all radial positions and of the same order of magnitude at all radial positions. The constant thermal boundary layer thickness and the magnitude are due to the combustion phenomena which are taking place along the impinging wall as shown in Fig. 8.18. The formation of thicker thermal boundaries compared to flow boundaries on an impinging wall proves that the mesh resolution taken for cold flow simulations is also sufficient for reacting cases. This is confirmed by the good agreement between simulated

Table 8.5: 3D case details, All cases with premixed methane at $\phi = 1.0$ and N_2 as Co-flow. Note that the case F5 corresponds to Re = 5000, Le = 1, Efficiency = 1, Mix = Yes RPV = Yes and with constant thickening factor of 2.

Case	N_{Re}	**FGM**	ATF	
		Table	Mix	RPV
F1	5000	Le = 1	No	Yes
F2	5000	Le = 1	Yes	Yes
F3	5000	MixAvg	No	Yes
F4	5000	MixAvg	Yes	Yes

results and experimental data of velocity components and scalars near the wall (Fig. 8.19, 8.20, 8.21 and 8.22).

8.5 Dependency of wall heat flux on Lewis number in FGM table

The 3D simulations of the previous section were carried out using a single mixture fraction FGM table. Therefore, the combustion properties in the mixing region with the ambient and especially with the co-flow cannot be captured precisely. All flamelets covering the mixture fraction in the flammability region were considered to understand and analyze the effect of the fineness of flamelets construction in mixture fraction space. Further to understand the influence on wall heat flux in non-adiabatic combustion systems effect of integrating Lewis number into the FGM table were analyzed. The LES solver however considered here is a unity Lewis number based for both types of FGM tables considered, namely unity Lewis and Mixture averaged Lewis number tables. Note that more accurate method is to consider the Lewis number effect also in LES solver and thereby solving the equations Eq. 3.86, Eq. 3.85 and Eq. 3.84 for enthalpy, mixture fraction, and reaction progress variable respectively, which is not in the scope of the present thesis work.

In this part of work four different test cases were analyzed and their details are presented in Table. 8.5. The thickening influence on mixture fraction transport equation is critical as the configuration allows mixing of the partially burnt mixture with ambient. This phenomenon cannot be captured using the single mixture fraction definition adapted in the previous sections of this work. Therefore thickening effect of mixture fraction is also investigated here.

The mean axial profiles starting from the impinging wall for axial velocities and their fluctuations are shown in Fig. 8.27 and corresponding radial velocities are shown in Fig. 8.28. Axial mean velocities are decreasing from the nozzle towards the flame front. They are increasing at the flame front, further decreasing behind the flame front and becoming zero at the wall. F1, F2 and F5 cases capture well experimental measurements of axial velocity magnitudes, trends and locations in both acceleration and deceleration regions, whereas F3 and F4 cases, which were simulated with a mixture averaged FGM

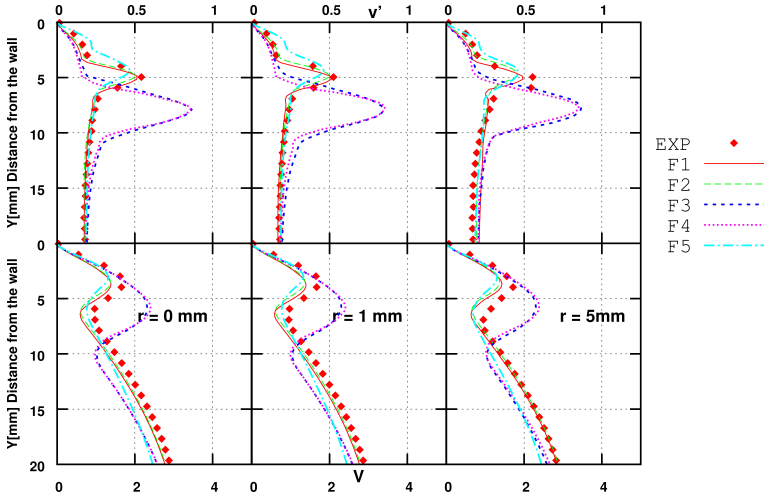

Figure 8.27: Axial profile at three radial positions (r = 0 mm(left), r = 1 mm(middle) and r = 5 mm(right)) of time-averaged axial velocities(bottom) and their fluctuations(top) normalized by the bulk velocity of reacting cases,♦ = Experimental reacting case

table, were not able to capture trend or magnitude in the flame region. Axial velocity fluctuations from both F1 and F2 agree well with the experimental data. F5 (RFN05) case describes satisfactory this behavior but over-predicts near wall turbulence. Though F3 and F4 cases were estimating wall turbulence well, the location and magnitude of peak could not be captured satisfactorily. Similar behaviors were found for radial velocity profiles, though F1 case achieves better prediction than the other cases. It was expected that both F1 and F2 provide exactly the same behavior in the fuel jet region. The flame wrinkling was influenced by the shear layer and, in turn, was modifying the wall turbulence. This results in different predictions from F1 and F2 in the flame region. The temperature profiles for all five cases were compared with the experimental data at the radial positions r = 0 mm and 20 mm in Fig. 8.29. All cases F1-F5 could predict well the steep temperature drop at the cold wall. The flame starting position was different in F3 and F4 from other three simulated cases. F1, F2 and F5 (RFN05) were starting at the same position and agree well with experimental findings. Interestingly the flame thickness zone with higher temperature was better predicted at r = 20 mm by both F3 and F4 cases. The higher temperature at r = 20 mm in the upstream is due the flame tending to attach to the nozzle in F3 and F4 cases. This agrees with the second flame stabilization point of this investigated configuration.

All cases investigated here could capture two peaks in temperature fluctuations, temperature magnitude, trend, and flame thickness but could not capture well the flame position accurately as shown in Fig. 8.29. The Lewis number unity FGM table (RFN05) with a thickening of the RPV transport equation was only able to produce measured data more accurately than its counterpart cases considered here. The simulated cases with non-unity Lewis FGM tables which were constructing using mixture averaged diffusion coefficient based flamelets were resulting the final flame tending to attain the second flame stabilization point of the configuration as observed in experimental findings. Only F4 and F5 cases are compared with experimental data for CO mass fraction in Fig. 8.29 due to availability the statistical data collected. The CO annihilation experimentally

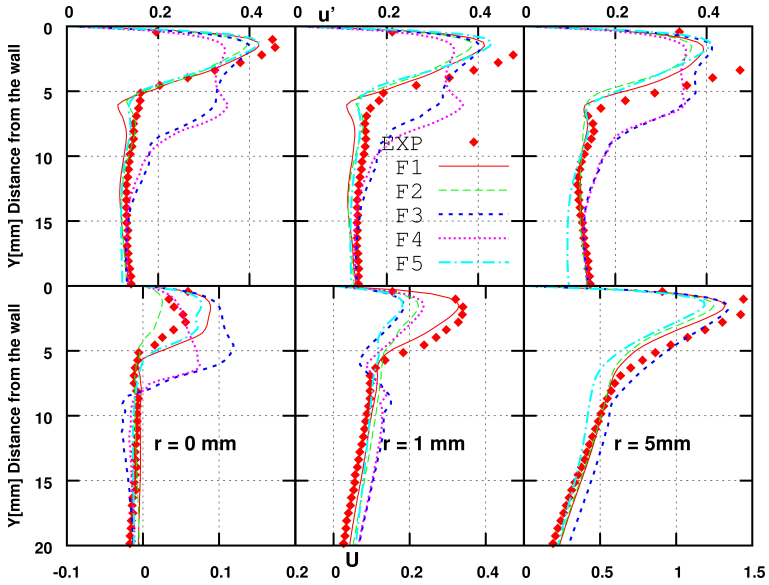

Figure 8.28: Reacting cases: Axial profile at three radial positions (r = 0 mm(left), r = 1 mm(middle) and r = 5 mm(right)) of radial velocities(bottom) and their fluctuations(top) normalized by the bulk velocity

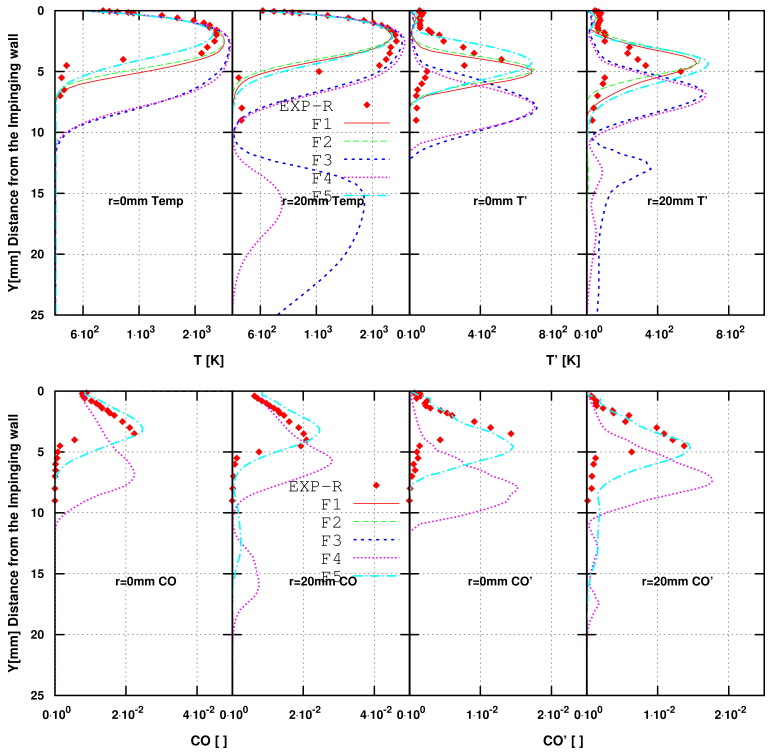

Figure 8.29: Bottom: Axial profile at two radial positions (r = 0 mm, r = 20 mm) of averaged CO species mass fraction (First two from left) and their fluctuations(last two from right), Top: Axial profile at two radial positions (r = 0 mm, r = 20 mm) of averaged temperature (First two from left) and their fluctuations(last two from right)

measured was captured well by both F4 and F5 cases at r = 20 mm and only by F5 at r = 0 mm; again CO starting position in the flame was captured better by F5 case. The F5 case could reproduce measured fluctuations of CO in annihilation region. The reason for the missing prediction of CO may be due to the difference between the variable Lewis number considered in FGM table flamelets construction and unity Lewis number assumption used in LES solver, which need to be investigated further by having consistency between both FGM table and CFD solver.

Interestingly near wall combustion physics was captured well by both FGM tables here considered. A mathematically consistent ATF model by thickening both mixture fraction and RPV and the one that thickens only RPV were analyzed. It was found though major differences were not observed between them; the shear layer which was enhanced by impinging flow is very sensitive to ATF model. It is evident that both shear layer and RPV may not be present in all CVs at the same point in time and/or physical space. The especially presence of shear layer in the case of coarse mesh next to the flame is very prone to produce susceptible results. This leads to better predictions of F1 case over F2. The fine mesh should be retained in shear layer, where there is a chance of the presence of the flame even in the distant neighbor CVs.

It was found that, though the flame sensor within the ATF model is active only in the flame region, the thickening of the mixture fraction is very sensitive to the mesh resolution. If the thickening of the mixture fraction is excluded, better agreement of predictions from the model with experimental data was achieved. However, very fine meshes are required even in the shear layer, as the turbulent fluctuating flame sometimes also present in far-reaching coarse mesh regions. Secondly, the effects of including the Lewis number unity and the mixture averaged diffusion coefficients in generating FGM tables' flamelets have been pointed out. Especially, the unity Lewis number table allows for performing better predictions of the flow field, the thermal and combustion properties. Whereas the mixture averaged FGM (MFGM) table tends to produce a flame attached to the fuel jet nozzle. It was observed from experimental investigations that two flame stabilization points could be established for a given fuel jet velocity with the Reynolds number around 5000, depending on the flame initialization on the physical space. These flame stabilization points were on nozzle and on the water cooled impinging disk.

Further, the heat transfer phenomenon associated with FWI was analyzed following the same methodology of section 8.4.3. The heat flux into the wall is obtained based on the wall temperature from experimental (see Fig. 8.23) investigation imposed in LES model. The obtained wall heat fluxes from all 5 cases here are presented in Fig. 8.30. All five simulated cases were able to produce heat flux trends of experimental findings. Interestingly the F3 and F4 cases accurately predicting measured heat flux both in magnitude and trend. F5 case partly predicting the magnitude, whereas F1 and F2 case were under predicting the wall heat flux. The difference between the wall heat flux predictions clearly shows the influence of FGM table considered here and partly also ATF model. For F3 and F4 cases the flame predicted by it is away from the other cases considered here independent of ATF model for mixture fraction is active or not. It is also observed that ATF model for mixture fraction doesn't influence the wall heat flux predictions (F1 vs F2 and F3 vs F4). However, ATF model of RPV

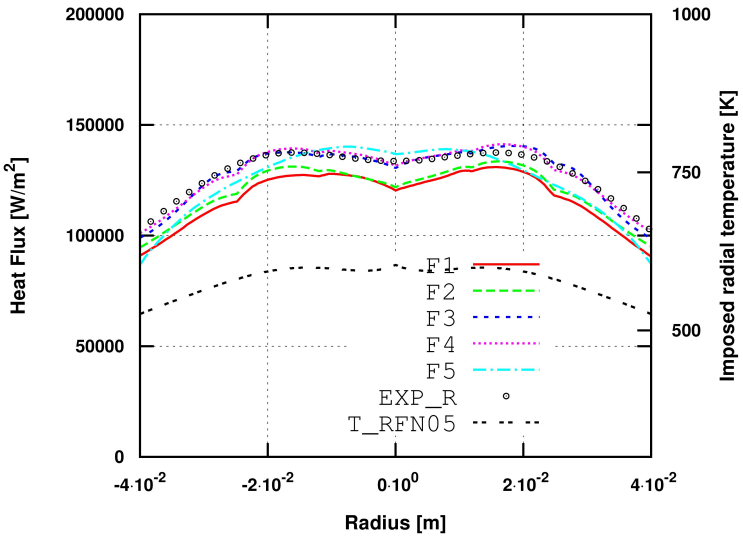

Figure 8.30: Radial heat flux on impinging wall, radial temperature profile imposed on the impinging wall in CFD simulations for F1, F2, F3, F4 and F5 cases

is influencing the prediction of wall heat flux as compared F2 with that of F5 case. The heat flux values on the impinging wall could be predicted more accurately by the MFGM than the unity Lewis number based FGM table. This seems to be the accurate methodology to generate FGM tables to include near-wall kinetic effects. Therefore, it is interesting to investigate further the influence of ATF model by considering thickening of enthalpy equation on wall heat flux, on flame position and flame stabilization point.

8.6 Conclusions

A premixed methane-air fuel jet injected through a pipe and impinged on a water cooled spherical disk has been investigated at three different Reynolds numbers using a coupling of the FGM and ATF combustion models in LES context. Two aspects were especially addressed in this thesis. The first focus was on the grid resolution required near the wall without including a special wall-adapted SGS modeling in reacting configurations. The second aspect was devoted to the integration of the near wall kinetic effects into the FGM framework. Though advanced wall SGS models are advantageous, the detailed analysis has shown that a fine resolution can be sufficient for capturing both flow and scalar fields in near-wall regions for both reacting and non-reacting cases. Mesh resolutions near the wall satisfy the condition y^+ equal to 1 for resolving flow and thermal boundary layer with LES. In particular for reacting case, the new FGM development that includes enthalpy as additional variable to account for non- adiabaticity allowed to predict well both combustion and flow properties near the wall. An evaluation of the thermal boundary layer has also been provided. Secondly, the effects of including the Lewis number unity and the mixture averaged diffusion coefficients in generating FGM table's flamelets have been pointed out. Particularly, the unity Lewis number table allows for performing better predictions of the flow field, the thermal and combustion properties. Whereas the mixture averaged FGM (MFGM) table tends to produce a flame attached to the fuel

jet nozzle. Finally, the heat flux values on the impinging wall could be predicted more accurately by the MFGM than the unity Lewis number based FGM table. This seems to be the accurate methodology to generate FGM tables including near-wall kinetic effects. Comparisons with achievements by integrating wall adapted SGS modeling is left for future work.

Chapter 9

Conclusions and Outlook

The objective of this work was to develop a Large Eddy Simulation-based method including an advanced sub-grid scalar flux model for reactive flows, and extending the FGM combustion modeling technique in order to handle complex fuels and non-adiabatic flame wall interactions. The focus has been placed mainly on four aspects:

1. Modeling of advanced sub-grid scalar fluxes for reactive high and low Schmidt number flows. This allows predicting the scalars on coarser meshes more accurately than with existing models

2. Use of the FGM approach to avoid the solving hundreds of species and thousands of reactions for complex fuels including pre-vapourized kerosene

3. Thickening of the flame on coarser grid to reduce fine mesh requirement especially for premixed case

4. Extension of FGM table to non-adiabatic combustion for predicting heat loss

The 3D CFD code used FASTEST3D LES solver is a pressure based flow solver suitable for complex configurations. The scalars are solved using a TVD scheme to achieve a bounded, monotonous transport of the combustion physics. To account for large spatio temporal density variations of low Mach number flow combustion systems, the standard pressure correction approach is adapted.

In this work, a new anisotropic SGS scalar flux model has been assessed using highly resolved experimental measurements in both non-reacting and reacting premixed configurations characterized by high Reynolds numbers for which DNS-data are not available. To better describe the premixed combustion, a flamelet generated manifold (FGM) tabulated chemistry approach has been used, in which a variable local equivalence ratio due to a possible entrainment of the environment air was included through a mixture fraction variable. The behavior of SGS scalar fluxes was especially analyzed. Besides experimental data, LES results obtained by the use of other existing SGS scalar flux models have been considered. In both configurations, the new anisotropy model showed a better predicting ability for both the SGS and the resolved quantities than the classical eddy diffusivity model with or without a dynamic computation of the model coefficient as usually applied. The new model also allowed achieving LES results for the flow and scalar field that are in a better agreement with experimental data. The computational cost for same grid resolution is not substantially different (around 1%) in both reacting

and non-reacting environments.

The same approach is extended for a more complex fuel, flow, and geometrical system. Here a LES based advanced combustion model for a reliable description of combustion processes in a gas turbine combustion chamber has been developed and implemented in the FASTEST-3D code. In addition, both simple scalar flux model and advanced scalar flux models were analyzed for this purpose. The numerical approach including FGM method based combustion model was successfully assessed with respect to its prediction capability of the flow and combustion characteristics. In particular, the complex flow field properties in the single sector combustion chamber are captured well. However, it could be pointed out that turbulent kinetic energy at 5 mm from the exit of the nozzle is not in agreement with the experimental data. The results further show that the flame is not always attached to the nozzle and appears to fluctuate in time. Power spectral densities deduced from temporal autocorrelations (via FFT) predicted by the LES CFD model from simulations could capture accurately the two peak frequency recorded from experimental finding.

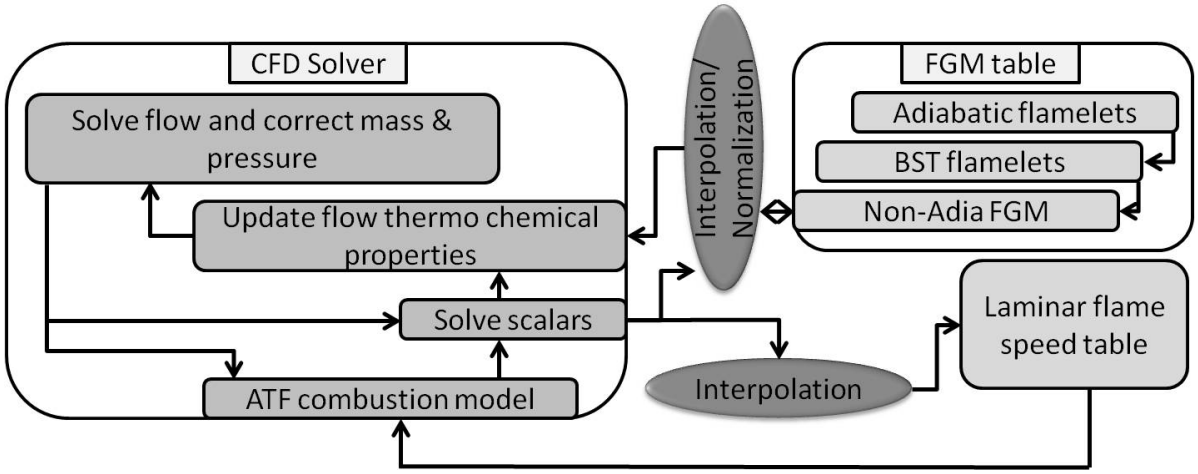

Figure 9.1: Flow diagram for chronological interactive flame wall interaction CFD model in FASTEST3D CFD solver

In the last part, the work is dedicated to extending the LES based FGM combustion modeling to non-adiabatic combustion. Here non-adiabatic combustion is described using the FGM table which accounts for enthalpy by means of an additional variable (total enthalpy) and is coupled with LES based CFD solver FASTEST3D taking advantage of ATF combustion model. The investigated configuration is a premixed methane-air fuel jet injected through a pipe and impinged on a water cooled spherical disk. It operated at three different Reynolds numbers. Two aspects were especially addressed in this work, the first focus was on the grid resolution required near the wall without including a special wall-adapted SGS modeling in reacting configurations. The second aspect was devoted to the integration of the near wall kinetic effects into the FGM framework. Though advanced wall SGS models are advantageous, the detailed analysis has shown that a fine resolution can be sufficient for capturing both flow and scalar fields in near-wall regions for both reacting and non-reacting cases. Mesh resolutions near the wall

satisfy the condition y^+ equal to 1 for resolving flow and thermal boundary layer with LES. In particular for reacting case, the new FGM development that includes enthalpy as an additional variable to account for non-adiabaticity allowing to predict well both combustion and flow properties near the wall.The complete model developed, successfully validated and applied here can be represented for flame-wall interaction study by the flow chart in Fig.9.1.

Furthermore, an evaluation of the thermal boundary layer has also been provided. Thereby, the effects of including the unity Lewis number and the mixture averaged diffusion coefficients in generating FGM table's flamelets have been presented. Especially, the unity Lewis number table allows for performing better predictions of the flow field, the thermal and combustion properties. Whereas the mixture averaged FGM (MFGM) table tends to produce a flame attached to the fuel jet nozzle. Finally, the heat flux values on the impinging wall could be predicted more accurately by the MFGM than the unity Lewis number based FGM table. This seems to be the accurate methodology to generate FGM tables for including near-wall kinetic effects. The use of consistent transport equations for the variables with non-unity Lewis numbers as well as comparisons with achievements by integrating wall adapted SGS modeling are left for future work.

Reference list

[1] W. Ahmadi. "Study of turbulent dispersion modelling effects on dispersed multiphase flows properties." PhD thesis. Darmstadt: Technische Universität Darmstadt, June 2013.

[2] J. Alam, Z Wadud, and J. Polak. "Energy demand and economic consequences of transport policy." In: *International Journal of Environmental Science and Technology* (2013), pp. 1–8.

[3] B. Albrecht, S. Zahirovic, R. Bastiaans, J. Van Oijen, and L. De Goey. "A Premixed Flamelet- PDF Model for Biomass Combustion in a Grate Furnace." In: *Energy & Fuels* 22.3 (2008), pp. 1570–1580.

[4] A. Alkidas. "Combustion-chamber crevices: the major source of engine-out hydrocarbon emissions under fully warmed conditions." In: *Progress in energy and combustion science* 25.3 (1999), pp. 253–273.

[5] J. Andrae, P. Björnbom, and L. Edsberg. "Numerical studies of wall effects with laminar methane flames." In: *combustion and Flame* 128.1 (2002), pp. 165–180.

[6] J. Andreopoulos and W. Rodi. "Experimental investigation of jets in a crossflow." In: *J. Fluid Mech* 138.1 (1984), pp. 93–127.

[7] C. Angelberger, T. Poinsot, and B. Delhay. "Improving near-wall combustion and wall heat transfer modeling in SI engine computations." In: *Training* 2009 (1997), pp. 01–26.

[8] C. ANSYS. *Release 14.0–Documentation*. 2011.

[9] I. C. ANSYS. "13: Geometry and Mesh Generation Preprocessor." In: *Ansys Inc* (2012).

[10] S. Armfield. "Ellipticity, accuracy, and convergence of the discrete Navier-Stokes equations." In: *Journal of Computational Physics* 114.2 (1994), pp. 176–184.

[11] J. Bardina, J. Ferziger, and W. Reynolds. "Improved Subgrid-Scale Models based on Large-Eddy Simulation of Homogeneous, Incompressible, Turbulent Flows." In: *Stanford Report TF-19* 194 (1983), pp. 53–63.

[12] G. K. Batchelor. *An introduction to fluid mechanics*. Cambridge University Press, 1967.

[13] H. Baya Toda, O. Cabrit, K. Truffin, G. Bruneaux, and F. Nicoud. "A Dynamic Procedure for Advanced Subgrid-scales Models and Wall-bounded Flows." In: (2011).

[14] C. Bekdemir, B. Somers, and P. de Goey. "DNS with detailed and tabulated chemistry of engine relevant igniting systems." In: *Combustion and Flame* (2013).

[15] J. B. Bell, M. S. Day, and J. F. Grcar. "Numerical simulation of premixed turbulent methane combustion." In: *Proceedings of the Combustion Institute* 29.2 (2002), pp. 1987–1993.

[16] L. L. C. Berselli, T. Iliescu, and W. W. J. Layton. *Mathematics of large eddy simulation of turbulent flows*. Springer, 2006.

[17] R. Bilger. "Conditional moment closure for turbulent reacting flow." In: *Physics of Fluids A: Fluid Dynamics* 5 (1993), p. 436.

[18] R. B. Bird, W. E. Stewart, and E. N. Lightfoot. *Transport phenomena*. Wiley. com, 2007.

[19] B. Boehm, O. Stein, A. Kempf, and A. Dreizler. "In-Nozzle Measurements of a Turbulent Opposed Jet Using PIV." In: *Flow, Turbulence and Combustion* 85 (2010), pp. 73–93.

[20] R. Borghi. "On the structure and morphology of turbulent premixed flames." In: *Recent advances in the Aerospace Sciences*. Springer, 1985, pp. 117–138.

[21] R. Borghi. "Turbulent combustion modelling." In: *Progress in Energy and Combustion Science* 14.4 (1988), pp. 245–292.

[22] B. Boust, J. Sotton, S. Labuda, and M. Bellenoue. "A thermal formulation for single-wall quenching of transient laminar flames." In: *Combustion and flame* 149.3 (2007), pp. 286–294.

[23] D. Bradley. "How fast can we burn?" In: *Symposium (International) on Combustion*. Vol. 24. 1. Elsevier. 1992, pp. 247–262.

[24] N. Branley and W. Jones. "Large eddy simulation of a turbulent non-premixed flame." In: *Combustion and Flame* 127.1 (2001), pp. 1914–1934.

[25] G. Brethouwer, B. Boersma, M. Pourquié, and F. Nieuwstadt. "Direct numerical simulation of turbulent mixing of a passive scalar in pipe flow." In: *European Journal of Mechanics-B/Fluids* 18.4 (1999), pp. 739–756.

[26] G. Bruneaux, T. Poinsot, and J. Ferziger. "Premixed flame–wall interaction in a turbulent channel flow: budget for the flame surface density evolution equation and modelling." In: *Journal of Fluid Mechanics* 349.1 (1997), pp. 191–219.

[27] G. Bruneaux, K. Akselvoll, J. Ferziger, and T. Poinsot. "Flame wall interaction in channel flow Combustion and Flame." In: 107 (1996), pp. 27–44.

[28] G. C. Burton and W. J. Dahm. "Multifractal subgrid-scale modeling for large-eddy simulation. I. Model development and a priori testing." In: *Physics of Fluids* 17.7 (2005), p. 075111.

[29] T. Butler and P. O'Rourke. "A numerical method for two dimensional unsteady reacting flows." In: *Symposium (International) on Combustion*. Vol. 16. 1. Elsevier. 1977, pp. 1503–1515.

[30] W. Cabot and P. Moin. "Large eddy simulation of scalar transport with the dynamic subgrid-scale model." In: *Large eddy simulation of complex engineering and geophysical flows* (1993), pp. 141–158.

[31] W. Cabot and P. Moin. “Approximate wall boundary conditions in the large-eddy simulation of high Reynolds number flow.” In: *Flow, Turbulence and Combustion* 63.1-4 (2000), pp. 269–291.

[32] Cantera. *An object-oriented software toolkit for chemical kinetics, thermodynamics, and transport processes*. available at https://code.google.com/p/cantera/, 2013.

[33] N. Chakraborty and R. Cant. “Direct numerical simulation analysis of the flame surface density transport equation in the context of large eddy simulation.” In: *Proceedings of the Combustion Institute* 32.1 (2009), pp. 1445–1453.

[34] F. Charlette, C. Meneveau, and D. Veynante. “A power-law flame wrinkling model for LES of premixed turbulent combustion Part I: Non-dynamic formulation and initial tests.” In: *Combustion and Flame* 131.1 (2002), pp. 159–180.

[35] M. Chauvy, B. Delhom, J. Reveillon, and F.-X. Demoulin. “Flame/Wall interactions: laminar study of unburnt HC formation.” In: *Flow, turbulence and combustion* 84.3 (2010), pp. 369–396.

[36] Chem1D. *A one-dimensional laminar flame code*. available at www.tue.nl/combustion: Eindhoven University of Technology, 2013.

[37] J. Chen, J. Katz, and C. Meneveau. “Implication of mismatch between stress and strain-rate in turbulence subjected to rapid straining and destraining on dynamic LES models.” In: *Journal of fluids engineering* 127.5 (2005), pp. 840–850.

[38] A. Chorin and J. Marsden. *A Mathematical Introduction to Fluid Mechanics*. Texts in Applied Mathematics. Springer, 1993. ISBN: 9780387979182.

[39] M. Chrigui. “Eulerian-Lagrangian approach for modeling and simulations of turbulent reactive multi-phase flows under gas turbine combustor conditions.” PhD thesis. TU Darmstadt, 2005.

[40] M. Chrigui, J. Gounder, A. Sadiki, A. R. Masri, and J. Janicka. “Partially premixed reacting acetone spray using LES and FGM tabulated chemistry.” In: *Combustion and Flame* 159.8 (2012), pp. 2718–2741.

[41] R. A. Clark, J. H. Ferziger, and W. Reynolds. “Evaluation of subgrid-scale models using an accurately simulated turbulent flow.” In: *Journal of Fluid Mechanics* 91.01 (1979), pp. 1–16.

[42] O. Colin, F. Ducros, D. Veynante, and P. T. “A thickened flame model for large eddy simulations of turbulent premixed combustion.” In: *Phys. Fluids* 12 (2000), pp. 1843–1863.

[43] A. W. Cook. “Determination of the constant coefficient in scale similarity models of turbulence.” In: *Physics of Fluids* 9 (1997), p. 1485.

[44] A. W. Cook and J. J. Riley. “A subgrid model for equilibrium chemistry in turbulent flows.” In: *Physics of fluids* 6 (1994), p. 2868.

[45] A. W. Cook and J. J. Riley. “Direct numerical simulation of a turbulent reactive plume on a parallel computer.” In: *Journal of Computational Physics* 129.2 (1996), pp. 263–283.

[46] F. Dabireau, B. Cuenot, O. Vermorel, and T. Poinsot. "Interaction of flames of H_2 + O_2 with inert walls." In: *Combustion and flame* 135.1 (2003), pp. 123–133.

[47] L. Davidson. "Large eddy simulations: how to evaluate resolution." In: *International Journal of Heat and Fluid Flow* 30.5 (2009), pp. 1016–1025.

[48] L. Davidson. "Fluid mechanics, turbulent flow and turbulence modeling." In: *Div. of Fluid Dynamics, Dep. of Applied Mechanics, Chalmers University of Technology, Göteborg, Sweden* (2011).

[49] A. De and S. Acharya. "Dynamics of upstream flame propagation in a hydrogen-enriched premixed flame." In: *International Journal of Hydrogen Energy* 37.22 (2012), pp. 17294 –17309. ISSN: 0360-3199.

[50] E. Demosthenous, G. Borghesi, E. Mastorakos, and R. Cant. "Direct Numerical Simulations of n-Heptane Spray Autoignition in Methane-air Mixtures Relevant to Dual-fuel Engines." In: *52nd Aerospace Sciences Meeting, AIAA SciTech, American Institute of Aeronautics and Astronautics* (2014).

[51] B. Despres. "Lax theorem and finite volume schemes." In: *Mathematics of computation* 73.247 (2004), pp. 1203–1234.

[52] F. Dinkelacker and S. Hölzler. "Investigation of a turbulent flame speed closure approach for premixed flame calculations." In: *Combustion science and technology* 158.1 (2000), pp. 321–340.

[53] P. Domingo, L. Vervisch, S. Payet, and R. Hauguel. "DNS of a premixed turbulent V flame and LES of a ducted flame using a FSD-PDF subgrid scale closure with FPI-tabulated chemistry." In: *Combustion and Flame* 143.4 (2005), pp. 566–586.

[54] A. Donini, R. J. Bastiaans, J. A. van Oijen, and L. P. H. de Goey. "The Application of Flamelet-Generated Manifold in the Modeling of Stratified Premixed Cooled Flames." In: *ASME Turbo Expo 2014: Turbine Technical Conference and Exposition*. American Society of Mechanical Engineers. 2014, V04BT04A022–V04BT04A022.

[55] L. Durand and W. Polifke. "Implementation of the thickened flame model for large eddy simulation of turbulent premixed combustion in a commercial solver." In: pp. 869–878.

[56] F. Durst and M. Schäfer. "A parallel block-structured multigrid method for the prediction of incompressible flows." In: *International journal for numerical methods in fluids* 22.6 (1996), pp. 549–565.

[57] F. Durst. *Fluid mechanics: an introduction to the theory of fluid flows*. Springer, 2008.

[58] M. Düsing, A. Sadiki, and J. Janicka. "Towards a classification of models for the numerical simulation of premixed combustion based on a generalized regime diagram." In: *Combustion Theory and Modelling* 10.1 (2006), pp. 105–132.

[59] C. Duwig and M. J. Dunn. "Large Eddy Simulation of a premixed jet flame stabilized by a vitiated co-flow: Evaluation of auto-ignition tabulated chemistry." In: *Combustion and Flame* 160.12 (2013), pp. 2879 –2895. ISSN: 0010-2180.

[60] T. M. Eidson. “Numerical simulation of the turbulent Rayleigh–Bénard problem using subgrid modelling.” In: *Journal of Fluid Mechanics* 158.1 (1985), pp. 245–268.

[61] A. Faghri, Y. Zhang, and J. R. Howell. *Advanced heat and mass transfer*. Global Digital Press, 2010.

[62] A. Favre. “Statistical equations of turbulent gases.” In: *Problems of hydrodynamics and continuum mechanics* (1969), pp. 231–266.

[63] J. H. Ferziger and M. Perić. *Computational methods for fluid dynamics*. Vol. 3. Springer Berlin, 1996.

[64] B. Fiorina, R Mercier, G. Kuenne, A. Ketelheun, A. Avdić, J Janicka, D Geyer, A Dreizler, E Alenius, C Duwig, et al. “Challenging modeling strategies for LES of non-adiabatic turbulent stratified combustion.” In: *Combustion and Flame* (2015).

[65] B. Fiorina, R. Baron, O. Gicquel, D. Thevenin, S. Carpentier, N. Darabiha, et al. “Modelling non-adiabatic partially premixed flames using flame-prolongation of ILDM.” In: *Combustion Theory and Modelling* 7.3 (2003), pp. 449–470.

[66] B. Fiorina, O. Gicquel, L. Vervisch, S. Carpentier, and N. Darabiha. “Premixed turbulent combustion modeling using tabulated detailed chemistry and PDF.” In: vol. 30. 1. Elsevier, 2005, pp. 867–874.

[67] A. Fluent. “12.0 Theory Guide.” In: *Ansys Inc* 5 (2009).

[68] H. Forkel and J. Janicka. “Large-eddy simulation of a turbulent hydrogen diffusion flame.” In: *Flow, turbulence and combustion* 65.2 (2000), pp. 163–175.

[69] R. O. Fox. *Computational models for turbulent reacting flows*. Cambridge University Press, 2003.

[70] D. A. Frank-Kamenetskii and N. Thon. *Diffusion and heat exchange in chemical kinetics*. Princeton University Press Princeton, 1955.

[71] M. Freitag, M. Klein, M. Gregor, D. Geyer, C. Schneider, A. Dreizler, and J. Janicka. “Mixing analysis of a swirling recirculating flow using DNS and experimental data.” In: *International journal of heat and fluid flow* 27.4 (2006), pp. 636–643.

[72] J. Fröhlich and D. von Terzi. “Hybrid LES/RANS methods for the simulation of turbulent flows.” In: *Progress in Aerospace Sciences* 44.5 (2008), pp. 349–377.

[73] C. Fureby, G. Tabor, H. Weller, and A. Gosman. “A comparative study of subgrid scale models in homogeneous isotropic turbulence.” In: *Physics of fluids* 9 (1997), p. 1416.

[74] M. Germano, U. Piomelli, P. Moin, and W. H. Cabot. “A dynamic subgrid-scale eddy viscosity model.” In: *Physics of Fluids A: Fluid Dynamics* 3 (1991), pp. 1760–1765.

[75] L. Y. Gicquel, G. Staffelbach, and T. Poinsot. “Large Eddy Simulations of gaseous flames in gas turbine combustion chambers.” In: *Progress in Energy and Combustion Science* (2012).

[76] O. Gicquel, N. Darabiha, and D. Thévenin. "Liminar premixed hydrogen/air counterflow flame simulations using flame prolongation of ILDM with differential diffusion." In: *Proceedings of the Combustion Institute* 28.2 (2000), pp. 1901–1908.

[77] A. Gruber, R. Sankaran, E. Hawkes, and J. Chen. "Turbulent flame-wall interaction: a direct numerical simulation study." In: *Journal of Fluid Mechanics* 658 (2010), pp. 5–32.

[78] Y. Guo, C.-X. Xu, G. Cui, Z. Zhang, and L. Shao. "Large eddy simulation of scalar turbulence using a new subgrid eddy diffusivity model." In: *International journal of heat and fluid flow* 28.2 (2007), pp. 268–274.

[79] R. Haghighi. "Towards understanding multicomponent chemistry interaction using direct numerical simulation." PhD thesis. Darmstadt: Technische Universität Darmstadt, June 2015.

[80] C. Hasse and N. Peters. "A two mixture fraction flamelet model applied to split injections in a DI diesel engine." In: vol. 30. 2. Elsevier, 2005, pp. 2755–2762.

[81] J. Hertzberg, I. Shepherd, and L. Talbot. "Vortex shedding behind rod stabilized flames." In: *Combustion and Flame* 86.1 (1991), pp. 1–11.

[82] J. L. Holechek. "Global trends in population, energy use and climate: implications for policy development, rangeland management and rangeland users." In: *The Rangeland Journal* (2013).

[83] K. Horiuti. "A new dynamic two-parameter mixed model for large-eddy simulation." In: *Physics of Fluids* 9 (1997), p. 3443.

[84] Y. Huai, B. Kniesner, A. Sadiki, and S. Jakirlić. "Large Eddy Simulations of Passive-scalar Mixing using a Tensorial Eddy Diffusivity-based SGS-Modeling." In: *Advances in Turbulence XI*. Ed. by J. Palma and A. Lopes. Vol. 117. Springer Proceedings Physics. 2007, pp. 630–632.

[85] Y. Huai. "Large Eddy Simulation in the Scalar Field." PhD thesis. Technische Universitität Darmstadt, 2005.

[86] Y. Huai and A. Sadiki. "Analysis and optimization of turbulent mixing with large eddy simulation." In: *ASME 2nd Joint US-European Fluids Engineering Summer Meeting, FEDSM*. Vol. 98416. 2006.

[87] M. Ihme, L. Shunn, and J. Zhang. "Regularization of reaction progress variable for application to flamelet-based combustion models." In: *Journal of Computational Physics* (2012).

[88] D. Incropera. "Bergman, and Lavine." In: *Fundamentals of heat and mass transfer* (2007).

[89] M. Irannezhad and L.-E. Eriksson. "Large Eddy Simulation of premixed flames with multi-step global reaction mechanisms." In: *Journal of Physics: Conference Series*. Vol. 318. 9. IOP Publishing. 2011, p. 092006.

[90] F. A. Jaberi and P. J. Colucci. "Large eddy simulation of heat and mass transport in turbulent flows. Part 1: Velocity field." In: *International Journal of Heat and Mass Transfer* 46.10 (2003), pp. 1811 –1825. ISSN: 0017-9310.

[91] F. A. Jaberi and P. J. Colucci. “Large eddy simulation of heat and mass transport in turbulent flows. Part 2: Scalar field.” In: *International journal of heat and mass transfer* 46.10 (2003), pp. 1827–1840.

[92] J. Janicka and W. Kollmann. “A two-variables formalism for the treatment of chemical reactions in turbulent H_2Air diffusion flames.” In: *Symposium (International) on Combustion*. Vol. 17. 1. Elsevier. 1979, pp. 421–430.

[93] J. Janicka and A. Sadiki. “Large eddy simulation of turbulent combustion systems.” In: vol. 30. 1. Elsevier, 2005, pp. 537–547.

[94] B. Janus, A. Dreizler, and J. Janicka. “Experiments on swirl stabilized non-premixed natural gas flames in a model gasturbine combustor.” In: *Proceedings of the Combustion Institute* 31.2 (2007), pp. 3091–3098.

[95] C Jiménez, F. Ducros, B. Cuenot, and B. Bédat. “Subgrid scale variance and dissipation of a scalar field in large eddy simulations.” In: *Physics of Fluids (1994-present)* 13.6 (2001), pp. 1748–1754.

[96] A. V. Johansson and P. M. Wikström. “DNS and modelling of passive scalar transport in turbulent channel flow with a focus on scalar dissipation rate modelling.” In: *Flow, turbulence and combustion* 63.1-4 (2000), pp. 223–245.

[97] G. Jung, Y. Sung, B. Choi, C. Lee, and M. Lim. “Major sources of hydrocarbon emissions in a premixed charge compression ignition engine.” In: *International Journal of Automotive Technology* 13.3 (2012), pp. 347–353.

[98] H. S. Kang and C. Meneveau. “Passive scalar anisotropy in a heated turbulent wake: new observations and implications for large-eddy simulations.” In: *Journal of Fluid Mechanics* 442 (2001), pp. 161–170.

[99] S. Kawai and J. Larsson. “Wall-modeling in large eddy simulation: Length scales, grid resolution, and accuracy.” In: *Physics of Fluids* 24 (2012), p. 015105.

[100] K. Kemenov, H. Wang, and P. SB. “Turbulence Resolution Scale Dependence in Large-eddy Simulations of a Jet Flame.” In: *Flow, Turbulence and Combustion* (2011), pp. 1–33.

[101] K. A. Kemenov, H. Wang, and S. B. Pope. “Modelling effects of subgrid-scale mixture fraction variance in LES of a piloted diffusion flame.” In: *Combustion Theory and Modelling* 16.4 (2012), pp. 611–638.

[102] A. Kempf. *Large Eddy Simulation of Non Premixed Turbulent Flames*. Fortschritt-Berichte VDI.: Energieerzeugung. VDI-Verlag, 2004. ISBN: 9783183513062.

[103] A. Ketelheun, C. Olbricht, F. Hahn, and J. Janicka. “ASME Turbo Expo Conf. Proc.” In: (2009), pp. 695–705.

[104] A. Ketelheun, G. Kuenne, and J. Janicka. “Heat Transfer Modeling in the Context of Large Eddy Simulation of Premixed Combustion with Tabulated Chemistry.” In: *Flow, Turbulence and Combustion* (2013), pp. 1–27.

[105] J. Kim, P. Moin, and R. Moser. “Turbulence statistics in fully developed channel flow at low Reynolds number.” In: *Journal of Fluid Mechanics* 177.1 (1987), pp. 133–166.

[106] W.-W. Kim and S. Menon. "A new dynamic one-equation subgrid-scale model for large eddy simulations." In: *AIAA, Aerospace Sciences Meeting and Exhibit, 33 rd, Reno, NV*. 1995.

[107] M. Klein, A. Kempf, and J. Janicka. "Mixing analysis of a plane jet using direct numerical simulation." In: *Proceedings of Euromech 10th European Turbulence Conference*. 2004.

[108] M. Klein, A. Sadiki, and J. Janicka. "A digital filter based generation of inflow data for spatially developing direct numerical or large eddy simulations." In: *Journal of Computational Physics* 186.2 (2003), pp. 652–665.

[109] A. Y. Klimenko. "Multicomponent diffusion of various admixtures in turbulent flow." In: *Fluid Dynamics* 25.3 (1990), pp. 327–334.

[110] O. M. Knio, H. N. Najm, and P. S. Wyckoff. "A semi-implicit numerical scheme for reacting flow: II. stiff, operator-split formulation." In: *Journal of Computational Physics* 154.2 (1999), pp. 428–467.

[111] A. N. Kolmogorov. "A refinement of previous hypotheses concerning the local structure of turbulence in a viscous incompressible fluid at high Reynolds number." In: *J. Fluid Mech* 13.1 (1962), pp. 82–85.

[112] B. Kosovic. "Subgrid-scale modelling for the large-eddy simulation of high-Reynolds-number boundary layers." In: *Journal of Fluid Mechanics* 336.1 (1997), pp. 151–182.

[113] G. Kuenne, A. Ketelheun, and J. Janicka. "LES modeling of premixed combustion using a thickened flame approach coupled with FGM tabulated chemistry." In: *Combustion and Flame* 158.9 (2011), pp. 1750–1767.

[114] G. Kuenne, F. Seffrin, F. Fuest, T. Stahler, A. Ketelheun, D. Geyer, J. Janicka, and A. Dreizler. "Experimental and numerical analysis of a lean premixed stratified burner using 1D Raman/Rayleigh scattering and large eddy simulation." In: *Combustion and Flame* 159.8 (2012), pp. 2669–2689.

[115] V. Kumar. *Modeling and Numerical Simulations of Complex Transport Phenomena in Crystal Growth Processes: Modellierung und Numerische Simulationen Komplexer Transportvorgänge in Kristallzüchtungsprozessen*. Berichte aus der Strömungstechnik. Shaker, 2006.

[116] T. Landenfeld, A. Sadiki, and J. Janicka. "A turbulence-chemistry interaction model based on a multivariate presumed beta-pdf method for turbulent flames." In: *Flow, turbulence and combustion* 68.2 (2002), pp. 111–135.

[117] B. Launder, G. J. Reece, and W. Rodi. "Progress in the development of a Reynolds-stress turbulence closure." In: *Journal of fluid mechanics* 68.03 (1975), pp. 537–566.

[118] H. Le, P. Moin, and J. Kim. "Direct numerical simulation of turbulent flow over a backward-facing step." In: *Journal of Fluid Mechanics* 330.1 (1997), pp. 349–374.

[119] T. Lehnhäuser and M. Schäfer. "Improved linear interpolation practice for finite-volume schemes on complex grids." In: *International journal for numerical methods in fluids* 38.7 (2002), pp. 625–645.

[120] H. Leister and M. Peric. "Vectorized strongly implicit solving procedure for a seven-diagonal coefficient matrix." In: *International Journal of Numerical Methods for Heat & Fluid Flow* 4.2 (1994), pp. 159–172.

[121] A. Leonard. "Energy cascade in large-eddy simulations of turbulent fluid flows." In: *Advances in Geophysics* 18 (1975), pp. 237–248.

[122] H. Li, H. Zhen, C. Leung, and C. Cheung. "Nozzle effect on heat transfer and CO emission of impinging premixed flames." In: *International Journal of Heat and Mass Transfer* 54.1 (2011), pp. 625–635.

[123] D. Lilly. "A proposed modification of the Germano subgrid-scale closure method." In: *Physics of Fluids A: Fluid Dynamics* 4 (1992), p. 633.

[124] A. Linan, P. Orlandi, R. Verzicco, and F. Higuera. "Effects of non-unity Lewis numbers in diffusion flames." In: *Proceedings of the CTR Summer Program, Stanford University* (1994), pp. 5–18.

[125] A. Lipatnikov and J. Chomiak. "Dependence of heat release on the progress variable in premixed turbulent combustion." In: *Proceedings of the Combustion Institute* 28.1 (2000), pp. 227–234.

[126] B. Llc. *Turbulence Models: Reynolds-Averaged Navier-stokes Equations, Spalart-allmaras Turbulence Model, Large Eddy Simulation, Cebeci-smith Model*. General Books LLC, 2010. ISBN: 9781158502967.

[127] M. Löffler, S. Pfadler, F. Beyrau, A. Leipertz, F. Dinkelacker, Y. Huai, and A. Sadiki. "Experimental determination of the sub-grid scale scalar flux in a non-reacting jet-flow." In: *Flow, Turbulence and Combustion* 81.1-2 (2008), pp. 205–219.

[128] U. Maas and S. B. Pope. "Implementation of simplified chemical kinetics based on intrinsic low-dimensional manifolds." In: *Symposium (International) on Combustion*. Vol. 24. 1. Elsevier. 1992, pp. 103–112.

[129] U. Maas and S. B. Pope. "Simplifying chemical kinetics: intrinsic low-dimensional manifolds in composition space." In: *Combustion and Flame* 88.3 (1992), pp. 239–264.

[130] B. Manickam, S. Muppala, J. Franke, and F. Dinkelacker. "Numerical Simulation of Rod Stabilized Flames." In: *Fifth European Conference on Computational Fluid Dynamics, ECCOMAS, Lisbon (Portugal)*. 2010.

[131] M. Mann, A. Singh, T. Kissel, and A. Dreizler. *Simultane Messung von CO Konzentrationen und Temperatur in Staupunkt-stabilisierten Flammen*. Karlsruhe: Deutscher Flammentag Verbrennung und Feuerung Karlsruhe, 2011.

[132] T. Mantel and J.-M. Samaniego. "Fundamental mechanisms in premixed turbulent flame propagation via vortex–flame interactions part II: numerical simulation." In: *Combustion and Flame* 118.4 (1999), pp. 557–582.

[133] C. Meneveau and J. Katz. "Scale-invariance and turbulence models for large-eddy simulation." In: *Annual Review of Fluid Mechanics* 32.1 (2000), pp. 1–32.

[134] S. Menon, P. McMurtry, and A. Kerstein. "A linear eddy mixing model for large eddy simulation of turbulent combustion." In: *LES of Complex Engineering and Geophysical Flows (ed. B. Galperin and S. Orszag)* (1993), pp. 287–314.

[135] S. Menon, P. Yeung, and W. Kim. "Effect of subgrid models on the computed interscale energy transfer in isotropic turbulence." In: *Computers & fluids* 25.2 (1996), pp. 165–180.

[136] S. K. Menon, P. A. Boettcher, and G. Blanquart. "Enthalpy based approach to capture heat transfer effects in premixed combustion." In: *Combustion and Flame* (2013).

[137] Y. Mizobuchi, J. Shinjo, S. Ogawa, and T. Takeno. "A numerical study on the formation of diffusion flame islands in a turbulent hydrogen jet lifted flame." In: *Proceedings of the Combustion Institute* 30.1 (2005), pp. 611–619.

[138] P. Moin and K. Mahesh. "Direct numerical simulation: a tool in turbulence research." In: *Annual Review of Fluid Mechanics* 30.1 (1998), pp. 539–578.

[139] H. Muhamed. "LES, RANS and combined simulation of Impinging Flows and Heat Transfer." PhD thesis. TU Delft, 2006.

[140] F. Nicoud and F. Ducros. "Subgrid-scale stress modelling based on the square of the velocity gradient tensor." In: *Flow, Turbulence and Combustion* 62.3 (1999), pp. 183–200.

[141] Y.-S. Niu, L. Vervisch, and P. D. Tao. "An optimization-based approach to detailed chemistry tabulation: Automated progress variable definition." In: *Combustion and Flame* 160.4 (2013), pp. 776–785.

[142] J. v. Oijen and L. d. Goey. "Modelling of premixed laminar flames using flamelet-generated manifolds." In: *Combustion Science and Technology* 161.1 (2000), pp. 113–137.

[143] J. A. van Oijen. *Flamelet-generated manifolds: development and application to premixed laminar flames*. Technische Universiteit Eindhoven, 2002.

[144] A. E. Outlook. "Energy Information Administration." In: *United States* (2010).

[145] B. E. Outlook. "2030." In: *London, January* (2012).

[146] H. Ouvrard, B. Koobus, M.-V. Salvetti, S. Camarri, and A. Dervieux. *Variational Multiscale LES and Hybrid RANS/LES Parallel Simulation of Complex Unsteady Flows*. Springer, 2008, pp. 465–478.

[147] S. V. Patankar. *Numerical heat transfer and fluid flow*. Taylor & Francis, 1980.

[148] S. Patil and D. Tafti. "Large-Eddy Simulation of Flow and Convective Heat Transfer in a Gas Turbine Can Combustor With Synthetic Inlet Turbulence." In: *Journal of engineering for gas turbines and power* 134.7 (2012).

[149] S.-H. Peng and L. Davidson. "On a subgrid-scale heat flux model for large eddy simulation of turbulent thermal flow." In: *International journal of heat and mass transfer* 45.7 (2002), pp. 1393–1405.

[150] N. Peters. "Laminar diffusion flamelet models in non-premixed turbulent combustion." In: *Progress in energy and combustion science* 10.3 (1984), pp. 319–339.

[151] N. Peters. *Turbulent combustion*. Cambridge university press, 2000.

[152] S. Pfadler, F. Beyrau, and A. Leipertz. "Flame front detection and characterization using conditioned particle image velocimetry (CPIV)." In: *Optics express* 15.23 (2007), pp. 15444–15456.

[153] S. Pfadler, J. Kerl, F. Beyrau, A. Leipertz, A. Sadiki, J. Scheuerlein, and F. Dinkelacker. "Direct evaluation of the subgrid scale scalar flux in turbulent premixed flames with conditioned dual-plane stereo PIV." In: *Proceedings of the Combustion Institute* 32.2 (2009), pp. 1723–1730.

[154] S. Pfadler, F. Dinkelacker, F. Beyrau, and A. Leipertz. "High resolution dual-plane stereo-PIV for validation of subgrid scale models in large-eddy simulations of turbulent premixed flames." In: *Combustion and Flame* 156.8 (2009), pp. 1552–1564.

[155] C. D. Pierce and P. Moin. "Progress-variable approach for large-eddy simulation of non-premixed turbulent combustion." In: *Journal of Fluid Mechanics* 504 (2004), pp. 73–97.

[156] U. Piomelli. "Large-eddy simulation: achievements and challenges." In: *Progress in Aerospace Sciences* 35.4 (1999), pp. 335–362.

[157] U. Piomelli. "Wall-Modeled Large-Eddy Simulations: Present Status and Prospects." In: *Direct and Large-Eddy Simulation VII*. Ed. by V. Armenio, B. Geurts, and J. Frï¿½hlich. Vol. 13. ERCOFTAC Series. Springer Netherlands, 2010, pp. 1–10. ISBN: 978-90-481-3651-3.

[158] U. Piomelli and E. Balaras. "Wall-layer models for large-eddy simulations." In: *Annual review of fluid mechanics* 34.1 (2002), pp. 349–374.

[159] U. Piomelli and J. Chasnov. "Large-eddy simulations: theory and applications." In: (1996), pp. 269–336.

[160] H. Pitsch. "Large Eddy Simulation of Turbulent Combustion." In: *Ann. Rev. Fluid Mech.* 38 (2006), pp. 453–482.

[161] H. Pitsch and L. d. Lageneste. "Comparison of turbulent premixed flames at different turbulence levels." In: *Center for Turbulence Research Annual Research Briefs* (2002), pp. 91–101.

[162] H. Pitsch. "Large-eddy simulation of turbulent combustion." In: *Annu. Rev. Fluid Mech.* 38 (2006), pp. 453–482.

[163] T. Poinsot and D. Veynante. *Theoretical and numerical combustion*. RT Edwards Incorporated, 2005.

[164] T. Poinsot, D. Haworth, and G. Bruneaux. "Direct simulation and modeling of flame-wall interaction for premixed turbulent combustion." In: *Combustion and Flame* 95.1 (1993), pp. 118–132.

[165] S. Pope. "Computations of turbulent combustion: progress and challenges." In: *Symposium (International) on Combustion*. Vol. 23. 1. Elsevier. 1991, pp. 591–612.

[166] S. B. Pope. *Turbulent flows*. Cambridge university press, 2000.

[167] F. Porté-Agel, C. Meneveau, and M. Parlange. "A scale-dependent dynamic model for large-eddy simulation: application to the atmospheric boundary layer." In: *APS Division of Fluid Dynamics Meeting Abstracts*. Vol. 1. 1998.

[168] F. Porté-Agel. "A scale-dependent dynamic model for scalar transport in large-eddy simulations of the atmospheric boundary layer." In: *Boundary-layer meteorology* 112.1 (2004), pp. 81–105.

[169] K. Protocol. "United Nations framework convention on climate change." In: *Kyoto Protocol, Kyoto* (1997).

[170] D. I. Pullin. "A vortex-based model for the subgrid flux of a passive scalar." In: *Physics of Fluids* 12 (2000), p. 2311.

[171] C. Rhie and W. Chow. "Numerical study of the turbulent flow past an airfoil with trailing edge separation." In: *AIAA journal* 21.11 (1983), pp. 1525–1532.

[172] G. Ribert, M. Champion, O. Gicquel, N. Darabiha, and D. Veynante. "Modeling nonadiabatic turbulent premixed reactive flows including tabulated chemistry." In: *Combustion and flame* 141.3 (2005), pp. 271–280.

[173] A. Roux, L. Gicquel, Y. Sommerer, and T. Poinsot. "Large eddy simulation of mean and oscillating flow in a side-dump ramjet combustor." In: *Combustion and Flame* 152.1 (2008), pp. 154–176.

[174] M. RUBINSTEIN and R. Nelson. "Automated structural synthesis using a reduced number of design coordinates." In: *Aiaa Journal* 11.4 (1973), pp. 489–494.

[175] A. Sadiki. *Extended Thermodynamics as Modeling Tool of Turbulence in Fluid Flows*. Ed. by Y. Wang and K. Hutter. Berichte aus der Mathematik. Shaker Verlag GmbH, 2005. ISBN: 9783832236007.

[176] A. Sadiki, S. Jakirlic, and K. Hanjalic. "Towards a thermodynamically consistent, anisotropy-resolving turbulence model for conjugate flow, heat and mass transfer." In: *Turbulence, Heat and Mass Transfer* 4 (2003), pp. 545–552.

[177] P. Sagaut. *Large eddy simulation for incompressible flows*. Vol. 3. Springer Berlin, 2000.

[178] P. Sagaut. *Large Eddy Simulation for incompressible Flows*. Berlin: Springer, 2001.

[179] M. V. Salvetti, H. Ouvrard, B. Koobus, and A. Dervieux. "Mixed subgrid scale models for classical and variational multiscale large-eddy simulations on unstructured grids." In: *Direct and Large-Eddy Simulation VIII*. Springer, 2011, pp. 107–112.

[180] F. Sarghini, U. Piomelli, and E. Balaras. "Scale-similar models for large-eddy simulations." In: *Physics of Fluids* 11.6 (1999), p. 1596.

[181] M. Schäfer. *Computational engineering: introduction to numerical methods*. Springer, 2006.

[182] T. Schmitt, A. Sadiki, B. Fiorina, and D. Veynante. "Impact of dynamic wrinkling model on the prediction accuracy using the F-TACLES combustion model in swirling premixed turbulent flames." In: *Proceedings of the Combustion Institute* (2012).

[183] M. Schwind. “Modeling and investigation of perforated plateï¿½s influence on turbulence in nozzle flow using Large Eddy Simulation.” Bachelor Thesis. Institut fuer Energie und Kraftwerkstechnik, Technische Universität Darmstadt, 2013.

[184] O. Sergeev, A. Shashkov, and A. Umanskii. “Thermophysical properties of quartz glass.” In: *Journal of engineering physics* 43.6 (1982), pp. 1375–1383.

[185] V. Sick, M. Drake, and T. Fansler. “High-speed imaging for direct-injection gasoline engine research and development.” In: *Experiments in Fluids* 49 (2010), pp. 937–947.

[186] A. Singh, M. Mann, T. Kissel, J. Brübach, and A. Dreizler. “Simultaneous measurements of temperature and CO concentration in stagnation stabilized flames.” In: *Flow, Turbulence and Combustion* (2011), pp. 1–17.

[187] J. Smagorinsky. “General circulation experiments with the primitive equations: I. the basic experiment*.” In: *Monthly weather review* 91.3 (1963), pp. 99–164.

[188] G. Smith, D. Golden, M Frenklach, N. Moriarty, B Eiteneer, M. Goldenberg, C. Bowman, R. Hanson, S. Song, V. Lissianski WCG Jr., and Z. Qin. *GRI-Mech 3.0. www.me.berkeley.edu/gri_mech/*, 2000.

[189] L. Somers. *The simulation of flat flames with detailed and reduced chemical models.* Eindhoven University of Technology., 1994.

[190] K. Sone. “Modeling and simulation of axisymmetric stagnation flames.” PhD thesis. California Institute of Technology, 2007.

[191] P. R. Spalart. “Detached-eddy simulation.” In: *Annual Review of Fluid Mechanics* 41 (2009), pp. 181–202.

[192] C. Speziale. “Turbulence modeling for time-dependent RANS and VLES: a review.” In: *AIAA journal* 36.2 (1998), pp. 173–184.

[193] C. G. Speziale and T. B. Gatski. “Analysis and modelling of anisotropies in the dissipation rate of turbulence.” In: *Journal of Fluid Mechanics* 344 (1997), pp. 155–180.

[194] K. R. Sreenivasan. “The passive scalar spectrum and the Obukhov–Corrsin constant.” In: *Physics of Fluids* 8 (1996), p. 189.

[195] O. T. Stein, B. Böhm, A. Dreizler, and A. M. Kempf. “Highly-resolved LES and PIV analysis of isothermal turbulent opposed jets for combustion applications.” In: *Flow, turbulence and combustion* 87.2-3 (2011), pp. 425–447.

[196] H. L. Stone. “Iterative solution of implicit approximations of multidimensional partial differential equations.” In: *SIAM Journal on Numerical Analysis* 5.3 (1968), pp. 530–558.

[197] L. Su. “Measurements of the three-dimensional scalar dissipation rate in gas-phase planar turbulent jets.” In: *Center for Turbulence Research Annual Briefs* (1998).

[198] O. Sun and L. Su. “Experimental assessment of scalar mixing models for large-eddy simulation.” In: *AIAA paper* 2550 (2004), p. 2004.

[199] L. Temmerman, M. A. Leschziner, C. P. Mellen, and J. Fröhlich. "Investigation of wall-function approximations and subgrid-scale models in large eddy simulation of separated flow in a channel with streamwise periodic constrictions." In: *International Journal of Heat and Fluid Flow* 24.2 (2003), pp. 157–180.

[200] S. R. Turns et al. *An introduction to combustion*. Vol. 499. McGraw-Hill New York, 1996.

[201] N. Uddin, S. O. Neumann, B. Weigand, and B. A. Younis. "Large-eddy simulations and heat-flux modeling in a turbulent impinging jet." In: *Numerical Heat transfer, Part A: Applications* 55.10 (2009), pp. 906–930.

[202] D. R. Unger and F. J. Muzzio. "Laser-induced fluorescence technique for the quantification of mixing in impinging jets." In: *AIChE Journal* 45.12 (1999), pp. 2477–2486.

[203] J. Van Oijen, R. Bastiaans, and L. De Goey. "Low-dimensional manifolds in direct numerical simulations of premixed turbulent flames." In: *Proceedings of the Combustion Institute* 31.1 (2007), pp. 1377–1384.

[204] J. Van Oijen and L. De Goey. "A numerical study of confined triple flames using a flamelet-generated manifold." In: *Combustion Theory and Modelling* 8.1 (2004), pp. 141–164.

[205] J. Van Oijen, F. Lammers, and L. De Goey. "Modeling of complex premixed burner systems by using flamelet-generated manifolds." In: *Combustion and Flame* 127.3 (2001), pp. 2124–2134.

[206] L. Vervisch and T. Poinsot. "Direct numerical simulation of non-premixed turbulent flames." In: *Ann. Rev. Fluid Mech* 30 (1998), pp. 655–692.

[207] D. Veynante, J. Piana, J. Duclos, and C. Martel. "Experimental analysis of flame surface density models for premixed turbulent combustion." In: *Symposium (International) on Combustion*. Vol. 26. 1. Elsevier. 1996, pp. 413–420.

[208] D. Veynante and L. Vervisch. "Turbulent combustion modeling." In: *Progress in energy and combustion science* 28.3 (2002), pp. 193–266.

[209] R. Viskanta. "Heat transfer to impinging isothermal gas and flame jets." In: *Experimental Thermal and Fluid Science* 6.2 (1993), pp. 111–134.

[210] A. Vreman. "An eddy-viscosity subgrid-scale model for turbulent shear flow: Algebraic theory and applications." In: *Physics of Fluids* 16 (2004), p. 3670.

[211] G. Wang, M. Boileau, and D. Veynante. "Implementation of a dynamic thickened flame model for large eddy simulations of turbulent premixed combustion." In: *Combustion and Flame* 158.11 (2011), pp. 2199–2213.

[212] Y. Wang and A. Trouv. "Direct numerical simulation of non-premixed flame-wall interactions." In: *J. Phys.: Conf. Ser.* 16 (2005), pp. 119–123.

[213] Z. Warhaft. "Passive scalars in turbulent flows." In: *Annual Review of Fluid Mechanics* 32.1 (2000), pp. 203–240.

[214] J. Warnatz, U. Maas, and R. Dibble. *Combustion. 1999*. Springer-Verlag.

[215] G. M. Watson, J. D. Munzar, and J. M. Bergthorson. "Diagnostics and modeling of stagnation flames for the validation of thermochemical combustion models for NOx predictions." In: *Energy & Fuels* (2013).

[216] J. Weckering, A. Sadiki, J. Janicka, E. Mastorakos, and R. Eggels. "A forced ignition probability analysis method using LES and Lagrangian particle monitoring." In: *Proceedings of the Combustion Institute* 33.2 (2011), pp. 2919–2925.

[217] J. Weckering. "Development of numerical modeling methods for prediction of ignition processes in aero-engines." PhD thesis. TU Darmstadt/EKT, 2011.

[218] B. Wegner. "A Large-Eddy Simulation Technique for the Prediction of Flow, Mixing and Combustion in Gas Turbine Combustors." PhD thesis. Technische Universität Darmstadt, 2007.

[219] B. Wegner, Y. Huai, and A. Sadiki. "Comparative study of turbulent mixing in jet in cross-flow configurations using LES." In: *International Journal of Heat and Fluid Flow* 25.5 (2004), pp. 767–775.

[220] B. Wegner, M. Staufer, A. Sadiki, and J. Janicka. "Study of flow and mixing in a generic GT combustor using LES." In: *Flow, Turbulence and Combustion* 79.4 (2007), pp. 389–403.

[221] C. K. Westbrook and F. L. Dryer. "Simplified reaction mechanisms for the oxidation of hydrocarbon fuels in flames." In: *Combustion science and technology* 27.1-2 (1981), pp. 31–43.

[222] F. M. White. *Viscous Fluid Flow 3e*. Tata McGraw-Hill Education, 1974.

[223] P. Wikström, S. Wallin, and A. V. Johansson. "Derivation and investigation of a new explicit algebraic model for the passive scalar flux." In: *Physics of fluids* 12 (2000), p. 688.

[224] D. Wilcox. "Turbulence modeling for CFD, 1998." In: *DCW Industries* (1998), p. 537.

[225] F. Williams. *Combustion Theory: The Fundamental Theory of Chemically Reacting Flow Systems*. Combustion science and engineering series. Perseus Books, 1985. ISBN: 9780201407778.

[226] W. Wu and U. Piomelli. "Large-eddy simulations of impinging jets at high Reynolds numbers." In: *Bulletin of the American Physical Society* 58 (2013).

[227] C. S. Yoo, E. S. Richardson, R. Sankaran, and J. H. Chen. "A DNS study on the stabilization mechanism of a turbulent lifted ethylene jet flame in highly-heated coflow." In: *Proceedings of the Combustion Institute* 33.1 (2011), pp. 1619–1627.

[228] C. S. Yoo, T. Lu, J. H. Chen, and C. K. Law. "Direct numerical simulations of ignition of a lean n-heptane/air mixture with temperature inhomogeneities at constant volume: Parametric study." In: *Combustion and Flame* 158.9 (2011), pp. 1727–1741.

[229] D. You and P. Moin. "A dynamic global-coefficient subgrid-scale eddy-viscosity model for large-eddy simulation in complex geometries." In: *Physics of Fluids* 19 (2007), p. 065110.

[230] A. Yun. "Development and analysis of advanced explicit algebraic turbulence and scalar flux models for complex engineering configurations." PhD thesis. TU Darmstadt, 2005.

[231] Y. B. Zeldovich and D. Frank-Kamenetskii. "A theory of thermal propagation of flame." In: *Zh. Fiz. Khim* 12.1 (1938), pp. 100–105.

[232] Y. Zhang and K. Bray. "Characterization of impinging jet flames." In: *Combustion and flame* 116.4 (1999), pp. 671–674.

List of own publications

[233] N. Aluri, P. Pantangi, S. Muppala, and F. Dinkelacker. "A numerical study promoting algebraic models for the Lewis number effect in atmospheric turbulent premixed bunsen flames." In: *Flow, turbulence and combustion* 75.1-4 (2005), pp. 149–172.

[234] A. Hosseinzadeh, P. Pantangi, A. Sadiki, and J. Janicka. "Large Eddy Simulation of Scalar Field in a High-Pressure Combustor fueled with Pre-Vaporized Kerosene." In: In: 83rd Annual Meeting of the International Association of Applied Mathematics and Mechanics, The GAMM, March 26-30, 2012.

[235] S. Kneissl, D. Sternel, M. Schäfer, P. Pantangi, A. Sadiki, and J. Janicka. "Integral Model for Simulating Gas Turbine Combustion Chambers." In: *Flow and Combustion in Advanced Gas Turbine Combustors*. Springer, 2013, pp. 325–347.

[236] J. M. Mejía, A. Sadiki, A. Molina, F. Chejne, and P. Pantangi. "Large Eddy Simulation of the Mixing of a Passive Scalar in a High-Schmidt Turbulent Jet." In: *Journal of Fluids Engineering* 137.3 (2015), p. 031301.

[237] P. Pantangi, d. H. Ying, and A. Sadiki. "A Tensorial Eddy Diffusivity based Subgrid Scale Model for Scalar Flux and its Validation in Turbulent Reactive Flow." In: In: 83rd Annual Meeting of the International Association of Applied Mathematics and Mechanics, The GAMM, March 26-30, 2012.

[238] P. Pantangi, M. Chirgui, F. Dinkelacker, and A. Sadiki. "LES of Premixed V-Flame Using Anisotropic SGS Scalar Flux Model." In: Seventh Mediterranean Combustion Symposium, Cagliari, Sardinia, 2011.

[239] P. Pantangi, A. Sadiki, J. Janicka, M. Hage, A. Dreizler, v. J. Oijen, C. Hassa, J. Heinze, and U. Meier. "Study of flow and combustion in a generic combustor fuelled with prevaporized kerosene using LES and FGM." In: Tagungsband 25. Deutscher Flammentag, 14. 15.09.11, Karlsruhe (2011).

[240] P. Pantangi, Y. Huai, and A. Sadiki. "Mixing Analysis and Optimization in Jet Mixer Systems by Means of Large Eddy Simulation." In: *Micro and Macro Mixing*. Springer, 2010, pp. 205–226.

[241] P. Pantangi, A. Sadiki, J. Janicka, M. Hage, A. Dreizler, J. van Oijen, C. Hassa, J. Heinze, and U. Meier. "Les of pre-vaporized kerosene combustion at high pressures in a single sector combustor taking advantage of the flamelet Generated manifolds method." In: Vancouver, Canada: Proceedings of ASME Turbo Expo 2011, 2011.

[242] P. Pantangi, M. Chrigui, J. v. Oijen, A. Hosseinzadeh, A. Sadiki, and J. Janicka. "LES of low turbulent non-adiabatic combustion with tabulated chemistry." In: *Engineering Turbulence Modelling and Measurements*. Vol. ETMM10: 10th International ERCOFTAC Symposium. Marbella, Spain, 2014.

[243] P. Pantangi, A. Sadiki, J. Janicka, M. Mann, and A. Dreizler. "LES of Premixed Methane Flame Impinging on the Wall Using Non-adiabatic Flamelet Generated Manifold (FGM) Approach." In: *Flow, Turbulence and Combustion* (2014), pp. 1–32. ISSN: 1386-6184.

[244] P. Pradeep and S. Amsini. "Subgrid Scale Modeling of Scalar Flux Transport based on a Tensorial Eddy Diffusivity and Validation in Turbulent Reactive Flows." In: *GAMM 2014*. Erlangen, Germany, 2014.

[245] P. Pradeep, S. Amsini, and J. Janicka. "Evaluation of Heat Flux Near Wall while Flame-Wall Interaction." In: *GAMM 2014*. Erlangen, Germany, 2014.

[246] TRDDC. *Helping Jhagadia Copper Limited reduce cost of production by 8-10 %*. available at http://www.tcs.com/resources/case_studies/Pages/Jhagadia-Copper-reduce-cost-of-production.aspx: Tata Research Development and Design Centre (TCS), 2008.

[247] A. Wahid, M. Amir, C. Mouldi, P. Pradeep, and S. Amsini. "Effect of unsteady calculations and their influence on the dispersion modeling." In: Agadir, Morocco: International Symposium on Multiphase flow and Transport Phenomena, April 22-25, 2012.

Curriculum Vitae

Name	Pradeep Kumar Goud Pantangi	
Birthdate	22.04.1979	
Birthplace	Nalgonda, Telangana, India	
High school (5-10)	06/1990- 04/1995	Jawahar Navodaya Vidyalaya, chalakurthy camp, Dist. Nalgonda, India High school certificate
Higher secondary school(11-12)	07/1995 - 06/1997	Board of Intermediate Education, Andhra Pradesh, India Higher secondary school certificate
Bachelor	07/1997 - 06/2001	Jawaharlal Nehru Technological University, Hyderabad, INDIA Bachelor of Technology in Chemical Engineering
Master	10/2001 - 06/2004	Friedrich-Alexander University Erlangen-Nuernberg, Erlangen, Germany Master of science in Chemical Engineering
Internship	1/2003 - 10/2003	Draeger Safety AG & Co. KGaA, Luebeck, Germany Internship
Employer	11/2004 - 04/2005	Fluidyn - Consultancy & Software Ltd. Bangalore, INDIA Research Engineer
Employer	05/2005 - 11/2007	Tata Research Development & Design Centre, Pune, INDIA Scientist
Employer	11/2007 - 01/2014	Technische Universität Darmstadt, Germany at the department of Energy and Power Plant Technology (EKT), Prof. Dr.-Ing. Johannes Janicka Wissenschaftlicher Mitarbeiter
Employer	02/2014 - 11/2014	Bundy Refrigeration GmbH, Munich, Germany Sales Application Engineer
Employer	12/2014 - Present	Hi-Lex Europe GmbH, Schweinfurt, Germany Key Account Manager